University of Southampton

Faculty of Engineering and Physical Sciences

School of Chemistry

Instrument Development and a Total Scattering Investigation of Aqueous Magnesium Sulfate

by

Daniel John Michael Irving

Thesis for the Degree of Doctor of Philosophy

April 2022

University of Southampton

Abstract

Faculty of Engineering and Physical Sciences

School of Chemistry

Doctor of Philosophy

Instrument Development and a Total Scattering Investigation

of Aqueous Magnesium Sulfate

by

Daniel John Michael Irving

Non-crystalline materials, such as amorphous and glassy phases, and aqueous systems, remain an understudied yet important class of condensed materials. Many techniques can be used to enable structure elucidation of these materials, but few can match the application of total scattering and subsequent fitting of the observed data with atomistic models.

This work will examine the feasibility of using a laboratory-based single crystal diffractometer for total scattering experiments that previously would often have required synchrotron radiation. The instrument has a rather unique curved image-plate detector that is ideal for collecting very low noise data over a large scattering angle. When a silver tube is fitted this enables a theoretical Qmax of 22.4 $Å^{-1}$ to be reached and data collected rapidly. Suitable data collection strategies and data reduction processes were evaluated through the study of a number of standard materials ranging from crystalline and nanocrystalline to amorphous and aqueous. The quality of the data and refined models were then evaluated.

Using X-ray data from this novel setup, in combination with neutron scattering data, it was possible to use an empirical potential structure refinement (EPSR) approach to model the structural features of an aqueous sample of magnesium sulfate. Combining the isotopically substituted neutron data with the high quality in-house X-ray data enabled an extensive study of the structural features that exist within this aqueous salt. The structural features observed via this methodology highlight both the short-range ordering (first shell), similar to that found in previous studies, but also a distinct medium-range order describing the intermolecular structure not previously discussed in the literature. This highlights both the power of the refinement technique but also the capabilities of the laboratory X-ray scattering instrument.

With this initial study as a foundation, it was possible to use just X-ray data to confidently study changes to the structure induced by changing conditions. Firstly, the effects of varying temperature on a constant concentration solution were investigated and found to have minimal effect. Secondly varying temperature was used as a method of stabilising higher concentrations above the ambient saturation limit to begin weaving a narrative of how the structure changes as a function of concentration with the aim of probing conditions as the crystallisation point is approached. In these studies, large, more structured features were observed that resembled those found in the various crystalline phases of hydrated magnesium sulfate. EPSR has proven to be a very powerful technique, and in combination with the unique laboratory X-ray scattering instrument, has examined an aqueous structure in more detail than previous studies.

Table of Contents

Table of Tables

Table of Tables

Table of Figures

Research Thesis: Declaration of Authorship

Print name: DANIEL JOHN MICHAEL IRVING

Title of thesis: A Total Scattering Study of Aqueous Magnesium Sulfate

I declare that this thesis and the work presented in it are my own and has been generated by me as the result of my own original research.

I confirm that:

1. This work was done wholly or mainly while in candidature for a research degree at this University;
2. Where any part of this thesis has previously been submitted for a degree or any other qualification at this University or any other institution, this has been clearly stated;
3. Where I have consulted the published work of others, this is always clearly attributed;
4. Where I have quoted from the work of others, the source is always given. With the exception of such quotations, this thesis is entirely my own work;
5. I have acknowledged all main sources of help;
6. Where the thesis is based on work done by myself jointly with others, I have made clear exactly what was done by others and what I have contributed myself;
7. Parts of this work have been published as:-
   D. J. M. Irving, D. A. Keen and M. E. Light, *Rev. Sci. Instrum.*, 2021, **92**, 043107

Signature: .....Date: 14/02/2022

Acknowledgements

There are many people that deserve thanks for contributing both directly and indirectly to this project. The first person is my PhD supervisor, Dr Mark Light, without his help, guidance and know how throughout my PhD, it would not have been possible. He has been around for both the good times, where exciting results have finally been elucidated, but also the bad times through the COVID-19 pandemic. It is not possible to show my gratitude enough for his support and could not have asked for a better supervisor.

Secondly, I would like to thank my friends and family for their support throughout the journey that is a PhD, particularly for listening to my scientific ramblings despite having no idea what was going on. Special thanks goes to my mum and sisters, who have been there throughout my educational journey and offered support, it would not have been possible to get where I am without them. A special shoutout goes to everyone on level 2 (building 30) for their support throughout my three years in Southampton, including but not limited to our stressed trips to Costa and SUSU shop, our pub trips to watch rugby and our lunchtime ramblings, without this I would not have remained semi-sane. I'd also like to thank Dr Darren Bradshaw for his support both academically and emotionally via his check ins, hour long chats during the day but most importantly his tweets. Of the level 2 people, I'd like to particularly thank Tom Crickmore and Iona Doig for being there throughout the entire time in Southampton, you guys made it special (especially Tom who had no choice when it came to the lockdown, but we survived (and arguable thrived)).

Finally, I would like to thank the many people who helped and contributed to the research itself, without these people, the exciting work presented here would not have been possible. These people include Matilda Rhodes, who really jump started the $MgSO_4$ project, and without her initial research the full scope of the project would not have been achieved. I'd like to also thank Dr David Keen and Dr Thomas Headen and who continually helped with the setup of the Spider, assisting with data, software, and refinements, and collecting complementary neutron data. This allowed for a more rapid progression of the project and ultimately more interesting results. The final team I'd like to thank are the I15-1 beamline staff, who offered support throughout my PhD and continue to do so as I work alongside them.

Like having a child, it takes a village to raise a PhD, and as this research is my child, it is ultimately the village above who allowed it to form, and I am eternally grateful and hope we all stay in contact.

Definitions and Abbreviations

PDF ..... Pair Distribution Function

RDF ..... Radial Distribution Function

SDF ..... Spatial Density Function

EPSR ..... Empirical Potential Structure Refinement

PBU/SBU ..... Primary/Secondary Building Units

RTP ..... Room Temperature & Pressure

SBR ..... Small-Box Refinement

LBR ..... Large-Box refinement

SRM ..... Standard Reference Material

RMC ..... Reverse Monte-Carlo

CIP ..... Contact Ion Pair

SSIP ..... Solvent Separated Ion Pair

Chapter 1 Background & Theory

Material development and understanding ultimately dictates the technological advances within society, and as these materials increase in complexity, so too must the analysis techniques. Many novel materials now deviate from the true crystalline state and these defects alter their short-range order and ultimately their properties. Traditional diffraction techniques cannot probe this local short-range order, and therefore more complex scattering techniques must be applied. Total scattering is one such technique and, alongside the pair distribution function (PDF), has the ability to elucidate not only defects within a system, but also the structure of fully amorphous and liquid systems thus unlocking information that is not possible using diffraction methods. The caveat with such experiments is the setup required, where traditionally a synchrotron source is needed to reach the correct conditions. Despite the excellent quality data that is acquired at such beamlines, the negatives can often discourage a user, with extensive proposals required, short allocations and the lack of ability to conduct an experiment ad-hoc, ultimately decreasing the number of scattering experiments available. However, the ability to conduct such measurements in-house can open a multitude of possible experiments and can collect data within hours.

In this chapter, an introduction to the structural importance of materials in modern science is described alongside the growing field of total scattering and pair distribution function analysis. A discussion of traditional crystalline defects with a comparison to defects described within total scattering, and how they differ between the techniques, developing into a discussion of the difference between liquids, amorphous, nanocrystalline and disordered materials is given. Although later aspects of this project focus on the structure of aqueous systems, the initial instrumentation development focussed on crystalline and amorphous materials for ease of comparison with regards to the commissioning of the instrument. Whilst it is shown that high quality data can be obtained for these solid materials, the instrument later shows that its strengths lie with aqueous phase studies, allowing for in-depth and novel elucidation of aqueous structure.

From the fundamentals, a more practical discussion of how total scattering data are collected, processed, and ultimately analysed will follow. End-to-end analysis involves a multitude of computationally complex steps and the different software used within this project and how each is used for a specific purpose will be discussed. Further to this, the different model analysis techniques ranging from simple visual interpretation to more complex refinements such as small- and large-box refinements will be detailed. Using literature studies, appropriate uses for each refinement type will be presented, and material specific methodologies discussed. The importance of the

development of in-house instrumentation and ultimately access to a larger audience of scientists will be highlighted.

From the initial concept of this project, the goals have evolved and allowed for the progression from basic measurements of fully crystalline materials, typically that of standard reference materials and relatively simple crystalline materials to fully aqueous systems. Crystalline systems enable basic instrumental setup and calibrations and allow benchmarking of the setup before progression to studying more complex aqueous systems.

1.1 Why is Structural Analysis Important?

Functionalised materials, systems and their synthetic routes dictate modern society. These materials can range from catalysts and zeolites that are used for petroleum refinements[1,2] to semi-conductors that allow for electricity to be run safely and efficiently through homes and workplaces[3] and pharmaceuticals, whether these be precursors or the final drug[4,5]. All of these materials have specific structural features that ultimately dictate the behaviour, such as effectiveness, catalytic turnover, conductivity or medical effectiveness. Without the ability to establish structure-property relationships, the chemistry that dictates these cannot be fully optimised. Furthermore, the synthesis of these materials are an underdetermined problem within structural chemistry, with limited studies available for the large scale analysis of these synthetic routes.[6]

Many common analytical techniques provide varying degrees of insight into the structure of a material, with each different technique providing a specific piece of structural information. Commonly used analytical methods include infrared spectroscopy, which can identify functional groups in a molecule, UV-visible spectroscopy that is sensitive to transition metal oxidation states and organic conjugation, and mass spectrometry that can give vital information on the chemical composition. Other techniques such as nuclear magnetic resonance (NMR) spectroscopy provide information on the local environments over an averaged structure.[7] XRD determines the average short-range and long-range structure of crystalline materials at the atomic scale.[8] However, these techniques generally provide either local structure at short-range or crystalline structure over long-range and none give the full picture of both short- and long-range order compatible with a bulk model of the system.[9]

Analysis of short-range order within a system is confined to analysis such as Extended X-ray Absorption Fine Structure (EXAFS) and X-ray Near Edge Structure (XANES)[10] which provides the local environments around a specific targeted atom type. EXAFS can be incredibly useful for analysis of short-range ordering of crystalline, nano-crystalline and amorphous materials, however as only one atom type can be analysed at a time (and are subject to matching the probe radiation and electronic transition energies), the information obtained is limited to that species and cannot be applied to the larger bulk structure.

Small Angle X-ray/Neutron Scattering (SAX/NS) can give information on pair-distances within solids, nanoparticles and solutions including such properties as particle shape and size.[11] Solid State NMR (ssNMR) spectroscopy can also reveal information on atoms in direct or close proximity to each other, allowing short-range interactions to be analysed in both crystalline and amorphous samples.[12] However, this is limited to short-range interactions and is dependent on species in the

sample being NMR active. All of these techniques give specific information of local structure but cannot extend further than a few atoms, thus the picture we obtain can be likened to individual pieces of a jigsaw, but not the bulk picture of the completed puzzle.

Total scattering and PDF data analysis is a technique that uses X-ray, neutron or electron scattering to elucidate both short-range order within a material whilst also being a bulk technique. In a traditional scattering experiment, the focus is on the distinct Bragg features, where information on the long-range crystalline structure as is contained, with the diffuse scattering often not recorded, discarded, or ignored. With the correct processing and treatment of both the Bragg diffraction (if present) and diffuse scattering data, often referred to as total scattering, information on the local structure can be obtained providing a full model of a system. This technique is not restricted to crystalline solids, and the diffuse scattering from amorphous materials, nanomaterials as well as liquids can be interpreted following a similar methodology to that of crystalline materials. There are, however, drawbacks to this technique, the largest of which is the general lack of in-house facilities for data collection. Therefore, the adaption of a lab-based diffractometer will provide easy access to experiments often conducted at central facilities such as synchrotron and neutron sources. Overall, the addition of such an instrument to a chemistry department will be game-changing and opens up the potential of scattering experiments on functional solids, amorphous solids, nanopowders as well as liquids and solutions.

1.2 Diffraction and Scattering Theory

1.2.1 Bragg Diffraction

Bragg diffraction is a physical phenomenon that links the interaction between electromagnetic radiation (X-ray) or particles (neutrons/electrons), with that of an extended repeating structure in the form of a crystalline solid. Dependent on the source of radiation, the interaction will be between the electron cloud (X-ray) or nucleus (neutrons). First conceptualised and studied by father and son, William and Lawrence Bragg in 1913,[10] the use of radiation to analyse materials, especially crystalline materials has evolved and grown to be a major area of structure analysis. The technique relies on the wavelength of radiation or particles being of a similar magnitude to that of the lattice plane spacings within a crystal structure, with typical wavelengths being around 1 Å. If said diffracted waves interact constructively, Bragg's law (eq 1-1) is obeyed and gives rise to a series of strong sharp peaks that constitute the diffraction pattern.

$$n\lambda = 2d\,sin(\theta) \qquad \textbf{(1-1)}$$

Where n is the integer representing the order of diffraction, λ is the wavelength of the radiation being used, d_{hkl} is the inter-planar spacing and θ is the angle of incidence. Using Bragg's law, it is possible to determine the unit cell of a material, whilst further information on atom type and distribution can be obtained from the structure factor and peak intensities.

A different interpretation of Bragg's law uses the scattering vector Q. This value is the momentum transfer and defines the difference between incoming 'k_i' and outgoing 'k_s' wave vectors, and is often used more in the fields of physics and specialised scattering science.[13] When the scattering is elastic, i.e. where the wavelength and energy of the scattered radiation is conserved throughout the scattering event, eq. (1-2) is satisfied.

$$|k_o| = |k_s| = |k| \qquad \textbf{(1-2)}$$

The difference in these wavevectors is what is defined as the momentum transfer, i.e. 'Q', which can be directly related to the scattering angle 2θ.[14] The momentum transfer can be depicted in figure 1-1.

$$sin\theta = \frac{Q/2}{k} \quad \textbf{(1-3)}$$

$$Q = 2k\,sin\,\theta = \frac{4\pi\,sin\,\theta}{\lambda} \quad \textbf{(1-4)}$$

This derivation shows the relationship between Q and the fundamental instrumental parameter of a powder diffractometer – i.e., the scattering angle. Thus, Q is dependent of the wavelength and can be interpreted identically irrespective of the instrument the data were collected on.

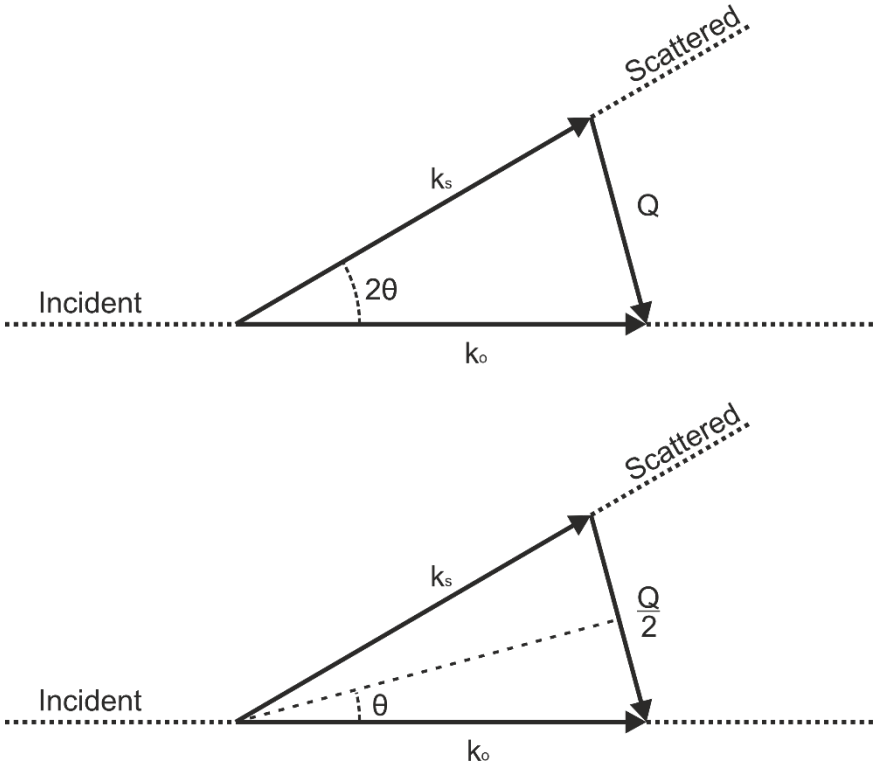

Figure 1-1. *Momentum transfer demonstrated by the incident and scattered wave.*

1.2.2 Diffuse and Total Scattering

Bragg peaks are produced from scattering from areas of the sample characterised by long-range crystalline order; however, many materials also possess areas where this long-range order breaks down and thus an incomplete picture is arrived at. Diffuse scattering contains the information from the areas that deviate from the average and can be used to analyse the local variations in the structure unlocking information that cannot be obtained by traditional diffraction experiments. Diffuse scattering is often ignored as its recording and interpretation is complex and it is the crystalline structure that is seen as most important. Typically, Bragg peaks will be observed at low Q values, typically Q < 10 $Å^{-1}$, as will be discussed in future sections, and most diffractometers are designed to measure this range with the most common wavelength employed being that of copper (1.54 Å). The interpretation of diffuse scattering requires a Fourier transform in which it is important to record as large a Q-range as possible, where a typical copper source with a

Q_{max} = 8.06 Å^{-1} would not be sufficient. Therefore, total scattering experiments are limited to lower wavelength laboratory X-ray sources, or more typically, a synchrotron. Furthermore, traditional diffraction methodologies focus on extracting only the intensities of the Bragg peaks, and the diffuse scattering is effectively ignored, not required, or removed as a background, depicted in figure 1-2. The above arguments overall describe why a sufficient Q-range and ability to identify diffuse scattering within a data set is required for information to be utilised in structure analysis.

$$I_{Total\ Scattering} = I_{Bragg} + I_{Diffuse} \quad \textbf{(1-5)}$$

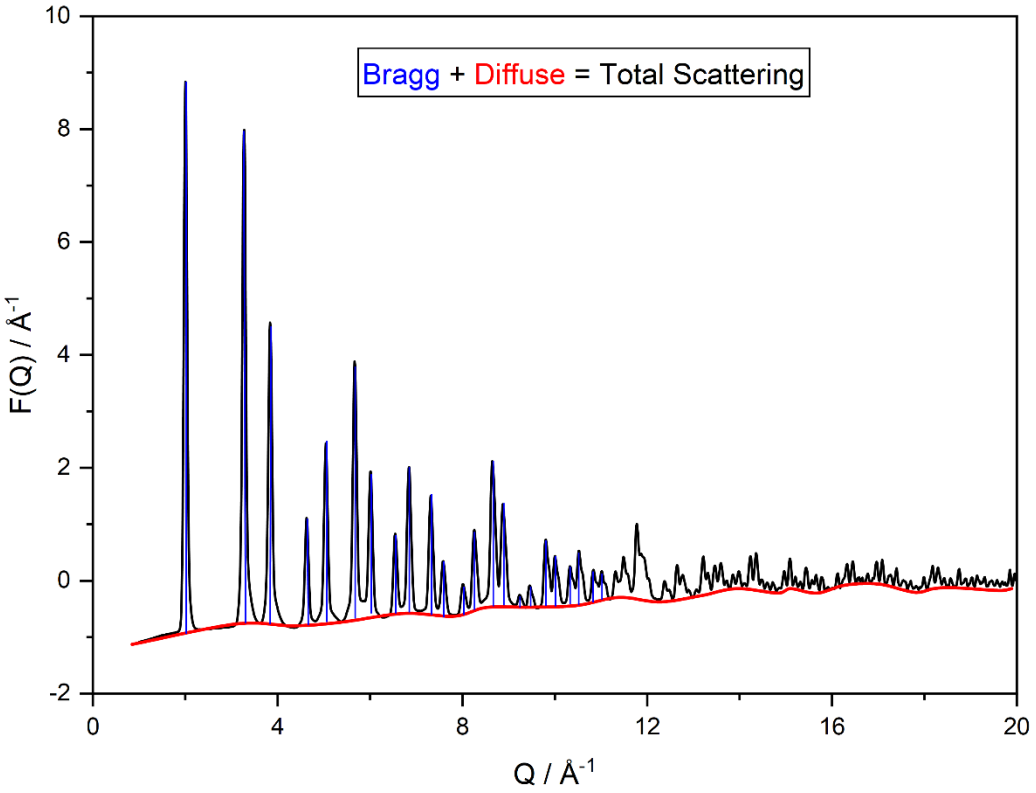

Figure 1-2. *Total scattering silica data comprised of sharp Bragg diffraction, denoting the long-range structure (blue) and diffuse scattering, denoting the short-range structure (red).*

Diffuse scattering, when combined with the Bragg scattering to give the total scattering, can provide additional information on the local structure of a material if recorded and processed correctly. Figure 1-2 shows the difference between Bragg intensity, which represents the long-range ordering, and diffuse scattering that occurs due to the short-range ordering and deviations from ideal crystallographic positioning. These data can be particularly useful for systems where periodic and repeatable patterns are not present, such as those of amorphous materials, liquids, and glasses. Furthermore, it can actually reveal information on a crystalline system where Bragg peaks may not be representative of the sample, and local disorder actually dictates the properties of the system.[15] The combination of both the weakly scattering Bragg peaks and the diffuse scattering gives rise to the term of total scattering, and can be summarised by equation (1-5) and depicted in figure 1-2.

1.2.3 Pair Distribution Function

Pair distribution function (PDF) analysis allows for the investigation of modern materials, where disorder, nanocrystalline and non-crystalline structure dictate the increasingly complex physical properties. Material development has therefore had an increased need for local structure analysis, and this is where PDF shows its importance as a modern analytical technique. The PDF is obtained by the correction and Fourier transform of the total scattering data, described in further detail in section 1.2.4, it is important to understand the relationship between the two functions.

In its simplest terms, the PDF (defined here as G(r), see section 1.2.4.2 for formalisms) can be described by the probability of finding two atoms within a distance of 'r', this is depicted in figure 1-3. On the surface, PDF presents as a very intuitive and easy to understand technique, however care must be taken as the complexity increases with 'real samples'.

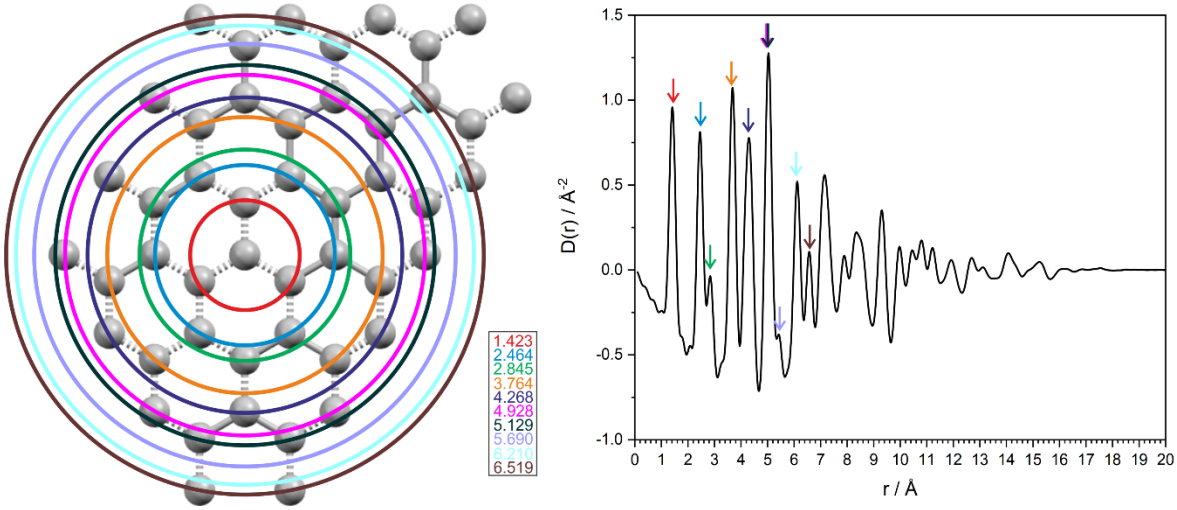

Figure 1-3. *A simulated graphene PDF plot with reference to a crystallographic model. Grey atoms are carbon. Coloured arrows represent the corresponding atom-atom distances from the origin carbon.*

Where G(r) denotes a function of PDF, ρ(r), is the atomic pair density function and ρ_0 is the atomic number density of a material. ρ(r) simply defines the interactions between atom i and j. ρ_0 is defined as the number of atoms per unit volume and is used in combination to find the probability of finding an atom within proximity of another. These functions will be analysed in further detail in section 1.2.4.

$$G(r) = 4\pi(\rho(r) - \rho_0) \qquad \textbf{(1-6)}$$

To understand the information gained from the PDF, one must also understand where the information originates from, and as previously described this comes from the raw total scattering data.

To understand this, the various functions related to total scattering will be discussed.

$$F(Q) = c_i c_j X_{ij}(Q)[A_{ij}(Q) - 1] \quad \textbf{(1-7)}$$

where F(Q) is the generic total scattering structure factor (radiation independent), $c_{i/j}$ are the concentrations of species i and j respectively, X_{ij} are the scattering component (i.e. scattering factor (X-ray) or scattering cross section (neutron)) of each species and A_{ij} are the weighted sum of the partial structure functions. These functions will be examined in more detail in section 1.2.4. However, it is important to understand how the Fourier transform of equation (1-7) allows access to the PDF, with the information contained within the data fully describing the concentration, abundance and scattering of each species and consequently the interactions between said species.

This basic discussion of the PDF and derivations allows for a basic understanding of the information obtained from the material and data but also highlights an important aspect of this analysis routine, and that is the reversibility of it. The data themselves are reversible, whereby Fourier and inverse Fourier transforms can allow for one to traverse between the total scattering and PDF data types, allowing for increased data. The structural information can be also two-way whereby data can be extracted from both a crystallographic model as well as from scattering data, in a similar way that diffraction patterns can be obtained. This becomes useful for predicting structures and what features can be expected from a known material, as well as being able to obtain PDF from scattering data, and this ability allows for refinements to be conducted.

1.2.4 Mathematical Description of Total Scattering and PDF

To fully understand PDF data analysis, it is important to understand the various functions used and the corrections applied. Fundamentally the raw observed or measured data are the 1D total scattering pattern obtained after correction for Lorentzian and polarization effects – this incorporates all the coherent scattering from the sample. The PDF can be considered as one form of the processed data and is the Fourier transform of total scattering data – converting reciprocal to real space.

Therefore, PDF (here denoted as G(r)) is commonly described as:

$$G(r) = \frac{2}{\pi}\int_0^\infty Q[S(Q) - 1]\, sin(Qr)\, dQ \quad \textbf{(1-8)}$$

Where Q is a scattering vector described in eq. (1-4). S(Q) is the total scattering structure function and $Q_{min/max}$ is the Q-range achievable on the instrument (this is will be discussed in further detail in chapter 2).[16]

1.2.4.1 General Corrections

Processing from the raw data involves general corrections relating exclusively to the instrument and sample container, these include; beam profile parameters, polarization terms, container and general background scattering terms as well as corrections for Bremsstrahlung and fluorescence. The aim of these corrections is to remove any scattering intensity not due to the sample, if they are not applied diligently, a false model will result.

A number of data processing packages are available to correct total scattering data e.g. PDFgetX3[17] and Gudrun[18] and the process can be summarised as:

$$I_m(Q) = a(Q)I_c(Q) + b(Q) \quad \textbf{(1-9)}$$

Where $I_m(Q)$ describes the measured total scattering intensities, $I_c(Q)$ in the coherent corrected total scattering intensities and a(Q) and b(Q) are additional multiplicative or additional system specific corrections. a(Q) corrections include the correction of factors that increase or decrease scattering data that are already present within the system. The most common of these factors are the beam polarization, a factor that is instrument and source specific[19], self-absorption and well-defined phenomenon such as Compton scattering. b(Q) corrections involve removal of non-sample scattering[17] such as subtraction of both the background of the instrument as well as the container in which the sample is mounted. These steps use additional data sets collected for an empty diffractometer and an empty container along with sample composition information.

1.2.4.2 Formalism of Total Scattering and PDF

As with many areas of science, the specific formalisation of total scattering and PDF is distinct to both the geographical region, area of research and refinement software of choice. Despite the numerous representations of these functions, the underlying theory is the same,[14] and therefore throughout this project the functions have been aligned to U.K. formalisms as described by Keen.[16,20]

Total scattering is often represented by the total scattering structure factor, F(Q), which can be further utilised via its Fourier transform or used in its own right for large-box refinements. The F(Q) is defined as follows where superscript x/n represent the X-ray and neutron forms respectively:

$$F^X(Q) = c_i c_j f_{ij}(Q)[A_{ij}(Q) - 1] \quad \textbf{(1-10)}$$

$$F^N(Q) = c_i c_j \bar{b}_i \bar{b}_j(Q)[A_{ij}(Q) - 1] \quad \textbf{(1-11)}$$

where $c_{i/j}$ are the concentrations of species i and j respectively, $f_{i/j}$ are the Q-dependent X-ray scattering factors of species i/j (X-ray only) defined as:

$$f_{ij}(Q) = \frac{f_i(Q)f_j(Q)}{\left(\sum_{i=1}^{n} c_i f_i(Q)\right)^2} \quad \textbf{(1-12)}$$

$\bar{b}_{i/j}$ are the neutron coherent scattering lengths of species i and j (neutron only) and A_{ij} are the weighted sum of the partial structure factors.

$$A_{ij}(Q) - 1 = \rho_0 \int_0^{\infty} 4\pi r^2 \left[g_{ij}(r) - 1\right] \frac{sin\, Qr}{Qr} dr \quad \textbf{(1-13)}$$

where ρ_0, as defined in equation (1-6), is the number density and g_{ij} is the partial PDF and is directly related to the above partial structure function by Fourier transform to form equation (1-14).

$$g_{ij}(Q) - 1 = \frac{1}{(2\pi)^3 \rho_0} \int_0^{\infty} 4\pi Q^2 \left[A_{ij}(Q) - 1\right] \frac{sin\, Qr}{Qr} dr \quad \textbf{(1-14)}$$

The PDF (G(r)), is related to the F(Q) in a similar way that A_{ij}(Q)-1 and g_{ij}(Q)-1 are related and that is via a Fourier transform, and can be described as:

$$G^N(r) = \sum_{i,j=1}^{n} c_i c_j \bar{b}_i \bar{b}_j (Q)[g_{ij}(Q) - 1] \quad \textbf{(1-15)}$$

However, G^X(r) is slightly more complicated due to the Q-dependence of the scattering factors and therefore G^X(r) can be described as:

$$G^X(r) = \frac{1}{(2\pi)^3 \rho_0} \int_0^{\infty} 4\pi Q^2 F^X(Q) \frac{sin\, Qr}{Qr} dQ \quad \textbf{(1-16)}$$

Which can be Fourier transformed to its equivalent F^X(Q) as such:

$$F^X(Q) = \rho_0 \int_0^{\infty} 4\pi r^2 G^X(r) \frac{sin\, Qr}{Qr} dr \quad \textbf{(1-17)}$$

It is worth noting that Q-dependence is often a complication with regards to the PDF calculation, as described thoroughly by Keen.[20] Often for xPDF, it is far more efficient to sum together the partial PDF (1-14) and subsequently Fourier transform the F(Q) formed by this summation. This is an issue that does not occur with nPDF and shows how care must be taken between radiation sources.

Other functions can be found within the realms of total scattering, particularly within the processing and calculation of these factors in the various software. One such function is the normalized total scattering structure factor S(Q):

$$S^N(Q) - 1 = \frac{F(Q)}{\left(\sum_{i=1}^{n} c_i \bar{b}_i\right)^2} \quad \textbf{(1-18)}$$

$$S^N(Q) = \left(\sum_{i=1}^{n} c_i \bar{b}_i\right)^{-2} \sum_{i=1}^{n} c_i c_j \bar{b}_i \bar{b}_j A_{ij}(Q) \quad \textbf{(1-19)}$$

$$S^X(Q) = \left(\sum_{i=1}^{n} c_i f_i\right)^{-2} \sum_{i=1}^{n} c_i c_j f_{ij} A_{ij}(Q) \quad \textbf{(1-20)}$$

A final alternative normalization that is often found within the PDF literature is the D(r), which scales the G(r) in such a way that the higher-r features are emphasized and enables the examination of longer-range features. D(r) can be described for both X-rays and neutrons as:

$$\mathrm{D(r)} = 4\pi\rho_0 \mathrm{G(r)} \quad \textbf{(1-21)}$$

It must be reiterated that different software packages often use different forms of the functions described above, and care must be taken to match the function with the software, the table below summarises the functions used by the different packages .

Table 1-1. *Table of commonly used total scattering and PDF software with the equivalent formalisms.*

Software	**Software Use**	**Function**	**File Type**
Gudrun	Calculation of total scattering and PDF	$F^N(Q)$ $F^X(Q)$ $D^X(r)$ $D^N(r)$ $G^X(r)$	.int01 .mint01 .dofr .mgor01 .gofr
TOPASv6	Small-box/PDF refinement	D(r)/G(r)	.xy from Gudrun (specify D(r) or G(r) and radiation source)
PDFgui	Small-box/PDF refinement	G(r)	
EPSR	Large-box/total scattering refinement	$F^N(Q)/F^X(N)$	.int01/.mint01

1.2.4.3 Experimental Considerations for Total Scattering Experiments

For total scattering experiments, X-ray, neutron and electrons can be used and the radiation of choice is ultimately up to the researcher depending on the requirements of the sample.[15] The most common sources are those of X-rays and or neutrons. The theory pertinent to X-rays and neutrons is basically the same, but with a few differences due to the different scattering mechanisms involved - these will be discussed. As described above a sufficient Q-range is essential for a successful total scattering experiment and an appropriate radiation wavelength and θ-range must be chosen. The effects of an insufficient Q-range are depicted in figure 1-4, where r-space resolution can be seen to greatly increase with increasing Q_{max}. When the PDF is generated from the experimental data, rather than a model, termination ripples and noise will be observed for data with lower Q_{max}. These features can be observed in the figure below, where particularly in the r = 0 – 4 Å region, ripples are prominent and without higher quality data it would be difficulty to differentiate these with real structural features.

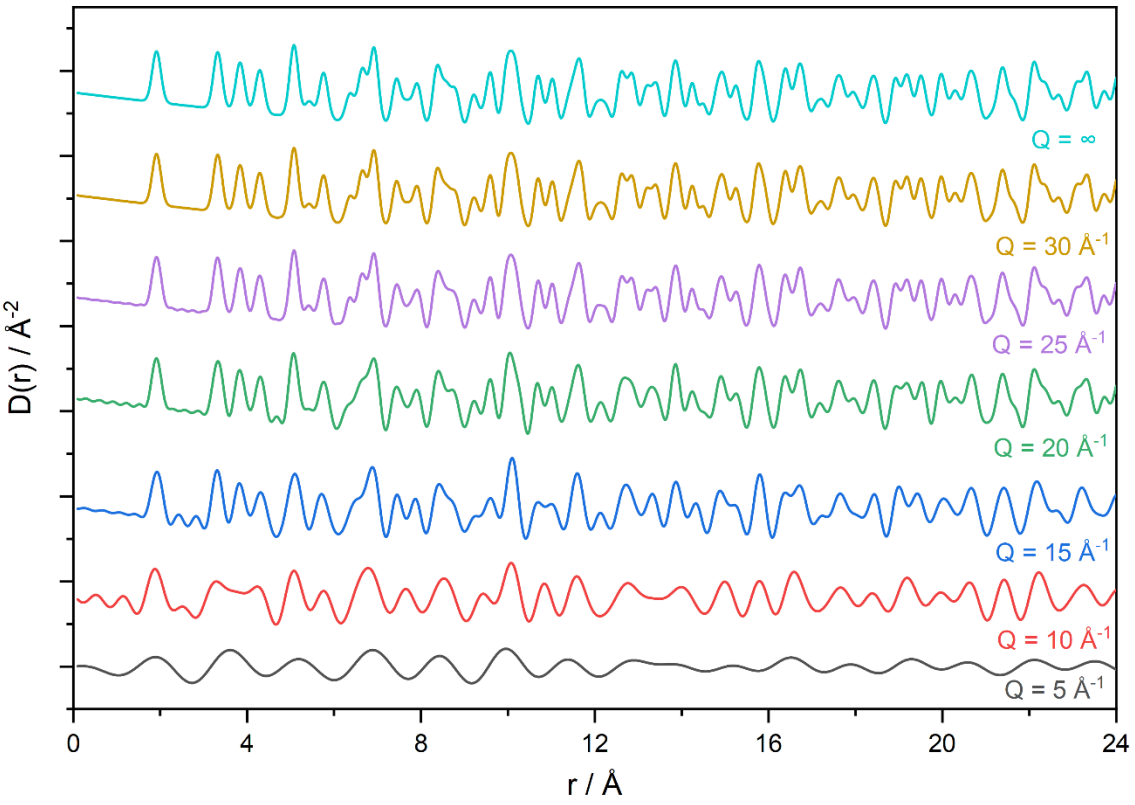

Figure 1-4. *Simulated PDF plots of a standard silicon sample using varying Qmax values, generated within PDFgetx3.*

The most obvious difference between X-ray and neutron radiation is their interaction with matter; X-rays interact with the electron cloud and neutrons interact with the nucleus. This leads to differences in the scattering event produced by the different radiation. The scattering power of X-rays typically increases with atomic number while the scattering power of neutrons follows a

complex trend that is quasi-random with respect to atomic number. Neutrons are assigned a theta-independent 'scattering length' which effectively gives the probability of interaction between a nucleus and neutron wave.[21] This scattering length can be positive or negative, which becomes increasingly useful for differentiating similar atoms in a structure, for example hydrogen and deuterium show a positive and negative scattering length of -0.374 $x10^{-12}$ cm and 0.667 $x10^{-12}$ cm respectively. These values can be utilised to determine the total scattering cross section, which incorporates the sum of the coherent and incoherent scattering and ultimately determines the effective neutron scattering of an element. This can be used to determine the effectiveness of a neutron experiment for a given sample.[22]

Another difference is the degree of absorption, where X-rays ultimately have a stronger absorption and therefore interaction leading to less sample being required. The lower absorption of neutrons leads to a larger amount of material being needed and longer exposure times needed for sufficient data collection. In terms of total scattering experiments, a small 2 mm capillary of sample can be collected in < 1 minute at a synchrotron source, whereas a neutron experiment requires a large can of several grams. However, the theta independent scattering of neutrons means there is no drop off in intensity with angle and this counting statistics at high angle are not compromised.

The increasing demand and recognition of total scattering experiments within mainstream science has led to many central facilities being oversubscribed and thus a drive to increase the number of laboratory-based X-ray diffractometers for such experiments.[23]

A typical copper source in a laboratory X-ray diffractometer will have a Q_{max} equal to approximately 8 $Å^{-1}$, whereas a typical synchrotron source can achieve a Q_{max} of 20-40 $Å^{-1}$. These Q_{max} values are dependent on a sufficiently small wavelength in combination with a large 2θ range, with instruments utilised for total scattering having a combination of both. 2θ is essentially limited to as close to 180° as the design and construction of the diffractometer allows.

1.2.5 Disordered Systems and Local Structure

Crystallographic disorder is common within the realms of modern-day diffraction, however less common is that of the analysis of disordered systems. Disordered systems therefore must be defined differently to that of traditional crystallographic disorder due to a lack of long-range order, whereby a totally disordered system has no underlying repeating nature. Common examples of such are liquids, glasses, solutions as well as amorphous materials. These systems appear to contain no periodic structure and as well as no real long-range order within the material, however, this does not mean that a system is completely devoid of any order, but rather that it exists on a much smaller length-scale. Classical crystallography and its definitions cannot be expanded to include disordered

systems, and therefore a different definitions, experimental procedure and analysis is needed, total scattering.

Disorder within a systems can be categorised into three distinct groupings: ordered, correlated disorder and random disorder and can be visualized in figure 1-5.[24] Ordered is typically what is described in classic crystallography as a repeatable unit cell with no disorder or defects. This system will have distinct Bragg peaks that can be analysed by traditional techniques however it is rare to find a completely perfect system. Random disorder often describes liquids and glasses whereby there is no obvious order or correlation between molecules and is fully random. This system will have fully diffuse scattering with no Bragg features. Like the fully ordered system, these are also rare as most systems will possess some degree of local ordering. Correlated disorder is a mixture of both ordered and random and will sit at a mid-point between the two systems. This system will possess both diffuse scattering as well as some Bragg peaks, with both adding to total scattering. All systems from fully crystalline to liquids and glasses will appear at some degree on this scale but highlights the importance of total scattering techniques.

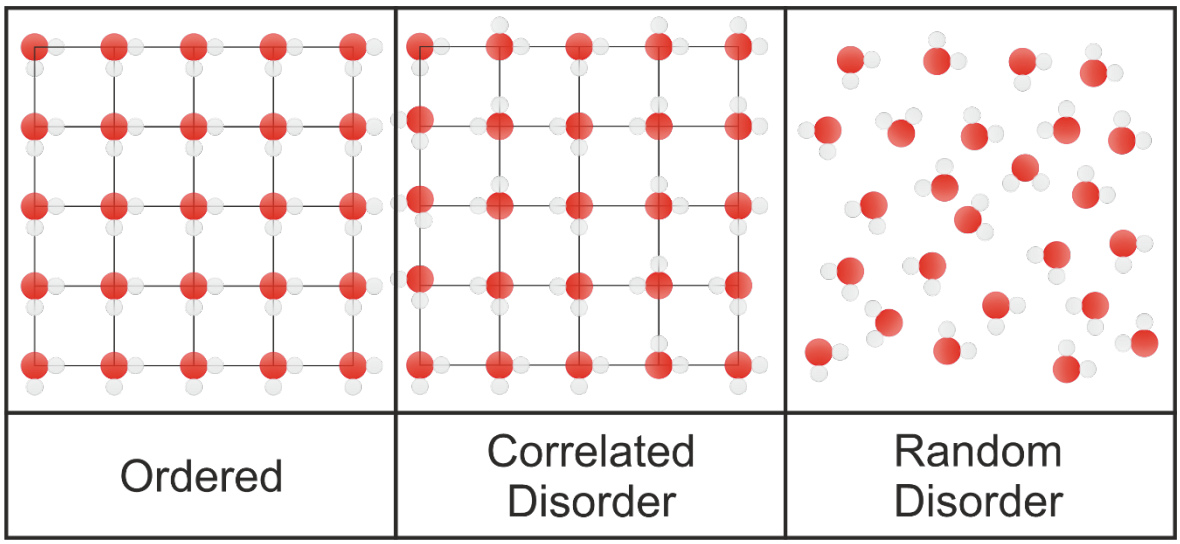

Figure 1-5. *Ordered, correlated and random disorder of water, where red atoms denote oxygen and white denote hydrogen. Adapted from Keen et al.20,24*

1.2.5.1 Crystalline, Nanocrystalline, Amorphous and Liquid Definitions

The definition of the terms crystalline, amorphous, glass, nanocrystalline and liquid and the differences between them are often unclear and even disputed.[16,20] The diffraction pattern observed for a nanocrystalline material can often look similar to that of an amorphous material the former exhibits long-range order whereas amorphous materials only exhibit short- to medium-range-order.[4,25,26] Sub-categories can be defined based on the thermodynamics and processing of

a material, for instance, glasses can be defined as amorphous, or more accurately non-crystalline solids (NCS) , but not all amorphous materials can be considered glasses. This is described by Gupta[27], whereby a melt-cooling process defines a glass, however this description is not universally agreed upon. This situation highlights the complexities and variations of the pertinent definitions, with no single system of classification being in common use. For the purposes of this work, figure 1-6 demonstrates a somewhat arbitrary scale of order to disorder.

An example of the complexity of these definitions is contained withing a study by Mavračić et al[28] where a simple system such as titanium dioxide (TiO_2) exhibits a number of polymorphs and discrete phases dependent on the formation conditions but with no change to the chemical composition. The authors conducted various computational simulations to compare the various phases of this simple material and these show a large similarity between liquid and amorphous phases, where the short-range structure is almost identical in both cases albeit with a slight change in density. A better way to consistently identify these phases is to use total scattering, where the exact range of the ordering can be determined.[29]

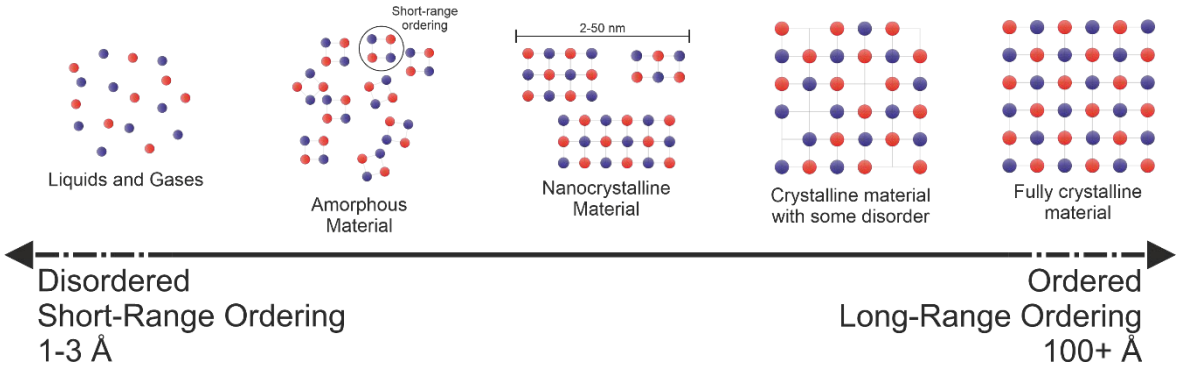

Figure 1-6. *An arbitrary scale, defining the evolution from fully disordered liquids and gases to fully ordered crystalline systems.*

1.3 From Total Scattering to the PDF: Calculation and Analysis

A variety of software packages are available for both the correction of and analysis of total scattering data including Gudrun[18] and PDFgetX3[17] for data reduction and PDFgui[30] and TOPAS v6[31] for small-box real-space Rietveld refinement against PDF data. RMCProfile[32] and EPSR[33] enable an alternative approach based on large-box Monte-Carlo type simulations. Other software packages are available, highlighting the need for different approaches in the area of modelling or refining total scattering, these include; DAWN[34], Dissolve[35], and DISCUS[36] among others.

During the initial stages of this project the various data correction and processing packages were evaluated, and Gudrun was selected as providing the most rigorous approach that could be adapted to work for data collected on an in-house instrument. In particular the input of instrumental parameters such as beam dimensions, X-ray source properties, monochromator geometry, as well as the treatment of non-sample scattering were particularly flexible. Outputs from Gudrun include the final Fourier transformed PDF, as well as the total scattering functions S(Q) and F(Q), and a multitude of other functions and diagnostic files.

In tandem with obtaining the PDF from the total scattering data, the ability to calculate the PDF from a set of atomic coordinates is highly important – this was achieved using PDFgetX3/PDFgui.[30,37] The ability of these software packages to model specified instrumental parameters, whether that be those of an in-house instrument or a central facility instrument (xPDF/SANDALS), allows for a closer match of observed and calculated patterns.

1.3.1 Analysis of Total Scattering data and the PDF

Approaches to total scattering and PDF analysis can range from very basic visual inspection to complex large box refinements incorporating thousands to tens of thousands of atoms. The main analysis techniques that will be discussed further are visual inspection, in which simple features can be deduced from peak positions, small-box refinement which is a least squares methodology similar to a Rietveld refinement and large-box refinement that may contain 1,000-10,000's of atoms and is typically based on a Reverse-Monte Carlo methodology.[38] These methods can be improved upon by including additional data sets to be refined in tandem as a dual refinement, for example, crystalline materials with defects can be effectively modelled with the combination of both Bragg (long-range order) and PDF data (short-range order). This dual refinement approach is a very

effective way of modelling a non-ideal material and produces results that have a higher degree of certainty.

1.3.2 Visual Inspection: Features of the PDF and Their Definitions

The most basic, but potentially the most important form of analysis of PDF data is a simple visual inspection and peak fitting, providing a multitude of information without the need to construct and refine a model. This can range from observations of changes in peak positions and profiles to the identification and extraction of specific atom-atom separations. Four structural elements can be extracted from PDF: atom-atom distances, co-ordination number, structural disorder and particle size. As it can be seen from figure 1-7, this information can be determined from characteristics of the plot, such as peak position, full-width half-maximum (FWHM), the integrated intensity of the peak and peak/signal cut-off. From a simple inspection of the PDF we can gather a vast amount of information about the material being analysed.[14]

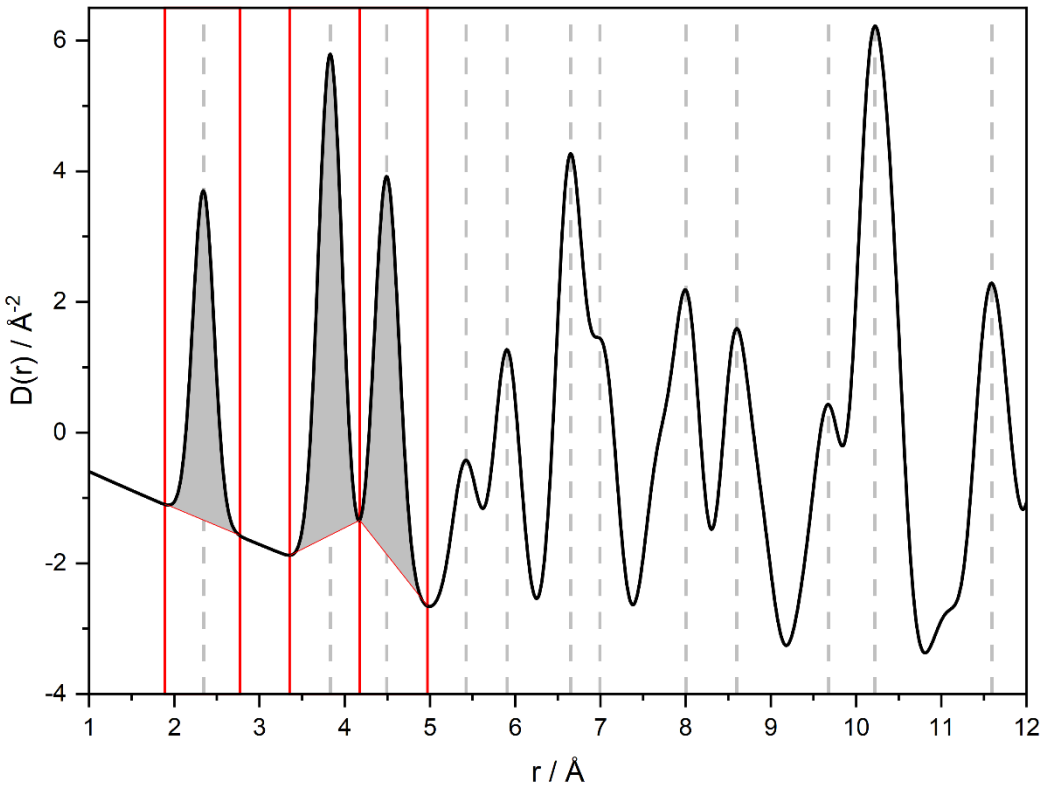

Figure 1-7. *The parameters that can be derived from PDF data, silicon used as an example. Dashed lines denote the PDF peak positions and thus pair correlations, the red lines denote the peak widths and therefore all available pair distances. The grey area represents the integrated area, where coordination numbers can be extracted. Not pictured for clarity: FWHM (thermal and instrumental parameters) and signal cut-off (particle size and instrumental parameters).*

Figure 1-7 denotes the basic features and information that can be extracted from a typical PDF plot and have been annotated as such. The main and most prominent features within any PDF plot are the peak positions, which directly relate to the atom-atom correlations within a system. As

described in section 1.2.3, peaks represent the probability of finding another atom at that correlation distance and therefore it is often very easy to assign correlations by simple visual inspection. This methodology is simple and reasonably intuitive at low-r values, but becomes more complex as r increases - therefore this approach is usually limited to approximately r = 8-10 Å. Further information can also be obtained by the measurement at the start and end of the peak, which gives the full range of the distance possible i.e. the distribution of specific atom-atom correlations. The integrated intensity of a peak provides information about the coordination number related to the corresponding atom-atom correlation - useful for determining the nature of the coordination sphere. The peaks full-width half-maximum (FWHM) relates predominantly to the motion and disorder at that specific atom-atom correlation. The final feature of note is the peak cut off or loss of signal, and this is usually indicative of the particle size due to the loss of atom-atom correlations, especially useful for amorphous materials and nanoparticles. However, one must be careful when interpreting this parameter as it is also an inherent property of the instrument and therefore it is often prudent to have complementary data such as TEM to confirm this value.[14,39–41]

Further to this analysis of an individual PDF, visual identification of changes in multiple PDFs, such as that of intensity, peak position, or broadness over the course of a reaction, crystallisation or other modification of the system can reveal structural and chemical properties not easily followed by other methodologies. The changes observed in the PDF features can therefore be interpreted as changes in local coordination, coordination spheres and ultimately the evolution of a crystallising system.

Visual inspection is often encountered in the literature where the time, resources and skills were not available for a more complex interpretation via modelling. Examples include work by Zhang et al.[42] who observed the evolution of the structural development, important structural motifs and general formation of a functional glass metal-organic framework (MOF) upon heat treatment, something that is not possible via traditional XRD due to the lack of long-range order. MOFs are an important functional material within structural science due to the highly porous network[43], and therefore traditionally are seen as crystalline materials, however more recently amorphous MOFs have been developed by groups such as that of Bennet where more complex analysis techniques have been needed.[44] The authors Zhang et al. discuss in detail the ability to use PDF analysis to compare various heat-treated and quenched ZIF structures, and utilising peak positions to confirm distances between the metal and linker atoms. Further to this, peak widths and shapes were analysed to confirm weaker metal-linker interactions dependent on the treatment method, and therefore the relaxation of the structure. This was fully analysed by visual interpretation of the PDF and highlights the incredible amount of information that can be extracted by simple inspection.

Another example of visual inspection can be seen in the crystallisation of zeolitic materials described in a study by Yamada et al.[45] Here, the authors observed the PDF at regular intervals during crystallisation of various zeolitic materials.[46,47] By investigating the differences between the PDF plots by both visual analysis as well as subtraction of plots, known as difference PDF or ΔPDF, the authors could confirm that the starting materials (SiO_4^{4-} and AlO_4^{4+} sources) initially form 5- and 6-coordinate species before forming the tetrahedral SiO_4^{4-} and AlO_4^{4+} 'building-blocks', common to most zeolitic structures. This happens relatively rapidly and larger blocks form before finally forming the larger porous structures. Further information can be obtained such as the Si/Al-O interactions present at short-range as well as longer-range cross-ring interactions. Further studies have been conducted more recently than these, showing how PDF can be utilised to examine the primary building blocks of a material, such as $AlPO_4$-5, as shown by the work of Potter et al.[6], all of which were found by visual analysis. From the time resolved experiments, the authors could define the key T-sites (where T = Al/P) within an aqueous environment, showing the prenucleation structures within the synthesis of this material. This not only shows the power of visual analysis, removing the limitations of refinements, but also its increasing popularity as both an experimental and analysis route for functional materials, especially that of non-crystalline systems.

1.3.3 Small-Box Refinements (SBRs)

A more rigorous form of PDF analysis is known as a small-box refinement (SBR), this a least-squares method also referred to as a 'real-space Rietveld refinement' and follows a very similar approach to its Bragg counterpart[48] involving fitting of the simulated PDF obtained from a model to the observed PDF.[49] This approach works well for crystalline materials where the features of interest are short-range deviations for the average structure and produces a more accurate model than arrived at solely from fitting Bragg data.

In a traditional Rietveld refinement the model consists of a unit cell in which an asymmetric unit of atomic coordinates is defined by the space-group.[50] If there is good agreement between the observed and calculated profiles, then the model is assumed to be a reasonably accurate representation of the material. SBRs against the PDF essentially follows the same methodology except increased degrees of freedom are allowed to capture the deviations from the average structure. The is usually achieved by removing the symmetry constraints or adapting a larger unit cell.[51] The goal of this approach is to produce a fit that is better than that obtained purely from the Bragg data. Furthermore, tandem refinement of the Bragg data and the PDF produces a model that simultaneously accounts for the average and local structure. Or to look at it another way, the Bragg data can act as a restraint for the refinement against the PDF.

Many different measures of how well the calculated and observed data match are possible and these residual/reliability factors are collectively described as R-factors. The most commonly used of these are: the profile R-factor (R_p) and the weighted-profile R-factor (R_{wp}) in addition to various goodness-of-fit factors such as χ^2.[52] For small-box refinements against the PDF the R_{wp} is defined as:

$$R_{wp} = \sqrt{\frac{\sum_{i=1}^{N} w(r_i)[G_{obs}(r_i) - G_{calc}(r_i)]^2}{\sum_{i=1}^{N} w\,(r_i) G_{obs}^2(r_i)}} \qquad \textit{(1-22)}$$

Where G_{obs} and G_{calc} are the observed and calculated PDFs sampled at points i=1 to N, and $w(r_i)$ is the weighting factor. χ^2 values from PDF refinements are not comparable to those from Rietveld, as seen in eq. (1-22), due to points within a PDF not being statistically independent. Therefore, a number of adapted χ^2 values can be used, for comparison purposes:

$$\chi^2 = \frac{R_{wp}^{PDF}}{(N - P)} \qquad \textbf{(1-23)}$$

Where N are the number of points and P are the number of parameters in the fit.

$$\chi^2 = \frac{R_{wp}^{PDF}}{\left(\left(\frac{(r_{max} - r_{min})Q_{max}}{\pi}\right) - P\right)} \qquad \textbf{(1-24)}$$

Where r_{min} and r_{max} are the minimum and maximum points where the refinement was taken and the Q_{max} being the Q_{max} used for the refinement.

In this work R_{wp} will be most commonly referred to and it is worth noting that its value is typically higher than that found in a single crystal refinement (<5%) or a Rietveld refinement (<10%) due to the fundamental nature of the materials often studied by PDF analysis. Therefore, an R_{wp} of 10-30% is considered a reasonable fit and a value of 10-20% is considered a good fit.

1.3.3.1 Parameters for SBRs

Similar to many refinements, a robust set of instrumental parameters must be found to accurately measure the instrumental contributions to an experimental data set, within PDF refinements, these are focussed on the Q_{max}, dampening and broadening factors.

The largest contribution to these parameters within a PDF refinement is the Q_{max} value, arguably the most important parameter with regards to total scattering experiments due to its effects on the Fourier transform as discussed in section 1.2.4. By understanding and correcting for the 'termination ripples' propagated by the abrupt cut-off and limited range of data. These ripples within the experimental data can be modelled within the refinement, but more often than not,

these should be mostly removed via smoothing in the data processing.[53] Another issue that propagates from the limited Q_{max} is the real-space resolution (Δr), where $\Delta r \approx 2\pi/Q_{max}$.[15] Effectively this describes that the increase in Q_{max} allows for finer detail in the real-space data and therefore Q_{max} is often prioritised over any other instrumental parameter.

Dampening and broadening, also referred to the dQ and α, are parameters that directly link the broadness of the Bragg peaks to both the instrumental cut-off in data and the increasing broadness of peaks in r-space. dQ is a major contributor and effectively describes how the broadness of the Bragg peaks will cause a drop-off in intensity in r, which needs to be modelled correctly. As Q_{max} and flux are prioritised, the Bragg peak broadness usually is increased and can therefore make most data sets look as if they are a nanoparticle. Therefore, one must use a standard material, such as silicon, to conduct a refinement in both reciprocal- and real-space to confirm the limitation to the r-range. α, another parameter that requires fitting against a standard, denotes the increase in the r-space peak broadness, which directly correlates with the Q-dependent FWHM broadening within the raw data. Again, the same rules apply, and this should also be fixed against a standard and this value utilised for future refinements.

1.3.4 Large-Box Refinements (LBRs)

The final common analysis technique for analysis of total scattering data is that of large-box modelling (LBM), a Reverse Monte-Carlo (RMC) methodology for fitting total scattering data.[15,54] This technique, as the name suggests, uses a much larger box of atoms to fit the total scattering compared to the unit cell size box used for small-box modelling. Typically, this approach is utilised in systems like amorphous solids and aqueous samples where a statistically large number of atoms are required to accurately model the sample in question. Similarly, to SBRs, a calculated total scattering pattern is modelled to fit the experimental data, however it is often the reduced structure function F(Q) that is fitted rather than the real space PDF. This approach has the advantage of not requiring a Fourier transform with all its inherent limitations, however often the derived functions such as PDF and RDF will be used for analysis.[38,51,55–57] However, it is often useful to examine the fit of the PDF simultaneously with the total scattering as they highlight different structural features.

Rather than refining a symmetry restrained model, a randomised box of typically 1000-10,000's atoms are generated which in turn are allowed to move based on various translation and rotation moves. This pioneering approach to the analysis of disordered systems, Reverse Monte Carlo (RMC) simulations, was first discussed by McGreevy et al.[38] and has been the basis for a variety of software packages and approaches. RMC simulations involve the systematic movement of atoms based on a

predetermined set of conditions, which are defined as definite physical properties of species such as densities, forces between species and the degree of overlap between said species. These conditions define whether a move is accepted, accepted within a probability or rejected, and a suitable number of iterations of these moves will give an accurate description of structure of crystalline, glassy, amorphous and aqueous systems, this flow of refinement can be seen in figure 1-8. This approach is far more suitable for these disordered materials due to the ability to both examine a large number of atoms, allowing for a statistically large number of possible arrangements, but also being able to probe the averaged structures of these via the auxiliary routines and accumulated configurations. These accumulations provide both meaningful statistics but also often will provide a snapshot model for one to examine post refinement, allowing for one to probe the structure directly for these structural motifs. This approach to analysis of non-crystalline materials allows for information on these disordered materials that are not accessible via other means.

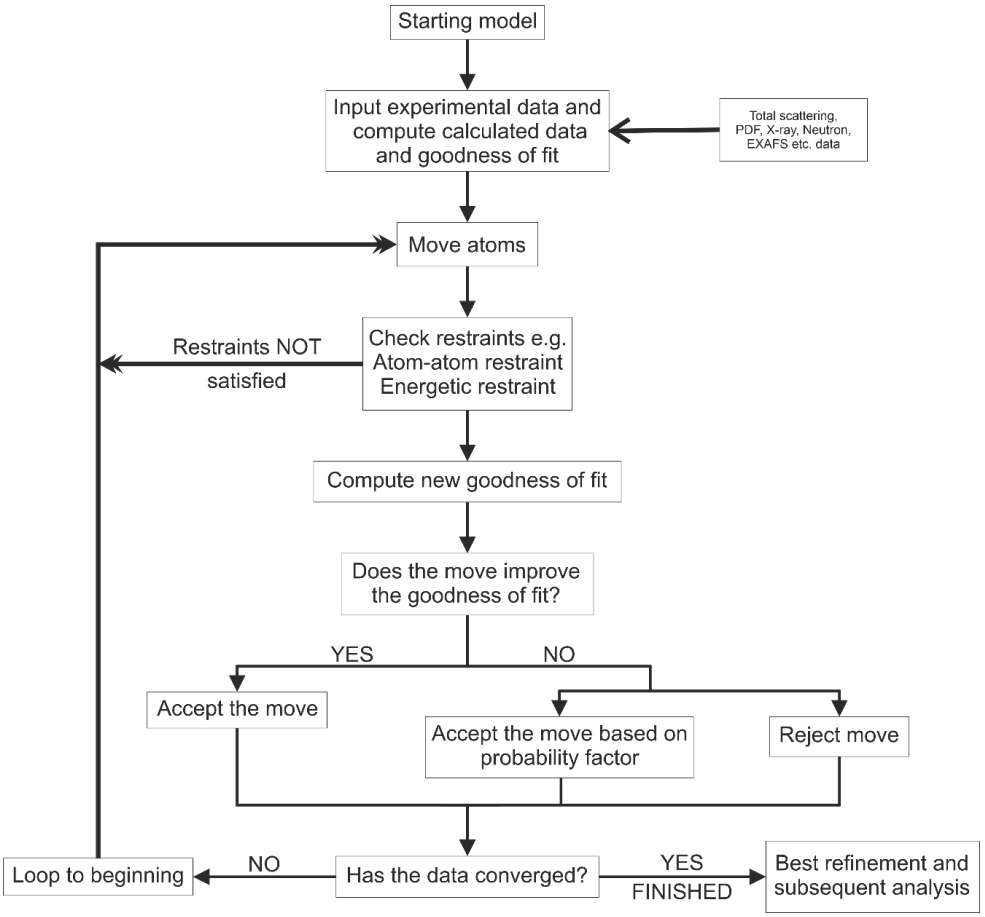

Figure 1-8. *A simplified schematic of the RMC approach to large box refinements adapted from Evrard et al*[32]

Unlike SBRs, LBRs are computationally expensive and more complex to run. Additionally, the analysis of the final model is far more difficult, due to its size and inherent lack of long-range order. It should be borne in mind that the underdetermined nature of the problem (large number of parameters and limited observed data) means a good looking fit can be arrived at that does not necessarily reflect reality! One way of checking this is to perturb the model (by adjusting some input parameters or restraints) and seeing if it converges back to the same answer. Despite its limitations, the ability to produce an atomistic model of large and complex systems is very powerful.

As with many other refinement methodologies, a number of different software packages are available, with some being more suitable for crystalline materials with defects and others being more applicable to amorphous materials and liquids.

An early adopter of the RMC approach to fitting total scattering data was RMCProfile by Keen et al.[56] This approach has proven popular mainly for semi-crystalline materials, focussing on those with defect structures, nanocrystalline materials and some glassy systems.

Empirical Potential Structure Refinement (EPSR) is another RMC approach to addressing the underdetermined problem of structure refinement of aqueous samples.[33,58] This approach uses

both prior chemical knowledge in the form of Lennard-Jones potentials[7] as a pseudo-restraint alongside experimental scattering data and an empirical potential to obtain an atomistic model of aqueous and liquid samples. Utilising the empirical potential as a means to minimise the difference between the experimental and simulated data sets, EPSR can use this difference to alter the atomistic model and perturb the reference potentials to agree with the experimental data. Using this computational approach that is driven by the experimental data allows for the extraction of a refined model of disordered systems, particularly those in an aqueous phase. Further discussion to the theory of EPSR and how it is used in a practical sense can be found in chapter 2.

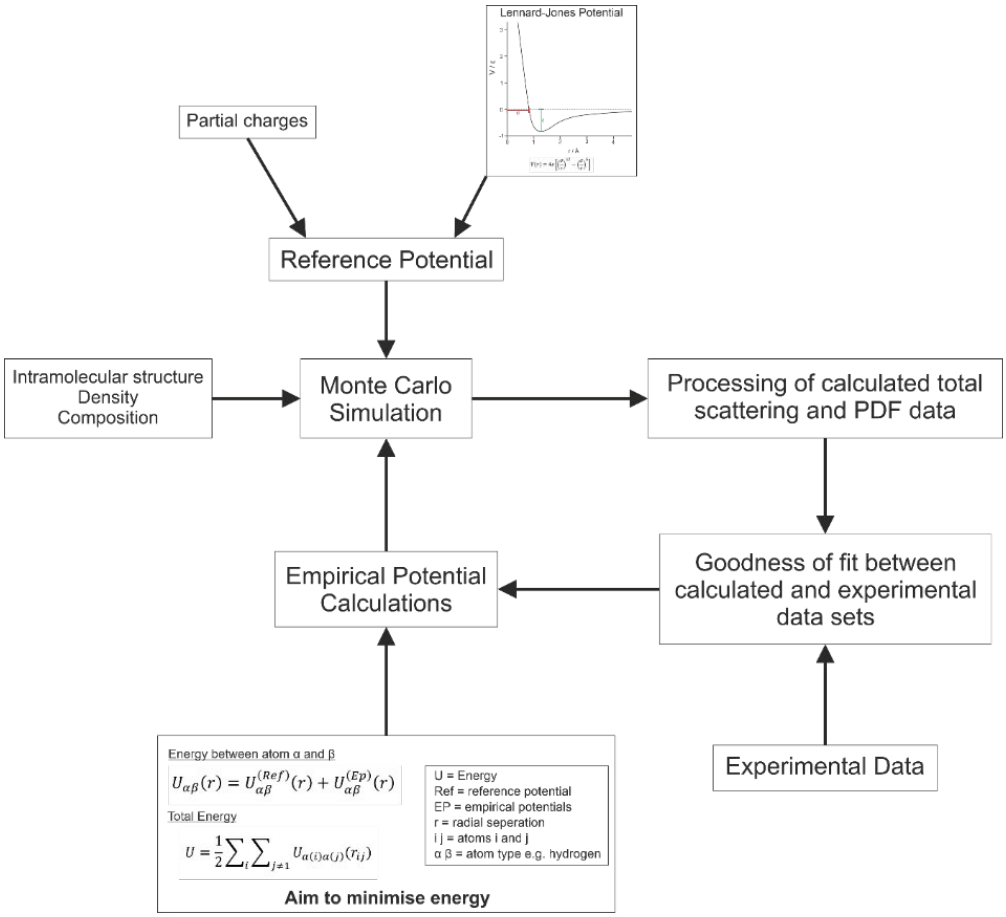

Figure 1-9. *A simple flowchart summarising the EPSR approach to refinements, adapted from EPSR user guide by Soper.*[58]

In the literature, large-box refinement approaches to data fitting have been used in a number of studies, however, potentially the most intriguing and extensive is that of water.[33,59–62] As water is a fundamental liquid, essential to life, a detailed knowledge of its structure is essential to science. However, somewhat surprisingly for this simple molecule, there is still great debate regarding its structure in liquid form. Soper has been a pioneer in total scattering studies of water over a large range of temperatures and pressures. From total scattering experiments using both neutron and X-ray data, Soper has been able to determine the decrease in coordination number between molecules from 4-coordinate to 3-coordinate as water warms from 258 K to 278K and further

decreases in coordination as the liquid approaches room temperature.[61] This has led to further studies at varied temperatures and the eventual realisation that ice exhibits tetrahedral arrangements where oxygen occupies almost crystallographic positions.[60] The suitability of this EPSR methodology to study the structure of water from total scattering data has led to further studies on the interactions of water with other components in solution such as divalent chlorides[63], alcohols[64], lanthanides[65] and perchlorate species[66].

1.4 Conclusion

This chapter summarises the importance of materials within modern science, the limitations of traditional analytical techniques, and the importance of different/new approaches to structural characterisation – exemplified by total scattering. An overview of total scattering and PDF analysis has been presented, including how it is collected, processed, and ultimately interpreted. A number of case-studies were discussed that highlight the power of the technique.

Overall, understanding the theory of total scattering and the pair distribution function allows for a fuller appreciation of the technique and lays a solid foundation for the data, data processing, calibrations, refinements and structures presented in later chapters.

References1 P. Vilarinho, in *Scanning Probe Microscopy: Characterization, Nanofabrication and Device Application of Functional Materials*, 2005, vol. 186, pp. 3–33.

2 Z. Ma, L. Wei, W. Zhou, L. Jia, B. Hou, D. Li and Y. Zhao, *RSC Adv.*, 2015, **5**, 88287–88297.

3 J. S. Chung and M. F. Thorpe, *Phys. Rev. B*, 1997, **55**, 1545–1553.

4 L. Yu, *Adv. Drug Delivery Rev.*, 2001, **48**, 27–42.

5 P. Bordet and P. Martinetto, in *Disordered Pharmaceutical Materials*, John Wiley & Sons, Ltd, 2016, pp. 283–300.

6 M. E. Potter, M. E. Light, D. J. M. Irving, A. E. Oakley, S. Chapman, P. Chater, G. Cutts, A. Watts, M. Wharmby, B. D. Vandegehuchte, M. W. Schreiber and R. Raja, *Phys. Chem. Chem. Phys.*, 2020, **22**, 18860–18867.

7 P. W. Atkins and Julio. De Paula, *Atkins' Physical chemistry*, 2014.

8 W. Clegg, *X-Ray Crystallography*, Oxford University Press, Oxford, 2nd edn.

9 M. Font-Bardía and X. Alcobé, in *Handbook of instrumental techniques from CCiTUB*, Barcelona, 2012.

10 W. H. Bragg and W. L. Bragg, *Proc R Soc Lond A Math Phys Sci*, 1913, **88**, 428.

11 A. G. Kikhney and D. I. Svergun, *FEBS Lett.*, 2015, **589**, 2570–2577.

12 E. Brunner and M. Rauche, *Chem. Sci.*, 2020, **11**, 4297–4304.

13 I. K. Robinson and D. J. Tweet, *Rep. Prog. Phys.*, 1992, **55**, 599–651.

14 T. Egami and S. J. L. Billange, *Underneath the Bragg Peaks Structural Analysis of Complex Materials*, Elsevier, Amsterdam, Second., 2012.

15 T. Egami and S. J. L. Billinge, *Underneath the Bragg Peaks*, Elsevier, Amsterdam, 2nd Edition., 2012.

16 D. A. Keen, *Journal of Applied Crystallography*, 2001, **34**, 172–177.

17 P. Juhas, T. Davis, C. L. Farrow and S. J. L. Billinge, *J Appl Crystallogr*, 2013, **46**, 560–566.

18 A. K. Soper, *GudrunN and GudrunX*, ISIS, Oxford, ISIS, Oxford, 2012.

19 P. Kirkpatrick, *Phys. Rev.*, 1927, **29**, 632–636.

20 D. A. Keen, *Crystallogr. Rev.*, 2020, **26**, 143–201.

21 M. T. Huchings, P. Withers, T. M. Holden and T. Lorentzen, *Introduction to the Characterization of Residual Stress by Neutron Diffraction*, CRC Press, Boca Raton, 1st edn., 2005.

22 J. Dawidowski, J. R. Granada, J. R. Santisteban, F. Cantargi and L. A. R. Palomino, in *Experimental Methods in the Physical Sciences*, eds. F. Fernandez-Alonso and D. L. Price, Academic Press, 2013, vol. 44, pp. 471–528.

23 S. L. J. Thomae, N. Prinz, T. Hartmann, M. Teck, S. Correll and M. Zobel, *Review of Scientific Instruments*, 2019, **90**, 043905.

24 D. A. Keen and A. L. Goodwin, *Nature*, 2015, **521**, 303–309.

25 I. Madsen, N. Scarlett and A. Kern, *Description and Survey of Methodologies for the Determination of Amorphous Content Via X-Ray Powder Diffraction*, 2011, vol. 226.

26 R. K. Hocking, H. J. King, A. Hesson, S. A. Bonke, B. Johannessen, M. Fekete, L. Spiccia and S. L. Y. Chang, *Aust. J. Chem.*, 2015, **68**, 1715–1722.

27 P. K. Gupta, *J. Non-Cryst. Solids*, 1996, **195**, 158–164.

28 J. Mavračić, F. C. Mocanu, V. L. Deringer, G. Csányi and S. R. Elliott, *J. Phys. Chem. Lett.*, 2018, **9**, 2985–2990.

29 B. H. Toby and T. Egami, *Acta Crystallogr. A Found Adv.*, 1992, **48**, 336–346.

30 C. L. Farrow, P. Juhas, J. W. Liu, D. Bryndin, E. S. Božin, J. Bloch, T. Proffen and S. J. L. Billinge, *J. Phys.: Condens. Matter*, 2007, **19**, 335219.

31 A. A. Coelho, *J. Appl. Crystallogr.*, 2018, **51**, 210–218.

32 G. Evrard and L. Pusztai, *J. Phys.: Condens. Matter*, 2005, **17**, S1–S13.

33 A. K. Soper, *Mol. Phys.*, 2001, **99**, 1503–1516.

34 M. Basham, J. Filik, M. T. Wharmby, P. C. Y. Chang, B. El Kassaby, M. Gerring, J. Aishima, K. Levik, B. C. A. Pulford, I. Sikharulidze, D. Sneddon, M. Webber, S. S. Dhesi, F. Maccherozzi, O. Svensson, S. Brockhauser, G. Náray and A. W. Ashton, *J. Synchrotron Rad.*, 2015, **22**, 853–858.

35 T. Youngs, *Mol. Phys.*, 2019, **117**, 3464–3477.

36 Th. Proffen and R. B. Neder, *J. Appl. Crystallogr.*, 1999, **32**, 838–839.

37 P. Juhás, T. Davis, C. L. Farrow and S. J. L. Billinge, *Journal of Applied Crystallography*, 2013, **46**, 560–566.

38 R. L. McGreevy and L. Pusztai, *Mol. Simul.*, 1988, **1**, 359–367.

39 T. L. Christiansen, S. R. Cooper and K. M. Ø. Jensen, *Nanoscale Adv.*, , DOI:10.1039/D0NA00120A.

40 V. Petkov, in *Characterization of Materials*, ed. E. N. Kaufmann, John Wiley & Sons, Inc., Hoboken, NJ, USA, 2012, p. com159.

41 E. Willinger, 65.

42 J. Zhang, L. Longley, H. Liu, C. W. Ashling, P. A. Chater, K. A. Beyer, K. W. Chapman, H. Tao, D. A. Keen, T. D. Bennett and Y. Yue, *Chem. Commun.*, 2019, **55**, 2521–2524.

43 S. R. Batten, N. R. Champness, X.-M. Chen, J. Garcia-Martinez, S. Kitagawa, L. Öhrström, M. O'Keeffe, M. P. Suh and J. Reedijk, *CrystEngComm*, 2012, **14**, 3001–3004.

44 T. D. Bennett and A. K. Cheetham, *Acc. Chem. Res.*, 2014, **47**, 1555–1562.

45 H. Yamada, S. Tominaka, K. Ohara, Z. Liu, T. Okubo and T. Wakihara, *J. Phys. Chem. C*, 2019, **123**, 28419–28426.

46 I. Díaz, E. Kokkoli, O. Terasaki and M. Tsapatsis, *Chem. Mater.*, 2004, **16**, 5226–5232.

47 Y. Hu, Y. Zhang and Y. Tang, *Chem. Commun.*, 2010, **46**, 3875–3877.

48 H. M. Rietveld, *Journal of Applied Crystallography*, 1969, **2**, 65–71.

49 Simon. J. L. Billinge, in *Local Structure from Diffraction*, eds. S. J. L. Billinge and M. F. Thorpe, Springer US, Boston, MA, 2002, pp. 137–156.

50 W. Clegg, *Crystal structure determination*, Oxford University Press, Oxford, 2nd edn.

51 T. Egami and S. J. L. Billange, in *Underneath the Bragg Peaks*, Elsevier, Amsterdam, 2nd edn., 2012, vol. 16, pp. 259–296.

52 R. E. Dinnebier, A. Leineweber and J. S. O. Evans, *Rietveld refinement*, De Gruyter, Berlin, 1st edn., 2019.

53 A. K. Soper and E. R. Barney, *J Appl Crystallogr*, 2012, **45**, 1314–1317.

54 M. Yoshimoto and Y. Shiramata, *Rigaku J.*, 2020, **36**, 9.

55 A. K. Soper, *Molecular Simulation*, 2012, **38**, 1171–1185.

56 D. A. Keen, M. G. Tucker and M. T. Dove, *J. Phys.: Condens. Matter*, 2005, **17**, S15–S22.

57 M. G. Tucker, M. T. Dove, A. L. Goodwin, D. A. Keen and H. Y. Playford, *RMCProfile Manual*, .

58 Soper, A.K., *Empirical Potential Structure Refinement: A User's Guide*, ISIS, Oxford, 26th edn., 2019.

59 A. H. Narten, W. E. Thiessen and L. Blum, *Science*, 1982, **217**, 1033–1034.

60 A. Soper, *Water and ice structure in the range 220 - 365K from radiation total scattering experiments*, 2014, vol. 187.

61 A. K. Soper, *J. Phys. Chem. B*, 2015, **119**, 9244–9253.

62 A. K. Soper, *ISRN Phys. Chem.*, 2013, **2013**, 279463.

63 F. Bruni, S. Imberti, R. Mancinelli and M. A. Ricci, *J. Chem. Phys.*, 2012, **136**, 064520.

64 S. Lenton, N. H. Rhys, J. J. Towey, A. K. Soper and L. Dougan, *J. Phys. Chem. B*, 2018, **122**, 7884–7894.

65 O. S. Hammond, D. T. Bowron and K. J. Edler, *ACS Sustainable Chem. Eng.*, 2019, **7**, 4932–4940.

66 S. Lenton, N. H. Rhys, J. J. Towey, A. K. Soper and L. Dougan, *Nat. Commun.*, 2017, **8**, 919.

Chapter 2 Optimisation and Benchmarking of an In-House Single Crystal Diffractometer for Total Scattering Experiments

This chapter discusses the adaptation of a single crystal diffractometer for total scattering experiments including changes to the instrument (X-ray source) and a discussion of the detector and optimisation of data reduction procedures. A summary of current lab-based instruments will highlight the advantages and limitations of the in-house system compared to commercially available and bespoke instruments. Data collected on standard materials will be compared to similar data presented in the literature allowing a direct comparison of the systems. Furthermore, a data collection and processing protocol has been developed and tested to the point where confidence can be placed in analysis of novel materials and systems.

Standard materials including silicon (Si), lanthanum hexaboride (LaB_6), amorphous silica (SiO_2) and titania nanoparticles (TiO_2) were collected, processed and evaluated as part of the protocol development. Ultimately, this resulted in a series of data sets and models refined against the collected and processed PDF confirming the suitability of the instrument for total scattering experiments on a variety of materials. In addition to the standard materials mentioned above, a study of liquid water was conducted using a slightly modified data collection strategy and the EPSR simulation approach. Water is a well-studied system and offered the chance to benchmark the instrument against a more challenging type of sample, that will form the mainstay of the results presented herein.

Paper supporting this chapter: D. J. M. Irving, D. A. Keen and M. E. Light, *Rev. Sci. Instrum.*, 2021, **92**, 043107

2.1 Laboratory-Based Instruments for Total Scattering

Total scattering and PDF are techniques that are gaining popularity and momentum across a number of fields within the physical sciences. Whilst standard approaches such as XRD enable the analysis of long-range crystalline structure and NMR, IR/Raman and UV-Visible spectroscopy can probe the shorter-range structure, these can be considered opposite ends of the structural 'order-range' with many materials being dominated by structural features that fall somewhere in the middle. The ability to conduct total scattering measurements has, until recently, been limited to a synchrotron (or neutron source) setting, where the required high-Q range and flux is available. However, with the increased popularity of the technique, instruments for total scattering and PDF analysis have begun to appear in a number of labs as both custom builds and adaptations.

2.1.1 Adapted Instruments for Total Scattering and PDF Analysis

Early attempts to collect total scattering data in the lab were based on adapting existing instruments to try and meet the requirements of precise measurements. These studies are relatively recent, with Brühne et al.[1] being early adopters of such a strategy. Referred to as 'FRA', their instrument adopted a molybdenum X-ray tube providing a $\lambda = 0.70932$ Å giving a $Q_{max} = 13.5$ Å^{-1}. Using this Huber-Guinier instrument they conducted a comparison study between in-house and synchrotron data sets, and whilst the refinements resulted in a low R-factor, the actual quality of data was poorer in comparison. With the increased noise in the collected data and poor resolution in both Q-space and real space it allows for a good starting position for in-house total scattering but far from the qualitative studies available from synchrotron sources.

Further attempts have been made at developing a more quantitative in-house instrument, adapting the radiation source further using silver radiation ($\lambda = 0.560886$ Å^{-1}) to increase the Q_{max}. As previously discussed, Q_{max} is arguably the most important factor with regards to good quality total scattering data, where often Q_{max} is prioritised over the resolution in order to obtain good quality low-r data.[2] The easiest way to increase the Q_{max} for a laboratory instrument is changing the source.

Despite the limited Q-range of common X-ray diffractometers, molybdenum sources do enable the collection of data with sufficient quality to refine structures against the PDF – but the significance of the results depends largely on the system studied. One consideration when trying to maximise Q is that of flux. Molybdenum possesses a higher flux than that of lower wavelength sources, due to intensity being scaled by $1/\lambda^3$, and therefore is a suitable choice of radiation for weakly scattering samples, where Q is less important. One example is the investigation of glass joints by Cormier et al.[3], where they fully characterise a $Mg/CaSiO_3$ glass by a reverse Monte-Carlo (RMC) methodologies, where neutron scattering data in combination with in-house data collected on a

molybdenum equipped PANalytical X'Pert Pro. This combined approach is beneficial with regards to how each radiation type interacts with matter, where neutrons interact with the nucleus, and X-ray interacting with the electrons. Interactions between Mg and O can then be analysed in-depth by the neutron data, whereby these atoms have the largest scattering length, and the X-ray data highlighting the heavier elements in the system such as calcium. Overall, the authors have demonstrated that despite the limited Q_{max}, that in-house total scattering is not only possible on a molybdenum X-ray diffractometer, that it also yields qualitative and complementary data for a complex system.

Further developments using molybdenum based total scattering instruments have come since these early studies, with Confalonieri et al.[4] directly comparing a molybdenum based PANalytical instrument, with that of two ESRF beamlines, ID11 and ID31. Both beamlines are multifunctional high-energy beamlines specialised for PXRD and equipped to conduct high quality PDF experiments. All data sets from this study provide good quality PDF data, with exemplary refinements, with small variations between the beamline and in-house instruments. The authors do note some discrepancies between the in-house and beamline data sets, with this being directly related to the reduced resolution of the in-house instrument, however it is noted that this does not largely affect the data quality or refinement. Overall, it can be shown that a standard molybdenum instrument is capable of total scattering and PDF experiment as long as high real-space resolution is not required. A further example is that of Galliez et al. who studied γ-MnO_2 using a molybdenum Bruker D8 diffractometer[5], characterising the intergrowth of this material with successful refinements. This shows the ability to conduct such experiments using a fairly standard setup (i.e., source and detector), however with the drawbacks of decreased real-space resolution and exceptionally high counting times, often in the range of 8-24 hour time range.

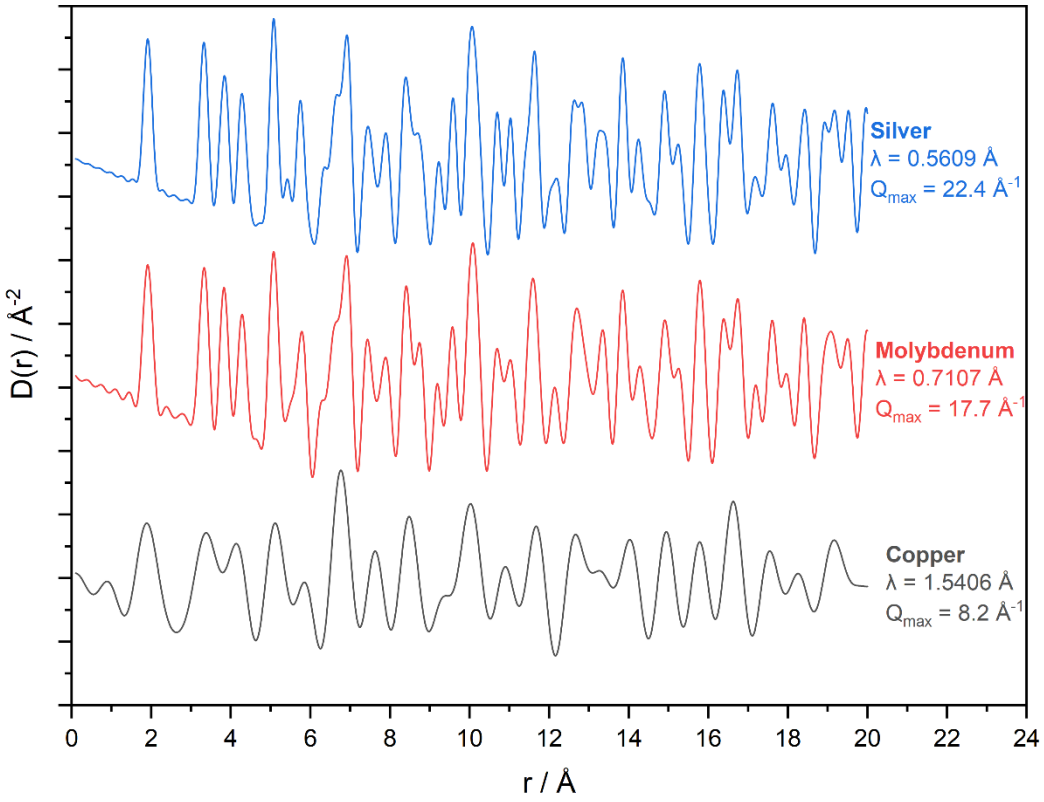

Figure 2-1. *A comparison of the simulated PDF of silicon based on the common X-ray sources of copper and molybdenum as well as the less-common silver anode. The source, wavelength and theoretical Q_{max} values are given.*

Further instruments have been used for in-house total scattering experiments but have gone under more modifications to improve the Q_{max} of the instrument, namely by use of a silver source. Whilst molybdenum enables a modest Q_{max} = 17.7 Å^{-1}, a silver source with its lower wavelength increases Q_{max} to 22.4 Å^{-1}. This increase exceeds the threshold discussed by Billinge[2], where they state that for sufficient quality PDF analysis, Q_{max} must exceed 20 Å^{-1}. However, as the studies shown above demonstrate, having a high Q_{max} does not help if the material being studied does not scatter sufficiently to take advantage of it.[1,3–5] It is also shown in figure 2-1 that, in an ideal scenario whereby instrumental parameters have a lesser impact on the resulting PDF, where the increased wavelength allows for smoother data less influenced by the Q_{max} truncation, leading to periodic ripples in the data. Nevertheless, adapting an in-house diffractometer with a silver source can be particularly beneficial, especially with an increased real-space resolution and the ability to probe low-r regions with more confidence.

As with the molybdenum instruments, some studies have been undertaken using a laboratory-based silver instrument with a variety of complementary data sets and refinement methodologies. Whilst these instruments do exist, they are less common due to the increased cost and decreased usability of an instrument for general diffraction experiments. An early study by Nijenhuis et al.[6] examines the possibilities as well as the limitations of a silver based instrument, with nanomaterials being their main area of interest. Despite the lower Q-range compared to a

synchrotron instrument, the refinements conducted on crystalline, nanocrystalline and amorphous samples yielded good data leading to confidence in the models obtained. Although good quality data can be obtained on such instruments, the counting times are often high, 20-24 hours per measurement.

Bennett et al.[7] use PDF data collected on the GEM neutron beamline in combination with laboratory data from a silver source PANalytical X'Pert Pro. Using both data sets, the study examines an amorphous MOF using an RMC methodology, similar to previously discussed studies using molybdenum instruments (see above). The ability to probe the heavier metal species, high X-ray scattering factor, as well as the strongly neutron scattering species enables the full characterisation of the amorphous material.

This combined approach becomes even more applicable to aqueous systems, where both Meersman et al.[8] and Hammond et al.[9] use neutron data alongside laboratory X-ray data - specifically data collected on SANDALS and NIMROD at the ISIS spallation source alongside complementary X-ray total scattering data on a silver PANalytical X'Pert Pro. Aqueous systems benefit hugely from such dual data approaches, with the neutron data being sensitive to the solvent structure which can be deuterated to capitalise on the differences in scattering lengths of the different isotopes.[10] X-ray total scattering can complement this by being sensitive to the heavier scattering species in the system, such as metals, allowing for both the solute and solvent to be probed in tandem. Both groups utilised an EPSR approach, refining against both the neutron and X-ray data sets simultaneously. Meersman et al. investigated the osmolyte trimethylamine N-oxide (TMAO), a common compound involved in the defensive mechanism route within many organisms[11], and as with all such processes in living organisms, the reaction takes place in a water medium. The authors were able to accurately model how TMAO interacts in water to gain insight to how this particular molecule behaves in an aqueous environment. Furthermore, they describe how the X-ray data complements the neutron data by being able to model the relatively heavier components of the system, such as carbon and nitrogen, whilst the neutron data provide scattering from the deuterated and non-deuterated solvent environment.

Hammond et al.[9] conducted a study into the use of lanthanide-based solvents as a more tuneable and environmentally friendlier alternative to organic solvents. An important feature of any solvent is how it interacts with the dissolved matter, which in this case was lanthanide (cerium, neodymium, or praseodymium) nitrate hexahydrates in a urea/water mixture. The salt-urea/water interactions were probed. It was found that the water formed an almost independent hydrogen bonded network whilst the lanthanides formed longer Ln-NO_3 chains. Urea was found also to strongly hydrogen bond to water, with fewer interactions to the nitrate. Their study summarises that there appear to be two almost independent networks, one dominated by the Ln-O Coulombic attractions

and the other dominated by the water/urea hydrogen bonding interactions. It is also stated that the combined approach was beneficial for probing both networks, where the neutron data revealed the hydrogen bonded network and X-ray highlighting the heavier lanthanide coordination within the solution.

A final notable instrument is that described by Thomae et al.[12], based on a STOE Stadi P powder X-ray diffractometer. As shown by the authors, the refinements are exemplary, with R-factors <0.22, similar to that of synchrotron-based instruments. Standard materials such as LaB_6 enables the truest interrogation of the quality of the data and is shown to have an impressively low $R_{wp} = 0.14$, similar to a goodness-of-fit to a standard PXRD experiment. Further to this, "*real materials*", such a nanocrystalline TiO_2 again show a good fit between the data and the model. Moreover, when compared to synchrotron data, the R-factor is only decreased by 6% over long ranges, and less so over shorter ranges. This not only proves the viability of laboratory-based instruments, but that high quality PDF experiments can be conducted on such instruments.

At the time of writing, very few manufacturers market dedicated X-ray total scattering and PDF instruments, although some do now provide some optimisation possibilities for such measurements. The main disadvantage of these instruments is the long collection times required.

2.2 Modification of a Rigaku Spider/Rapid-II for Laboratory-Based Total Scattering Experiments

The Rigaku Spider diffractometer, also referred to as the Rigaku Rapid and R-axis Spider[13], is a single crystal X-ray diffractometer designed for single-crystal structure determination, primarily those of small molecules and proteins. Although this diffractometer was marketed in the late 1990's and early 2000's making it somewhat antiquated in comparison to more modern instruments today, it is still being sold as the Rapid-II. Technological progression over the past 20-30 years has vastly improved data collection, specifically collection and readout time, flux of the beam and the increased usability in both the instrument and software. However, the Spider is still well placed as a very adaptable diffractometer and has proved itself to have excellent potential for total-scattering experiments.

2.2.1 Instrumental

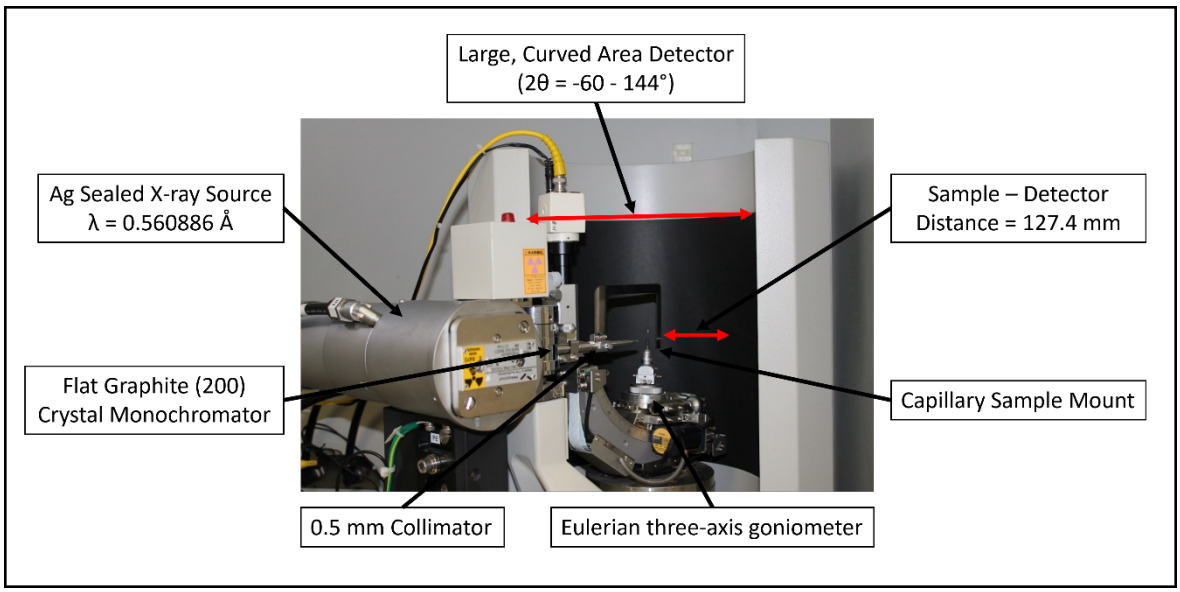

Figure 2-2. *Rigaku SPIDER (RAPID II) set up in a standard transmission geometry (Debye–Scherrer geometry) for capillary measurements. Key components are annotated.*

The Rigaku Spider/Rapid II is equipped with a unique curved Fujifilm image plate detector with dimensions of 460 x 256 mm and a 2θ range -60° - 144° allowing for a full 2θ range = 204°, with a usable range of 144°. The source is a sealed tube silver (Ag Kα1/Kα2 = 0.560886 Å) generator operating at 1.4 kW (40 kV, 35 mA). The beam is monochromated using a flat graphite (200) crystal, supressing K_β and Bremsstrahlung radiation. The capillary is positioned in a transmission geometry at a fixed distance of 127.4 mm from the detector with a beam stop positioned 13 mm behind the sample. The capillary is mounted on a Eulerian 3-axis goniometer with a software limited max oscillation of ϕ = 85°. Exposure time can vary from minutes to over 6 hours, sample dependent.

2.2.2 X-ray Source

As stated in section 2.2.1, the choice of radiation source is the most important factor with regards to total-scattering experiments. The main consideration is a sufficient Q-range and justifies the adaption from a molybdenum source to a silver source. As will be discussed, the large, curved detector used on the Rigaku Spider has an exceptionally low background whilst also being sensitive to the higher energy/lower wavelength, and therefore the reduced flux from the silver anode is less of an issue in comparison to other detectors.

The silver sealed-source has a graphite (200) crystal monochromator that allows $K_{\alpha1}$ and $K_{\alpha2}$ radiation to pass through freely but supressing the K_{β} which allows for the mitigation of a β-filter on the instrument, increasing the flux possible on the instrument. The resulting beam is a mix of $K_{\alpha1}$ and $K_{\alpha2}$ radiation, with a resultant average $\lambda = 0.560886$ Å. Treating α1/α2 separately in the data reduction process is problematical if the splitting is very sharp, however, the instrumental broadening of Spider effectively masks the splitting, and the average wavelength approach employed during data correction works very well. The overall increase in intensity (compared to a pure α1 system) is far more beneficial to the study of poorly crystalline materials than the gain in resolution would be.

Ideally the beam size should be matched to the capillary size to simply beam path corrections such as absorption. In reality, a good compromise was a beam collimated by a 0.5 mm pinhole collimator and the use of 1 or 2mm capillaries. Furthermore, the end of collimator is situated 10 mm from the sample, reducing the air scattering to a minimum, allowing for high confidence in the scattering data obtained and minimising any corrections needed for this phenomenon.

2.2.3 Detector

The detector plays a significant role in the potential and overall quality of total-scattering data extracted from a sample. The combination of a suitably large Q range, good real space resolution, low background, high dynamic range and single photon sensitivity combine to produce the ideal detector for total scattering experiments and enable fast collection times. The Rigaku Spider possess' a large, curved image plate capable of collecting a full range of $2\theta = 204°$, however the usable range is that of $2\theta = 144°$ in the positive direction, thus the theoretical Q_{max} of the instrument in this configuration is 22.4 $Å^{-1}$.

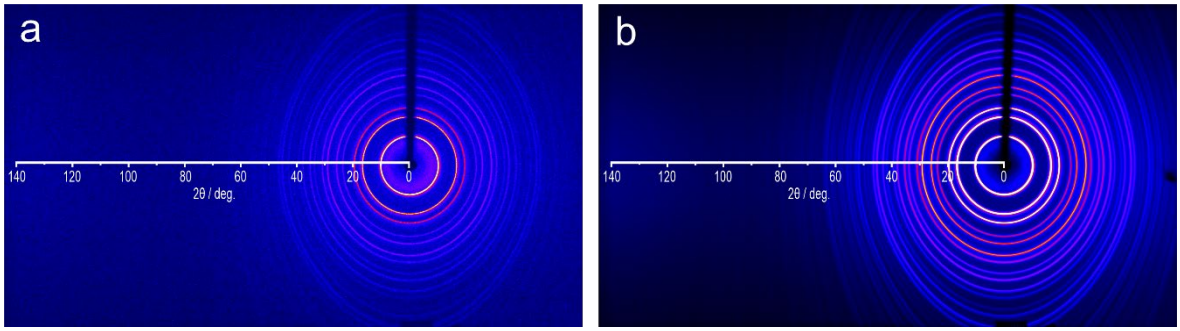

Figure 2-3. *A comparison of 2D patterns obtained by exposure of a SRM 640f silicon sample for (a) 5 minutes in a 0.5 mm capillary and (b) 120 minutes in a 1 mm capillary. Both display a 2θ range for ease of comparison.*

The large range of the image-plate detector has further advantages over alternative smaller 2D detectors and line detectors, this is the ability to record the full range of data with one exposure and no axis scanning. The full range of 2θ = 204° is recorded instantaneously, where other detectors have to scan throughout the measurement in order to collect the full range, leading to increased exposure times. With the Spider a readable signal can be obtained in as little as 5 minutes on a standard sample, as seen in figure 2-3. This also highlights the low background of the detector, even with weak scattering due to the reduced exposure time, the signal from the sample can be seen to extend to high values of 2θ, with a signal being clearly visible out to approximately 2θ = 100°. This can be quantified by background pixel counts seen in table 2-1 where very little increase in background is seen for large increases in exposure time. This is a result of the fundamental physics associated with image plate (IP) detectors. These work on the principle of ionisation and the conduction band of phosphor crystals bound to an organic linker, specifically BaFBr:Eu^{2+}, whereby incoming radiation further ionizes the europium to Eu^{3+}. These layers can be formed in flexible plates, allowing for the large 2θ range seen on the instrument. The ionization event liberates electrons to the conduction band, that are then trapped within the Br^- vacancies, which once exposed to visible light (usually a laser, line by line) are released and converts the Eu^{3+} back to Eu^{2+} leading to a luminescence event which can be recorded.[14,15] This process leads to the very low level background due to the high absorption efficiency of the phosphor crystals, leading to a higher detective quantum efficiency (DQE). DQE is a parameters that defines signal and noise attributed to a detector, with a higher value representing a higher efficiency and therefore better signal and less noise.[16] IP detectors typically have a high DQE of 0.7-0.8 with a fall off at higher exposure level[17], compared to a quoted value 0.74[16] for a modern Bruker Apex II CCD detector. This shows the low background levels of an image plate, comparable to the background of more complex and expensive detector types and much better than the previous generation of CCD detectors.

Table 2-1. *Comparison of accumulated total counts of various exposure times of the empty intstrument. Comparison between beamstop allows for a comparison between an area in which no X-ray should be detected.*

	Behind beam stop (2θ=0-2°)		**Beam Stop Edge (2θ=2-3°)**		**Detector Area (2θ=3°+)**	
Time Exposure / minutes	**Min Counts**	**Max Counts**	**Min Counts**	**Max Counts**	**Min Counts**	**Max Counts**
0	12	15	N/A	N/A	16	17
10	12	16	13	20	13	20
30	12	15	13	19	12	25
60	12	15	12	28	12	53
120	12	20	12	40	11	41
180	12	17	17	58	13	61

The use of a 2D detector also presents an advantage over that of a 1D line detector, especially in samples with large amounts of preferred orientation. The ability to integrate the area to obtain the 1D pattern essentially removes the preferred orientation from the sample, where a 1D detector will not be able to observe this phenomenon. This will therefore alter the raw data and alter further processing of total-scattering and PDF data, and ultimately providing false data. This is not an issue for a large 2D detector where this phenomenon is observable and can therefore be mitigated.

However, the IP detector is not perfect for total-scattering experiments, specifically regarding data readout. With more modern detectors, such as CCD and solid state (Hybrid pixel), data readout can almost be instantaneous, with very little delay between collection and readout. This makes these detector types particularly good for in-situ experiments whereby rapid collection and readout is needed to monitor time critical experiments such as crystallisation from aqueous reagents. The image plate is simply not capable of this rapid readout, and on average needs approximately a minute to read the detector and display the data acquired. This is due to the detector being read line-by-line by a laser to collect the pattern in a scanner like manner. Whilst this is not particularly an issue with regards to a singular sample where it is stable and no changes occur within the time frame of the exposure, this limits the possibility to monitor a reaction over time. This does not rule out the possibility of this type of experiment but puts the instrument at a disadvantage to other total scattering setups. The software used to integrate the 2D pattern (2DP) into a 1D profile (and perform Lp corrections) does not work well unless the integrated segment of reciprocal space is entirely encapsulated on the image – thus not all of the measured data are utilised (see figure 2-4). Theoretically it should be possible to incorporate the unused data and scale appropriately to improve the signal-to-noise ratio, however this would be an intensive procedure for future projects, but as will be shown in future sections, good quality data can be extracted from this area alone.

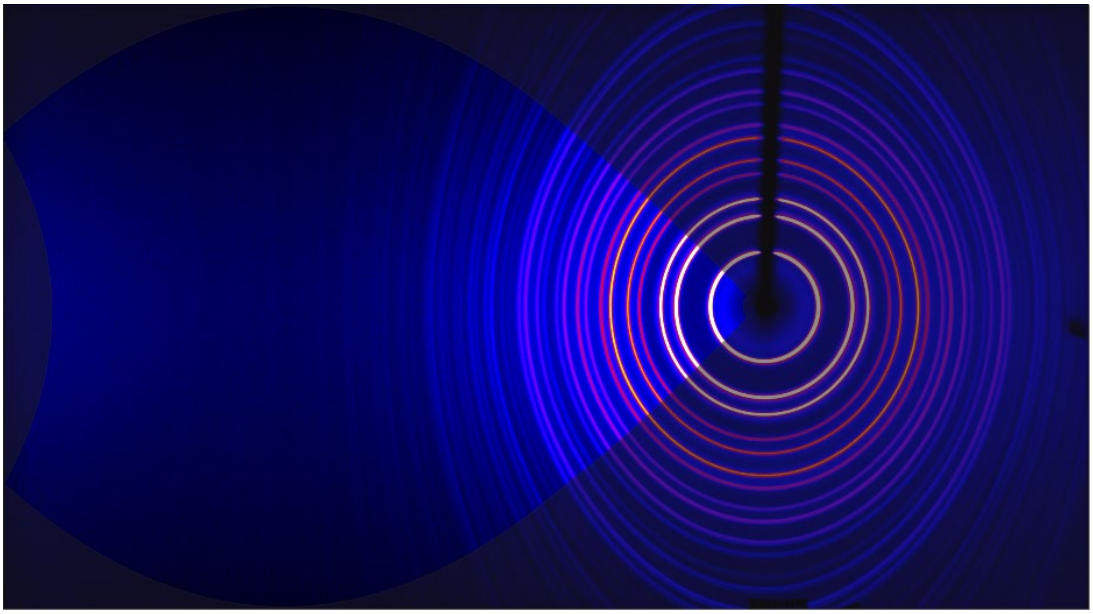

Figure 2-4. *Full 2D image with the non-greyed out area showing the area that undergoes azimuthal integration.*

The final disadvantage and potentially the largest issue is the fixed stage of the instrument, whereby if the source could be directed at the detector edge, an extended 2θ and ultimately greater Q could be obtained. Due to the design, the sample cannot be moved as close as possible to the detector and is in a fixed position at 127.4 mm from the detector. This stage is further limited to rotation of ϕ = 85° rather than a full 360°, limiting the amount of sample within the direct beam. These disadvantages may not be an issue due to the sheer size of the detector and being able to move it closer benefits the ability to collect a large enough Q-range. As this setup allows for the collection of the theoretical Q_{max} of the silver radiation source, the distance should not affect the instruments' ability to produce sufficient quality total-scattering data. The further limited ϕ range is also mitigated by the ability to oscillate the sample, and therefore allows for adequate rotation and view of the sample.

2.3 Central Facilities

Often, in-house instrument data is used as complementary to higher quality data sets collected at central facilities. As discussed in section 2.1.1, many studies have used in-house X-ray total scattering data in tandem with synchrotron/neutron data for various analysis and refinements, highlighting the benefits of such a combined data set approach. Within this study only one external data collection took place using the SANDALS instrument at ISIS, UK, which was refined with complementary in-house X-ray data. One must also consider the other instruments available for total scattering data, such as I15-1 (XPDF) at Diamond and NIMROD (NPDF) at ISIS, both based in the UK, however total scattering instruments exist worldwide and include, but are not limited to, 28-ID-1/2 (Brookhaven, US) and ID11 (ESRF, France) but many more non-dedicated instruments are available. However, due to reasonings beyond our control, data was not able to be collected from as large a number of sources as we would have liked.

2.3.1 SANDALS, ISIS

Small Angle Neutron Diffractometer for Amorphous and Liquid Samples (SANDALS) is an instrument based at Diamond's sister facility, ISIS, using neutrons as the radiation source. Unlike the dedicated total scattering beamline at the synchrotron, the collection of total scattering with neutrons can be performed on a number of multi-purpose beamlines - including SANDALS, GEM and NIMROD.

SANDALS is particularly good for total-scattering experiments on amorphous and liquid samples. The ability to reach high Q values of 50 $Å^{-1}$ with short wavelengths with a resolution of ≈0.1 Å enables collection of high-quality total-scattering data and generation of PDFs to 30 Å. This instrument is a time-of-flight (TOF) diffractometer, which is beneficial for measurement of samples where scattering nuclei experience nuclear recoil leading to distortions in the data, known as inelastic scattering.[18] Inelastic scattering is usually hard to remove experimentally and needs to be corrected for during data processing. However, SANDALS manages to combat inelastic scattering by using forward facing detectors at relatively small angles of 2θ = 2-38°, reducing the inelastic effects, especially from light atoms such as hydrogen. This produces better quality data, especially for aqueous solutions.

This instrument has a proven track record of investigating liquid and amorphous samples using total-scattering, with many having been conducted into the liquid and solid state of water[19–22], water-solvent interactions[23] as well as other solvents and systems such as benzene[24], hydration shells of chlorides in solution[25] as well as functionalised systems such as catalysts[26] and biological systems[27] in solution.

Overall a combination of in-house and central facility data provides the best set of observations possible and enables comparisons of data sets to assess quality of in-house instruments. Furthermore, as will be seen in later chapters, the combination of both central and in-house data enables more complex refinements that would be difficult to conduct without both data sets.

2.4 Calibration of Spider

As with all analytical instruments, calibration and proof of data accuracy is required to enable confidence in the results produced. Standard reference materials (SRMs) can be used for checking the accuracy of specific properties of a diffraction pattern, these are listed in

table ***2-2***[28,29]. While most of those listed are designed for diffraction, they can also be used as standard materials for total-scattering and for comparisons of different instruments. Using these quoted SRMs in combination with other PDF instrument calibration techniques[12] enables accurate calibration of the Spider.

Table 2-2. *A table of standard materials, SRM numbers and application, all applicable to standard XRD experiments.*

Application	**Standard Material (SRM Number)**
Line Position	Silicon (SRM 640), Micas (SRM 675)
Line Shape	LaB_6 (SRM 660), ZnO (SRM 1979)
Instrument Response	Sintered Alumina Plate (SRM 1976)
Quantitative Analysis	Alumina (corundum, SRM 676), ZnO (SRM 1979), TiO_2, CeO_2 & CrO_2 (SRM 674), Quartz (SRM 1878), Cristobalite (SRM 1879), Silicon Nitride (α & β, SRM 656)

2.4.1 Lanthanum Hexaboride (LaB_6)

Lanthanum hexaboride is a commonly used SRM due to its highly crystalline nature and intense scattering. This intense scattering makes it ideal for testing the response of a large detector right up to very high angles. However, when compared to other standard materials, such as silicon, the scattering obtained from LaB_6 is somewhat overpowering and coherent scattering dominates. This makes it less suitable for optimising the data correction strategies as the non-coherent scattering is comparatively much weaker and there is less to correct for whereas silicon provides a more realistic test of the instrument and data reduction procedure. However, to demonstrate the instrument preforms how it is expected, LaB_6 remains a vital first step in the instrument capabilities. Therefore, we present the Rietveld and PDF refinement of LaB_6 as an example that tests the

capabilities of the detector and as a comparison to data found in the literature, but it will not be used as the primary calibration standard for the instrument. Where LaB_6 can be used to check detector efficiency to high angle, it is not ideal for optimising the data reduction steps, so here we present the data obtained for LaB_6 as our first standard, with silicon following to examine the processing in more detail.

LaB_6 was obtained from Sigma-Aldrich. The powder was packed into a 1 mm borosilicate capillary purchased from Capillary Tubes Supplies Ltd. The sample was run for a total exposure time of 120 minutes with an exposure of 84 s/° oscillation. The empty capillary and empty diffractometer were subsequently collected utilising the same parameters to obtain container and empty scattering data sets. The data sets were processed in GudrunX, using a sample composition of LaB_6 and density 4.72 g/cm^3 and other parameters adjusted to obtain high quality total scattering and PDF data. Both XRD and PDF data was analysed via Rietveld (reciprocal and real-space) refinements using TOPAS v6.

The images collected from the sample, container and empty diffractometer were integrated to convert from a 2D to 1D pattern using 2DP[30] and an integration area covering 2θ = 3-134.8° and χ = 135.0-225.0°, as seen in figure 2-8, giving a Q_{max} = 20.68 Å^{-1}. This is lower than the theoretical Q_{max} of 22.4 Å^{-1} (for $\sin\theta = 1$), due to the fixed positioning of the detector and problems integrating right to the detector edge. The advantage of a single large fixed detector is the simplicity of data integration (does not require stitching together of images or geometrical flat plat corrections), the disadvantage is a slightly reduced Q_{max}. So, whilst not all the photons hitting the detector are included in the integration, this is outweighed by the sheer size of the detector. Standard Lorentz and polarisation corrections are included in the 2D integration with an optimisation required for the polarization due to the use of a monochromator.

2.4.1.1 LaB_6 Rietveld Refinement

A Rietveld refinement of LaB_6 was conducted over the full 2θ = 3-135° range with capillary background subtracted in combination with a Chebyshev background function and produced an excellent fit with R_{wp} = 0.075. The peak shape was not defined by a traditional Pseudo-Voigt/Gaussian shape, but rather by a dQ and alpha shape to allow for extraction of instrumental parameters essential for PDF refinements.

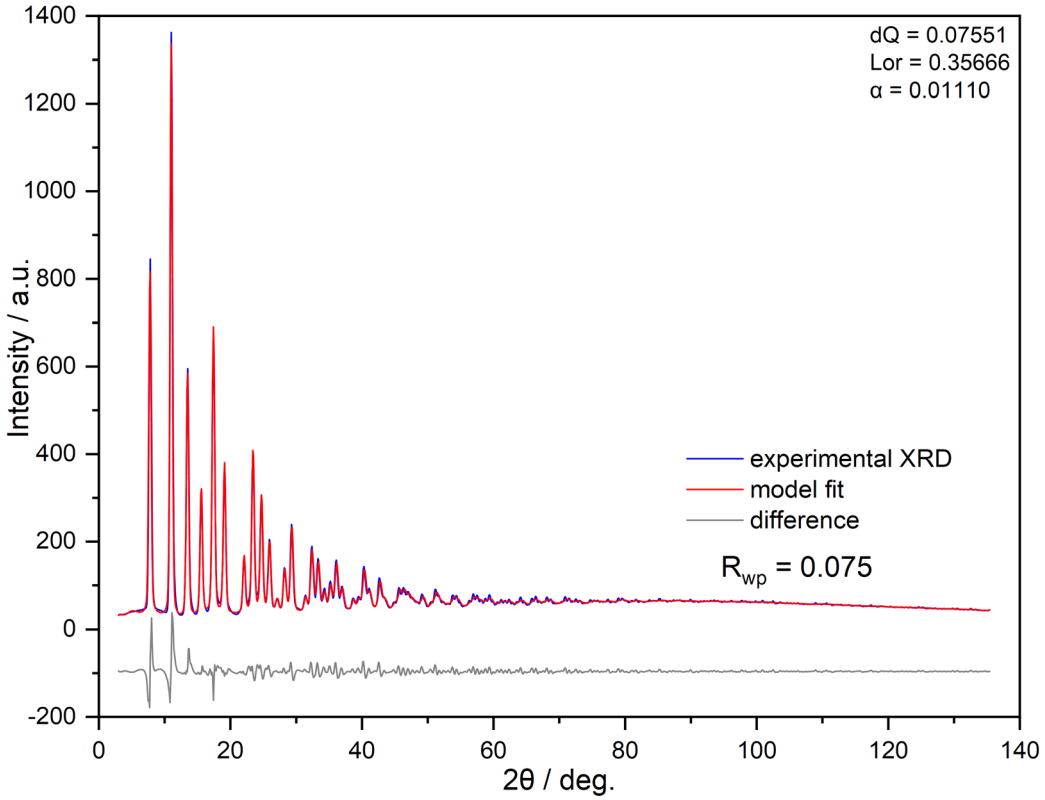

Figure 2-5. *The Rietveld refinement of experimental (blue), calculated model (red) and difference (grey) of LaB_6 in TOPAS with an R_{wp} = 0.075 where blue represents the experimental data, red the model fit and grey the difference.. Data were collected for 120 minutes. Background was removed by subtraction of a 1 mm borosilicate capillary scattering file.*

The use of a Rietveld refinement enables the evaluation of the raw diffraction data from the instrument, but also enables extraction of the instrumental parameters discussed in section 1.3.3. These parameters can be extracted by refinement of a standard material in reciprocal space, using the dQ and alpha terms defined in equation (2-1). The first parameter, dQ dampening defines the broadness (FWHM) of the recorded Bragg peaks, described by a Gaussian shape. This is often combined with a Lorentzian (Lor) contribution to account for the peak asymmetry that often occurs within Bragg data. The final descriptor, alpha (α) describes the increasing broadness with increasing 2θ. All of these descriptors can define the peak shape in Q-space but may also be used to refine against in real-space, and is often suggested to confirm the extracted values.

$$FWHM(Q) = dQ + \alpha Q \qquad \textbf{(2-1)}$$

Once determined from refinement of the Bragg scattering of a standard sample these values can be labelled as instrument specific and fixed in any subsequent PDF refinement. These Rietveld refinements were conducted using TOPAS academic v6[31] utilising both Evans (Rietveld) and Chater (PDF) macros.[32] During the Rietveld refinement data were included across the full 2θ = 3-135° range with capillary background subtracted in combination with a Chebyshev background function. The peak shape was described by the dQ and alpha broadening functions and refined to obtain the best fit. The model crystallographic structure was a silicon standard, CIF 9011998

obtained from the crystallography open database (COD), with lattice and thermal parameters refined. An R_{wp} = 0.065 was obtained, shown in figure 2-12, a good agreement between the experimental Rigaku Spider diffraction data and model.

2.4.1.2 LaB_6 PDF Refinement

The PDF refinement was again conducted within TOPAS across a full range r= 1-100 Å, showing a good agreement between the experimental data and model - highlighted by an R_{wp} = 0.12 in figure 2-6. The lattice parameters and scale factor were then refined followed by the instrumental parameters to obtain the best fit.

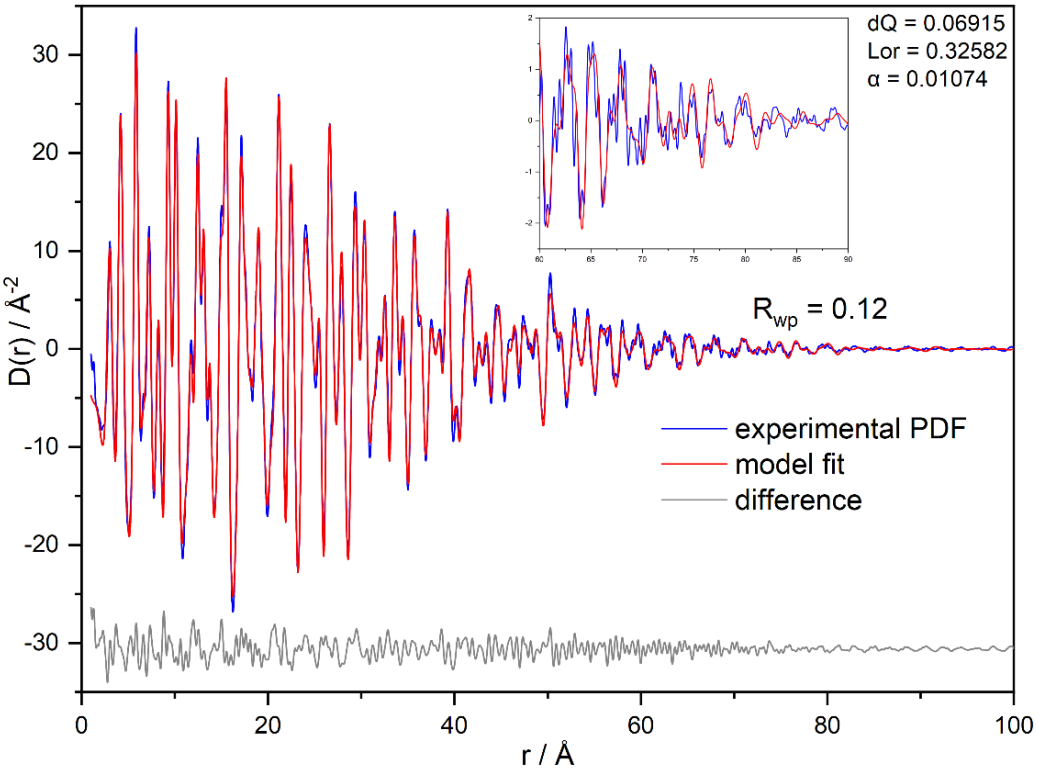

Figure 2-6. *PDF refinement of experimental (blue), calculated model (red) and difference (grey) of LaB_6 in TOPAS with R_{wp} = 0.12. Data was collected for 120 minutes and processed using GudrunX using backgrounds of an empty diffractometer and empty 1 mm borosilicate capillary collected for the same amount of time. An inlay for r = 60-90 Å is shown to highlight the fit at high-r.*

The comparison between the reciprocal and real space refinements can be seen in table 2-3, displaying very similar refined values and therefore allows for confidence in both the reciprocal and real-space refinements.

Table 2-3. *Comparison of lattice and instrumental parameters for LaB_6 derived from the Rietveld and PDF refinements shown in figure 2-5 and figure 2-6.*

Parameter	Reference CIF	XRD Refinement	PDF Refinement
R_{wp}	-	0.075	0.12
a = b= c (Fd-3m) / Å	4.1571	4.1427 (2)	4.1488 (6)
dQ dampening	-	0.07551	0.06915
dQ Lorentzian	-	0.35666	0.32582
Alpha broadening	-	0.01110	0.01074

2.4.1.3 Data Quality and Comparisons

Although, LaB_6 is not a particularly good sample for assessing data quality, especially the correction procedures due to the dominant coherent scattering it has been used as such in the literature. Thomae et al.[12] use LaB_6 not only to highlight the quality of their data but also to extract their instrumental parameters. As this study provides the most comprehensive and comparable data, using LaB_6 to compare between our system and theirs is beneficial in highlighting the advantages of the Rigaku Spider. To make the best comparison possible to the work of Thomae et al.[12] it was necessary to conduct additional refinements using the same software package, PDFgui[33], across the same r-range. This allowed for comparison of dQ/Q-damp values calculated in the same way.

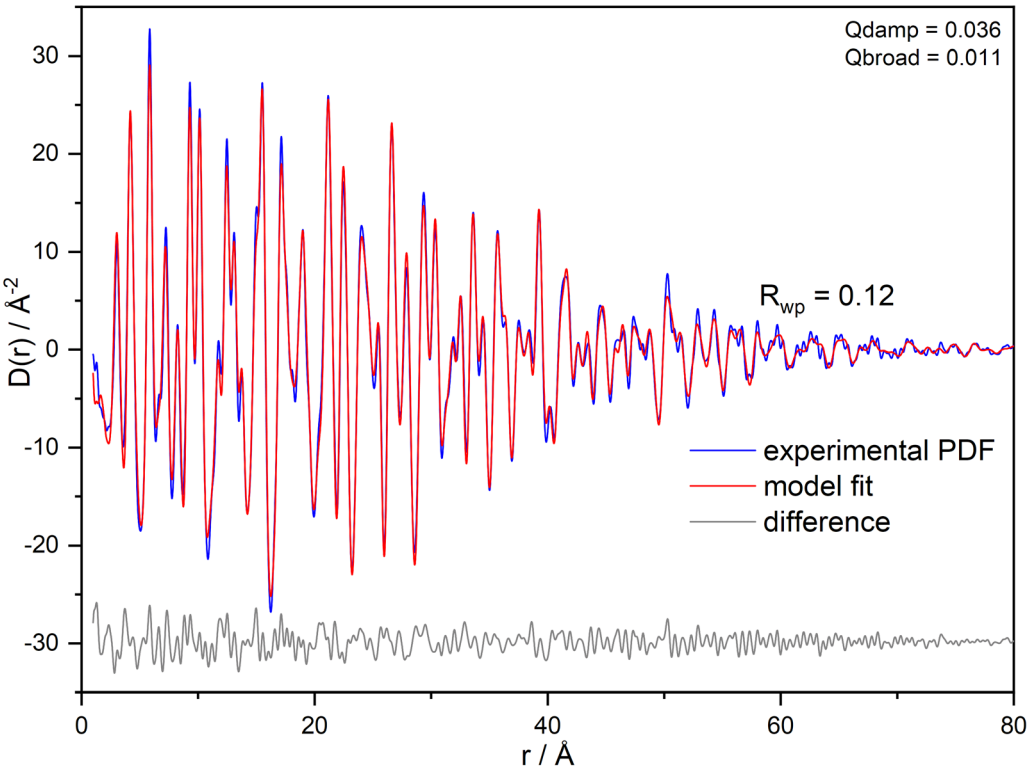

Figure 2-7. *PDF refinement of experimental (blue), calculated model (red) and difference (grey) LaB_6 conducted in PDFgui with R_{wp} = 0.12. Same data utilised from the TOPAS refinement in figure 2-6.*

As can be seen in figure 2-7, the R_{wp} does not differ to its TOPAS counterpart, showing the rigidity of the data set. Over this shorter range, used to compare to Thomae et al.[12], the R_{wp} is 0.02 (2%) lower than that of the STOE diffractometer, once again highlighting the quality of data obtained. Furthermore, the data on the Spider only required 120 minutes for exposure, compared to the STOE diffractometer which required 600 minutes.

Table 2-4. *Comparison of PDFgui refinements and instrumental parameters obtained for LaB_6 for the Rigaku Spider and Thomae et al[12] STOE diffractometers.*

PDFgui r = 1-80 Å	Spider	STOE	Difference
R_{wp}	0.12	0.14	-0.02
q_{damp}	0.036	0.011	+0.025
q_{broad}	0.011	0.010	+0.001

As demonstrated in table 2-4, whilst the R_{wp} is 0.02 smaller for the Spider compared to the STOE instrument and the q_{broad} terms are very similar, the q_{damp} term varies significantly between the two. The LaB_6 refinement supports what can be seen in the data, where intensity falls off rapidly on the Spider compared to other instruments, as shown by the 30.5% increase in q_{broad}. This quantitatively illustrates the lower Q-resolution that is obtained by the Spider. As the STOE adopts a curved Ge(111) monochromator that focuses the beam on the detector, the Bragg peak broadness is less

pronounced compared to the Spider and leads to less of a Q-dependent drop off in intensity. Whilst the Spider could be improved further by the adopting a similar monochromator setup, similar to the STOE instrument, there is always going to be a trade-off between intensity and Bragg peak resolution. The q_{broad} parameter is relatively constant between the two instruments, suggesting that they both exhibit similar r-space broadening and peak resolution with regards to PDF.

Whilst this comparison does highlight the lower Q-resolution originating from the broader Bragg peaks in Q-space, the ability to collect similar quality data in a third of the time shows the high capabilities of the Spider. It does further highlight that care must be taken with future measurements, particularly with regards to nanocrystalline materials, where the intensity drops off due to the Q-resolution may be mistaken for the peak cut-off due to spherical diameter. Therefore, for future studies, it is suggested that the instrument in its current state should not be used for quantified studies into nanocrystalline materials with a spherical diameter larger than 70-80 Å. Again, this is unlikely to cause significant issues as beyond 70 Å it is more suitable to analyse nanoparticle structure by more traditional techniques, with most PDF refinements being limited to 50 Å.

2.4.2 NIST Silicon 640f

NIST standard silicon 640f[34] is a commonly used standard across both XRD and total scattering. This material will be used as the primary calibration standard due to its 'medium' scattering power, and also as a comparison material against data found in the literature. As LaB_6 proved that we can acquire high quality data to a high 2θ value, next was assessing the data reduction process, and using a sample with a less scattering power allows for examination of the 'quirks' of the instrument.

A sample of silicon 640f were obtained from NIST. The powder was packed into a 1 mm borosilicate capillary purchased from Capillary Tubes Supplies Ltd. The sample was run with a total exposure time of 120 minutes with an exposure of 84 s/° oscillation. Scattering from the empty capillary and empty diffractometer were subsequently collected utilising the same parameters to obtain container and empty scattering data sets. The image integration used the same methodology as discussed in section 2.4.1.

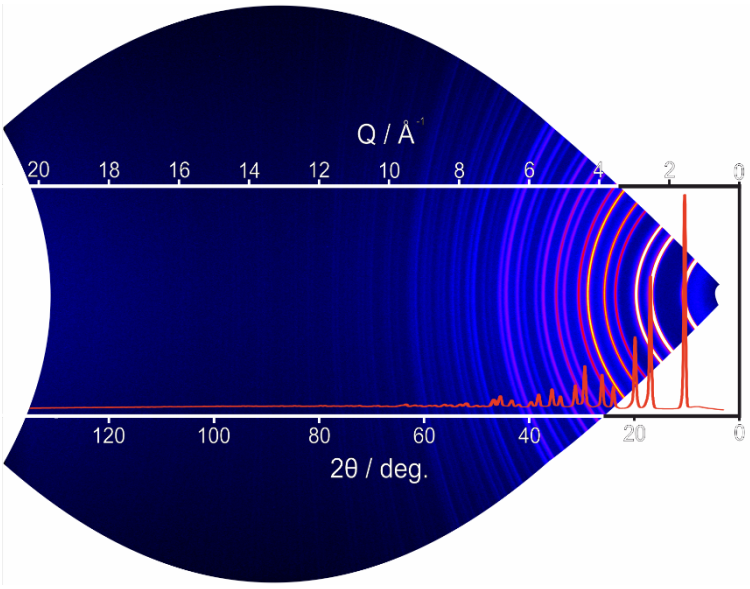

Figure 2-8. *2D diffraction pattern of NIST silicon 640f overlayed with the integrated 1D data. An approximate Q and 2ϑ range is included to highlight the range and data used for processing.*

Data reduction and Fourier transform of the corrected scattering data were conducted using GudrunX.[35] Gudrun was chosen over the alternatives due to its flexibility, allowing for the input of all the fundamental instrumental parameters such as the beam profile and instrument geometry. Table 2-5 shows a generic GudrunX input setup file for the Rigaku Spider highlighting the instrument specific parameters. Whilst a similar data reduction and processing routine to LaB_6 was conducted, silicon highlights inconsistencies in a far more obvious way and therefore lends itself to a more robust processing scheme.

As discussed in section 1.24, the corrections applied to the data are to remove multiplicative effects and scattering that does not originate from the sample. Care has to be taken not to double correct for some effects, such as polarization. This can be corrected for in Gudrun, but a correction has already been applied during integration – a value of -1 is used in Gudrun to turn off the option. Corrections of additive scattering events are also applied by Gudrun, with the main component being the removal of the background (empty instrument) and container (borosilicate capillary) scattering to leave only that coming from the sample itself. Compton effects are also accounted for at this stage and subtracted from the data. Due to the configuration of the instrument, the data reduction within Gudrun is relatively simple primarily due to the use of a monochromator which removes the need for Bremsstrahlung and K_β corrections. Finally, the data are scaled to follow the total scattering cross-section of the sample. The raw data and corrected scattering data sets can be seen in figure 2-9.

Table 2-5. Generic Gudrun input file where *denotes a value that is sample dependent, ᵗdenotes an instrumental parameter with all other values being the default values.

Instrumental	**Value/Parameter**
'Q-range /$Å^{-1}$	1 – 20.68
Step size	0.01
Beam	
Sample geometry	Cylindrical
ᵗIncident beam edges relative to centre of sample / cm	-0.25 0.25 -0.25 0.25
ᵗK-beta filter thickness / cm	0.0
Bremsstrahlung power	0.96
ᵗDetector cut-off / keV	36
Cut-off width / keV	3
ᵗLowest scattering angle / degree	3.00
ᵗHighest scattering angle / degree	134.80
Scattering angle step / degree	0.02
ᵗWavelength (weighted average α1/α2) / Å	0.5608848
Normalisation	
Divide $<F>^2$	1
Power for Breit-Dirac Factor	2
Krogh-Moe & Norman	1
<u>Background</u>	

Empty diffractometer total exposure time / minutes	30, 60, 120, 180 (sample dependent)
Background angle range / degree	3.00 – 135.40
Container (Borosilicate)	
Container total exposure time / minutes	30, 60, 120, 180 (sample dependent)
Container angle range / degree	3.00 – 135.40
Container exposure / minutes	30, 60, 120, 180 (sample dependent)
Inner/outer radii / cm	0.495/0.500 (1 mm capillary) 0.995/1.000 (2 mm capillary)
Atomic composition	$SiO_{2.21}B_{0.26}Na_{0.08}Al_{0.04}$
Density / gcm^{-3}	2.23
Container tweak factor	1
Sample	
Sample total exposure time / minutes	30, 60, 120, 180 (sample dependent)
Sample inner/outer radii / cm	0.000/0.495 (1 mm capillary) 0.000/0.995 (2 mm capillary)
*Atomic composition/density	Sample dependent
*Sample density / gcm^{-3}	Sample dependent
Incident beam polarization	-1
Top hat width / $Å^{-1}$	-14
*Minimum radius for Fourier Transform / Å	Sample dependent
*Width of broadening in r-space / Å	0.1-0.2 (lower for solid, higher for liquids)
*Broadening power	0.1-0.2 (lower for solid, higher for liquids)

Some steps of the data correction, such as background and container scattering are reasonably straightforward, but others require an iterative approach to obtain a sensible PDF. The general process of obtaining the total scattering data is explained in detail in section 1.3 and will therefore not be discussed in detail here. However minor comments can be made on the processing, allowing for the background reduction (seen in figure figure 2-9) and subsequent calculated functions in figure 2-10 and figure 2-11.

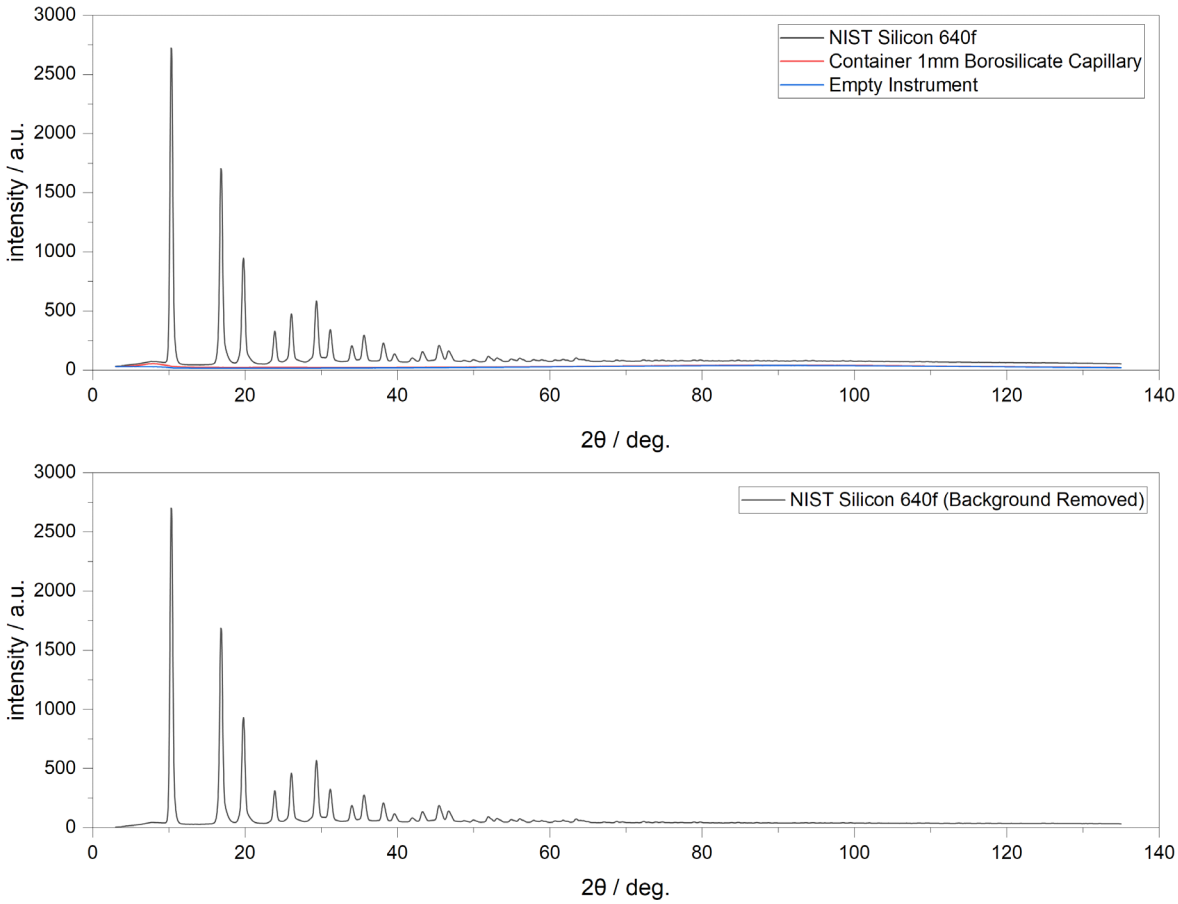

Figure 2-9. *Scattering data for both (top) raw sample, container and empty scattering and (bottom) background removed data, highlighting the need to remove the background and container scattering.*

Specific 'tweaks' include altering the minimum radius, cleaning up data below the first expected bond length and modelling the peak broadening in r-space using a Lorch function.[36] This function acts to smooth termination ripples due to the finite Q-range available and is typically set to 0.1 for a crystalline sample and between 0.15-0.2 for amorphous and aqueous samples. Gudrun produces a multitude of outputs enabling various analysis routes, however, the main functions used herein are the total scattering structure factor, S(Q), reduced total scattering factor, F(Q), and the pair distribution function, D(r). These outputs can be seen in figure 2-10 and figure 2-11. Note that whilst the above thoroughly discusses the process for the data reduction for the Rigaku Spider, data from other instruments and central facilities may vary based on both the instrumental setup and radiation source.

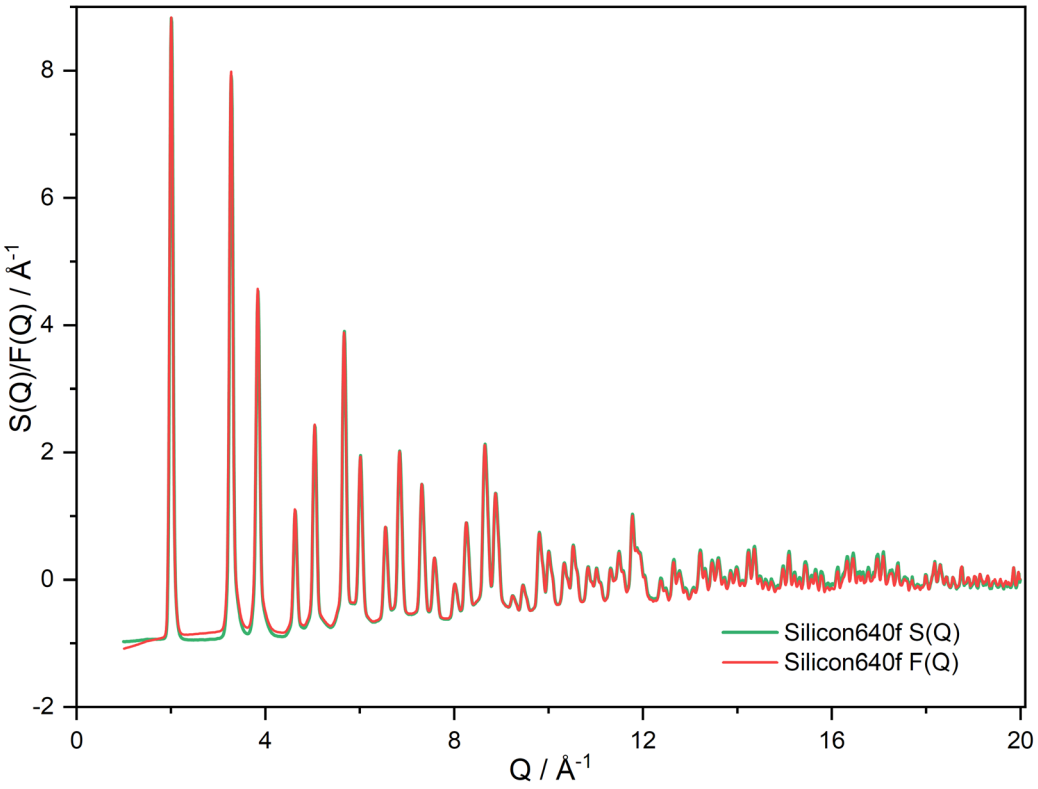

Figure 2-10. *Total scattering structure factor, S(Q) (green) and reduced total scattering factor, F(Q) (red) obtained for silicon 640f via GudrunX. The overlap of both functions suggests good data reduction and normalisation of data.*

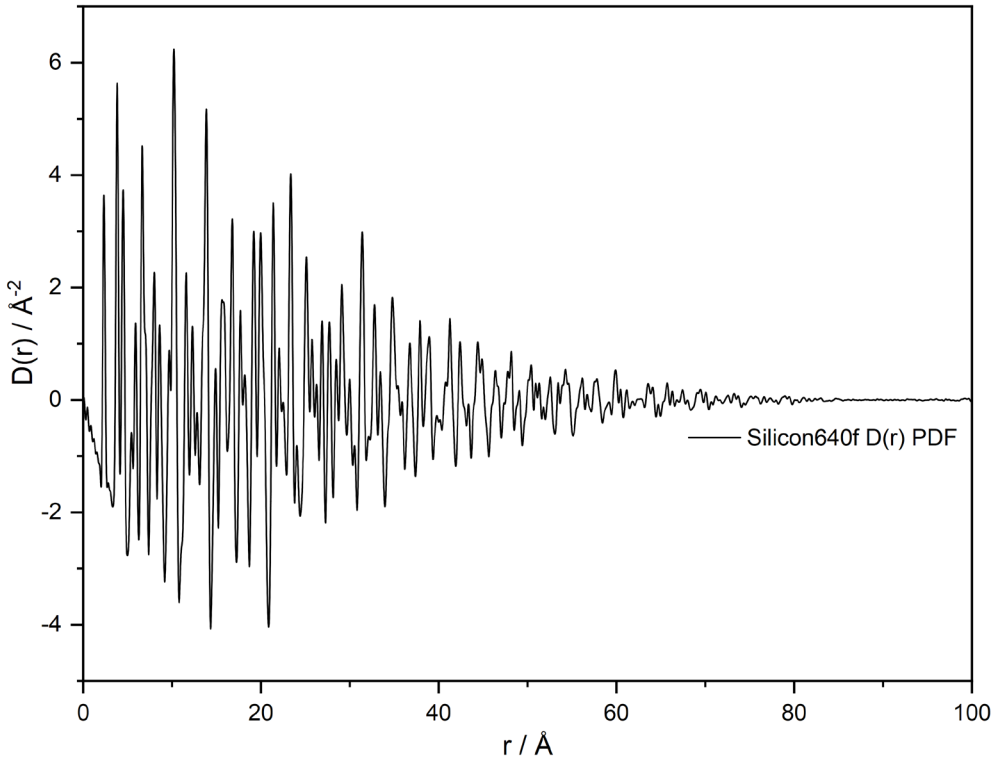

Figure 2-11. *Experimental pair distribution function of silicon 640f, D(r) calculated in GudrunX from* the raw scattering data in figure 2-9 and total scattering data in figure 2-10.

2.4.2.1 Silicon Rietveld Refinement

A Rietveld refinement of silicon 640f was conducted over the full 2θ = 3-135° range with capillary background subtracted in combination with a Chebyshev background function and produced an excellent fit with R_{wp} = 0.076. To allow comparison between the silicon and LaB_6 data sets, the same peak shape definition was employed, using the dQ and α peak shapes. The values obtained are similar to those of the silicon refinement, as seen in table 2-5, and the consistency provides a degree of confidence in the instrument.

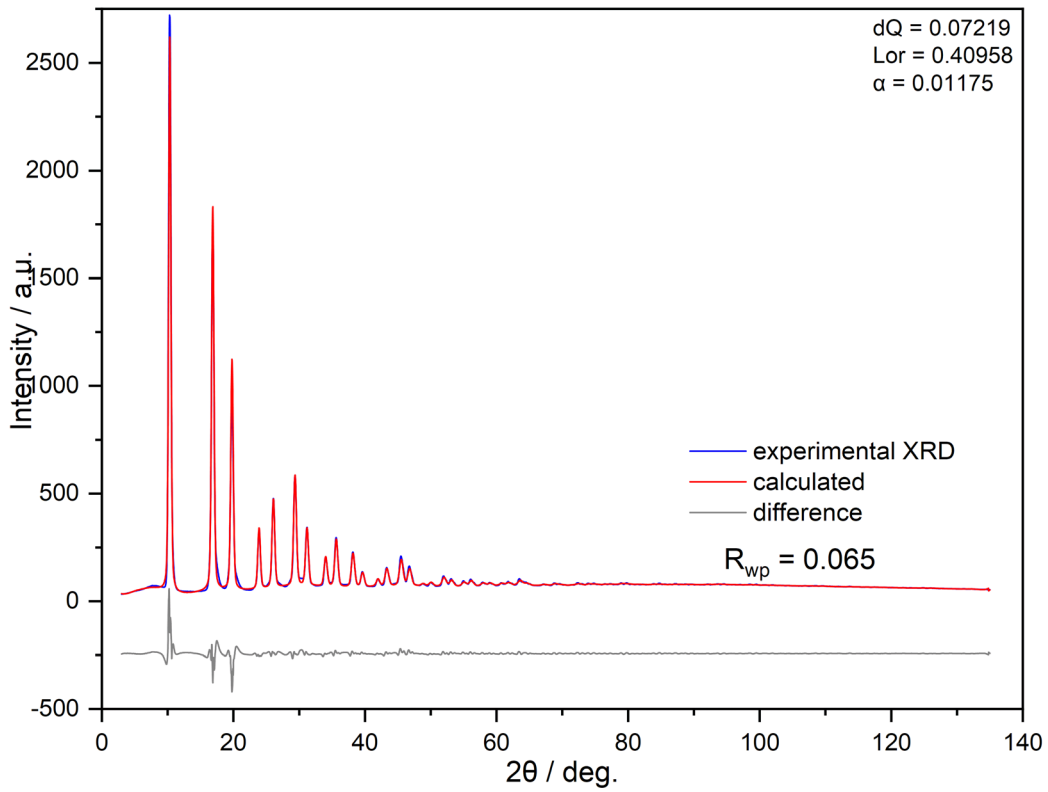

Figure 2-12. *Rietveld refinement of experimental (blue), calculated model (red) and difference (grey) NIST silicon 640f conducted within TOPAS v6, obtaining an R_{wp} = 0.065. Data was collected for 120 minutes. Background was removed by subtraction of a 1 mm borosilicate capillary scattering file.*

2.4.2.2 PDF Refinement

Using the instrumental parameters from the Rietveld refinement seen in figure 2-12, a PDF refinement was carried out, again using TOPAS v6. this was done across a full range r= 1.0 – 100.0 Å and shows a good agreement between the experimental data and model highlighted by an R_{wp} = 0.12. The lattice parameters and scale factor were allowed to refine for the first iterations until stable. Once the fit was adequate and no further changes were observed with regards to the lattice, the instrumental parameters were allowed to refine. This not only enables an improved fit but also justifies the instrumental parameters obtained. The minor variation observed between the Rietveld and PDF refinements solidifies these values for the Rigaku Spider. The good fit obtained for the PDF

and relatively small variation in both the lattice and instrumental parameters, seen in table 2-6, show a robust set of protocols for the data collection, reduction, and refinement, giving instrumental parameters that can be used for future experiments on this instrument.

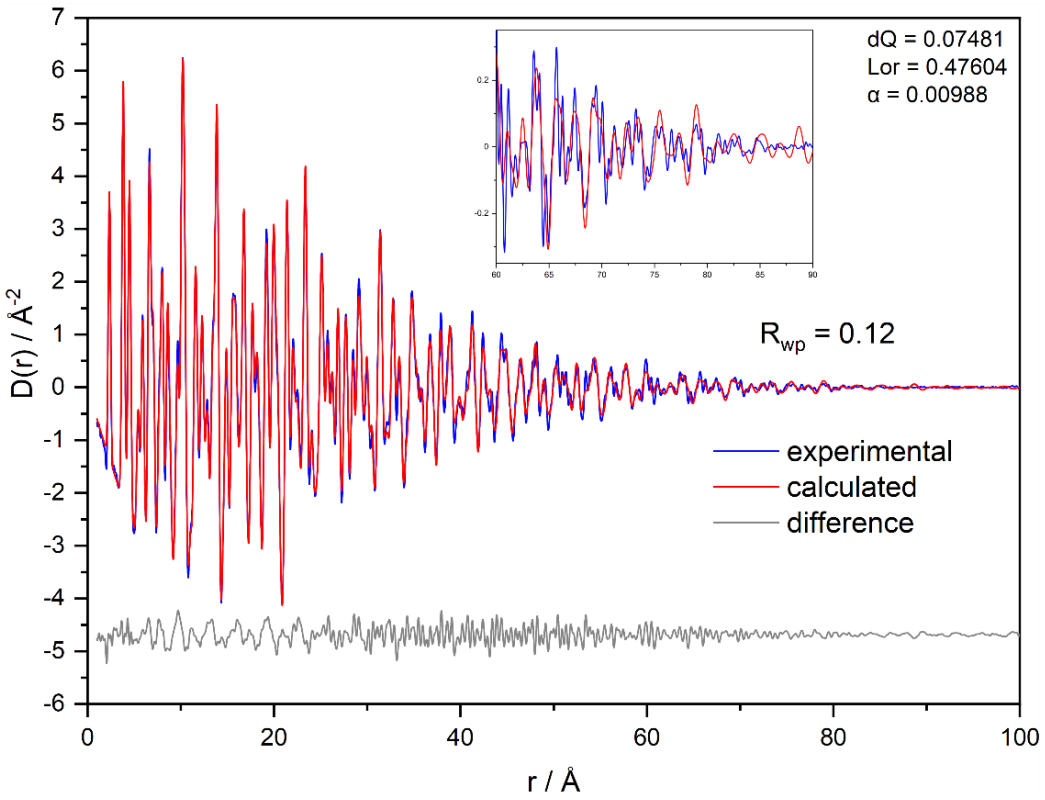

Figure 2-13. *PDF refinement of experimental (blue), calculated model (red) and difference (grey) NIST Silicon 640f in TOPAS with Rwp = 0.12. Data were collected for 120 minutes and processed using GudrunX using backgrounds of an empty diffractometer and empty 1 mm borosilicate capillary collected for the same amount of time. An inlay for r = 60-90 Å is shown to highlight the approximate data cut off.*

A similar comparison between the Rietveld and PDF refinements can be found in table 2-6, and whilst will be discussed in further detail in further sections, overall, it shows a good match between the reciprocal and real space refinements.

Table 2-6. *Comparison of refined and reference values for silicon 640f as derived from the refinements found in figure 2-12 and figure 2-13.*

Parameter	Reference CIF	XRD Refinement	PDF Refinement
R_{wp}	-	0.065	0.12
a = b= c (Fd-3m) / Å	5.43123	5.433 (8)	5.42504 (7)
dQ dampening	-	0.07219	0.07481
dQ Lorentzian	-	0.40958	0.47604
Alpha broadening	-	0.01175	0.00988

2.4.2.3 Data Quality and Comparisons

The data acquired from the Rigaku Spider highlights the quality of PDF data that can be obtained and the potential of this instrument for high quality PDF studies without the need for a central facility. Using the work of Thomae et al.[12] who report in detail the use of a STOE diffractometer as the current benchmark for laboratory-based PDF instrument, their R-factors are ca. $R_{wp} > 0.14$ over an r-range = 1-80 Å. In contrast the Rigaku Spider produces a lower R-factor with refinements extending over a longer range in r (if required). In addition, the sample exposure time is reduced significantly due to the large-curved detector. This decreases experiment time 3-fold when compared to the STOE instrument's four movable Si-strip detectors.

Table 2-7. *Comparison of the instrumental parameters across Rietveld (XRD) and PDF refinements for both standard material silicon 640f and LaB_6.*

	NIST Silicon 640f		**LaB_6**	
	XRD	**PDF**	**XRD**	**PDF**
dQ dampening	0.07219	0.07481	0.07551	0.06915
Lorentzian	0.40958	0.47604	0.35666	0.32582
Alpha broadening	0.01175	0.00988	0.01110	0.01074

As the table above shows, the main instrumental parameters of dQ and α only vary by a maximum of 8.41% and 8.42% respectively. This is well within a margin of error and due to the sensitive nature of total scattering and PDF experiments, variation is to be expected. As background and sample will vary from day-to-day, it is impossible to recreate the exact same conditions for every experiment. Therefore, a variation <10% between values shows consistent data output and refinement, and is similar to variations found in literature.[2,12] The Lorentzian contribution does vary more significantly than the other values, however this is more likely due to the sample induced peak shape rather than an inconsistencies in the instrumental parameters.

One disadvantage of the Rigaku Spider is the reduced Q-resolution obtained, with dQ being larger than other laboratory instruments. This can be seen in the broadness of the Bragg peaks and results in the PDF intensity falling away quicker as a function of r. This can be seen in figure 2-13, where the high r signal is very weak and does not vary significantly from the baseline. However, as many materials, including those studied in subsequent chapters, do not exhibit long-range order above 50 Å, this is not seen as a major problem.

2.4.3 Amorphous Silica (SiO_2)

Amorphous silica is an ideal standard for PDF due to its lack of long-range order, and the fact that it can not be characterised by standard diffraction methods. As the scattering is not dominated by Bragg peaks it was decided to use amorphous silica to evaluate the counting statistics of the instrument to optimise the exposure times chosen for each sample. The scattering of amorphous silica is dominated by a broad hump at ca. $2\theta = 20°$ ($\lambda = 1.54$ Å), typical of amorphous and nanocrystalline materials, due to the approximate inverse relationship between peak broadness and crystallite size, defined by the Scherrer equation.[37] Little to no information can be obtained from the pattern obtained. Khouchaf et al.[38] discuss in detail the structure of amorphous silica nanostructures, and demonstrate the difficulty in characterising such materials. Whilst the authors can highlight the peak maxima centred on $2\theta = 21°$($\lambda = 1.54$ Å) , no other useful information can be obtained on the material via PXRD, and other methods such as electron energy loss spectroscopy (EELS) and electron PDF (ePDF) being used to fully characterise these materials.

PDF has been used frequently to characterise the structure of amorphous silica, with Keen et al.[39] providing a comprehensive study into the material. The use of amorphous silica in this work is purely in the optimisation of counting times rather than structure refinement, already explored for silicon and LaB_6.

2.4.3.1 Varying Exposure Time

A sample of amorphous silica was obtained from Sigma-Aldrich. The powder was packed into a 1 mm borosilicate capillary purchased from Capillary Tubes Supplies Ltd. The samples were run for total exposure times of 30, 60, 120, 180 and 240 minutes with an exposure of 84 s/° oscillation. The empty capillary and empty diffractometer were collected utilising the same exposure times to obtain container and empty scattering data sets. The data were processed in GudrunX, following the same procedures as previously described, using a sample composition of SiO_2 and density 2.65 g/cm^3 and other parameters adjusted to obtain high quality total scattering and PDF data.

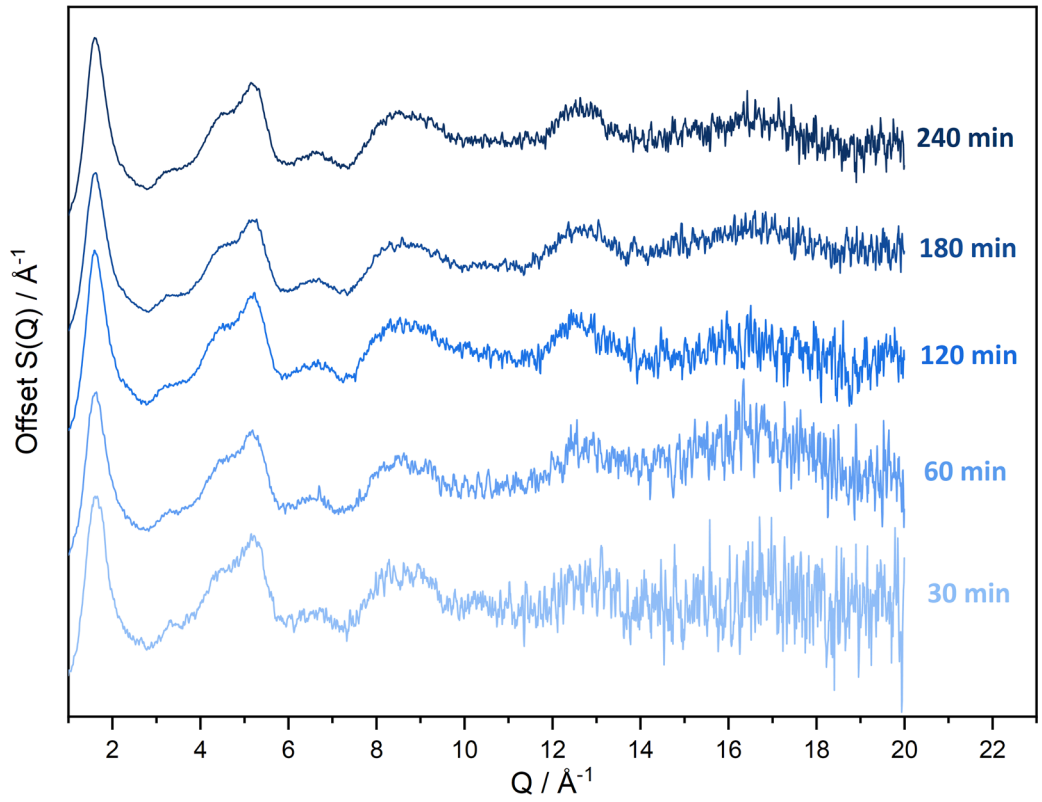

Figure 2-14. *Total scattering, S(Q), comparison for amorphous silica over varying exposure times, shown to the right of the data. All samples were processed and calculated using GudrunX.*

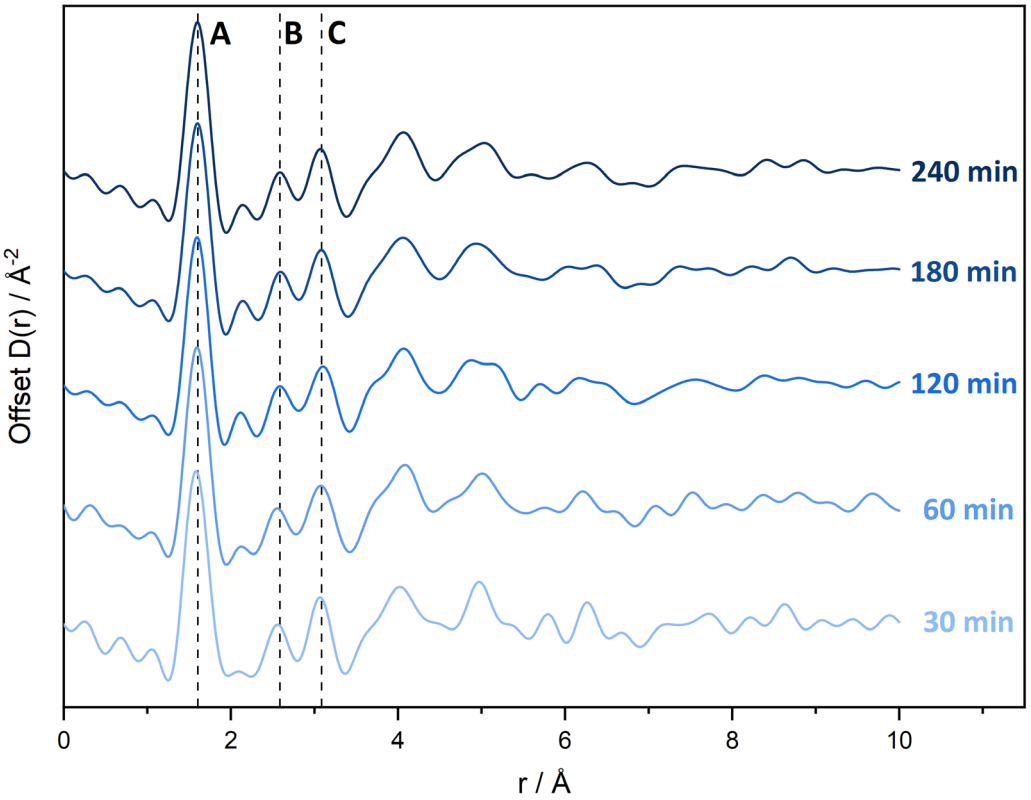

Figure 2-15. *PDF data for amorphous silica over various exposure times, obtained by Fourier transform of the S(Q) in figure 2-14. Peak assignment: A) Si-O (1.60 Å), B) **O**-Si-**O** SiO_2 oxygen edge atoms (2.60 Å) and C) **Si**-O-**Si** neighbouring central Si (3.08 Å)*

Figure 2-14 shows the S(Q) data processed from varying exposure times of amorphous silica. As the exposure time is increased, the noise is dramatically reduced, with little further change occurring above 180 minutes. This suggests an optimum time of 120 minutes with longer exposures not radically improving the data. This is particularly obvious in the final PDF data found in figure 2-15, where little change can be observed within the PDF with longer exposures than 120 minutes. Below this exposure, the additional noise seen within the S(Q) scattering data propagates itself as high frequency ripples, particularly at r = 5.0+ Å. Overall, an exposure time for this more challenging sample of 120 minutes is satisfactory for analysis and extending beyond this does not provide additional information. Despite the improvement of data as exposure times approach 120 minutes, three major features, denoted A, B and C, can be seen throughout all exposures with little to no deviation in the position or magnitude. This observation shows that even at very short exposure times correlations between Si-O, O-O and Si-Si can be recorded.

Quantifying the noise level in total scattering data is more difficult than for diffraction data where we can compare the height of the noise to the Bragg peaks and therefore a different approach must be taken. Table 2-8 shows a qualitative study into the noise, with the upper and lower bound of the signal being measured. Whilst this includes the obvious sample related scattering, as shown by the common feature at Q = 1.6 $Å^{-1}$, this is not indicative of the signal to noise. Therefore, further focus was put on the high Q-range, where noise will tend to be most obvious. Using the signal spread over high-Q ranges, it is obvious there is a significant decrease between 25% and 34% with longer exposure times. Whilst this study is qualitative, it provides an approximate magnitude of the decrease in noise.

Table 2-8*. Qualitative comparison of noise within the S(Q) over the exposure times seen in figure 2-14. This is shown by the upper and lower bound of the experimental data, range between these values and % noise reduction compared to the previous time exposure.*

Exposure time / minutes	Upper bound / $Å^{-1}$	Lower bound / $Å^{-1}$	Signal spread Q = 15-20 $Å^{-1}$ /$Å^{-1}$	% noise reduction between previous measurement
30	0.68902	-0.95925	1.64827	N/A
60	0.77674	-0.47623	1.25297	-24%
120	0.37259	-0.47688	0.84947	-32%
180	0.36401	-0.16208	0.52609	-38%
240	0.36774	-0.40538	0.77312	+46%

Other instruments tend to use either longer total exposure times by means of additional experiment time, as seen with the previously discussed STOE instrument by Thomae et al.[12]. Various attempts at measuring and combing multiple exposures from the same sample did not improve the data quality on the Spider, largely due to the inherently low noise on a single exposure. The study into exposure times largely justifies the choice of exposure times for solid samples, it is possible that additional exposure time will be needed for even more weakly scattering aqueous samples. Overall, we have proven the Spider can record high quality total scattering and PDF data more rapidly than other instruments described in the literature.

2.4.4 Titania (TiO_2, 5nm) Nanopowder

Nanomaterials are of great interest within modern material development[4,40–43] and are an ideal candidate for PDF analysis. Typically, nanocrystalline materials will still exhibit long-range order, akin to crystals, but due to the small size of the crystallites, the behaviour in an PXRD pattern is more akin to an amorphous material. However, PDF can enable analysis of these materials with relative ease, where structural features can be extracted from small-box refinements. Being able to analyse the bulk structure of such materials is highly beneficial to making structure/property links. 5 nm TiO_2 nanoparticles were chosen for two main reasons: TiO_2 is a quantitative standard material allowing for further confirmation of data quality and the 5 nm (50 Å) and it is the same material used by Thomae et al.[12] and will allow direct comparison to their work. A further comment on the instrument can also be highlighted through this study which is that the crystallite size is smaller than the dQ dependent cut off in intensity at approximately 8 nm (80 Å), whilst this was primarily discussed in section 2.4.1.1, it did not become truly apparent until the nanoparticle data found here.

A sample of TiO_2 (5 nm) nanopowder was obtained from GetNanoMaterials. The nanoparticles were packed into a 1 mm borosilicate capillary purchased from Capillary Tubes Supplies Ltd. The sample was run for a total exposure time of 120 minutes with an exposure of 84 s/° oscillation. The empty capillary and empty diffractometer were then collected utilising the same parameters as the silicon sample to obtain container and empty scattering data sets. The data sets were processed in GudrunX, using a sample composition of TiO_2 and density 4.23 g/cm^3 and other parameters adjusted to obtain high quality total scattering and PDF data. The PDF data was then refined within TOPAS v6.

2.4.4.1 TiO_2 (5 nm) PDF Refinement

The PDF refinement followed the same procedure as previous fits, being refined over the full r = 1-100 Å, however a spherical dampening factor was introduced to allow for peak cut-off due to

crystallite or nanoparticle size. The lattice parameters and scale were allowed to refine in a similar fashion to previous refinements, with the instrumental parameters allowed to refine at the end to justify the parameters and induce the best possible fit. Shown in figure 2-16 is the fit obtained, with a R_{wp} = 0.117 and a refined spherical diameter of 52.35 Å, displaying a good agreement between the experimental, calculated and with the spherical diameter in agreement with the value given by the manufacturers.

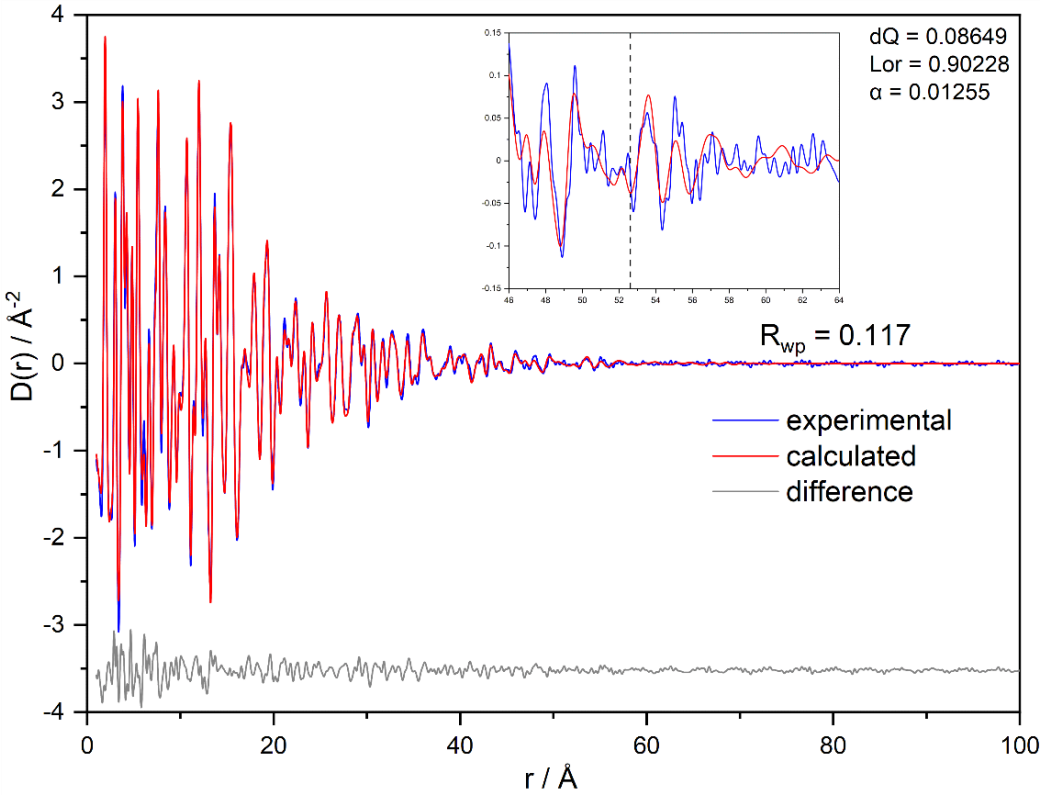

Figure 2-16. *PDF refinement of experimental (blue), calculated model (red) and difference (grey) TiO_2 in TOPAS with Rwp = 0.117. Data were collected for 120 minutes and processed using GudrunX using backgrounds of an empty diffractometer and empty 1 mm borosilicate capillary collected for the same amount of time. An inlay for r = 46-64 Å, with a dashed line to highlight the refined spherical diameter.*

2.4.4.2 Data Quality and Comparisons

The data obtained from the TiO_2 nanopowder and the refinement statistics not only highlight the quality of the data, but also the agreement between the refined parameters and those of the particle size. To further confirm the particle size, transmission electron microscopy (TEM) analysis was conducted by Miss Alice Oakley (Southampton) to directly image the particles. An average particle size of 5 nm was extracted, confirming both the manufacturers claim of particle size but also the refined particle diameter from PDF.

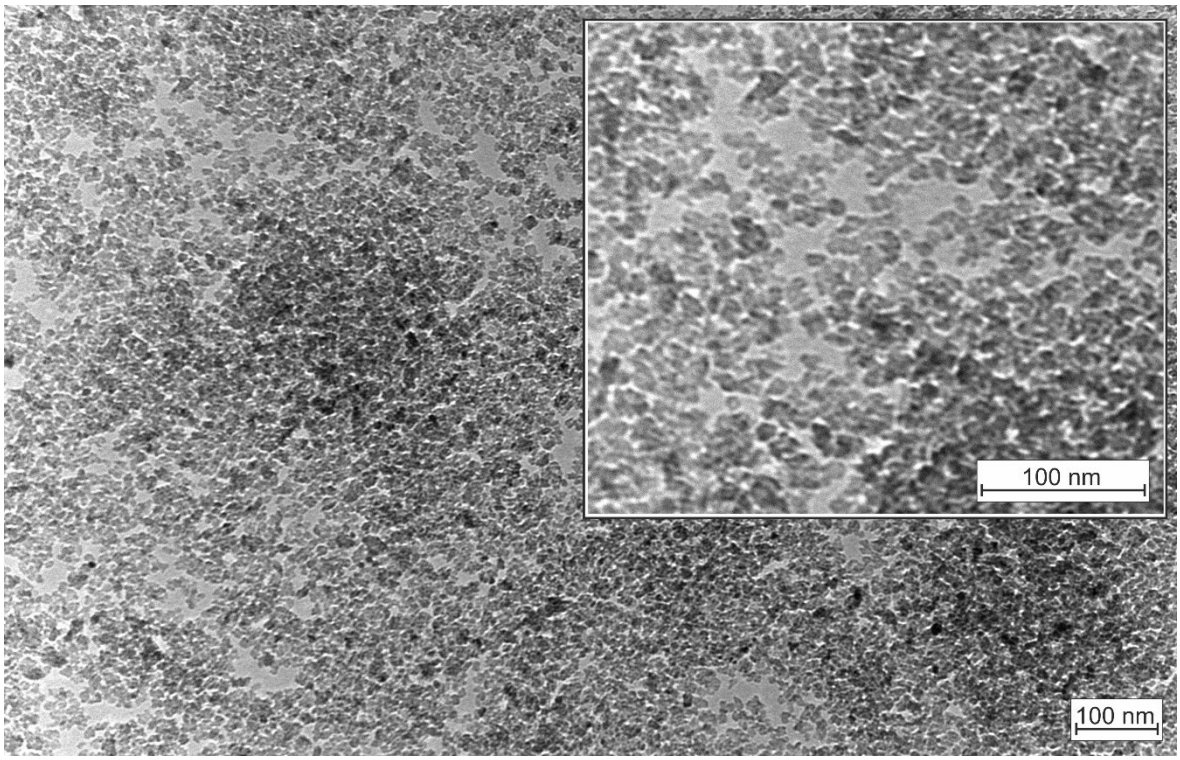

Figure 2-17. *TEM image collected externallu of TiO_2 used for PDF analysis, allowing for the confirmation of particle size.*

However, it must be noted the larger variation in the refined instrumental parameter, especially that of the dQ dampening. This value is approximately 0.015 larger than that of the other standard materials previously studied. This increase is likely due to the nanoparticle nature of the sample, where the peak in reciprocal space are likely to be broader due to the small crystallite size of the TiO_2, which is therefore manifesting itself as worsening Q-resolution. As the data do not extend into the typical r-range of the other standards (>70 Å), the deteriorating Q-resolution is expected. The use of a spherical dampening parameter is likely to affect this value further, showing a cut-off in the data due to particle size rather than instrumental Q-resolution. So whilst it suggests a worse dampening, it is likely due to the sample itself and how TOPAS refines samples of this nature.

***Table 2-9**. Refinement of TiO_2 (5 nm) compared between Thomae et al. STOE instrument and the Spider, over varying r-range.*

Parameter	PDF Refinement Reference	TiO_2 (r = 1-100 Å) Spider	TiO_2 (r = 1-70 Å) STOE	TiO_2 (r = 1-30 Å) Spider	TiO_2 (r = 1-30 Å) STOE
a,b / Å	3.7845	3.7847 (11)	3.7948	3.7844 (2)	3.7944
c / Å	9.5143	9.5059 (4)	9.5316	9.5031 (8)	9.5312
Scale	-	1.004	-	1.011	-
Particle Diameter / Å	50	52.35	-	51.4157	-
R_{wp}	-	0.117	0.22	0.11	0.18

Being able to compare the data to that collected on the STOE instrument allows for further confirmation of the Spider as a total scattering and PDF instrument. Table 2-9 shows the refinements obtained on both instruments over similar ranges. Whilst Thomae et al. do not use the same diameter nanoparticle, opting for a 7 nm particle compared to our 5 nm TiO_2, comparisons between the data are still possible. Firstly, the lattice parameters obtained on the Spider are a truer representation of the crystal lattice than the STOE refinement, where we obtain an a,b within 0.005% of the crystallographic value, whereas the STOE is within 0.271%, showing a larger variation (although there is a caveat relating to how closely the structures of nanoparticles do or do not resemble that of the bulk). Furthermore, the R_{wp} obtained on the Spider far exceeds the STOE over both ranges. It should be noted that in the data obtained on the STOE at the higher range show a large amount of noise, which is not present in the high-r from the Spider data, showing the lower noise obtained from our instrument.

Therefore, a comparison over the short-range r = 1.0-30.0 Å was conducted to allow a fairer comparison, where information in both refinements should not differ significantly. Over this shorter range, an improvement of 7% was obtained in the quality of fit, being closer to the data quality of the 11-ID-B synchrotron (Advanced Photon Source, APS, Chicago) data, with an R_{wp} = 0.15, than that of the STOE laboratory diffractometer. It is worth noting that whilst R-factors should not be compared directly between instruments that are not identical, it does provide a good indication of data quality and a comparison point. Whilst the R-space resolution may be worse on the Spider, this does not reduce the quality of data, refinements and refined values obtained.

2.4.5 Water

Water is a commonly studied system in the field of total scattering, with many researchers investing large amounts of time investigating both water itself as well as the roll of water aqueous systems. As water is an essential molecule to life on Earth, its intermolecular structure is of high importance, however, its structure beyond short-range interactions still evokes many questions, with many competing hypotheses in the literature. Studies have been conducted via traditional analysis techniques such as infrared spectroscopy[44], UV-Visible spectroscopy[45], NMR spectroscopy[46] as well as computer simulations[20]. Other studies have been conducted, such as small-angle X-ray scattering (SAXS)[19] that reveal further information on local environment and direct bonding modes. Therefore a total scattering approach enables larger models to be constructed, and studies have been conducted over multiple temperatures such as those of Soper[21,47].

Solid and liquid water have been studied extensively using both neutron and X-ray total scattering experiments. Such studies have revealed defined structure throughout, whereby oxygen occupies an almost crystallographic positioning in lower temperature samples, with a 3- or 4-coordinate hydrogen bonding network being abundant throughout the liquid phase, all of which being temperature dependent.[47] From these refinements, a multitude of structural information can be extracted utilising the information such as coordination number, angle, spatial density functions (SDF), radial distribution functions (RDF) as well as manually inspecting the model. Knowing the structure of water within a pure solution is also essential to studies of dissolved species as it makes up the majority of an aqueous solution. As the main thrust of this work is the analysis of aqueous solutions, it is essential to prove that we can use the Spider to collect data of sufficient quality to correctly refine the structure of pure water.

2.4.5.1 Water Refinement

Whilst all previous refinements discussed have been undertaken using a small-box real-space Rietveld approach, water cannot be modelled the same way due to its lack of long-range order. Previous examples up to and including amorphous silica have had some degree of ordering, even if that is at a very short range, however, water has very little ordering and a small-box approach would be inappropriate. It has therefore been decided to use a large-box EPSR approach – the details of which have been previously discussed in section 1.3.4.

Table 2-10. *Table describing the Lennard-Jones parameter utilised in EPSR where * denotes the mass for both hydrogens within the molecule.*

Component	Number of atoms	ε / kJmol^{-1}	σ / Å	Mass / gmol^{-1}	Partial charge / a.u.
O	10000	0.65000	3.20000	15.9994	-0.847600
H	20000	0.00000	0.00000	2.00000*	0.423800

A 2 mm borosilicate capillary purchased from Capillary Tubes Supplies Ltd was filled with deionised water. The sample was run for a total exposure time of 180 minutes with an exposure of 127 s/° oscillation. Scattering from the empty capillary and empty diffractometer were then collected utilising the same parameters to obtain container and empty scattering data sets. The data sets were processed in GudrunX, using a sample composition of H_2O and density 1.00 g/cm^3 and other parameters adjusted to obtain high quality total scattering and PDF data. The reduced scattering function, F(Q), was used as the data to be refined against for EPSR alongside the relevant water reference potentials (table ***2-10***), obtained from Soper[22], as well as the basic atomic model of water.

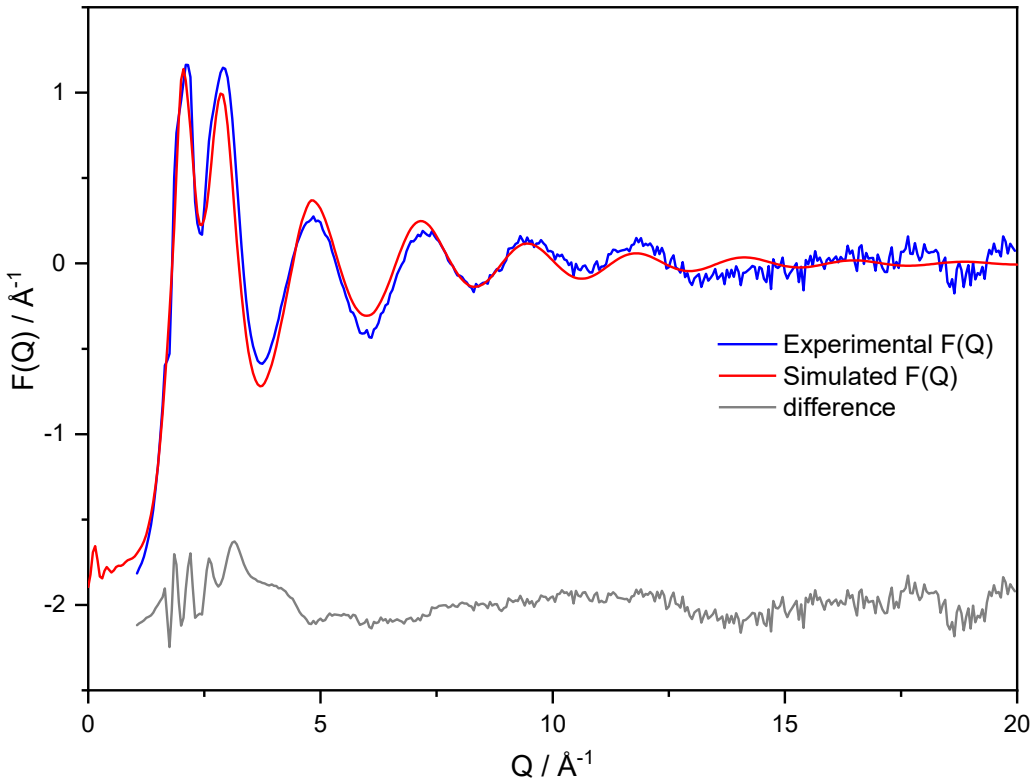

Figure 2-18. *F(Q) total scattering refinement of experimental (blue), calculated model (red) and difference (grey) of H_2O obtained via EPSR. Data was collected for 180 minutes and processed using GudrunX using backgrounds of an empty diffractometer and empty 1 mm borosilicate capillary collected for the same amount of time.*

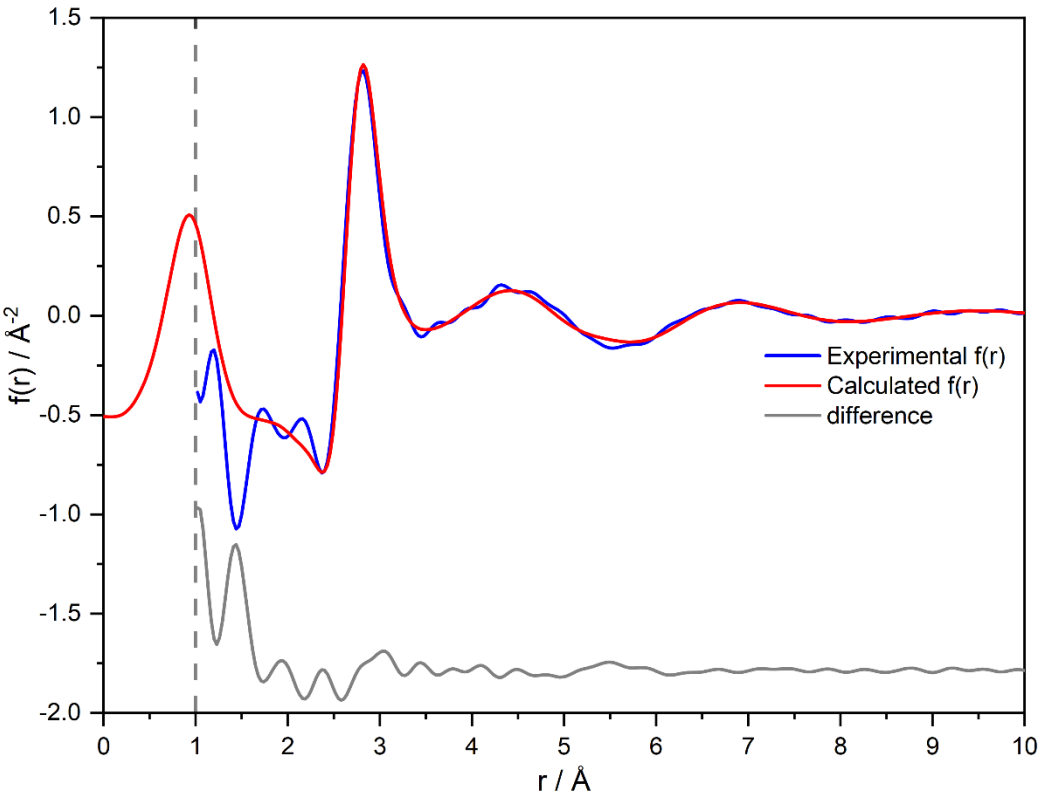

Figure 2-19. *f(r) RDF derived from F(Q) (figure 2-18) of experimental (blue), calculated model (red) and difference (grey) of H_2O obtained via EPSR. Data was collected for 180 minutes and processed using GudrunX using backgrounds of an empty diffractometer and empty 1 mm borosilicate capillary collected for the same amount of time.*

As figure 2-18 shows, the refinement produces a good fit between the experimental and calculated F(Q). Unlike more crystalline samples, the noise in the scattering data is more dominant particularly at higher Q ranges. A higher noise component is inherent in less ordered materials such as liquids that possess larger, more rapid motion during the experiment compared to a solid sample. This can be considered similar to the case of Bragg diffraction where Debye-Waller temperature factors describe the effect of motion on peak intensities, with increased vibrations in the lattice causing increased noise. This is due to the atomic vibrations giving rise to thermal diffuse scattering and ultimately decreases the Bragg peak intensities.[48–50] The same arguments can be posed to scattering data, where the increased motion will ultimately lead to inherently noisier scattering data.

These effects are more noticeable with total scattering experiments, where the measured Q extends to much higher values than a traditional diffraction experiment, and this is the region of scattering where noise is most obvious. However, it is important to treat the high Q data very carefully as they contain information on the shorter-range interactions and effects the overall quality of the PDF. The easiest methodology to reduce noise is to increase the exposure time, where the increased statistics improve the high Q region. This has been discussed in detail in section 2.4.3, where silica data were shown to improve significantly with increased exposure time and the same reasoning can be applied to aqueous systems.

The RDF plot shown in figure 2-19 also shows good agreement between the experimental and calculated data. Whilst EPSR defines the PDF data as f(r), this is essentially the same function as G(r), which highlights the low-r region of the PDF. In comparison to the solid samples previously discussed, the PDF data does not extend to large-r ranges, and are confined to interactions under 5.0 Å. This is not surprising in such a sample due to the lack of long-range order, with well-defined interactions only extending to a number of neighbouring molecules.

2.4.5.2 Water Structure & Comparison to Literature

Water has been studied in incredible detail via various approaches and by many researchers - with most known forms of water being tackled at some stage, from ice to high pressure forms of water. Particularly prolific in this area is the work of Soper.[20–23,25,51] Therefore, the description of the model presented here is predominantly to justify the data quality of the instrument and also to set the scene for describing aqueous solutions which have features in common. The structure of water is incredibly interesting, with ongoing studies largely debating the validity of the two-phase model[52] as well as the effects on the structure with the introduction of ions such as perchlorate[23,53], chloride[25] and sulfate.[54]

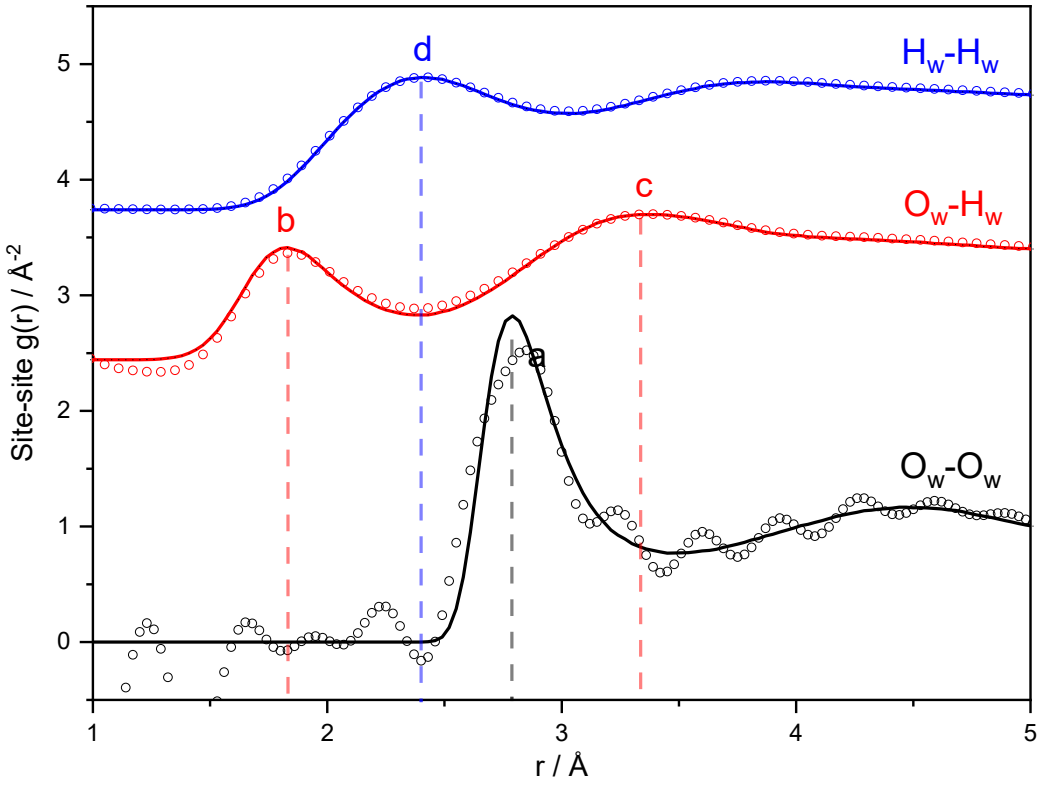

Figure 2-20. *Site-site RDF, g(r), for all atom-atom correlations within H_2O. Circles denote experimental data and lines denote calculated fit. Letters denote the correlations distances found in table X.*

Figure 2-20 shows the experimental and calculated site-site g(r), where all possible combinations for atom-atom correlations are denoted in table 2-11. The overall shape of the features shown in

the RDF match well those in literature[22], and the values obtained differ by no more than 5%. These values show a relatively good agreement to the literature values found by Soper, especially for that of a laboratory-based instrument, especially with weakly scattering species such as hydrogen, where a neutron scattering experiment would be more appropriate. However, as with many areas of total scattering and water studies, there are ongoing arguments as to the true values of these peak positions. As an example of such ongoing speculation, the first O_w-O_w peak has a reported range between 2.76-2.86 Å dependent on researcher, radiation source and refinement strategy. Our value lies well within this range and is close to that reported from another laboratory-based instrument.[55] This refinement gives us confidence in the suitability of the instrument for collecting data of sufficient quality to refine aqueous systems using the EPSR approach.

Table 2-11. *Atom-atom correlations from figure 2-20 compared to literature values obtained from Soper[22] with difference between.*

Atom-atom Correlation	Letter Denotation	Correlation Distance / Å	Literature Value[22] / Å	Difference / Å
O_w-O_w	a	2.79	2.89	-3.46%
O_w-H_w	b	1.83	1.92	-4.68%
	c	3.39	3.38	-0.29%
H_w-H_w	d	2.40	2.43	+1.23%

A more intuitive and visual approach to the investigation of water is via the SDF plots produced by EPSR. This 3D representation of the RDF enables a clearer picture to be built of the interactions occurring within the first and subsequent solvation shells.

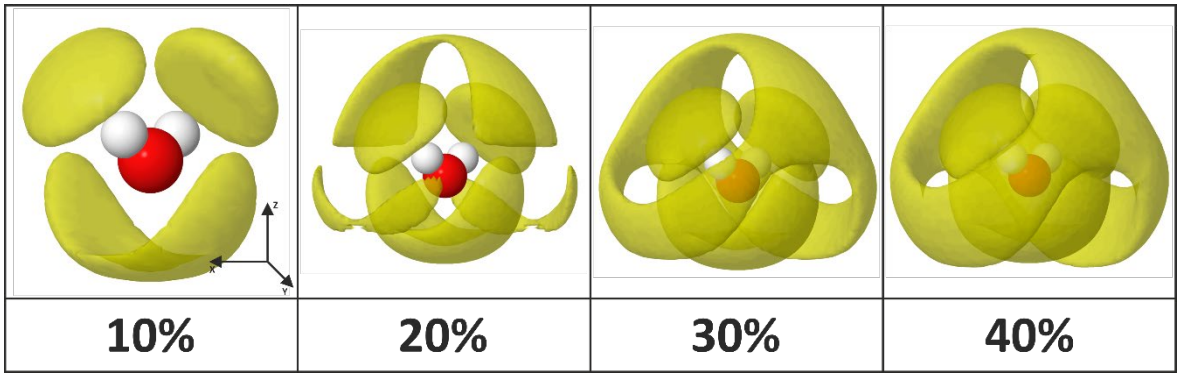

Figure 2-21. *Spatial density functio (SDF) for pure water obtained from EPSR with increasing isosurface percentage, defining the most to least probable interactions, roughly describing the 1st and 2nd hydration shells.*

From figure 2-21, two distinct hydration shells can be observed, with the first shell obvious from the lower isosurface fraction regions and the second evolving with the increasing fraction, consistent with previous studies of water by an EPSR methodology.[21,51] Focussing on the first shell interactions, three distinct areas of density can be observed, two being lobes that sit upon the O-H bond vector and the other being an arch that spans the Y-Z vector, enclosing the underside of the oxygen. Due to the fundamental structure of water, a tetrahedral geometry for the first shell of nearest neighbours is expected based on the geometry and hydrogen donation and accepting potential of the hydrogens and lone pairs respectively.

Figure 2-22 shows the coordination number for both O_w…H_w and the reverse H_w…O_w interaction, revealing potential structure evolving in the form of hydrogen bonding. Each H_w observes on average 3.30 oxygen atoms within the specified distance, which is higher than values stated in literature and is likely due to the use of X-ray radiation, where light atoms, such as hydrogen, do not scatter as well and therefore there is increased uncertainty in the definite positions of this species. However, using the inverse whereby the oxygen is the origin atom, can be found by the O_w…H_w coordination, where a central oxygen observes a coordination of 4.86, confirming the 4+-coordinate tetrahedral environment. This is in general agreement with literature values of for O_w...H_w interactions of on average 4.67, and confirms the suggested coordination.[22]

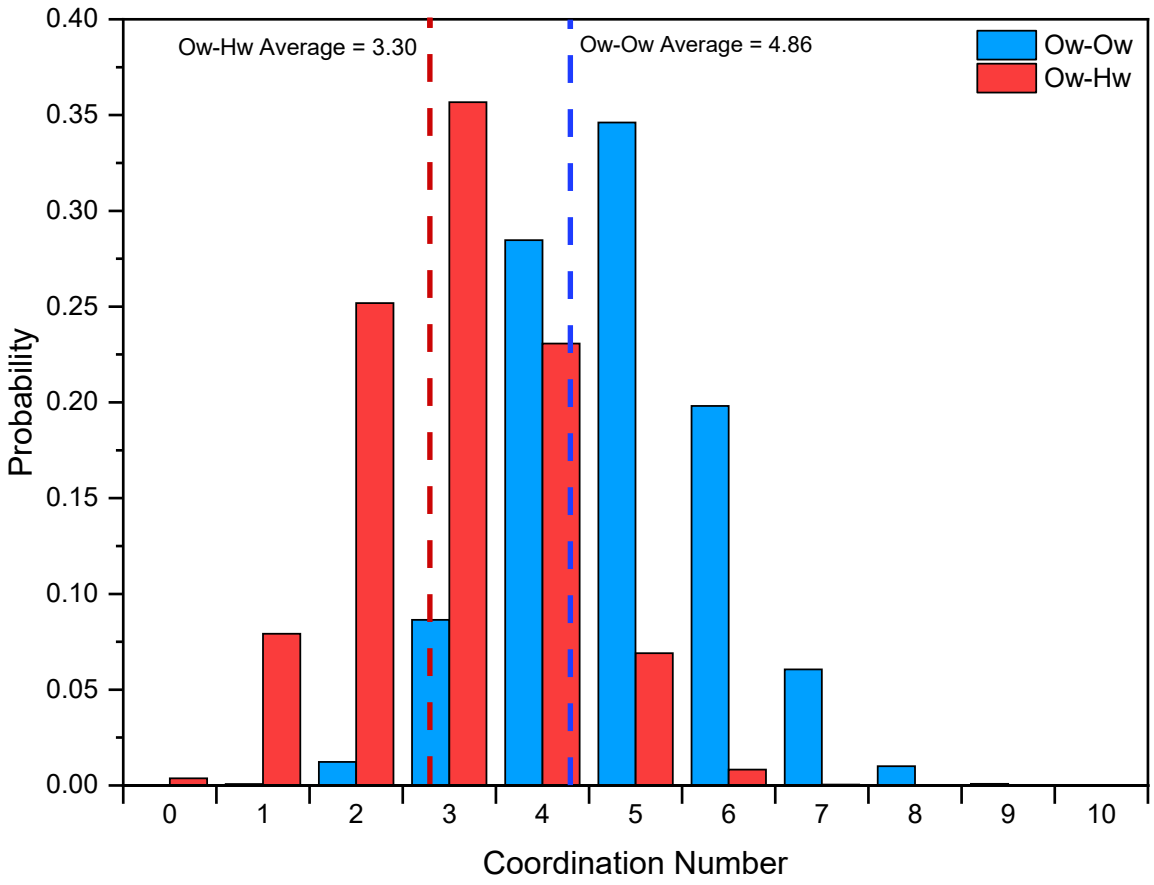

Figure 2-22. *Coordination number for water between each entity within the water. The coordination was calculated using a range of O_w-O_w = 1-3.4 Å and O_w-H_w = 1-2.5 Å, showing an average coordination of 5.23 and 3.41 respectively.*

The second solvation shell is also consistent with previous studies in both shape and magnitude. This second shell includes the more distant water molecules beyond the direct interactions of the first shell. Whilst the structure at this distance becomes increasingly more diffuse, due to the larger number of configurations possible, some structural elements can be identified from both the data and the auxiliary calculations. The most intriguing observation based on the SDF is that the second shell is the anti-phase of the first, suggesting that the second shell interacts in a similar way with the first shell as the first shell does with the central molecule. Further studies using high quality neutron scattering data[21,22,51] has confirmed the continuation of the phase, anti-phase, phase… structure, suggesting that the tetrahedral intermolecular hydrogen bond network extends throughout the entire structure. Whilst we cannot observe this structure using purely laboratory-based data, the first and second shell phase, anti-phase structure can be clearly determined. Further to this, the RDF found in figure 2-20, observes a second feature (c) centred on r = 3.35 Å which represents a second shell interaction, and when compared to the study by Soper[22] this value is within 0.9%.

Overall, this proves the ability to conduct robust total scattering and EPSR studies using modified in-house instrumentation to obtain reliable data that is consistent with extensive studies in the

literature. Whilst we are not contributing to the expansion of the understanding of water structure, we are able to obtain results that are consistent with that of synchrotron-based studies. Further to this, the ability to probe the water structure and understand it in the context of an EPSR refinement will be beneficial to our further studies of aqueous systems, where we aim to discuss the potential distortion to the robust hydrogen bond network observed for pure water. Water has been used successfully as a standard sample for evaluating the suitability of the Rigaku Spider for measuring liquid samples

2.5 Conclusion

In this chapter a variety of crystalline, nanocrystalline, amorphous and aqueous systems have been measured, processed, and refined using data collected on the modified Rigaku Spider. The data have proved to be as good as, if not better than data from other lab-based instruments detailed in the literature and have been collected over a significantly shorter time frame. The ability to rapidly collect multiple data sets in-house has enabled a much more rapid progression of this work than could have been achieved at central facilities. Whilst this instrument cannot compete directly with synchrotron data in terms of resolution, this is not a major disadvantage when studying systems dominated by short-range order.

Whilst this instrument is ideally suited to its current use, improvements can be envisaged. Replacing the sealed tube source with a rotating silver anode would greatly increase the flux, replacing the graphite monochromator with a narrow band one or focusing mirrors would improve resolution. Additionally, alteration of the detector position relative to the collimator would shift the beam centre closer to the detector edge increasing the 2θ range and thus Q_{max}.

References

1 S. Brühne, E. Uhrig, K.-D. Luther, W. Assmus, M. Brunelli, A. S. Masadeh and S. J. L. Billinge, *Z. Kristallogr. - Cryst. Mater.*, 2005, **220**, 962–967.

2 T. Egami and S. J. L. Billange, *Underneath the Bragg Peaks Structural Analysis of Complex Materials*, Elsevier, Amsterdam, Second., 2012.

3 L. Cormier and G. J. Cuello, *Geochim. Cosmochim. Acta*, 2013, **122**, 498–510.

4 G. Confalonieri, M. Dapiaggi, M. Sommariva, M. Gateshki, A. N. Fitch and A. Bernasconi, *Powder Diffr.*, 2015, **30**, S65–S69.

5 K. Galliez, P. Deniard, P.-E. Petit, D. Lambertin, F. Bart and S. Jobic, *J Appl Crystallogr*, 2014, **47**, 552–560.

6 H. Nijenhuis, M. Gateshki and M. Fransen, *Z. Kristallogr. - Cryst. Mater.*, , DOI:10.1524/zksu.2009.0023.

7 T. D. Bennett, A. L. Goodwin, M. T. Dove, D. A. Keen, M. G. Tucker, E. R. Barney, A. K. Soper, E. G. Bithell, J.-C. Tan and A. K. Cheetham, *Phys. Rev. Lett.*, 2010, **104**, 115503.

8 F. Meersman, D. Bowron, A. K. Soper and M. H. J. Koch, *Phys. Chem. Chem. Phys.*, 2011, **13**, 13765–13771.

9 O. S. Hammond, D. T. Bowron and K. J. Edler, *ACS Sustainable Chem. Eng.*, 2019, **7**, 4932–4940.

10 J. Dawidowski, J. R. Granada, J. R. Santisteban, F. Cantargi and L. A. R. Palomino, in *Experimental Methods in the Physical Sciences*, eds. F. Fernandez-Alonso and D. L. Price, Academic Press, 2013, vol. 44, pp. 471–528.

11 M. B. Burg and J. D. Ferraris, *J. Biol. Chem*, 2008, **283**, 7309–7313.

12 S. L. J. Thomae, N. Prinz, T. Hartmann, M. Teck, S. Correll and M. Zobel, *Review of Scientific Instruments*, 2019, **90**, 043905.

13 Rigaku, *The Rigaku Journal*, 2004, **21**, 43–46.

14 L. Brügemann and E. K. E. Gerndt, *Nuclear Instrument Nucl. Instrum. Methods Phys. Res.s and Methods in Physics Research Section A: Accelerators, Spectrometers, Detectors and Associated Equipment*, 2004, **531**, 292–301.

15 Yoshiyuki Amemiya, Atsushi Nakagawa, Shunji Kishimoto, Tadashi Matsushita, Masami Ando, Jun-ichi Chikawa, and Junji Miyahara, 1989, vol. 1140.

16 In *Two-dimensional X-ray Diffraction*, John Wiley & Sons, Ltd, 2018, pp. 87–140.

17 Y. Amemiya, in *Methods in Enzymology*, Academic Press, 1997, vol. 276, pp. 233–243.

18 A. K. Soper, *Mol. Phys.*, 2009, **107**, 1667–1684.

19 G. N. I. Clark, G. L. Hura, J. Teixeira, A. K. Soper and T. Head-Gordon, *Proc. Natl. Acad. Sci. U. S. A.*, 2010, **107**, 14003.

20 B. Santra, R. A. DiStasio, F. Martelli and R. Car, *Mol. Phys.*, 2015, **113**, 2829–2841.

21 A. Soper, *Water and ice structure in the range 220 - 365K from radiation total scattering experiments*, 2014, vol. 187.

22 A. K. Soper, *ISRN Phys. Chem.*, 2013, **2013**, 279463.

23 S. Lenton, N. H. Rhys, J. J. Towey, A. K. Soper and L. Dougan, *Nat. Commun.*, 2017, **8**, 919.

24 T. F. Headen, *Mol. Phys.*, 2019, **117**, 3329–3336.

25 F. Bruni, S. Imberti, R. Mancinelli and M. A. Ricci, *J. Chem. Phys.*, 2012, **136**, 064520.

26 M. Serrano-Ruiz, S. Imberti, L. Bernasconi, N. Jadagayeva, F. Scalambra and A. Romerosa, *Chem. Commun.*, 2014, **50**, 11587–11590.

27 S. Busch, C. D. Bruce, C. Redfield, C. D. Lorenz and S. E. McLain, *Angew. Chem., Int. Ed. Engl.*, 2013, **52**, 13091–13095.

28 J. P. Cline, D. Black, D. Windover and A. Henins, in *Modern Diffraction Methods*, John Wiley & Sons, Ltd, 2013, pp. 399–438.

29 C. Hubbard, *Acta Crystallogr. A Found Adv.*, 1984, **40**, C365–C365.

30 D. J. M. Irving, D. A. Keen and M. E. Light, *Rev. Sci. Instrum.*, 2021, **92**, 043107.

31 A. A. Coelho, *J. Appl. Crystallogr.*, 2018, **51**, 210–218.

32 P. Chater, presented in part at the Pair Distribution Function Refinements using TOPAS v6, Diamond, June, 2017.

33 C. L. Farrow, P. Juhas, J. W. Liu, D. Bryndin, E. S. Božin, J. Bloch, T. Proffen and S. J. L. Billinge, *J. Phys.: Condens. Matter*, 2007, **19**, 335219.

34 D. R. Black, D. Windover, A. Henins, D. Gil, J. Filliben and J. P. Cline, *Powder Diffraction*, 2010, **25**, 187–190.

35 A. K. Soper, *GudrunN and GudrunX*, ISIS, Oxford, ISIS, Oxford, 2012.

36 A. K. Soper and E. R. Barney, *Journal of Applied Crystallography*, 2012, **45**, 1314–1317.

37 D. W. Bruce, D. O`Hare, R. I. Walton, K. D. M. Harris and P. A. Williams, Eds., in *Structure from Diffraction Methods: Inorganic Materials Series*, John Wiley & Sons Inc, 2014, pp. 1–81.

38 L. Khouchaf, K. Boulahya, P. P. Das, S. Nicolopoulos, V. K. Kis and J. L. Lábár, *Materials*, , DOI:10.3390/ma13194393.

39 D. A. Keen and M. T. Dove, *J. Phys.: Condens. Matter*, 1999, **11**, 9263–9273.

40 S. Banerjee, C.-H. Liu, J. D. Lee, A. Kovyakh, V. Grasmik, O. Prymak, C. Koenigsmann, H. Liu, L. Wang, A. M. M. Abeykoon, S. S. Wong, M. Epple, C. B. Murray and S. J. L. Billinge, *The Journal of Physical Chemistry C*, 2018, **122**, 29498–29506.

41 S. J. L. Billinge and M. G. Kanatzidis, *Chem. Commun.*, 2004, 749–760.

42 T. L. Christiansen, S. R. Cooper and K. M. Ø. Jensen, *Nanoscale Adv.*, , DOI:10.1039/D0NA00120A.

43 C. Castillo-Blas, J. M. Moreno, I. Romero-Muñiz and A. E. Platero-Prats, *Nanoscale*, 2020, **12**, 15577–15587.

44 D. A. Draegert, N. W. B. Stone, B. Curnutte and D. Williams, *J. Opt. Soc. Am.*, 1966, **56**, 64–69.

45 Y. Ozaki, Y. Morisawa, A. Ikehata and N. Higashi, *Appl. Spectrosc.*, 2012, **66**, 1–25.

46 B. G. Pfrommer, F. Mauri and S. G. Louie, *J. Am. Chem. Soc.*, 2000, **122**, 123–129.

47 A. K. Soper, *J. Phys. Chem. B*, 2015, **119**, 9244–9253.

48 B. T. M. Willis, in *International Tables for Crystallography Volume B: Reciprocal space*, ed. U. Shmueli, Springer Netherlands, Dordrecht, 2001, pp. 400–406.

49 V. F. Sears and S. A. Shelley, *Acta Crystallogr., Sect. A: Found. Crystallogr.*, 1991, **47**, 441–446.

50 R. Naorem, A. Gupta, S. Mantri, G. Sethi, K. V. ManiKrishna, R. Pala, K. Balani and A. Subramaniam, *Int. J. Mater. Res.*, 2019, **110**, 393–405.

51 A. K. Soper, *Mol. Phys.*, 2001, **99**, 1503–1516.

52 A. K. Soper, *J. Chem. Phys.*, 2019, **150**, 234503.

53 H. Laurent, 2020, 14.

54 G. Balasubramanian, S. Murad, R. Kappiyoor and I. K. Puri, *Chem. Phys. Lett.*, 2011, **508**, 38–42.

55 A. K. Soper, *J. Phys.: Condens. Matter*, 2007, **19**, 335206.

Chapter 3 The Structure of Aqueous Magnesium Sulfate Using a Combined X-ray & Neutron EPSR Approach

Utilising large-box refinement methodologies, it is possible to model and refine the structure of more complex and less studied systems, such as aqueous salts, against experimental total scattering data. This chapter presents the application of the Empirical Potential Structure Refinement (EPSR) method as a means to investigate the structure of aqueous magnesium sulfate, $MgSO_4$ (aq). The discussion concludes with an in-depth analysis of the most detailed structural model refined to date and compares it to the mostly computational studies found in the literature.

In the literature, the EPSR approach to analysing the structure of aqueous systems is relatively novel, with <50 studies in total using this technique for aqueous phase structure refinement (Web of Knowledge – Search Terms "EPSR" & "Aqueous", August 2021). The ability to refine against neutron and X-ray total scattering data makes this methodology the gold standard for experimentally studying liquids on the atomic level. Furthermore, the ability to conduct ad-hoc X-ray experiments on an in-house instrument, with high quality data as demonstrated in chapter 2, allows for versatility in the choice of total scattering experiments. These studies are vital for the understanding of both the structural features and how the atoms interact in a dynamic environment, and how this reflects on the chemical properties of the system. Multiple total scattering data sets, with independent radiation sources, allow for a refinement that will more closely resemble the 'true' structure, with each radiation source being more sensitive to a particular element within the aqueous structure. X-ray radiation makes it possible to probe the heavier scattering elements within the refinable model, such as that of the magnesium and sulfate, whereas neutrons provides information on the lighter atoms such as hydrogen. This in combination with deuterated samples, allows for multiple data sets that are weighted in such a way that each unique feature of the model can be examined in detail.

The refined model possesses structural information pertaining to the environments surrounding the Mg^{2+}, SO_4^{2-} and H_2O entities and these can be extracted by various auxiliary routines once the final model has been achieved. Hence, the investigation of the local environment and comparison to the various crystalline hydrates of magnesium sulfate, and subsequent comparison between aqueous and solid-state structure can be conducted using these routines. Comparisons can also be made to the pure water structure, discussed in chapter 2, and the disruptive effect the solute has on its structure can be investigated. Whilst some of the structural features observed are broadly consistent with those reported in the literature, predominantly computational, it is the first atomistic presentation of a model of aqueous $MgSO_4$ derived from experimental data and highlights

some differences. Furthermore, this is, to the authors knowledge, the first joint X-ray/neutron study of aqueous $MgSO_4$ and highlights the benefits of a combined approach to aqueous phase structure analysis.

This chapter represents the culmination and extension of the instrumental studies of the work presented in chapter 2 and demonstrates how the instrument can be applied to '*real*' systems enabling a novel study. The optimisation of the EPSR approach chosen for these studies provides an insight to the structure of a typically difficult system to analyse, but also provides a foundation for further studies with regards to variable conditions.

3.1 The Applicability of Large-Box Refinements

Large-box refinement methodologies, such as Empirical Potential Structure Refinement (EPSR)[1] and RMCProfile[2], utilise a reverse Monte-Carlo (RMC) approach[3] to obtain the structure of non-crystalline samples that cannot be analysed via traditional XRD or small-box PDF refinement techniques. This refinement technique has been successfully applied to various systems such as the extensive studies of water[4–7], as well as other well-known solvents such as benzene[8], dimethylformamide (DMF) and dimethylacetamide (DMA)[9] as well as alcohols under varying conditions[10]. The ability to study the structure of these solvents in the aqueous state, the state in which they will be used in the laboratory, allows the possibility of explaining the aqueous phase interactions and applying these to gain insights into chemical behaviour. Interactions between ions and solvents have been studied for this very reason, and examples include studies into aqueous lanthanide nitrate hydrates to scrutinise how the aqueous phase structure can behave as an environmentally friendly organic solvent alternative.[11] The role of a solvent within any aqueous system is of upmost importance as it allows for the understanding the chemical processes that occur. Interpreting the structure on an atomistic level provides a deeper insight to these processes and overall has a large impact over many disciplines of chemistry and science in general.

EPSR simulations comprise five main steps, as seen in figure 3-1. Generically, all EPSR simulations will follow this progression, allowing for a general discussion of each step with regards to the full refinement.

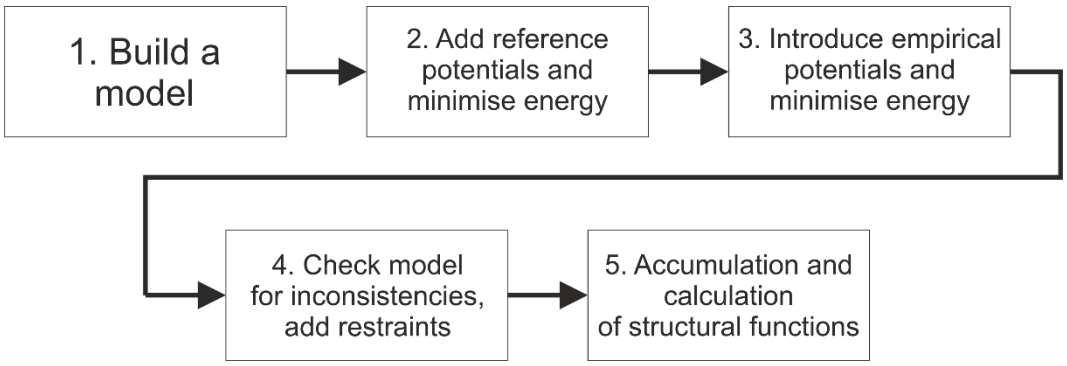

Figure 3-1. *Generic EPSR flow methodology, depicting the five main stages of refinement, described in detail in the following sections.*

3.1.1 Build a Model

EPSR refinements firstly rely on the creation of physically accurate fragments to populate the large box model. One must firstly create the smallest possible fragments that will allow for an accurate model, but not too large that a bias is introduced towards a specific structural motif. Examples of such fragments are individual ions, smaller robust units such as SO_4^{2-}, ClO_4^- as well as some larger

units such as benzene.[8,12] So long as these fragments are robust and unlikely to change chemically, they provide a suitable model for the sample of interest.

3.1.2 Add Reference Potentials and Minimise Energy

Once the immutable fragments have been constructed and mixed in a realistic and physically accurate manner, the inter-fragment interactions need to be defined by both the partial charge and Lennard-Jones (LJ) potentials.[13] Whilst these must be accurate to the fragments created, they do not necessarily need the precision of computational studies, as ultimately these will only act as restraints with the experimental data truly driving the evolution of the model. These values can often be found in the literature, especially from molecular dynamic simulations of the individual components or in solution with other components. For example, water is described in multiple publications utilising a various refinement methodologies – these provide a set of well-tested LJ parameters.[14–17] Within the EPSR approach the LJ parameters are referred to as the reference potentials and are based on a Lennard-Jones 6-12 potential, and the overall reference potential between atoms α and β can be described by equation (3-1).

$$U_{\alpha\beta}^{(Ref)}(r_{ij}) = 4\varepsilon_{\alpha\beta}\left[\left(\frac{\sigma_{\alpha\beta}}{r_{ij}}\right)^{n} - \left(\frac{\sigma_{\alpha\beta}}{r_{ij}}\right)^{6}\right] + \frac{q_\alpha q_\beta}{4\pi\varepsilon_0 r_{ij}} \qquad \textbf{(3-1)}$$

Where $U^{(Ref)}$ is the reference potential energy, ε is the potential energy well, σ is the distance at which the interatomic potential is zero, r is the distance between atoms α and β and q is the partial charge.[18]

To enable a statistically representative ensemble of atoms within the simulation box, one must choose an adequate number of atoms as well as a physically accurate number density. Firstly, the choice of the exact number of each prior made fragment allows for both a representative system with regards to the concentration and abundance of each fragment type. Secondly, the number of fragments must be large enough to represent the structure as a whole, allowing for all potential structural elements and variation, whilst not being large enough to be computationally intensive. Typically, 2,000+ molecules are used within literature studies for a statistically accurate model, but this will vary dependent on the sample being analysed, with simpler single molecule systems, such as water, needing fewer molecules to describe all structural elements.

The second structural input needed for the model is the number density. The number density is described as the number of atoms per unit area and can be described by equation (3-2).

$$Number\ Density = \frac{\left(\frac{N_A}{Molecular\ Mass} \times \rho_{Sample}\right)}{1 \times 10^{24}} \qquad \textbf{(3-2)}$$

where N_A is Avogadro's number and ρ is the density. This description of the number density at an atomic scale is far more useful than traditional density, as it allows for the description of the number of atoms allowed within a set area and can more accurately describe the physical properties than standard density. Standard density describes the mass per unit area, and whilst this is useful for larger volumes, it does not do particularly well at modelling as the atomic density due to the need for refinements and modelling on the nanometre scale. Assuming that the number density has been correctly calculated, and the relative proportions are representative of the system, EPSR will determine a box size of approximately 50-100 Å in length. This size has been found to accurately model a sample and allow for elements of the system to be able to move and interact to create a model that can satisfactorily fit the experimental data.

Both the number of fragments and number density must be correctly input to allow for an accurate system, as if either is incorrect, it will lead to unphysical interactions within the model. Examples of such is a number density that is too large, i.e., too many atoms per unit area, will create unphysical overlap of atoms, creating large low-r spike in the RDF calculated model. Likewise, a number density that is too small will cause fragments to be too far from one another to interact, creating void like structures and a large low-Q peak in the total scattering calculated data. Therefore, one must ensure that both variables are representative of the system to accurately model the sample and successfully refine against the experimental total scattering data.

However, the reference potentials and number density alone may not be adequate to avoid unrealistic features within the model, and therefore one may need to introduce restraints upon the model to remove such interactions. This is done in such a way to improve the fit to the experimental data and balance the attractive and repulsive forces within the model, particularly on lighter elements such as hydrogen whereby the LJ is relatively non-restrictive. It is an iterative and time-consuming process to obtain the ideal reference potentials and restraints to model the system without introducing unrealistic features. Once one is happy with the progress of the refinement, it can then be left to equilibrate to reach an energy minimum solely based on the reference potentials.

3.1.3 Introducing Empirical Potentials and Minimise Energy

After the refinement has converged to a lowest energy state based on the reference potentials, the empirical potential can be introduced to improve the fit to the experimental data, this situation is described in eq. (3-3).

$$U^{Total} = U^{(Ref)} + U^{(EP)} \quad \textbf{(3-3)}$$

U^{Total} represents the energy of the system as an entire entity, U^{Ref} are the reference potentials based on the LJ parameters as discussed in section 1.3.4, and U^{EP} are the empirical potentials derived from the experimental data. One must remember that the U^{Ref} is used throughout the refinement procedure but U^{EP} is only used in the later stages and can be expressed as:

$$U^{(EP)}(r) = kT \sum_i C_i P_{n_i}(r, \sigma_r) \quad \textbf{(3-4)}$$

Where $U^{(EP)}$ is the empirical potential energy, k is the Boltzmann constant, T is the temperature, C_i is a constant determined by comparison of the simulated and experimental structure factors . $P_{ni}(r, \sigma_r)$ is a function that incorporates the LJ parameters in combination with physical properties of the system such as the atomic number density, ρ, and can be described as:

$$P_n(r, \sigma_r) = \frac{1}{4\pi\rho\sigma^3(n+2)!}\left(\frac{r}{\sigma}\right)^n exp\left[-\frac{r}{\sigma}\right] \quad \textbf{(3-5)}$$

This function allows for larger fluctuations in the intermolecular potential at lower r and smallervariation as r increases.[19] $U^{(EP)}$, can be directly Fourier transformed into Q-space, shown in equation (3-6) ($U^{EP}(Q)$), and therefore bypasses the common issues that are associated with the Fourier transformation of the diffraction data, such as noise and termination effects, and allows refinements directly against the total scattering data.

$$U^{(EP)}(Q) = \sum_i C_i P_{n_i}(Q, \sigma_Q) \quad \textbf{(3-6)}$$

The combination of both equation (3-4) and equation (3-6) allows for the refinement of the total scattering (reciprocal space) and accurate derived functions found within the software routines. The use of both reference and potential energies allows for a low energy structure to evolve from the data and minimise the total energy of the system. The minimisation of the energy can be represented by the increasing agreement between the simulated data and the experimental data.

Upon implementation of the empirical potential, the simulation is allowed to converge to an energetically sensible structure, where interactions are physically and chemically realistic., defined by a low U value described in eq. (3-3). When a fully converged model has been arrived at, such that there is a good agreement between the refined model and experimental scattering data, it must be 'sanity' checked for physical features that may be unrealistic but fit the data well. Whilst EPSR does often create a well refined-model based on the experimental data, less sensitive features may emerge where prior structural knowledge needs to be applied. This can include short-range atom overlap and void formation, as discussed thoroughly in section 1.3.4, however further but sensible adjustments to both the reference potentials and restraints must be made to remove these artifacts without compromising the fit to the experimental data. Once one is happy with the overall fit of the data, auxiliary routines and accumulation can occur.

3.1.4 Auxiliary Routines and Analysis

Whilst a good refinement shows consistency between the experimental data and the model, accumulation of refinement versions and calculation of various structural functions should be conducted. The aim of this is to extract more readily understandable structural descriptions of the system using a well-fitting and accurate model. Firstly, accumulation of configurations, whereby successive equivalent solutions to the refinement are built to enable the calculation of smoother averaged derived functions. Often the simulation would be run for at least 1000 iterations for good statistics but were accumulated for far longer when running the refinement on a supercomputer cluster.

Accumulation allows for the averaging of the derived functions to occur, particularly that of the atom-atom RDF and the auxiliary routines such as the coordination number and bond angles. EPSR accumulates and saves the large-box of atoms every five cycles allowing for an averaged structure to be obtained. This is particularly useful, especially when examining the large-box of atoms seen in figure 3-2, whereby structural features are difficult to extract. Using the derived functions and auxiliary routines, it is possible to focus on the average structure of particular features without the complex examination of thousands of atoms. Examining the refined model itself is also beneficial for understanding the model, even if it is a snapshot of one of many possible configurations. Whilst this does not represent the average like the auxiliary routines do, it does allow for one to probe the model to find examples of such interactions formed via the averaged structures extracted.

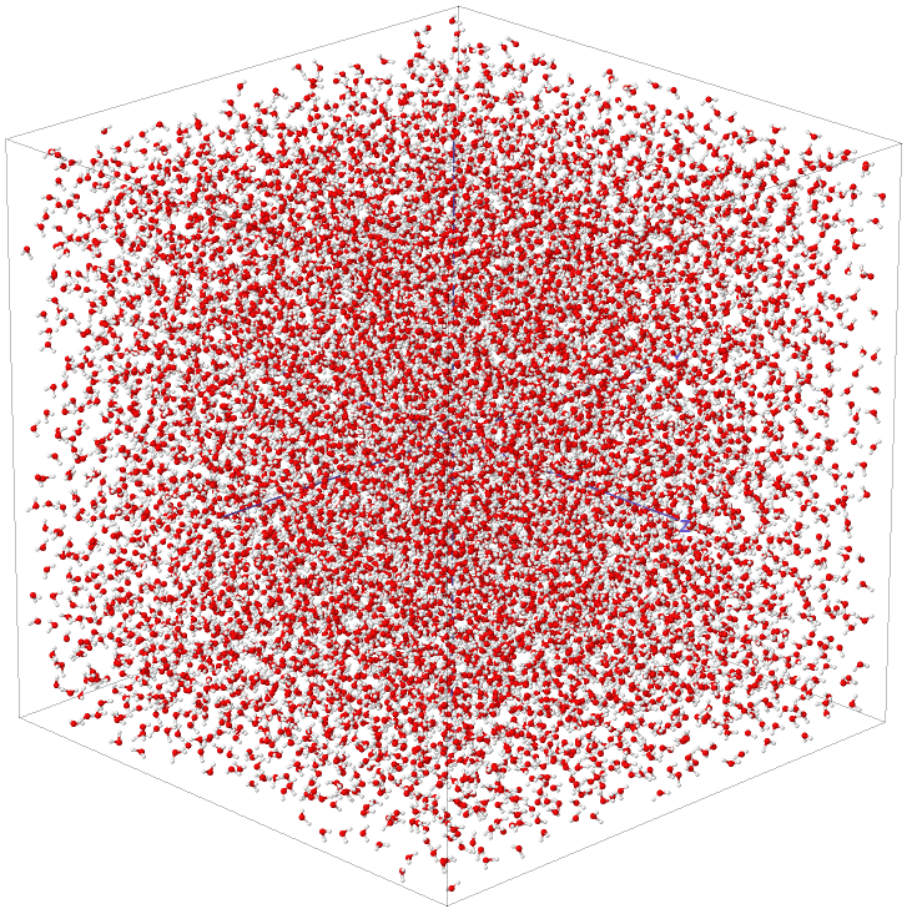

Figure 3-2. *Large-box of H_2O fragments created within EPSR, highlighting the sheer number of molecules and difficulty in analysis.*

Therefore, within the accumulation stage, various functions are calculated to provide more intuitive structural representations of the refined model. Thus, interrogation of the model begins by careful examination of the refinement fit, spatial density functions (SDF) and the outputs of various auxiliary routines.

3.1.4.1 Refinement Fit

Many derived functions can be obtained from the total scattering structure factor, F(Q), which all allow for the analysis of reciprocal and real space information. As discussed in previous chapters, the nomenclature surrounding total scattering is complex with no universal naming conventions, and care must be taken within EPSR to be sure of the function being analysed. Firstly, F(Q) is the only experimental data which the model is refined against, and whilst is useful for monitoring the progression of the experiment, its rather non-intuitive for analysis purposes and therefore the derived functions provide more insight into the structure being investigated.[20]

One important distinction to highlight especially when using EPSR is the difference between the PDF and RDF functions, whilst almost identical in their description, the scaling factor allows for different information to be extracted from each respectively. In chapter 2 these functions are discussed with relevance to the mathematical composition, however it is worth stressing the scaling

factors utilised, with the RDF being the standard PDF function multiplied by $1/(2\pi r)^2\rho_0$. This function essentially describes the atomic density within a specified radius and allows for additional information to be inferred beyond the standard atom-atom distribution of the PDF.

$$g_{ir}(r) = \frac{n_{ij}(r)}{4\pi r^2 dr \rho_j} \quad \textbf{(3-7)}$$

The radial distribution function does not give complete information about pair correlations in crystals because they are neither homogeneous nor isotropic. Of course, one is still free to define translationally and rotationally averaged versions of the full pair correlation function of a crystal, which give some useful information about the typical surroundings of the atoms. However, it becomes particularly useful when defining the atom-atom g(r), described by eq. (3-7) where one is investigating the structure between two atoms allowing for coordination numbers and bond angles to be extracted. Overall, the RDF is far more common for aqueous and amorphous systems than PDF due to the lack of orientational information allowing for the description of less ordered systems.

3.1.4.2 Spatial Density Function (SDF)

The spatial density function (SDF) is the probability of finding another specified atom within distance r and orientation in real-space. Whilst other auxiliary routines can describe other parameters such as the atom-atom distances, coordination numbers and bond angles, they are not very intuitive for examining the true structural arrangement of atoms. Using this real-space 3D function, allows for a hands on and intuitive investigation of molecular interactions.

As discussed previously, the visual inspection of the atomic arrangement of the large-box model is unable to provide an intuitive understanding of the basic rules that dictate the structure of these disordered samples. By defining a central species, its orientation in space via axes defined by the Euler angles[21], as well as an expected distance range between the origin species and the species of interest, it is possible to create a probability density plot between the two. This distance can be approximated by using the atom-atom g(r) described to incorporate all expected interactions. It is possible to then construct a 3D plot of densities surrounding the origin species, that includes the many possible interactions between the two species into a singular probability plot.

Figure 3-3 demonstrates the surface contours that enclose the highest density of water molecules, that of the top 30% population within distance range 1.0 – 5.0 Å from an origin water molecule. Whilst it does not show specific molecular positions and rather describes the average of the most probable positions, one must infer the likely interactions and, in this case, it is likely originating from the O-H···O hydrogen bonding.

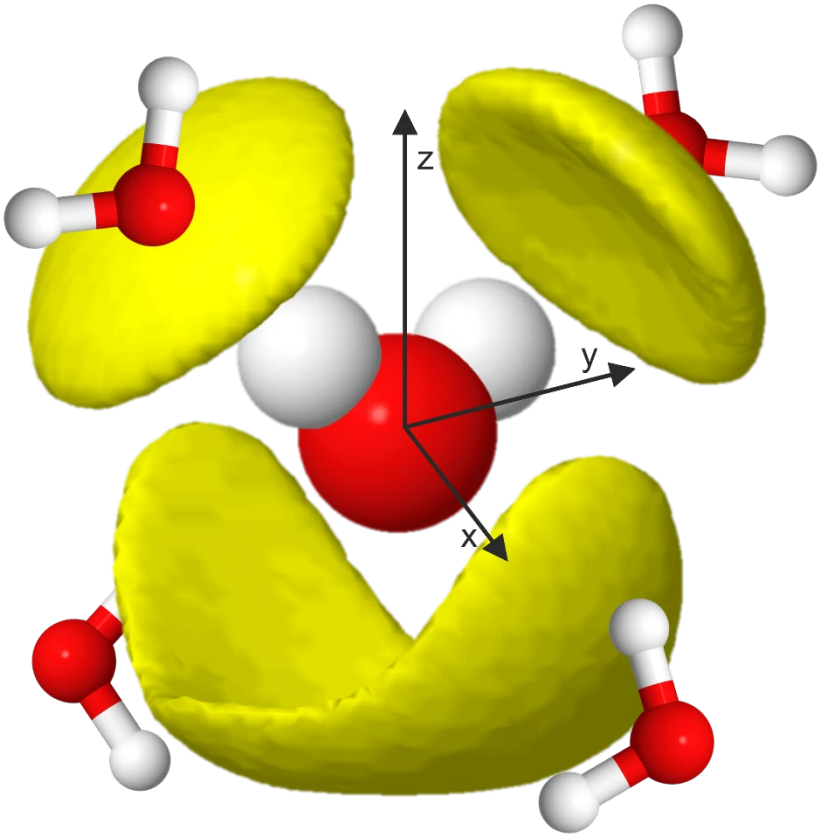

***Figure 3-3**. A example of SDF plot of water adapted from the EPSR user manual by Soper[19] and work by Svishchev et al.[22]. Red spheres represent oxygen, white spheres represent hydrogen, and yellow areas of density representing the areas that interacting water molecules can occupy. Note that the dipiction of a single water molecule in each high density area represents just one of the positions encompased by the density.*

It is possible to visualise the most common locations for a water molecule around the central species by specifying different isosurface levels.[19] This essentially defines the most probable to least probable locations via either a low or high isosurface percentage i.e., top 1% of population to 100% of the population, as depicted in figure 3-4. This allows one to focus on the highly structured elements of the model, usually that of direct intermolecular interactions found in the first coordination shell. Expanding that population range will start including less probable locations, such as second coordination shells, and, by analogy to microscopy, allows one to effectively alter the depth of field. Using this feature of the SDF, it is possible to build a narrative of the coordination/solvation shell structure and visualise the probable populations, typically that of the first shell, to less probable populations, typically that of second and further shells.

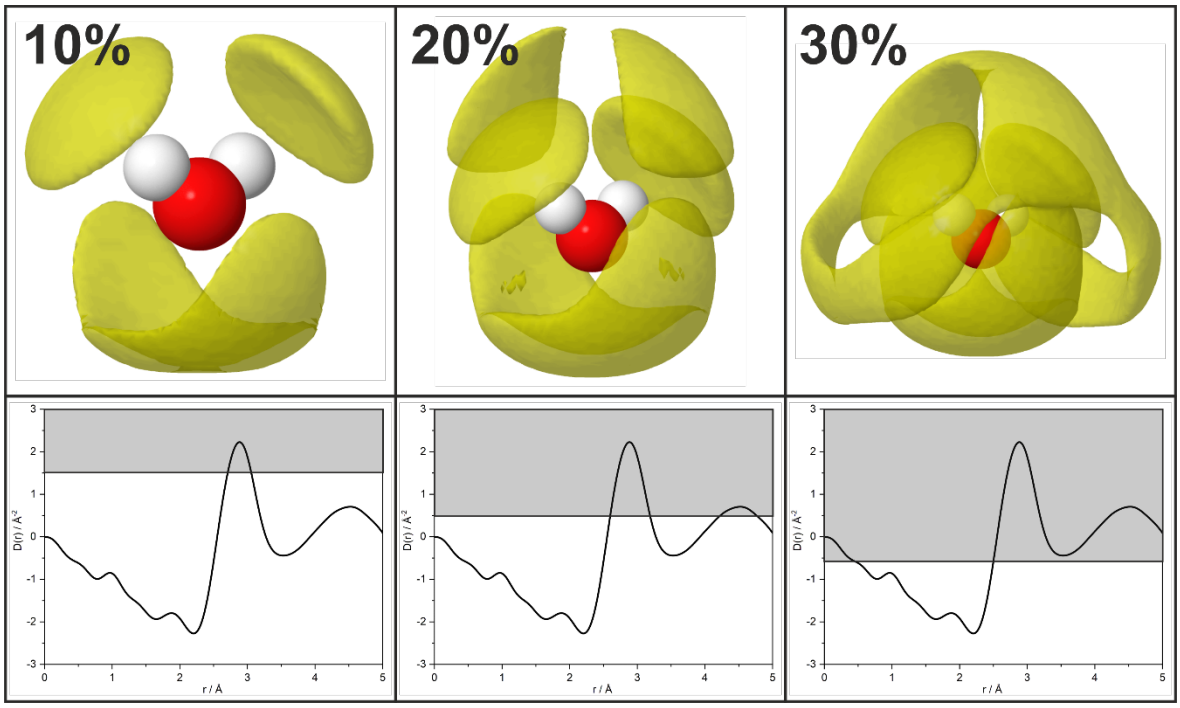

Figure 3-4. *Spatial density function (SDF) relating to the radial distribution function (RDF) to represent how the fractional isosurface is found, exagerated to highlight the close relationship. Top row represents the SDF, bottom row represents the RDF with the greyed out area demonstrating the appoximate isosurface fraction.*

3.1.4.3 Additional Auxiliary Routines

EPSR has a variety of routines built in that can be run alongside the accumulation stage to gather quantitative data on various predefined structural features, enabling a deeper understanding of the interactions taking place. The main routines used herein include the coordination number and bond angles (triangles) for carefully chosen central atoms/fragments. The ability to confirm the average coordination environment, typically around a central metal ion, is invaluable for probing the structure of these embryonic coordination clusters. Coordination angles provide additional information on the geometries of such clusters, and how they deviate from their expected ideal symmetry due to the presence of 'interfering' species.

3.2 Aqueous Magnesium Sulfate

Magnesium sulphate, $MgSO_4$, is a common chemical utilised in a variety of sectors, from chemical synthesis,[23] agriculture,[24] heat storage[25] and pharmaceuticals both as a single component[26–28] as well as in combination with other components[26]. Its use within many sectors shows $MgSO_4$ is a highly important material within industry and research. Whilst studies have been conducted on both the physical properties[29,30] and crystalline structures of the many hydrates of $MgSO_4$[31–35] , there is a lack of information of the structure in the aqueous phase[36–38], with many of these studies focussed on physical properties and molecular dynamic simulations rather than through direct experimental observation. Within this section, the structure of a 2.00 M $MgSO_4$ solution is examined by a dual X-ray/neutron EPSR approach. This will enable the examination of the hydration shells with regards to the ionic components, the aggregation into clusters and the disruption they impart upon the well-defined water structure.

3.2.1 Previous Work

Examining the crystalline structures of magnesium sulfate and its hydrated forms, the most striking and pervading feature is the 6-coordinate magnesium octahedra. This basic structural motif occurs in all the known hydrates, $MgSO_4 \cdot xH_2O$ (x = water of crystallisation), with the only variable being the ratio of coordinated sulfate:water. As a general trend, an increasing level of hydration tends to increase the preference of water coordination over the sulfate, and these trends are summarised in table 3-1.

Table 3-1. *Relationship between the hydration number and the magnesium coordination environment. * denotes bridging water. O1s represents a sulfate oxygen, and Ow a water oxygen.*

$MgSO_4 \cdot xH_2O$	0	1	2	4	5	6	7	9	11
O1s:Ow	6:0	4:2*	3:3	2:4	0:6	0:6	0:6	0:6	0:6

As the above table shows, the increase in hydration leads to more water being coordinated to the metal, and at $MgSO_4 \cdot 5H_2O$ and beyond, the metal becomes fully hydrated with sulfate adopting an isolated environment coordinated through hydrogen bonding. This highlights the importance of intermolecular interactions, namely hydrogen bonding, within these higher hydrate systems, where there is a reliance on the intermolecular interactions for the bulk structure whereas the lower hydrates rely on the ionic/electrostatic attraction between oppositely charged ions.

This work highlights the gradual bond preference change from a purely ionic/covalent system, specifically for the interactions between the Mg^{2+} and SO_4^{2-} in lower hydrates, where intramolecular bonds prevail, to a more hydrogen bond-based system with an increased abundance of water

molecules. The stabilities and energies of both bonds have been extensively studied primarily via DFT methodologies and allow for a fuller understanding of the stabilities of the hydrated crystalline $MgSO_4$ structures. One such study by Iype et al.[39] examines the hydrogen bond network for the hydrated species, and shows the increasing strength and corresponding decreasing in the length of the hydrogen bonds, showing the significance and influence this bond has on the structure. The scope of research regarding the bonding within such ionic materials in the solid-state is limited, with many being focussed on the structure itself rather than the forces at play that cause such structural motifs.[31,32,34,40] A study by Corà et al.[41] discusses the ionic interactions between the ions Al^{3+} and PO_4^{3-} with regards to the structure of aluminophosphates, a large area of zeolitic chemistry. Overall, whilst the structure does include elements of covalent and ionic bonding, it is the ionic bonding that is the dominating factor between the two species. In fact, this ionicity allows for the high stability of the aluminophosphate structure and provides reasoning via a DFT methodology to why such materials are so stable in their crystalline forms. Whilst a similar study regarding $MgSO_4$ would be beneficial for this comparison, it is way beyond the scope of this project and deviates from the aqueous structure studies being studied. Therefore, whilst the nature of bonding remains elusive within this materials, one can expect a degree of both covalent and ionic character within the system, but the electrostatic attraction between oppositely charged ions being a large contributor to the overall stability.

The aqueous structure of $MgSO_4$ has been extensively studied by both experimental and computational methodologies, however most focus on specific aspects of the structure rather than the structure as a whole. Whilst this is beneficial for extracting structural elements that exist within the aqueous system, it does not elucidate the both the bulk features and the multiple potential bonding modes available to each species. Many experimental methodologies, such as NMR, EXAFS, and Raman spectroscopies, allow for the experimental probing of direct and short-range structure including the Mg^{2+}-SO_4/H_2O[2-36,38,42–45] and SO_4^{2}-H_2O[46–48] interactions, these are a small aspect of a much larger structural model.

The studies introduced above are particularly useful for probing the magnesium environment, with all studies concluding the existences of the 6-coordination Mg-O_6 species. The relative ratio of sulfate oxygen: water oxygen varies with concentration, with the fully hydrated cluster being prominent in the lower concentration solutions and increasing sulfate presence in the octahedra as the ionic concentration is increased. This trend follows the that seen in the solid state, where an increasing solute:solvent ratio, i.e., lower hydrates, increases the number of ion pair interactions and allows more sulfate within the 1st coordination shell of the magnesium. Further to this, additional bonding modes can be possible within the aqueous state due to the increased dynamics within the systems, and therefore it is suggested that sulfate could adopt a bidentate bonding mode

with the magnesium, and whilst this is still compatible with the 6-coordinate species, this does reduce the ion pair ratio.[44] Some of the aforementioned studies do suggest the beginnings of longer-range structure and multiple bonding modes, however are very limited by the chosen experimental technique, and therefore direct or short-range structure is the only largely accessible information.

Computationally, it is possible to probe the longer-range structural elements of an aqueous system where the limitation is mainly the computational expense – this contrasts to experimental techniques where the scale length limitations are due to the lack of corresponding observable signal. Several studies have investigated aqueous $MgSO_4$, and largely agree with the previous experimental studies.[36,44,49,50] These studies not only agree with the 6-coordinate setup of the central metal ion, but also model the possibility of bidentate ion pair interactions by both chelating and bridging structure, suggested by the Raman studies.[44] Other potential interactions that can be modelled via the computational method include bridging sulfate oxygen, chain formation and larger structural features of more concentrated systems, describing the alternative and longer-range bonding modes not possible via the previous experimental studies. Finally, with the ability to probe the longer- and shorter-range structure, it is possible to examine the metal clustering, the solvation environments around each ion as well as how the introduction of these ionic clusters disrupt the bulk water structure. Experimental measurements, such as Raman spectroscopy, tend to cope well with the short-range order, we cannot examine how this structure extends beyond the localised environments. Further to these limitations, only indirect information can be inferred from the data, with structural elements such as geometry being extracted from vibration modes rather than being directly observed.[13] Limitations also extend to the computational methods, where the long-range interactions become increasingly computationally extensive to model, showing the unique downfalls of each method. Total scattering refinements, such as that of EPSR, is bringing together experimental data with the computational methods, allowing for an atomistic model to be derived from experimental data. This model can then be interrogated via the previously discussed methodologies in section 1.3, allowing for direct, short- and long-range structural elements to be extracted from a predominantly experimental basis.

3.2.2 Total Scattering Experiments

In total, four data sets were collected for the 2.00 M aqueous $MgSO_4$ sample using both in-house X-ray total scattering alongside neutron scattering collected on the Small Angle Neutron Diffractometer for Aqueous and Liquid Samples (SANDALS) instrument at ISIS Neutron and Muon Source, Didcot, UK.

Anhydrous magnesium sulfate was acquired from Sigma-Aldrich and used as received. For each sample, 2.4 g of the solid was dissolved in 10 mL of water to form a 2.00 M solution. For the X-ray total scattering experiments, deionised water was used as the aqueous component. The sample was loaded in a 2.0 mm borosilicate capillary purchased from Capillary Tubes Supplies Ltd. Data collection and reduction broadly followed the scheme outlined in chapter 2 with only the sample specific elements described here. The samples were run for a total exposure time of 180 minutes with an exposure rate of 127 s/° oscillation. The empty capillary and empty diffractometer were then measured utilising the same parameters to obtain container and empty scattering data sets. The data sets were processed in GudrunX[51], using a sample composition of $MgSO_4 \cdot 27.75H_2O$ and number density 0.1074 atoms/Å^3 and other parameters, such as Compton scattering, (described in section 2.4) to be adjusted to obtain the reduced total scattering function F(Q).

Three isotopically distinct samples were prepared for the neutron scattering experiments at ISIS, all with the same concentration but varying degrees of deuteration. The samples prepared were as follows: $MgSO_4 \cdot 27.75H_2O$, $MgSO_4 \cdot 27.75D_2O$ and $MgSO_4 \cdot 27.75HDO$. Each sample was placed into a flat-plate non-scattering titanium/zirconium cell with a total sample thickness of 1 mm. Each sample were collected for approximately 8 hours with similar empty sample cell and empty instrument for data corrections. These data sets were then processed within GudrunN[51] for background subtraction and normalisation to calculate the F(Q) for each sample. In total three neutron data sets and one X-ray data set were measured for this study. The multiple data sets used in this study span both different radiation types (X-ray and neutron) and sample scattering modifications through isotopic substitution in the neutron experiments. Each data sets is more sensitive to a specific feature within the sample, such as heavier elements via the X-ray data and water structure from the deuterated neutron experiments. Combining these multiple data sets within one refinement, by simultaneously fitting the data, gives us a more complete picture than simply refining one data set.

3.2.3 EPSR Setup

Akin to the water EPSR refinement discussed in chapter 2, the simulation requires starting values for the reference potentials, number densities and suitable restraints. As magnesium sulfate is a common material, there are several computational studies from which these values can be obtained, and with only slight modification these produced a successful reifnement.[4,15,36,52,53] These literature values, alongside the modified values can be found in table 3-2.

EPSR is relatively resilient to inaccurate reference potentials compared to computational studies from which many reference potentials originate. As the main structural aspect of the refinement is driven by the experimental data and the associated empirical potential, the reference potentials

assigned to each atom type act as a mild restraint. As previously discussed previously, the reference potentials are primarily used as physical values to avoid unphysical structural features, such as atomic overlap, allowing for a semi-reasonable lowest energy structure. Further to this argument, the aqueous structure of most samples is a very underdetermined problem, and the more chemical knowledge input into the refinement to supplement the experimental data, the more chemically and physically accurate the refined model will be. The reference potentials can also be utilised as a model test, whereby altering these values but obtaining the same final model justifies the structure obtained from the experimental data. Overall, the reference potentials are an incredibly important step within the EPSR refinement, and care must be taken to input the correct and most accurate value possible.

Table 3-2. *Reference potentials comparing the range of data used from literature and the values used in the refinement.*[1,36,42,52,54]

	Literature Value			Refinement Value		
Reference Potential	ε / kJmol^{-1}	σ / Å	q / e	ε / kJmol^{-1}	σ / Å	q / e
Mg1	0.3216 - 0.936	1.436-1.933	+2.0	0.8000	1.90	+2.0
S1 (Sulfate)	0.7322 - 1.9043	3.555[1]/3.308[2]	+0.54- +2.4	0.7327	3.55	+2.4
O1s (Sulfate)	0.8374 - 1.7245	1.8 - 2.835	-0.635 - -1.1	0.8374	2.10	-1.1
Ow (Water)	0.3 - 0.6503	3.166/3.20	-0.82 - -1.0	0.6500	3.20	-0.8476
Hw (Water)	0.00	0.00	+0.41 - +0.5	0.0000	0.00	+0.4238

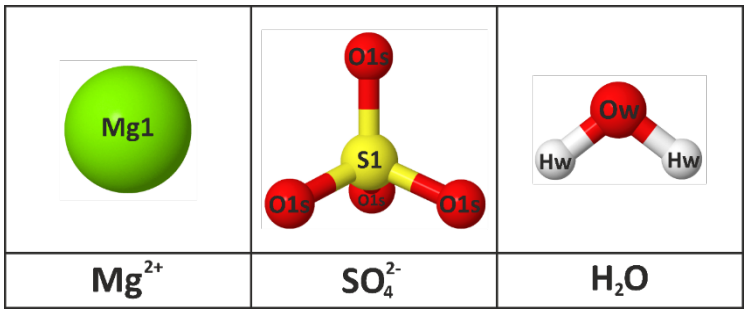

Figure 3-5. *Atom type labels for all fragments used in $MgSO_4$ EPSR simulation.*

The above species are assembled for the large-box refinement and a choice regarding the size of the box is required. In the literature box sizes tend to vary between 5,000 and 10,000 molecules, dependent on the system being analysed and the analysis approach being used. Based on this and previous successful refinements of similar systems the following model size was chosen: 6938 H_2O, 250 Mg^{2+} and 250 SO_4^{2-} to give a total molecule count of 7,438 or 22,064 atoms. This was combined with the calculated number density for the system of 0.107355 atoms/Å^{-3}.

Each of the above species require a weight associated to it, described in table 3-3, accounting for the neutron scattering lengths or X-ray form factors respectively, allowing for the accurate representation for each atom type. Effectively both are setup in a similar fashion, with most atomic species being allowed to remain at the default value, but specific differences occur between the radiation types. X-ray form factors are Q-dependent and therefore EPSR handles these values differently to the neutron scattering cross sections, which are not dependent on Q. The neutron scattering cross sections, for the most part, can also be left at the default values with the exception of hydrogen and its isotopes, especially when multiple data sets of deuterated samples are being refined against. Firstly, one must take care in correctly changing the isotope atomic mass as well as the abundance if it is a mixed hydrogen/deuterium sample. Further to a mixed sample, the hydrogen/deuterium should be allowed to 'exchange' allowing for the hydrogen and isotopes to exchange throughout the model, allowing for a more physically accurate representation of the sample.

Table 3-3. *X-ray atomic scattering factors and neutron scattering cross sections.*

Species	X-ray Form Factor at Q = 0 $Å^{-1}$	Neutron Scattering Cross Section / barn
Mg	11.98650	3.710
S	15.99980	1.026
O	7.999400	4.232
H	0.999872	83.03
D	N/A	7.640

This box was then randomised and equilibrated, following previous EPSR procedure. As the refinement progressed appropriate restraints were introduced to avoid unphysical behaviour (and supplement the reference potentials), such as hydrogen overlap, as well as circumventing the oxygen atoms approaching the magnesium too closely, these restraints are found in table 3-4. Finally, the empirical potential was introduced with a value of 10 $kJmol^{-1}$. This value effectively represents the difference between the energy minimum, i.e., the minimised structure found via the reference potentials alone, and the maximum energy of the system. Introducing this value allows for the fragments of the system additional energy to adopt a model that is equivalent to the scattering data. Note that this value requires a significant amount of trial and error to allow for a value that is not too small that it does not allow for additional movement but not too large that the atoms become 'stuck'. There is no 'one size fits all' value with EPSR and therefore the best value must be found from sample to sample. The system was finally allowed to converge before accumulating over several thousand iterations using the supercomputer cluster, IRIDIS, to provide

better statistics. Alongside this, auxiliary calculations in the form of SDF, coordination number, coordination angles and chain lengths were made.

Table 3-4. *Refinement restraints for the EPSR simulation. Min r shows the minimum distance allowed between atom types and the min r coefficient demonstrates the strength needed to allow for said restraints.*

Restraint	Min r / Å	Min r coefficient
Mg1 – O1s	1.8	0.000
Hw – Hw	1.5	7.897
Hw – Mg1	1.5	9.411
Hw – S1	1.5	0.000
Hw – O1s	1.5	69.605
Mg1 – Mg1	3	0.000
Mg1 – S1	2	0.000
Mg1 – O1s	1.8	221.621
S1 – S1	3	0.000

3.2.4 Justifying EPSR Refinement – Structure Beyond Water.

The scattering observed from the 2.00M $MgSO_4$ solution is dominated by that from the water structure, with only one Mg^{2+}/SO_4^{2-} for every 27.75 H_2O molecules. This can be seen in figure 3-6 with the F(Q) following the general envelope of the water scattering. Observing the scattering data for both aqueous $MgSO_4$ and pure water, there are visible differences in the data that does suggest that there is quantifiable structure that can be extracted via EPSR.

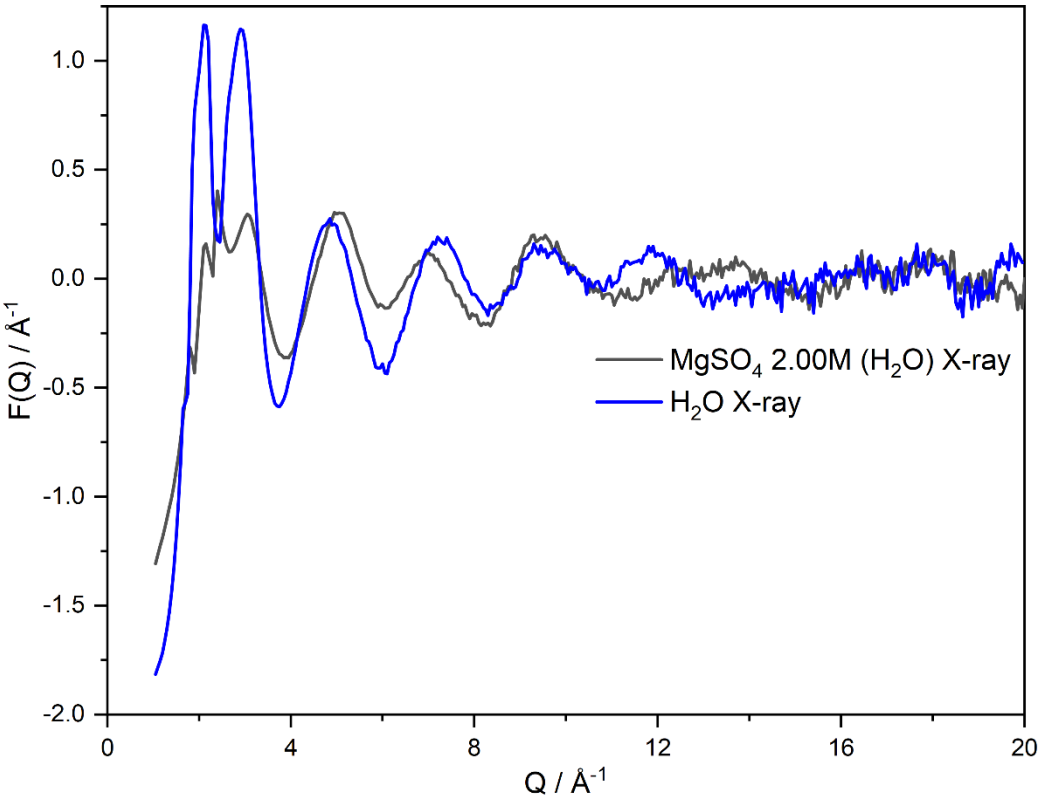

Figure 3-6. *Experimental F(Q) comparison of 2.00M $MgSO_4$ (black) and H_2O (blue) F(Q) X-ray data collected in-house with exposure time 180 minutes. Data were processed using Gudrun X.*

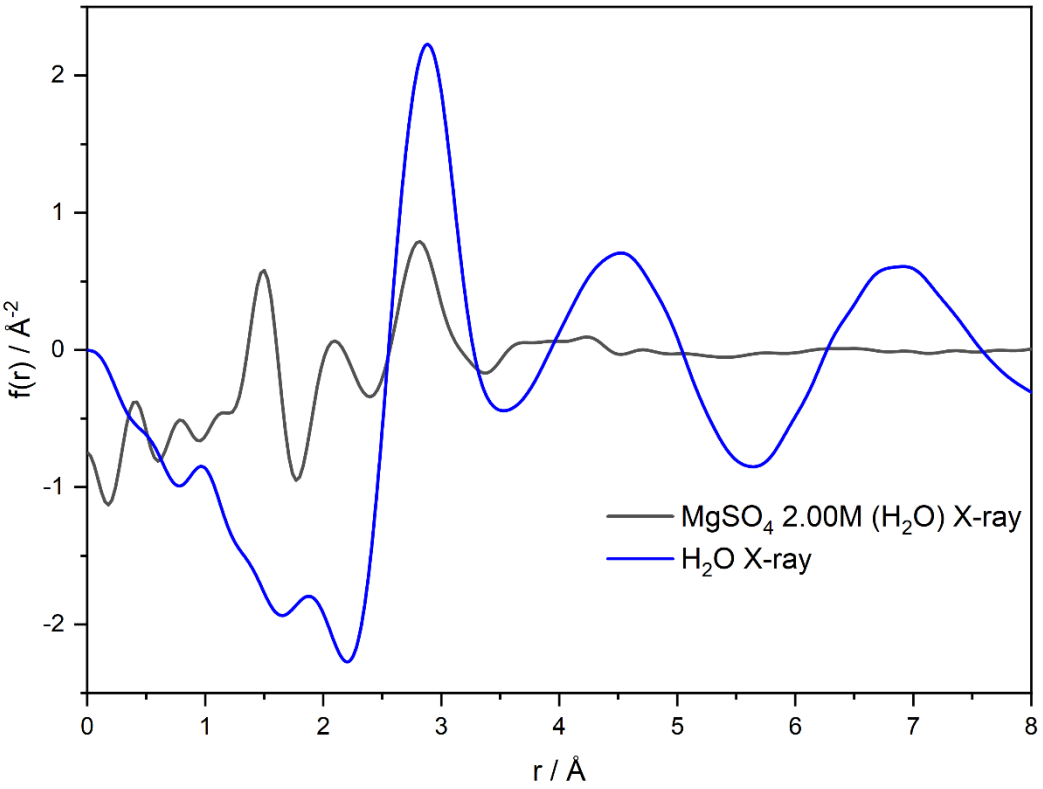

Figure 3-7. *Experimental f(r) comparison of 2.00M $MgSO_4$ (black) and H_2O (blue) F(Q) X-ray data collected in-house with exposure time 180 minutes. Data were processed using Gudrun X.*

As can be seen from figure 3-6, the scattering originating from the pure water and aqueous $MgSO_4$ share some features, as to be expected from samples that both a majority water. However, there are also obvious differences between the two, this points to a significant signal being recorded from both the ionic species in solution as well as how this species disrupts the pure water signal.

The f(r), seen in figure 3-7, may be more intuitive for identifying the most obvious deviations to the structure. Between r = 1.0 – 2.5 Å, two distinct features can be observed within the $MgSO_4$ data that are not present in the water data, these features correspond to the intramolecular S-O bond (1.49 Å) and another undefined bond, likely originating from a Mg-O distance at approximately 2.0 Å. The features centred at approximately r = 1.6 Å and 2.2 Å in the water f(r) can be attributed to O···H and H···H structure, defined by Soper[4,6], and whilst these are also likely to be present in the aqueous $MgSO_4$ data, they are probably overshadowed by the stronger scattering features described above. At approximately r = 2.8 Å, the two samples have a shared feature that can be attributed to the well-defined tetrahedral intermolecular interactions identified. Beyond r = 3.0 Å, the task of attributing structural features increases in complexity and this is compounded by a plateauing of the features in the aqueous $MgSO_4$ compared to H_2O. The water structure extends beyond these values, with stronger oscillations centred on approximately r = 4.5 Å and 7.0 Å, demonstrating the longer-range structure in pure water. The same long-range features are not visible in the aqueous $MgSO_4$ data, with only a small oscillation at approximately r = 4.0 Å, this suggests either a loss of long-range order, compared to water, or deficiencies in the data. Overall, both the F(Q) and f(r) data suggests significant and observable differences in the data that justify further investigation via a large-box refinement such as EPSR.

3.2.5 EPSR Refinements

As EPSR exclusively refines against the total scattering structure function, F(Q), this should be monitored throughout the refinement. Similar to all refinement types, the aim is to reach a good agreement between the experimental scattering data and the calculated obtained from the model. A ‘perfect fit’ between the experimental data and refined model is difficult to achieve in a meaningful way and while it is easier to input any reference potential and not observe the model to obtain a good fit, the fit is unlikely to be physically and chemically accurate to the sample. Simplifications and assumptions are also made about the model and refinement process which increase the complexity in obtaining a good and physically accurate fit, and further complicate the fitting process. Furthermore, the data typically collected for total scattering are often of poorer quality with regards to the signal obtained, especially when compared to diffraction data on crystalline samples. Consequently, whilst a perfect fit is easy to obtain, a good fit that is accurate to the sample is far more difficult.

Compared to the reciprocal space F(Q), functions such as the f(r) and atom-atom g(r) are more intuitive for probing the structure and improving the fit, as they represent the real space structure. Often it is useful to examine the plots of these functions to identify physically unrealistic features and adjust the refinement accordingly. For instance, peaks observed in the calculated g(r) that do not correspond to the experimental data may indicate atoms being too close to one another, these can often be fixed by altering parameters such as restraints or the reference potentials. Care must be taken when altering these parameters to avoid introducing bias into the model therefore changes must only be accepted if they produce an improved fit to the data. Thus, by examining various different functions it is possible to arrive at a fit that is broadly consistent with all of the relevant functions.

As both figure 3-8 and figure 3-9 show, a good agreement was reached between the experimental and calculated data for the F(Q), and for the derived functions such as the RDF showing a good fit providing confidence in the model obtained. There is a small discrepancy in the H_2O neutron data and that can be traced to the uncertainties in the inelasticity corrections implemented during the correction of the total scattering data. However, this only shows a small difference in the overall model, and with the other data sets showing good agreement between the two, this small discrepancy is not considered an issue.

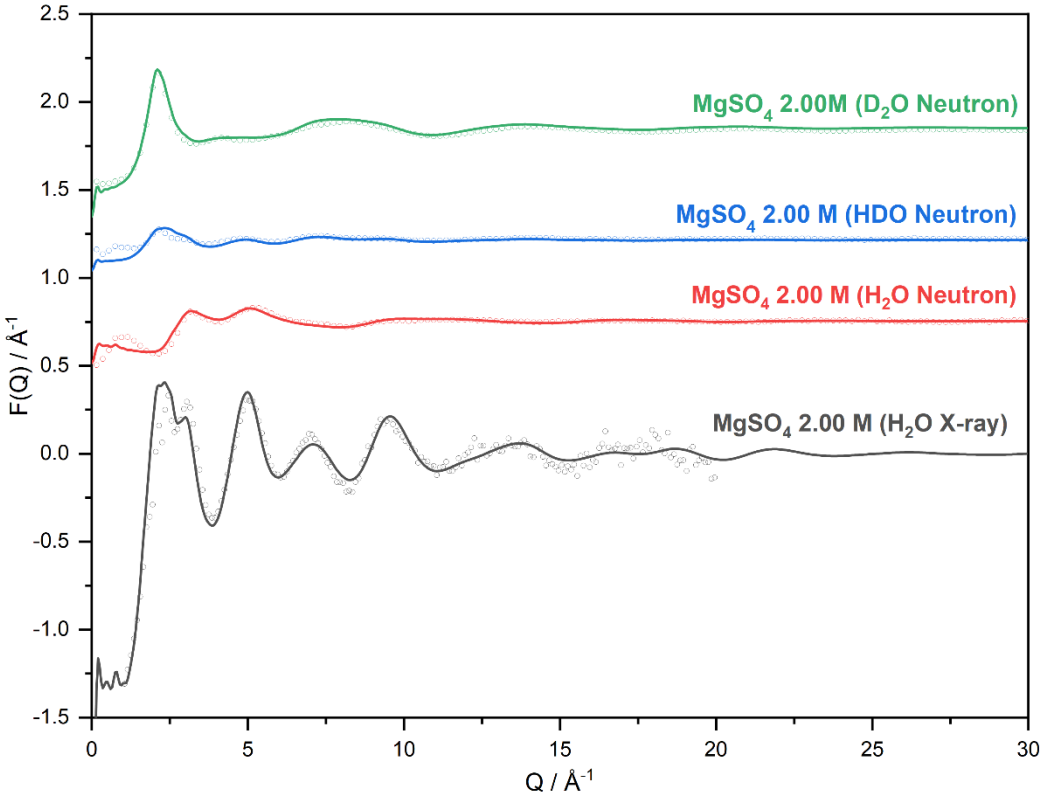

Figure 3-8. *Stacked F(Q) EPSR refinement for 2.00 M $MgSO_4$ (black: H_2O X-ray, red: H_2O neutron, blue: HDO neutron, green D_2O neutron) where circles denote experimental data and solid lines represent the model fit.*

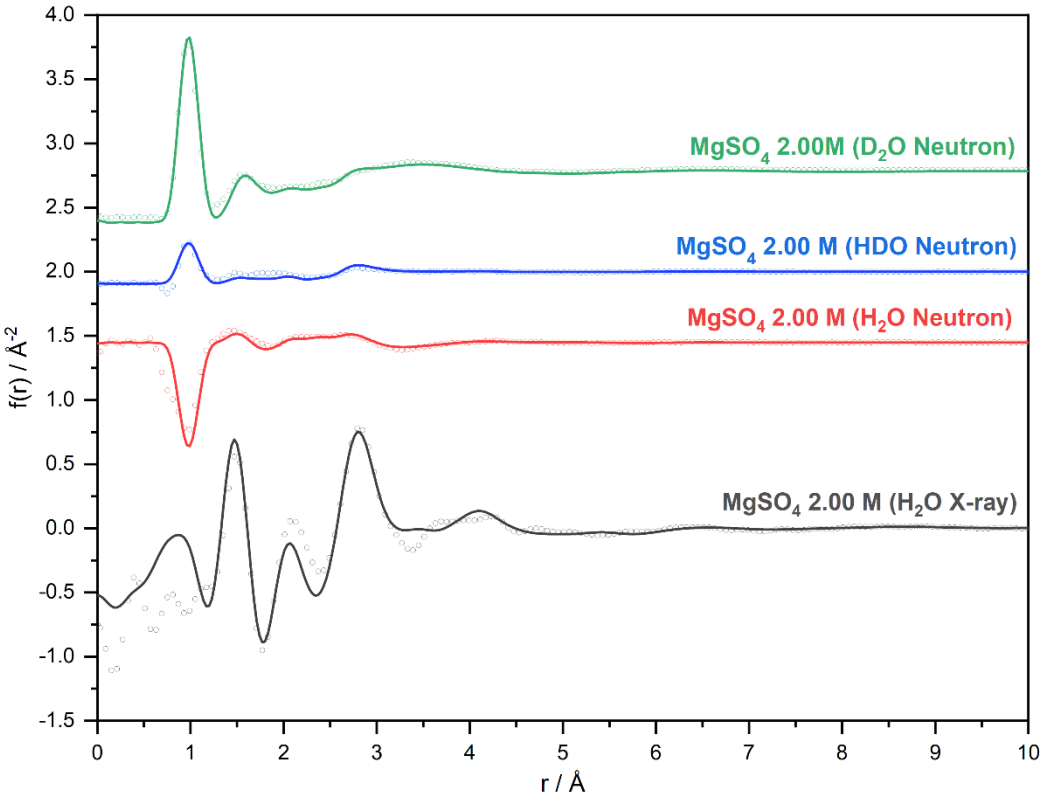

Figure 3-9.*Stacked derived f(r) for 2.00 M $MgSO_4$ (black: H_2O X-ray, red: H_2O neutron, blue: HDO neutron, green D_2O neutron) where circles denote experimental data and solid lines represent the model fit.*

3.3 Extracting Structural Features

To fully examine both the ionic and aqueous environments the following auxiliary routines were used: atom-atom g(r), coordination number, bond angles and SDF. Using these routines, in combination with direct observations from the model itself, the local coordination environment will be examined around the magnesium ion and sulfate ion as well as the bulk water structure and how it deviates from that of pure water. In this context, *bulk* is defined as extended areas of adjacent water molecules not disrupted by magnesium or sulfate ions. Examining the structure in terms of these well-defined chemically intuitive fragments should aid in construction of a more coherent description of the overall structure.

3.3.1 Magnesium Coordination Shell

From previous studies and through analogy with the solid-state, it is anticipated that the magnesium will show well defined correlations to the oxygens of both the water and the sulfate. To test this assumption, we can examine the atom-atom correlations derived from the refined model and these are presented in figure 3-10.

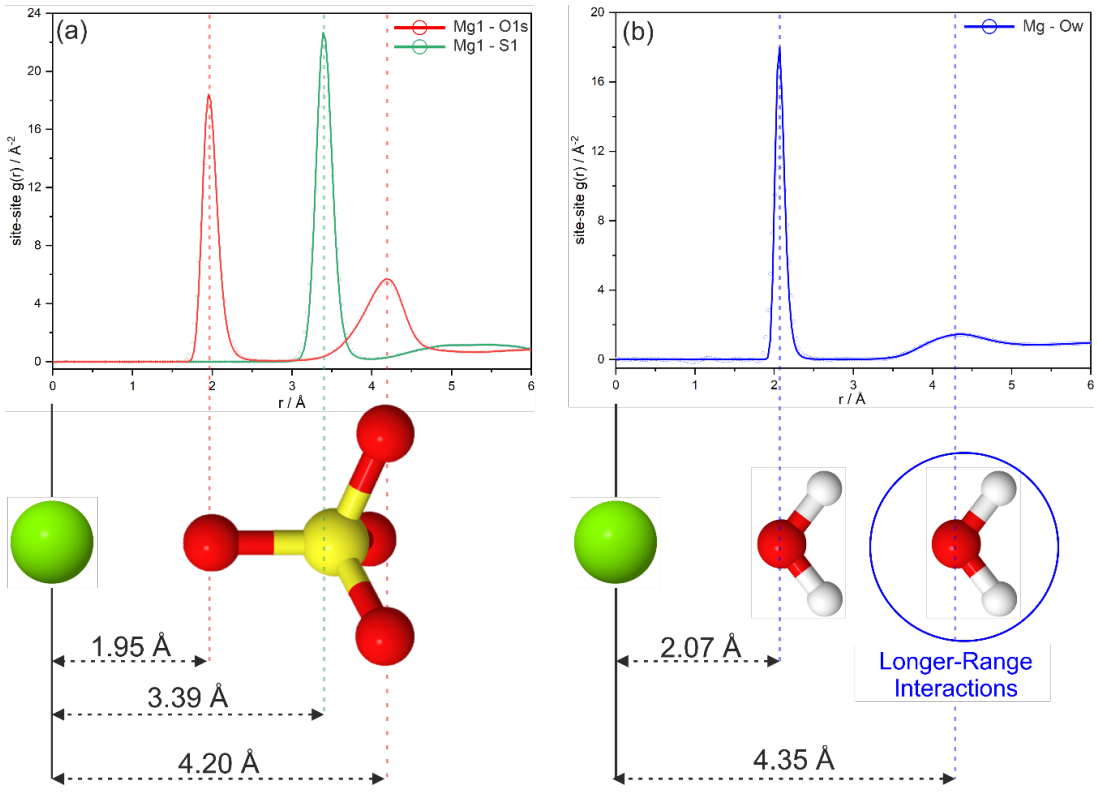

Figure 3-10. *Atom-atom g(r) for (a) Mg1-S1/O1s and (b) Mg1-Ow, highlighting the atom-atom distances by the cartoon dipiction of fragment interactions, where fragments follow the conventions of figure 3-5.*

The above figure shows the atom-atom correlations extracted from the accumulations of the final refinement, this clearly shows discrete features representing local structure and ordering within a

radius of 6 Å from the central atom. Figure 3-10(a) represents the atom-atom correlations observed between a magnesium and the sulfate ions, where three distinct features can be identified. Focussing firstly on the Mg-O1s g(r), two features can be observed, the first at 1.95 Å which suggests a direct coordination of the sulfate to the metal ion within a distance in agreement with crystalline magnesium sulfate structures.[31,32,36,37,43,44,50,54–56] A second, broader feature for Mg-O1s occurs at 4.20 Å, this broadening is due to the increased distribution of possible distances of non-coordinated O1s atoms. The directly coordinating oxygen of the sulfate acts like a tether and results in a sharp peak, whereas the remaining oxygens have a higher degree of freedom and their exact distance is influenced by the rotation of the ion. Overall, the atom-atom g(r) for magnesium with respect to the sulfate is consistent with the existence of ion contact-pairs similar to those reported previously in the literature and can be rationalised by the electrostatic stabilisation of the oppositely charged ions.[44,56,57] The affinity and charge stabilising effects of the sulfate ion will be discussed in more detail in later sections.

Figure 3-10(b) shows the atom-atom distances observed between the magnesium ions and water molecules, showing correlation distances at 2.07 Å and 4.35 Å. The first feature at 2.07 Å is similar in profile to that of the Mg-O1s (sulfate) correlation and is attributed to direct coordination between magnesium and water oxygen. The similar distance range observed for both oxygens suggest a well-defined Mg-O coordination shell, a structure that is observed in both the solid-state[40,55,58] and aqueous phase structures[36,50,54]. The second feature centred at r = 4.35 Å is much broader and represents a larger distribution of atom-atom distances attributable to the second coordination shell. These interactions as well as the interactions between the water and bulk structure will be discussed in more detail in section 3.3.5.

The coordination numbers found in figure 3-11, show the average coordination between the magnesium ion and the oxygens of sulfate (O1s) and water (Ow). A radius of r = 1.0 – 2.5 Å was chosen to encompass the first coordination sphere, as determined from the g(r) in figure 3-10.

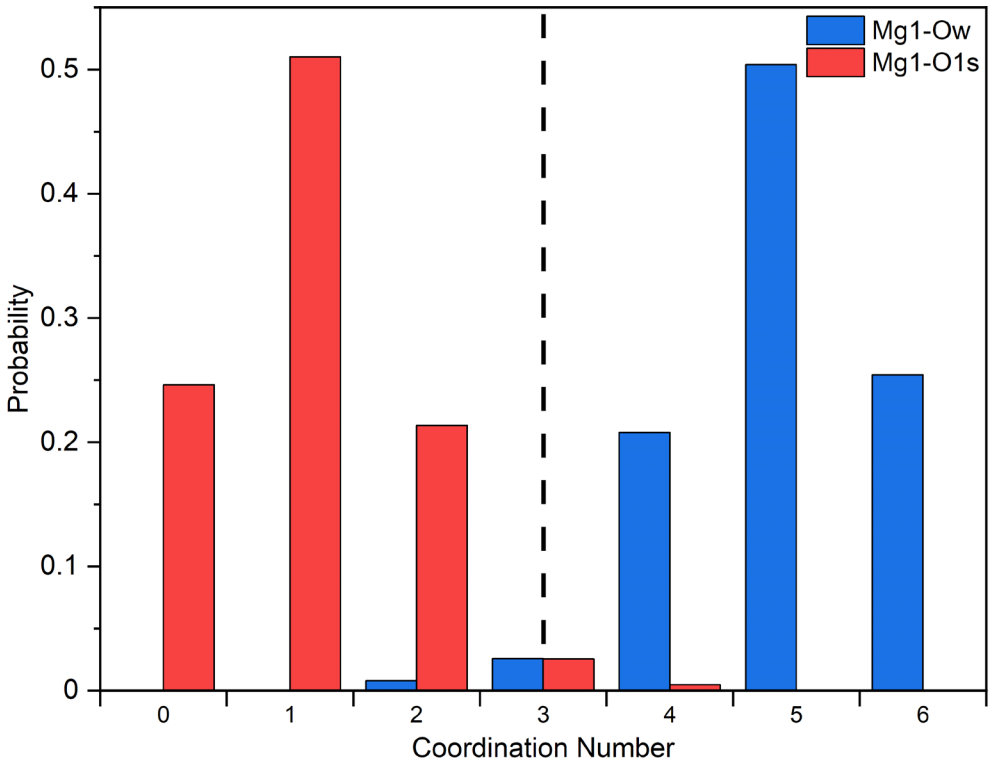

Figure 3-11. *Coordination number for Mg – Ow (blue) and Mg – O1s (red) with dashed line to show the 'mirror relationship'.*

The above figure shows the coordination number around the magnesium ion, with the most striking feature being that of the almost mirror image relationship between each oxygen type. This relationship is a direct result of the dominance of a single coordination $MgOw_xO1s_{6-x}$ environment for magnesium. Again, this draws parallels to the solid-state structure discussed in section 3.2.1, where all structures have a common octahedral motif with varying oxygen ratios. The form of the histogram in figure 3-11 shows the existence of a range of different 6-coordinate structures/modes varying from fully hydrated $Mg(H_2O)_6$ to $Mg(SO_4)_4(H_2O)_2$, with varying probabilities of finding each mode within the refined model. The most probable structure is the 5:1 water to sulfate, making up over half of the 6-coordinate modes, this is not unexpected as the equal and opposite charges of the Mg^{2+} and $SO4^{2-}$ ions are likely to attract one another to stabilise the two species, forming the foundations of ionic/electrostatic interactions.

Other significantly populated configurations exist within the refined model, including that of a fully hydrated $Mg(H_2O)_6$ and $Mg(SO_4)_2(H_2O)_4$ structure with an approximate 25% and 20% probability respectively. The fully hydrated configuration, making up almost a quarter of the 6-coordinate structures, can also be found within the solid state in the higher hydrated crystal structures, but also within the weaker concentration aqueous studies.[36,42,43,50] This commonality between both the

solid and aqueous state provides further confidence in our refined model, drawing parallels between both states. Finally, the $Mg(SO_4)_2(H_2O)_4$ is a less common configuration found in the model, making up only a fifth of all 6-coordinate clusters. The same configuration can be found in the monohydrate crystalline structure, with the caveat of the sulfate adopting a bridging role, however it is rarely reported in literature studies of aqueous systems. This relatively common structural motif shows a potential structure that may be abundant within the system, however, are either overlooked or difficult to define in previous experimental and theoretical experiments. This is highlighted by Balasubramanian et al.[36] where two-coordinate sulfate clusters are not observed at lower concentration, and this higher coordination is only possible at higher concentrations and when structures are examined over an extended r-range (i.e. beyond a few angstroms from the central atom). This is where the model developed in this work deviates from previous studies, with structural features being observed that span 10's of angstroms. It can therefore be hypothesised that we may be observing extended chains of $MgSO_4$ within the refined model, assuming a charge stabilised structure is assembling and a dual coordinated sulfate requires an additional magnesium for a neutral species or a potential stabilisation via the water, as discussed by Kulichenko et al.[46]

To further evaluate the geometry of the 6-coordinate clusters, bond angle calculations were conducted for O-Mg-O. This routine can aid in the quantification of the geometries and conformations of these species, creating additional links between the refined model, literature and solid-state structure. Using the atom-atom distances found in figure 3-10, the calculation was set up to include solely the directly coordinating oxygens to the magnesium, and therefore a distance of r = 2.5 Å was used for the maximum radius. It is worth noting for this routine that it utilises as sin(θ) dependence, and as it approaches 180°, where sin(180) = 0, probability will be non-existent. Therefore, when approaching this angle there appear to be no bonding angles in this region, so care must be taken when interpreting the results. This sin(θ) function also effectively inverts the probability distributions but have been converted back to θ for clarity within this study.

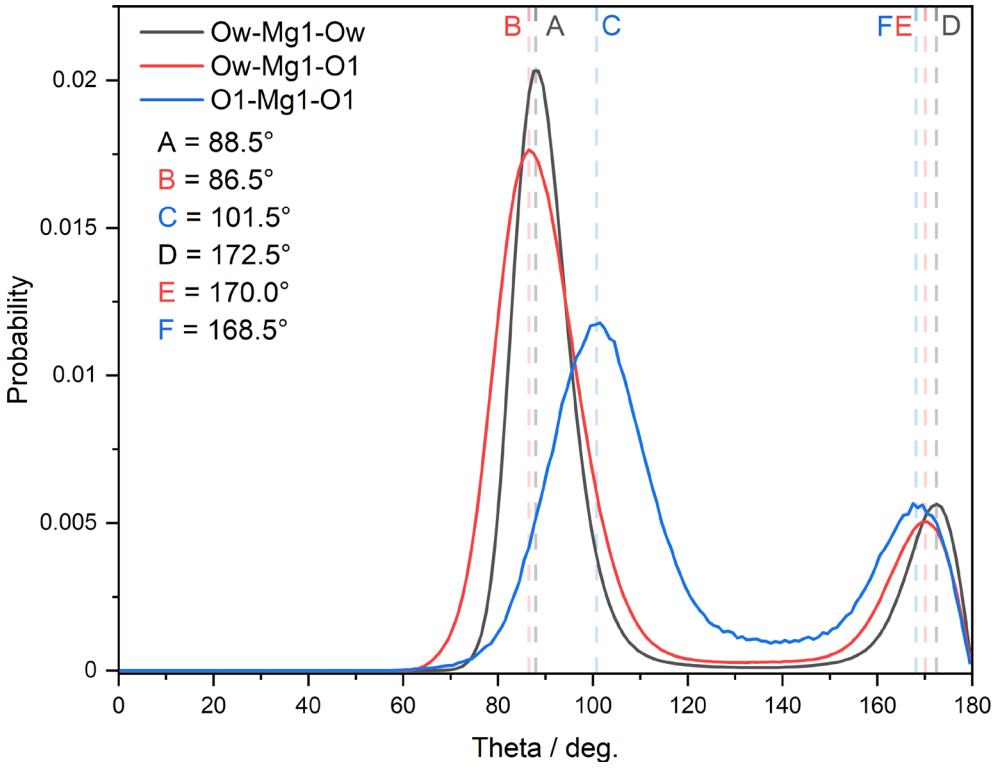

Figure 3-12. *Bond angle for Ow-Mg1-Ow (black), Ow-Mg1-O1 (red) and O1-Mg1-O1 (blue) with faded dashed lines to denote peak maxima at A – F.*

The plot in figure 3-12 demonstrates two distinct bonding regions, focussed around 90° and 180°, the angles expected for a 6-coordinate octahedral geometry. This is unsurprising based upon the well-established 6-coordinate octahedral structures found in almost all of the previously discussed literature in the solid and aqueous states. Focusing initially on the Ow-Mg-Ow bond angles, two well-resolved peaks can be found at 88.5° (A) and 172.5° (D), describing the cis and trans bound water within the metal cluster. Whilst these Ow do not occupy the 'perfect' 90° and 180° positions, often found in fully crystalline materials, they do exist within the angle range expected. Two main factors are likely to cause these deviations from the ideal positions, that being the dynamic nature of the system as well as the other bulkier coordinating species. The dynamic nature here, it represents both the higher degree of movement of the water molecules compared to the rigid state found in the crystalline phase, as well as the higher degree of water transfer to and from the metal cluster and the bulk, expected from an aqueous phase sample.[13] Whilst the 'dynamics' of the system are well documented within the literature, it is incredibly difficult to measure such movement from a scattering/EPSR point of view. However, Gaffney et al.[59] discuss in detail the proton/ligand exchange within a $NaClO_4$ and $Mg(ClO_4)_2$ system via vibrational spectroscopy and molecular dynamics, drawing parallels to the system being studied here i.e. metal ion and tetrahedral counter ion. The complexity with regards to exchange, proton transfer and ion pair interactions is highlighted, fully demonstrating the difficulty with regards to instantaneous structure analysis.

Considering the effect of the other coordinating species (although we are only looking at Ow-Mg-Ow angles, the numbers will include instances of where sulfate is coordinated), sulfate is a much bulkier species in comparison to the water, and therefore the water position is likely to adjust to allow for this coordination. As previously discussed with the coordination numbers, the most likely configuration is that of $MgSO_4(H_2O)_5$, with one coordinating sulfate species, and this is likely to force the remaining coordinated water closer together. A similar hypothesis can be applied to the larger angle feature, with the obvious caveat of the $\sin(\theta) = 0$ where $\theta = 180°$, but the dynamics and bulky substituent argument remains true.

The above bulky coordinating argument is supplemented by the Ow-Mg-O1s bond angles observed, especially at peak (B) which is less resolved and contains a larger range of potential angles. This again is likely due to both the dynamics and bulkier species involved. The trans bond angle also experiences a larger degree of conformations, however less broad compared to peak (B) as the trans coordinating species have less influence due to the bulky nature being non-adjacent.

O1s-Mg-O1s shows the largest deviation from the ideal octahedral positions, with peak (C) being centred on 101.5°, showing a 13.0 - 15.0° difference compared to the water-based bond angles. The angle observed lies between the ideal octahedral (90°) and tetrahedral (120°) positions and has bond angles closer to the 'seesaw' geometry found in molecules such as SF_6. This increase in angle is only possible in the $Mg(SO_4)_2(H_2O)_4$ clusters and is likely highly influenced by the increased sterics of two bulky coordinating sulfates cis to one another. There is less of an influence at larger angles where the SO_4^{2-} adopts a trans conformation, as they are no longer competing for the same space. Overall, both this configuration as well as the mono-coordinate SO_4^{2-} will affect the other bond angles, as previously discussed, deviating from the ideal octahedral positions. The dual coordinating will obviously have a larger influence, but as these conformers only exist in 20% of the model, they are only the 3rd most like configuration, and therefore the O1s-Mg-O1s is less representative of the model as a whole.

To summarise, it is observed that the magnesium metal clusters adopt a 6-coordinate species within the refined model, as confirmed by the coordination numbers found in figure 3-11, and this is complimented by the close to octahedral bond angles observed. The configurations determined via these routines can also be observed directly in the large-box model, with fragments shown in figure 3-13.

	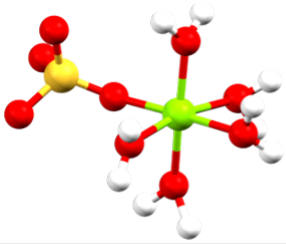	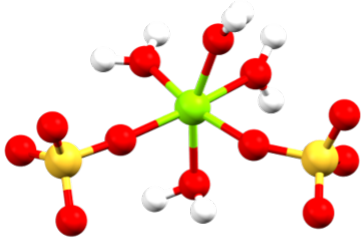
$Mg(H_2O)_6$ ≈ 25%	$MgSO_4(H_2O)_5$ ≈ 50%	$Mg(SO_4)_2(H_2O)_4$ ≈ 20%

Figure 3-13. *Common structural motifs found within the refined model with relative probabilities as derived from figure 3-11.*

Using the probabilities of coordination in figure 3-11, we can approximate the relative population of these three most common configurations. The remaining 5% of configurations are likely due to structures outside the parameters of the calculations such as isolated ions, octahedra with bond distances 2.4 Å+, higher sulfate coordination and other coordination environments such as MgO_5, however at least 95% of the species exist in the octahedral form and therefore these species have minimal effect on the auxiliary routines. Using the auxiliary routines as well as probing the structure directly, it has been possible to confirm the hypothesis of octahedral metal clusters within the aqueous system, confirming this local structure via an experimental total scattering EPSR approach.

3.3.2 Contact Ion Pair (CIP) vs. Solvent Separated Ion Pair (SSIP)

In various studies of different ionic aqueous systems, many argue between two bonding modes: CIP where ions are directly bonded[44,54,56,60] vs. SSIP where the interactions between ions is accommodated via a solvent/hydrogen bonding mode[45] or a mixture of the two bonding modes[42,50,58]. These interactions are graphically described in figure 3-14.

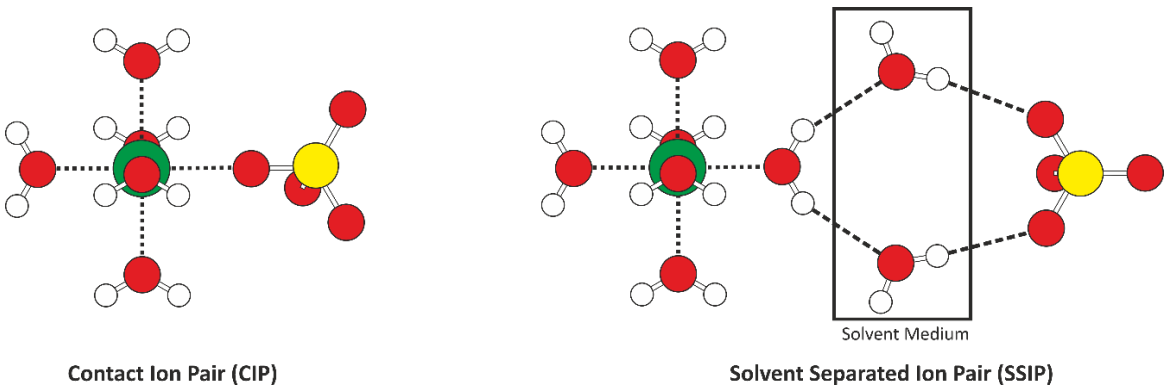

Figure 3-14. *Basic graphical representation of contact ion pair (CIP) and solvent separated ion pair (SSIP) based on the interaction between magnesium and sulfate ions in a water medium.*

As the above figure shows and assuming a 6-coordinate species, the interactions can go via a direct interaction (CIP) or via the solvent medium (SSIP). Previously discussed studies debate whether aqueous $MgSO_4$ interacts via a CIP or SSIP mode, CIP being the more favoured, with different

conclusions being drawn depending on the methodology applied[42,44,45,54,56,60], it is important, therefore, to investigate what our current model tells us.

Whilst all previous calculations, such as the RDF and coordination number highly suggest that the sulfate, specifically O1s, does interact with a central magnesium, using an additional Mg-O1s restraint r = 2.8 Å allows for the modelling of a systems whereby magnesium and sulfate cannot form interactions within a typical metal-oxygen bond distance. So, contact pairing is the dominant and most obvious bonding mode within the system, however one must still consider the effect of solvent stabilisation upon the clusters. The electrostatic attraction is the dominant force, however, as will be discussed within the sulfate structure section, the stabilisation from the solvent plays a larger role in the system than one may have considered.

3.3.3 Comparing Aqueous- and Solid-State Magnesium Local Structure

One of the main questions with regards to the aqueous structure found in this refinement is how it compares to its solid-state counterparts. Figure 3-10, found in the magnesium coordination structure discussion, shows multiple atom-atom correlations attributed to the Mg-O bond, all of which exist within the distance range expected for this bond type. Using the solid-state structures as a comparison point, described in table 3-5, the crystalline hydrate bond lengths are of a similar magnitude to the aqueous structure with some deviations in the midpoint/peak maxima values.

As the table below shows the comparison of the aqueous 2.00M system compared to that of the crystalline $MgSO_4 \cdot xH_2O$, and whilst the Mg-Ow and Mg-S1 remain within the distance ranges found for the solid phase, there is a substantial decrease of the Mg-O1s distance. This decrease of at least 0.5 Å is likely due to the dynamic nature of the sulfate ion, with many degrees of freedom allowing for a larger range of distances which can be described by the broader feature found in the atom-atom g(r) in figure 3-9. Whilst the Mg1-Ow shows a sharp feature for its correlation distance, the Mg-O1s feature shows a larger distribution of distance values alongside a degree of asymmetry tending towards the higher-r. Whilst the peak maxima lie at a lower-than-expected length, the broad distribution of atom-atom correlations fully incorporate all values described within the solid-state. Further to this, the distance range for Mg-S1 is within the expected distance range for this ion, which allows for confidence in the model due it being a more central point compared to the more dynamic O1s. One must also consider the thermodynamic nature of an aqueous system compared to a solid phase structure, where overall there is more internal energy which allows for much more movement of the ions in the aqueous medium. Subsequently, this will allow for not only a larger range of distance values facilitated by a more dynamic environment in which atoms, ions and molecules will be moving and exchanging more rapidly, defined by both the kintetics[13] and general transfer of atoms/ions within the solution.[58] So whilst the simulation and atom-atom g(r)

gives a more 'averaged' view of this system; the nature of such aqueous structure is always going to remain more dynamic and therefore direct comparisons to the crystalline state may not be as straightforward as first envisaged. Overall, however, the similarities between the average bond length does lend itself to similar structure forming, and overall does suggest a degree of overlapping structure, likely on the more basic end of structure.

Table 3-5. *Mg-O1s/S1/Ow atom-atom distances. * denotes no coordinated sulfate/water, values within brackets denotes midpoint (crystalline)/peak maxima (aqueous).*

$MgSO_4 \cdot xH_2O$	Mg-O1s (Sulfate) / Å	Mg1-S1 (Sulfate) / Å	Mg-Ow (Water) / Å
0	2.011 – 2.093 (2.052)	3.343 (3.343)	*
1	2.018 – 2.092 (2.055)	3.252 – 3.286 (3.269)	2.172 (2.172)
2	2.059 – 2.068 (2.064)	3.303 – 3.378 (3.341)	2.101 – 2.109 (2.105)
4	2.072 – 2.080 (2.076)	3.225 – 3.274 (3.250)	2.037 – 2.091 (2.064)
5	2.097 – 2.105 (2.101)	3.405 – 3.407 (3.406)	2.051 – 2.062 (2.057)
6	*	*	2.049 – 2.080 (2.065)
7	*	*	2.010 – 2.121 (2.066)
9	*	*	2.056 – 2.075 (2.066)
11	*	*	2.057 – 2.062 (2.060)
27.75 (aqueous)	1.71 – 2.49 (1.95)	3.06 – 3.90 (3.39)	1.86 – 2.46 (2.07)

Comparing these values to literature values, particularly that of the purely computational aqueous $MgSO_4$ study by Balasubramanian et al.[36] allows for the direct comparison of these atom-atom distances. Using the 16.91wt% system as a comparison point, as it is closest to the 2.00M $MgSO_4 \cdot 27.75H_2O$ (19.4wt%) model, we can see that all atom-atom g(r) plots visually appear similar, with all features expected present in both studies. Starting with the Mg-Ow data, we can observe the dual feature of a sharp 1st peak and broader 2nd peak, akin to our structure, however the authors here describe a distance of 1.9-2.0 Å showing a decrease of 0.5-1.0 Å and is actually more similar to our Mg-O1s distance. As both O1s and Ow are the same atom type, this is unsurprising and is likely due to how the simulation and reference potentials are assigned for each species, alongside the similarity in bond lengths expected, as seen in the crystalline bond lengths. Upon use of the same reference potentials alongside an increase Mg-O1s restraint, the refinement fit was adequate but showed a worse fit using stricter restraints. Therefore, whilst the Mg-O1s/Ow will appear at similar atom-atom distances, it is suggested that the Mg-Ow will coordinate at longer range than Mg-O1s, as shown in the EPSR refinement as well as correlating with the solid-phase $MgSO_4$.

3.3.4 Sulfate Environment

Whilst the magnesium environment is remarkably similar to that in the solid-state, the aqueous sulfate structure is very different and warrants a detailed investigation. For this analysis, a focus will be put on the $SO_4^{2-}\cdots H_2O$ structure primarily, as most of the electrostatic interactions between the SO_4^{2-} and Mg^{2+} have been probed in previous sections. Unlike the structure, with regards to the magnesium, where the electrostatic interactions dominate and are far easier to quantify, the sulfate can participate in both the electrostatic ion interactions as well as hydrogen bonding to the water molecules. This, and the massively increased size of the sulfate ion compares to the magnesium, makes the analysis of the direct environment far more complex. Therefore, for the analysis of the sulfate environment and that of bulk water, we need to employ an additional visualisation tool in the form of the SDF alongside the standard g(r) and model analysis.

3.3.4.1 Previous Sulfate Structure Studies

Similarly to aqueous structure of Mg^{2+}, a variety of both purely computational studies[46,47,61] as well as dual spectroscopic/computational studies[48,62,63] have been conducted on the aqueous structure of sulfate, SO_4^{2-}, both as an individual ion and also with appropriate counter ions. As sulfate is very uncommon in a purely anionic state, the studies of such an entity are gross simplifications. Smeeton et al.[47] use a combined empirical potential and DFT approach to model the interaction and stabilisation of a sulfate anion in water. Building from an initial cluster of $SO_4^{2-}(H_2O)_3$ to the largest cluster of $SO_4^{2-}(H_2O)_{50}$, they postulate how water orientates itself, with the most basic structure being a trigonal, 3-membered ring upon the face of the sulfate, seen in figure 3-15(b). They found that this structural feature appears to be the most stabilised, and forms the basic solvation environment, capping each face in turn until all have been fully solvated at $SO_4^{2-}(H_2O)_{12}$. Beyond this basic capped structure, additional water molecules are introduced which distort each solvated face but introduce hydrogen bonding between faces which increases the water ring size to 4 - this reduces further the energy of the cluster by removing the strained 3 membered rings, depicted in figure 3-15(c). Beyond these basic structures, the authors describe larger cluster sizes with what is referred to as 'a dangling OH bond' whereby the water directly donates to the sulfate ion electrostatically but does not participate in the hydrogen bond network of the 1st solvation shell. These dangling bonds may suggest indications of the previously described SSIP interactions, providing a route between the sulfate ion and longer-range structures. Overall, these structures represent the lowest energy configurations of solvated sulfate anions and provide evidence of shell-like structure stemming from a hydrogen bond network.

Kulichenko et al.[46] expand on the work of Smeeton et al.[47] however they focus primarily on the charge transfer between the central sulfate and the water in terms of the overall stabilisation of

the system. The initial solvation structures described by the authors differ to those described by Smeeton et al.[47], as the initial solvation environment (a) involves a bridging, double hydrogen bonding mode between the water and two sulfate oxygens. This mode dominates the $SO_4^{2-}(H_2O)_{1-3}$ (a) structures. Upon the evolution of these basic bonding modes, a similar trigonal capped structure emerges, (b), and again follows the general structural features found previously. This suggests that an isolated sulfate anion will adopt this configuration if no external factors are considered. Overall, a common theme can be evolved from both computational and experimental sulfate-water structure studies, this is the double hydrogen bond for the lower hydrated clusters from $SO_4(H_2O)_n$ n = 1-4 (a). This is followed by the expansion to the aforementioned trigonal caps in (b) Additional water molecules are introduced face-by-face until every face of the sulfate has this extra birding water molecules, summarising the structures n = 5 – 12 (c). The evolution of these structures can be depicted below.

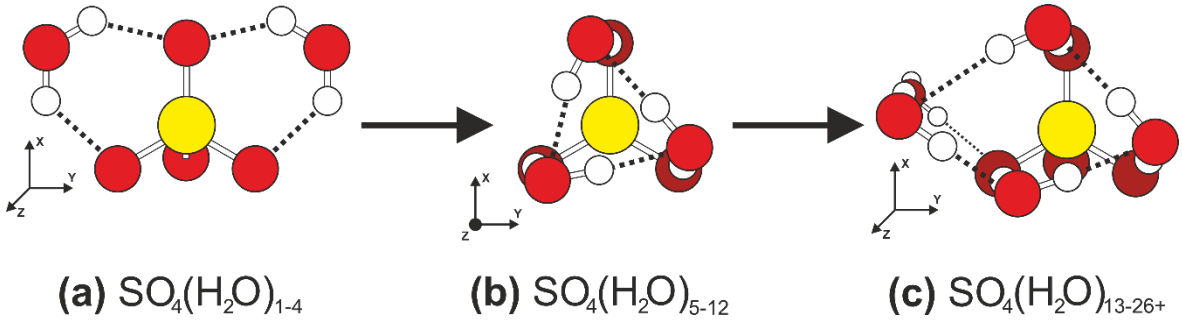

Figure 3-15. *Common $SO_4^{2-}\cdots(H_2O)_x$, where x = number of water, bonding modes adapted from Kulichenko et al.[46] and Smeeton et al.[47]*

However, the existence of sulfate as an isolated anion is relatively uncommon, and it often is found coordinated to a central metal ion, which in turn stabilises the negative charge. Therefore, studies have been conducted on the structural arrangement between sulfate and bulk water with a counter-ion present, with these studies again being both experimental and computational.[44,54,56,57] The majority of these studies agree that sulfate will form a CIP with an oppositely charged ion in order to create a stable and energetically favourable neutral coordination species. This in itself is unsurprising and agrees with the data discussed around the magnesium ion in section 3.3.1, however what is useful is the study of how the introduction of a sulfate ion disrupts the sulfate-bulk water interactions.

Perhaps the most similar study to our work based on the methodology and sample choice is that of an EPSR investigation of magnesium perchlorate as it might exist on Mars.[12] Although the counterion is different, the systems are similar in a number of ways and provide a good comparison point for both the refinement itself as well as the auxiliary routines. Comparing the SDFs of both systems, we see a similarity in the structural features observed, with density lying along the O-Cl-O vector as well as along the Cl-O bond, representing an octahedral/tetrahedral bonding modes for

the sulfate ion. This suggests a potentially common tetrahedral ion-water interaction mode in both cases. Whilst this is particularly interesting, the amount of research on such phenomenon is limited and may warrant further studies on similar metal-tetrahedral ion systems. The magnesium is stabilised by a 6-coordinate octahedral water shell and the perchlorate is stabilised by a water shell that appears to be a similar geometry to the sulfate water stabilisation, suggesting that the ion-water stabilisation is key to the structure observed and the physical characteristics observed for both salts, namely the high solubility. The most striking difference is that the authors find no evidence of CIPs. This again highlights the importance of the ion-water interactions, and whilst many studies examine the structure rather rudimentarily using RDF and coordination numbers, being able to examine the structure via EPSR allows us to describe the 3D structure in detail. In this section, we hope to elucidate more on these structures, specifically upon the sulfate ion.

3.3.4.2 Sulfate-Water Structure in 2.00 M $MgSO_4$

It is therefore established that isolated sulfate ions within the bulk aqueous system are uncommon and far more likely to exist in a CIP as discussed. It is important to note that many studies do suggest that there are two bonding modes working in tandem, a hybrid CIP/SSIP – indeed this is what a cursory examination of our model also suggests. Therefore, it is important to investigate fully how the sulfate interacts with the bulk water despite this system being dominated by the CIP as discussed in section 3.3.2 and using the above SO_4-H_2O studies in combination with $MgSO_4$ studies will elucidate the harder to define intermolecular ion-solvent structure.

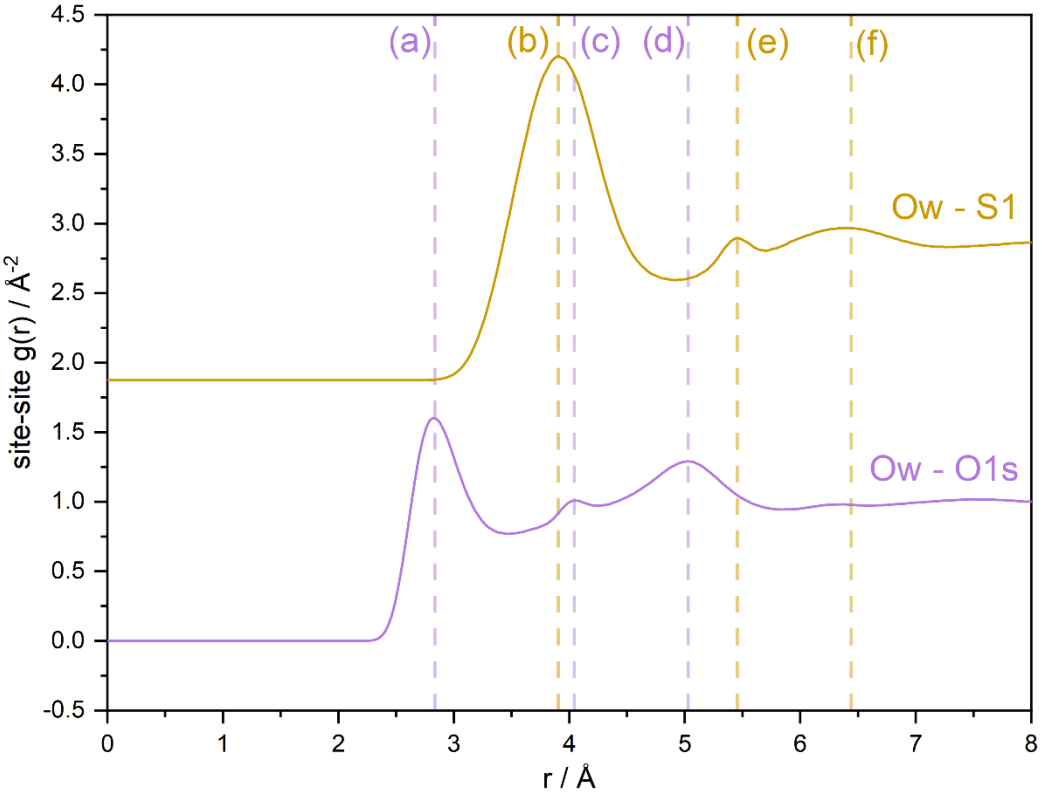

Figure 3-16. *Atom-atom g(r) for Ow – O1s (purple) and Ow – S1 (yellow) with distance: a) 2.84 Å, b) 3.91 Å, c) 4.04 Å, d) 5.03 Å, e) 5.46 Å & f) 6.44 Å.*

The distances observed between the sulfate ion and the bulk water can be seen in figure 3-16 and gives the first indications of distinct interaction modes between the two entities. Overall, the shape of both the Ow-O1s and Ow-S1 are of a similar shape, formed of a large initial peak followed by a smaller peak approximately 1.0 – 1.5 Å after the initial feature. This is expected for the interaction between these two atom types as it defines essentially the same interaction, just by two different species between the SO_4^{2-} and H_2O. This pattern can also be observed in the literature[36] for both RDFs, showing that our data is also consistent with previous experimental studies. One difference we do see compared to the literature is a broader first feature (b), for Ow-S1, which is likely attributed to the EPSR approach giving a more realistic picture of the true structure, including increased variability that is likely in an aqueous structure.

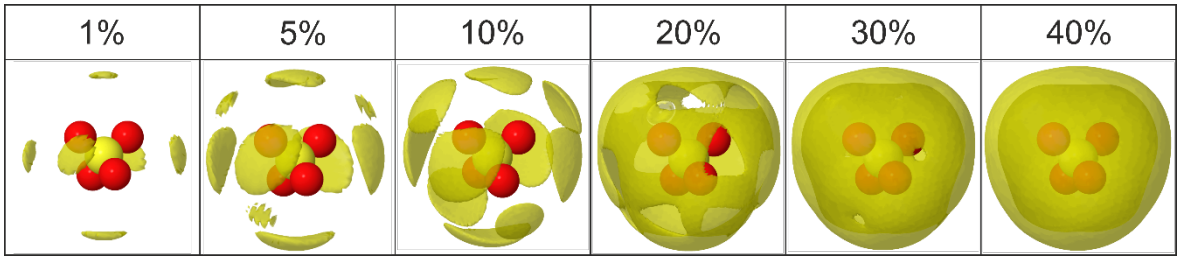

Figure 3-17. *SDF for $H_2O@SO_4$ with increasing isosurface fraction level over r = 1.0 – 5.0 Å. The most common structure (1%) highlights the octahedral strcuture, expanding to the dual octahedral/tetrahedral (5%) structure before becoming increasingly homogenous.*

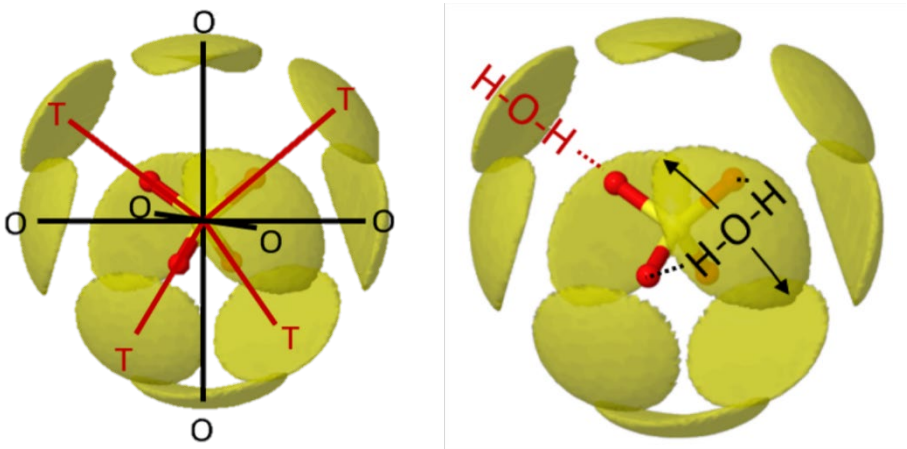

Figure 3-18. *SDF 10% highlighting the most probable octahedral (black) and tetrahedral (red) bonding modes alongside potential structure elements.*

Whilst the RDF can quantify the intermolecular interactions and prove that they are occurring within a meaningful range, they do not provide information on the 3-dimensional structure of these interaction - for this, we need to examine the SDF. Starting at the lowest isosurface of 1%, representing the most likely configuration of water around sulfate, we see an octahedral arrangement around the ion, specifically along the O-S-O vector. This suggests a double hydrogen bond mode across this edge, forming a hydrogen bond to each oxygen, this is similar to the structures observed in literature, depicted in figure 3-15(a). As this feature increases in density with the increasing isosurface, it becomes more pronounced in the oval shape, and this suggests a larger degree of freedom of the hydrogen bonded water, whilst also demonstrating the larger number of potential configurations. The second prominent feature observed is the tetrahedral nodes found along the S-O bond that represent a linear hydrogen bonding mode letting the water hydrogen bond to both the larger bulk water structure or a capped mode, with a double hydrogen bond structure. This structure, to our current knowledge, has not been reported in previous studies, and represents an additional bonding mode that may only possible due to the unique aqueous $MgSO_4$ environment. Beyond 20%, the SDF becomes more homogenous as more interactions are introduced, creating a sphere like environment around the ion.

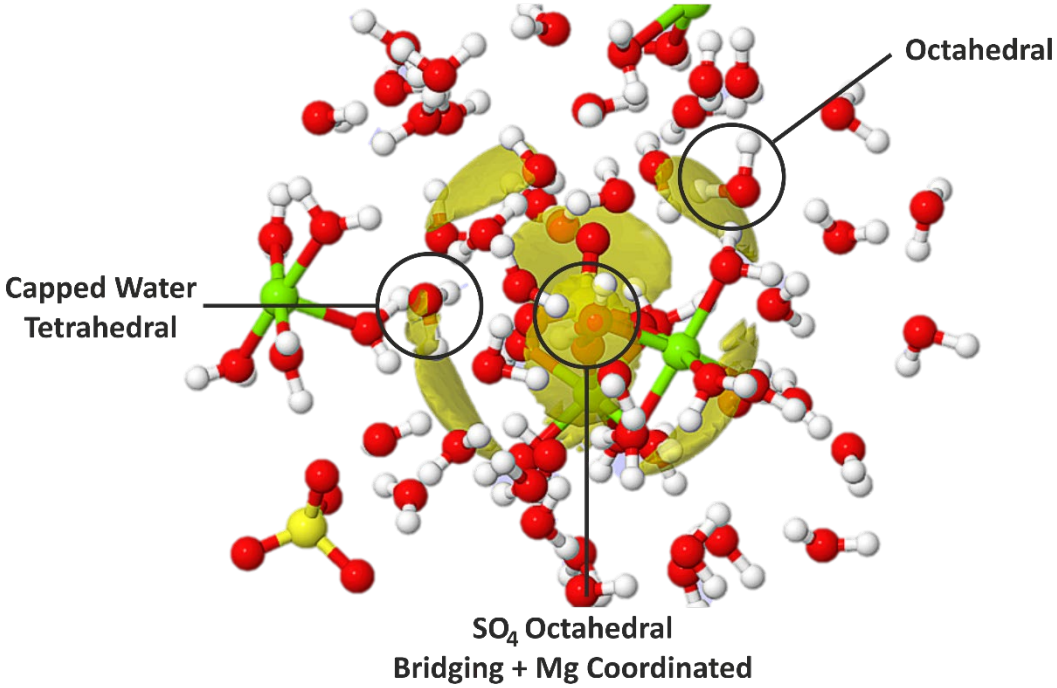

Figure 3-19. *Example of an overlay SDF (SO_4-H_2O @ 10%) with extract of model. Circles highlight examples of common $SO_4^{2-}\cdots H_2O$ interactions.*

Whilst the SDF does give a more visual picture of the water structure around the sulfate ion, one must not forget that the sulfate is, in many cases also coordinated to a magnesium ion and therefore part of the larger cluster system, this will modify the interpretation somewhat. Therefore, this cluster is likely to have an effect on the SO_4-H_2O structure, whether that is a magnesium coordinated water existing in an octahedral position, as seen in figure 3-19, or how the water may act as a hydrogen bonded bridge between the sulfate ion and the magnesium cluster. This influence of the cluster can be shown by the coordination number in figure 3-20, whereby a median coordination of 17 is far higher than the literature values of 8 – 12 for pure aqueous sulfate studies.[47,48,63] This increase in coordination is most likely due to the magnesium sulfate coordination formation, and therefore increases the water surrounding the central ion via the closely coordinated magnesium water ligands. In combination with the cluster formation, an increased water population density forces a much closer alignment of the water to the sulfate, and therefore increasing the coordination between the two species. By *increased water population density*, we are defining the increased water molecules per unit area compared to that of a pure water system. This so-called increase in the water population density and its effects will be discussed within the water structure section.

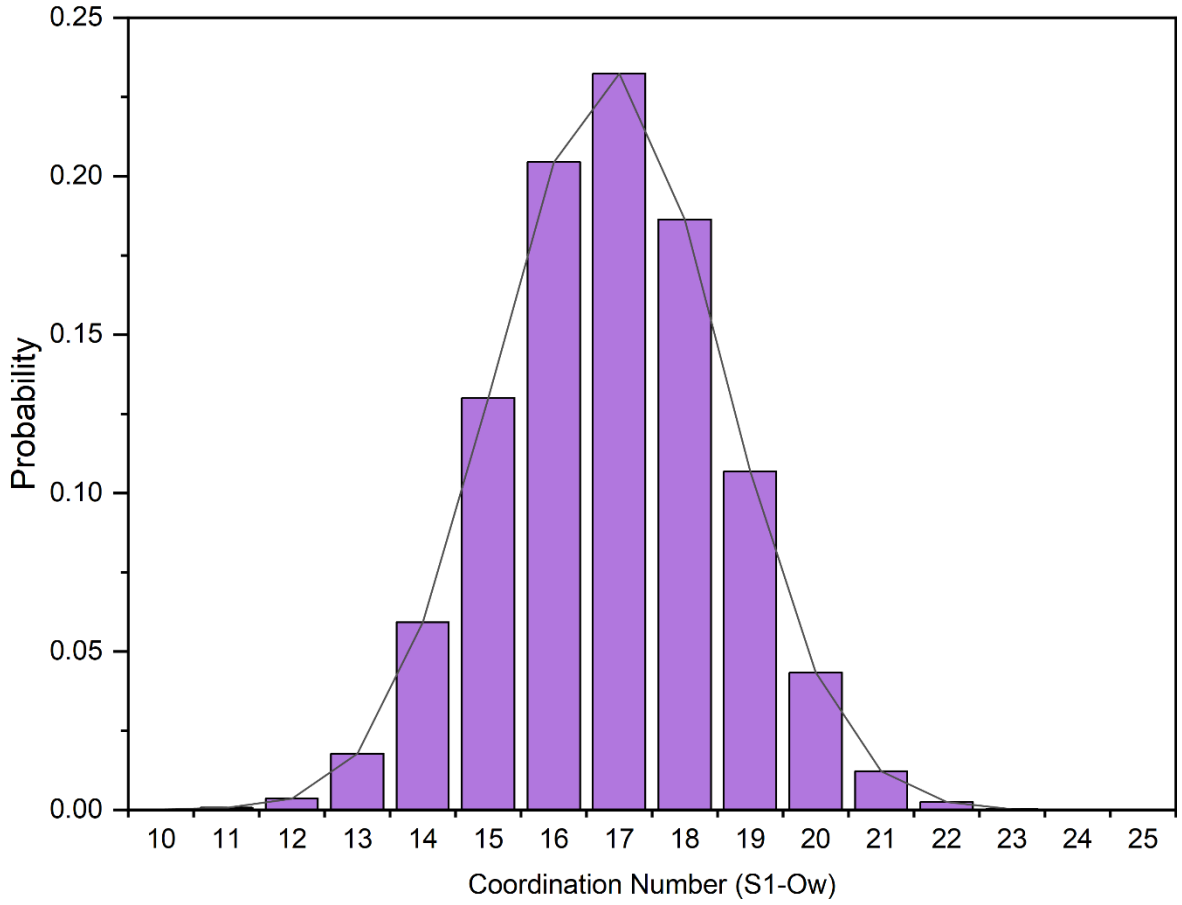

Figure 3-20. *Coordination number S1 – Ow over r = 1.0 – 5.0 Å, showing a largely Gaussian shape.*

Comparing the coordination numbers observed in figure 3-20 to those of other studies in the literature, we generally observe a higher coordination number when considering isolated sulfate but are in better agreement with previous $MgSO_4$ studies.[12,36,44] Firstly comparing to the isolated sulfate studies described previously[46,47], it was found that the SO_4-H_2O coordination that was most energetically favourable ranged between 6 and 14, which is very much at the lower end of the coordination found for our $MgSO_4$ model.[61,63,64] However, many studies have revealed that the coordination number around the sulfur does increase with the introduction of a counterion and these values vary from system to system.[12,36,43,50,54] The most compelling aqueous phase $MgSO_4$ study by Balasubramanian et al. suggest a coordination of 16 at an r range of 5 Å and concentration of 16.4wt%, similar to the 2.00 M system we are examining with an approximate 19.4wt%. Whilst this cannot be a like for like comparison, due to the differing system concentration, one can assume that based on the increasing coordination with increasing concentration displayed by the authors, that we would expect our system to lie slightly above that of the 16.4wt% system. Nevertheless, the coordination of 16 is very similar to the mean coordination of 16.9 derived from our work.

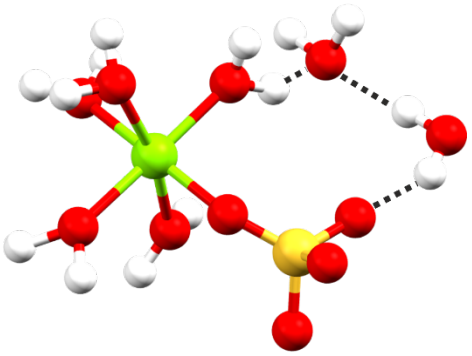

Figure 3-21. *Example of sulfate interacting via both CIP and SSIP from the model directly. Dotted lines denote hydrogen bonding. This demonstrates the overall hybrid nature of this bonding.*

Using the SDF and the coordination number, highly suggests a combination of the CIP and SSI bonding modes available to the sulfate to stabilise the anion. The SDF between the sulfate and water shows how the solvent stabilises the sulfate in solution, allowing for a stable SO_4^{2-} in the water medium. The sulfate is also stabilised by the Mg^{2+} by the CIP interactions discussed extensively in section 3.3.2. However, what is found within the refined model is actually a combination of the two bonding modes. Figure 3-21 shows an extract from the model showing the CIP between the ions and also the hydrogen bond network forming between the magnesium coordination and the sulfate via the water network. This further justifies the increased coordination observed in figure 3-20, where the SO_4^{2-} is stabilised further by the water through the bulk structure and by the interactions with the magnesium structure. The close interactions possible via the CIP brings further water molecules within the range of the coordination number calculation, further explaining the increases found. Overall the SO_4^{2-} stabilisation aligns mostly with previous studies and further justifies the hybrid interactions between the sulfate and other components in the system.

Overall, this study has allowed us to investigate the aqueous sulfate structure in the presence of a magnesium counter ion to elucidate bulk structure via an experimental methodology not previously applied to this system. In particular EPSR has enabled visualisation of the actual structural elements and has revealed a dual octahedral/tetrahedral structural mode between the sulfate ion and the bulk water. This interaction mode is similar to previous sulfate studies but deviates from that found in the higher hydrated species, likely due to the previously discussed magnesium clusters. The interaction between the sulfate and water is likely to both stabilise the ion itself, via charge transfer, as discussed by Kulichenko et al.[46], as well as by the formation of a different hydrogen bond network via the octahedral cluster, which stabilises both the metal and sulfate. This hydrogen bonding network enables interactions between coordinated water, bulk water and sulfate, and results in a more favourable hydrogen bonding mode than discussed in pure sulfate studies. Using an EPSR

methodology has enabled our structural investigation of this under-researched aqueous structure and revealed previously unknown features whilst also forming a strong foundation for further investigation into the aqueous behaviour of $MgSO_4$.

3.3.5 Water Structure

The structure of water has been extensively studied in its pure form, under varying conditions as well as a solvent in aqueous systems, there are thus ample comparison points that can be made between pure water and the bulk water in aqueous $MgSO_4$. Further to this, the previous refinement of pure water as a standard material described in section 2.4.5 allows for a direct comparison using an identical methodology.

Firstly, the H_2O-H_2O RDF comparison between Ow-Ow and Ow-Hw for both pure water and aqueous 2.00 M $MgSO_4$ show similarities in the shapes of both profiles but with subtle differences, suggesting that there is a variation in the bulk water structure. Starting with Ow-Ow in figure 3-23, the shape of the first feature remains relatively constant between the two systems with only a difference of 0.03 Å which is almost certainly within the margin of error. This feature represents the tetragonal water-water interactions arising from the hydrogen bond network which have been fully described in both the literature[1,4,6] and section 2.4.5. However, it is worth noting that another Ow-Ow feature is expected at this distance within the $MgSO_4$ system, and that is the corner to corner O_w coordinated to the central magnesium. Using an average Mg-Ow atom-atom distance of r = 2.07 Å, it is expected the distance between two coordinated Ow at 90° within the magnesium cluster will approximately exist at 2.93 Å, which may explain the slight increase in the correlation distances observed in the Ow-Ow RDF. Beyond approximately r = 3.4 Å it is possible to see a much larger deviation from standard bulk water structure, this is perhaps more obvious using the SDF seen in figure 3-24.

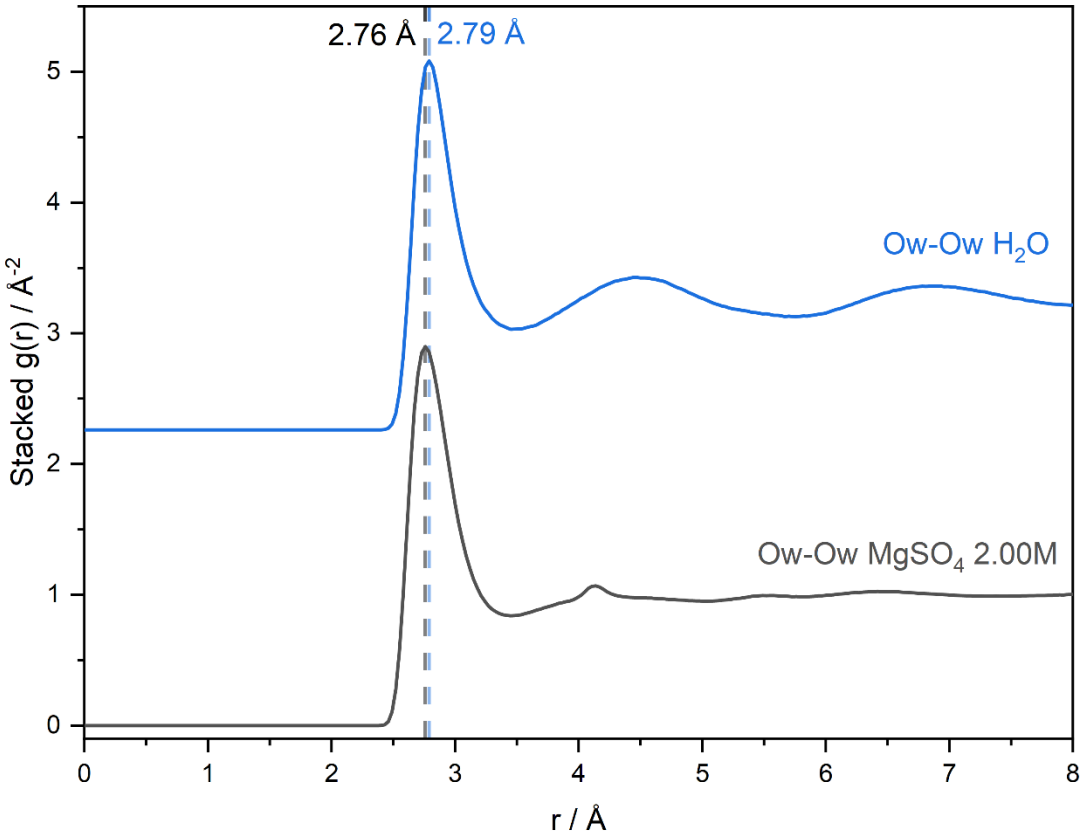

Figure 3-22. *Site-site g(r) calculated comparison for Ow – Ow 2.00M $MgSO_4$ (black) and pure water (blue). Dashed lines denote the 1st shell interactions.*

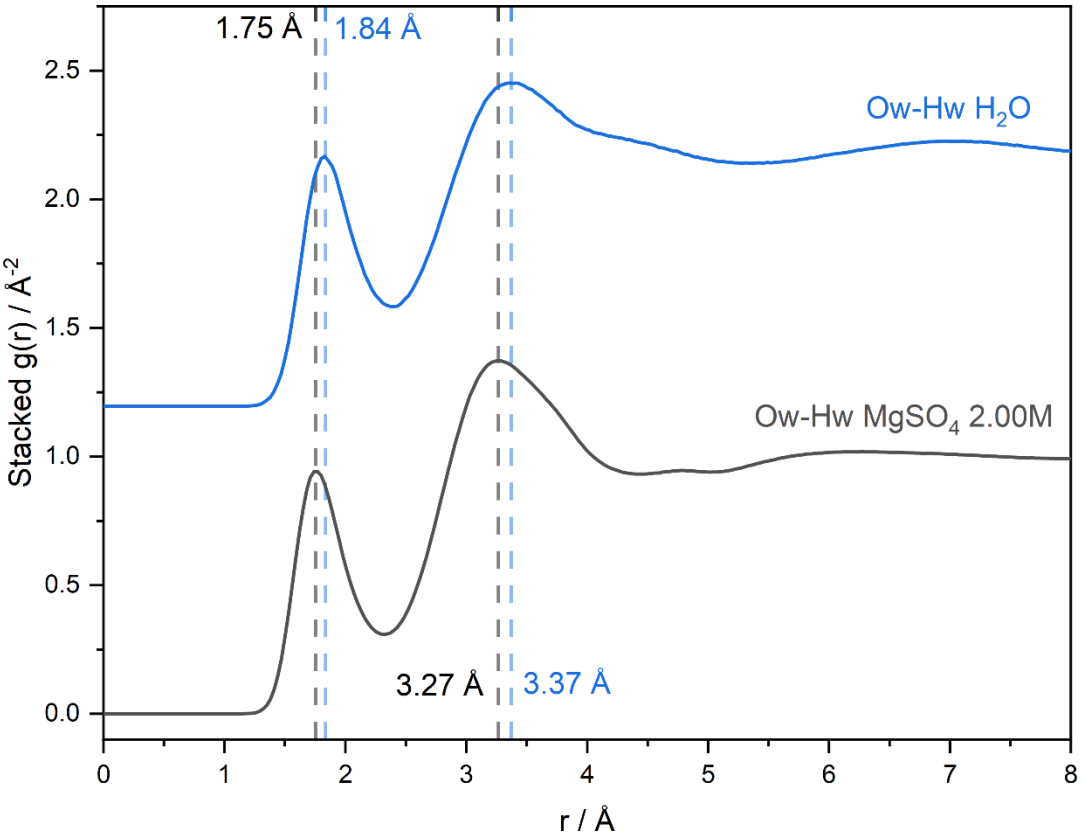

Figure 3-23. *Site-site g(r) calculated comparison for Ow – Ow 2.00M $MgSO_4$ (black) and pure water (blue). Dashed lines denote the 1st and 2nd shell interactions.*

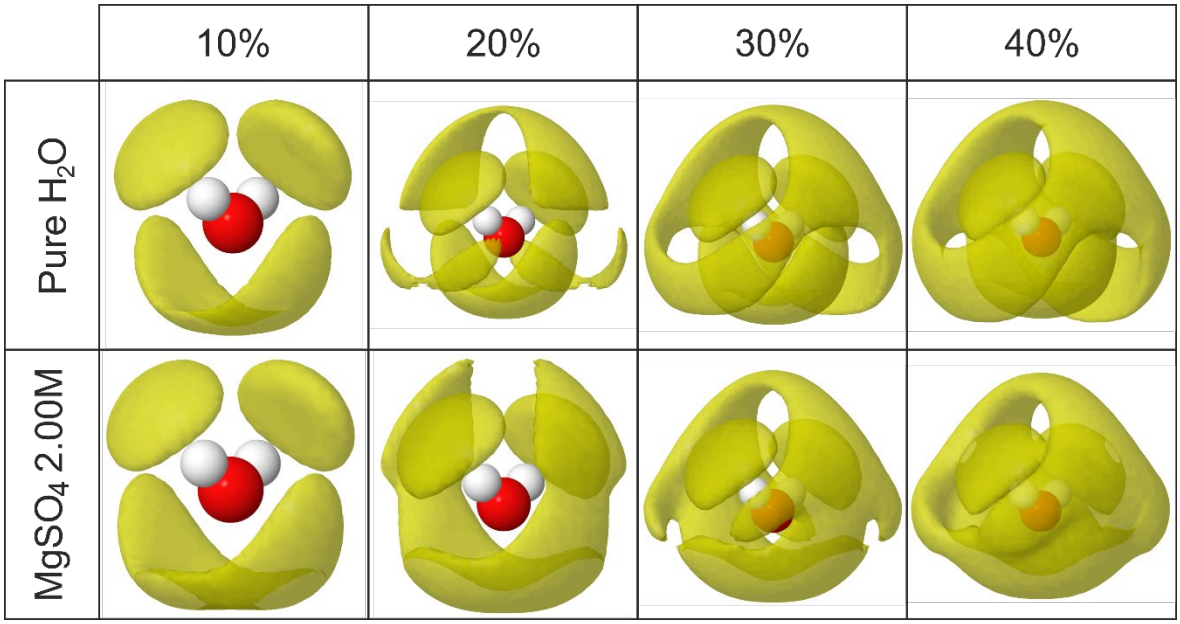

Figure 3-24. *SDF H_2O – H_2O for 2.00 M $MgSO_4$ (top) and pure water (bottom) over r = 1.0 – 5.0 Å and increasing isosurface%, demonstrating the similar 1st shell interactions (10%) that decrease with increasing isosurface.*

From the SDF for both systems, it is obvious that whilst the base tetrahedral structure and phase/anti-phase relationship between successive shells is present for both, the introduction of the ionic species has resulted in some observable differences. Whilst the pure water remains consistent with this trend, and the literature as stated in section 2.4.5, the $MgSO_4$ model is more homogenous in nature and starts to show more commonality with the compressed water structures found in the literature.[12,65,66] This is particularly obvious at higher populations where the density becomes more homogenous and it becomes more difficult to differentiate between the first and second solvation shell structures, in itself suggesting a compression of the second shell upon the first and ultimately the origin. At lower population densities, particularly at 10%, there is only a small deviation from the standard 4-coordinate structure centred above the O-H bond and the lone pairs of the oxygen, this implies that the direct H_2O-H_2O interactions at the first solvation shell remain consistent. This hypothesis is further corroborated with the Ow-Ow RDF, whereby the first feature remains consistent for both systems and as this represents this first shell. Overall, the first solvation shell for bulk water remains fairly consistent despite the introduction of ionic species.

The second solvation shell is more disrupted than the first, as seen by both the lack of longer-range features found in the RDF as well as the disruption to the densities found in the SDF. The Ow···Ow RDF for $MgSO_4$ effectively tends to zero beyond r = 5.0 Å, suggesting a lack of longer-range order which can be observed in the pure water systems with oscillations centred on approximately r = 4.5 and 6.9 Å respectively. The lack of these oscillations in the $MgSO_4$ Ow···Ow ultimately suggests that the ionic structures that have formed, as discussed in section 3.3.1, disrupt the longer-range order typically found in a pure water system. The Ow···Hw RDF further suggests this large disruption to the bulk water, with little observable features beyond 4.0 Å. This feature also

appears 0.1 Å closer than that of the pure water, this suggests that the second shell may be observed at a shorter correlation distance compared to a pure water system. One must not forget that this corelation range will also include inter-cluster water species, and whilst this will only account for a small percentage of water interactions, approximately 20% assuming an average cluster of $MgSO_4(H_2O)_5$, this will ultimately influence the structural features observed. However, as the majority of the water will be within the bulk phase, the majority of the scattering will be come from this and not from the inter-cluster interactions. To investigate further, it is possible to compare the coordination numbers between the two situations.

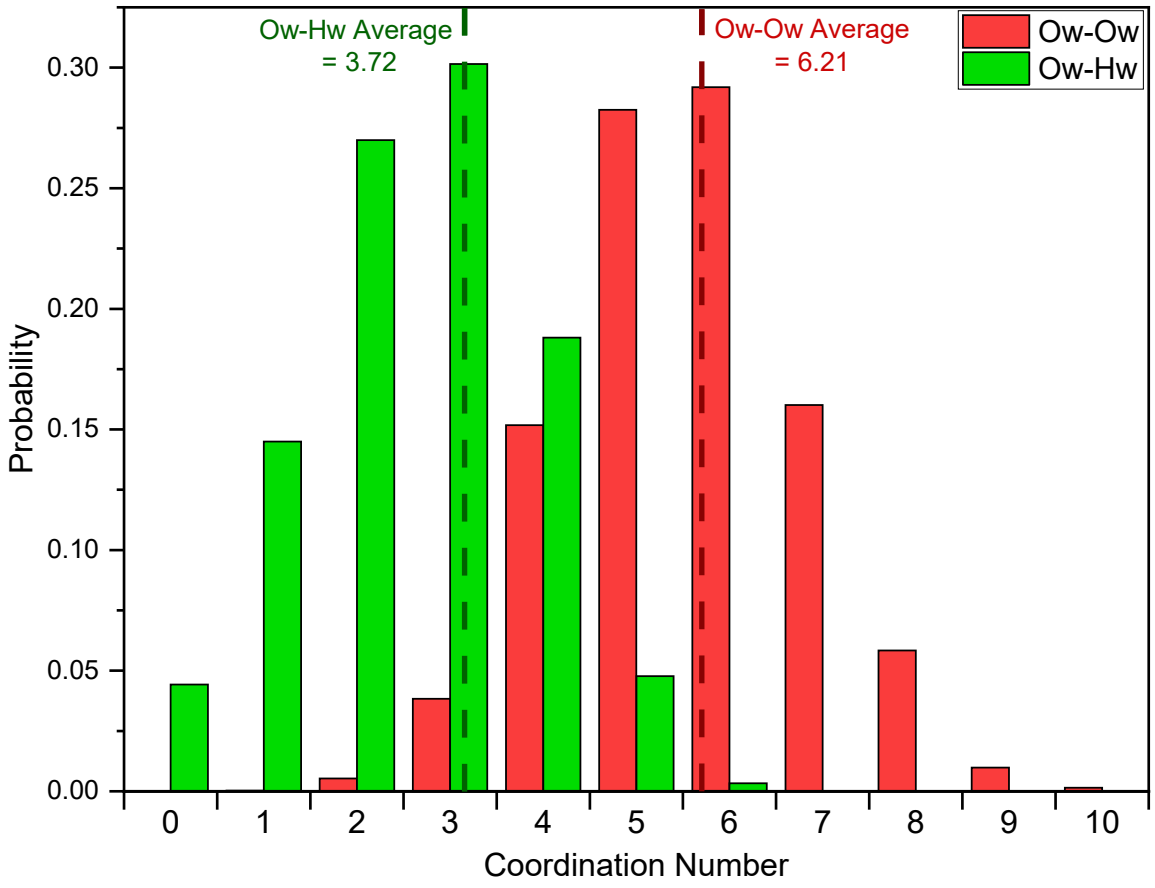

Figure 3-25. *Coordination number of Ow – Ow (red) and Ow – Hw (green) in 2.00M $MgSO_4$ for distance range r = 1.0 – 3.4 Å and r = 1.0 – 2.5 Å respectively. Dashed lines denote the average coordination number.*

Comparison of the coordination numbers between the water in pure water and in 2.00 M $MgSO_4$, summarised in table 3-6, reveals a dramatic increase in the $H_2O\cdots H_2O$ coordination within the same distance range. This suggests a denser water population around the origin water molecule, likely mediated by the ionic structure evolving within the system. Whilst the hydrogen bond network is likely to be curtailed, it is still existent within the sample, however its role changes to accommodate the ionic structure. Similarities between the aqueous $MgSO_4$ and pure water SDF still exist, suggesting that the typical hydrogen bond network exists in a similar format, but is diminished and altered, similar to previous aqueous phase EPSR studies.[12] The authors here discuss the similarities

of the water structure and ionic water structure, whereby the aqueous perchlorate shows more similarities to water under pressure than it does to pure water in ambient conditions. We can observe something similar here, perhaps to less of an extreme, but it is a likely similar scenario occurs for both systems. Further to this, the increase in coordination number in both systems compared to pure water really emphasises this 'compression' of the water structure, leading to a conclusion that the introduction of ions to an aqueous system causes a denser water population compared to its pure form.

Table 3-6. *Coordination number comparison between bulk water in aqueous $MgSO_4$ and pure H_2O found in section 2.4.5.*

	Average Coordination	
	Ow – Ow (r = 1 – 3.4 Å)	Ow – Hw (r = 1 – 2.5 Å)
$MgSO_4$ 2.00 M	6.21	3.72
Pure H_2O (Figure 2-22)	4.86	3.30

The disruption to the well-defined hydrogen bond network of bulk water observed can therefore be attributed to three main factors: the introduction of the metal cluster structure that disrupts the long-range bulk structure, the water coordinating to the magnesium, reducing the relative proportion of bulk solvent and then the participation of bulk water in hydrogen bonding to stabilise the sulfate ion, as discussed in section 3.3.4. The use of water for stabilisation of such a structure also elucidates some of the physical properties observed for such aqueous systems, such as its high solubility, which without the stabilisation of via hydrogen bonding would not be possible. This is truly highlighted when examining solubility tables, whereby most if not all salts containing NO_3^-, ClO_4^-, X^- (halide ion), SO_4^{2-} or NH_4^+ are soluble to some extent, with the common theme of all being the possibility of hydrogen bonding (or halide, where applicable).[13,67] The full aqueous structure of most of these salts are unknown, so confirmation of the hydrogen bond structure mediating the solubility is purely a hypothesis but provides a multitude of potential samples for future aqueous studies.

3.4 Conclusion

Using an EPSR dual X-ray/neutron refinement approach, it has been possible to elucidate the magnesium, sulfate and water environments in this aqueous salt. From this it has been possible to extract a multitude of structural features related to each species present. It was possible to observe the structure of the magnesium clusters via CIP interactions and determine that the $Mg(SO_4)_x(H_2O)_y$ clusters are the primary building units. From this, investigation of the sulfate ion and how it interacts with the bulk water was conducted and revealed that the sulfate-water behaves in a similar way to other $MgSO_4$ systems with regards to both the RDF and the coordination numbers observed. What is unique to this study was the clarification of the interaction modes present between the two entities. This led to observation of distinct interaction modes, the octahedral bridging mode and tetrahedral linear mode, and whilst the bridging mode is common in the isolated sulfate studies, the linear mode had not been previously observed. Whilst these interactions incorporate both inter-cluster and sulfate-water interactions, the majority are with the bulk water, demonstrating how the charge of the sulfate is stabilised by both the oppositely charged magnesium but also via the solvent structure. The interaction between the sulfate, the full cluster and the bulk water does disrupt the well-defined water hydrogen bond network by hindering the longer-range interactions and ultimately compressing the water structure, a phenomenon previously observed in the literature.[12] This work forms the basis for much further work on both this system as well as other ionic, aqueous systems.

References

1 A. K. Soper, *Mol. Phys.*, 2001, **99**, 1503–1516.

2 M. G. Tucker, M. T. Dove, A. L. Goodwin, D. A. Keen and H. Y. Playford, *RMCProfile Manual*, .

3 D. A. Keen, M. G. Tucker and M. T. Dove, *J. Phys.: Condens. Matter*, 2005, **17**, S15–S22.

4 A. Soper, *Water and ice structure in the range 220 - 365K from radiation total scattering experiments*, 2014, vol. 187.

5 A. H. Narten, W. E. Thiessen and L. Blum, *Science*, 1982, **217**, 1033–1034.

6 A. K. Soper, *ISRN Phys. Chem.*, 2013, **2013**, 279463.

7 A. K. Soper and M. A. Ricci, *Phys. Rev. Lett.*, 2000, **84**, 2881–2884.

8 T. F. Headen, *Mol. Phys.*, 2019, **117**, 3329–3336.

9 N. Basma, P. L. Cullen, A. J. Clancy, M. S. P. Shaffer, N. T. Skipper, T. F. Headen and C. A. Howard, *Mol. Phys.*, 2019, **117**, 3353–3363.

10 S. Lenton, N. H. Rhys, J. J. Towey, A. K. Soper and L. Dougan, *J. Phys. Chem. B*, 2018, **122**, 7884–7894.

11 O. S. Hammond, D. T. Bowron and K. J. Edler, *ACS Sustainable Chem. Eng.*, 2019, **7**, 4932–4940.

12 S. Lenton, N. H. Rhys, J. J. Towey, A. K. Soper and L. Dougan, *Nat. Commun.*, 2017, **8**, 919.

13 P. W. Atkins and Julio. De Paula, *Atkins' Physical chemistry*, 2014.

14 K. Kasahara, Y. Takimoto, R. Ashida and T. Takahashi, *Molecular Simulation*, 2020, **46**, 83–91.

15 S. V. Sambasivarao and O. Acevedo, *J. Chem. Theory Comput.*, 2009, **5**, 1038–1050.

16 Y. Liu and T. Ichiye, *J. Phys. Chem.*, 1996, **100**, 2723–2730.

17 M. W. Mahoney and W. L. Jorgensen, *J. Chem. Phys.*, 2000, **112**, 8910–8922.

18 J. E. Jones, *Proc R Soc Lond A Math Phys Sci*, 1924, **106**, 463–477.

19 Soper, A.K., *Empirical Potential Structure Refinement: A User's Guide*, ISIS, Oxford, 26th edn., 2019.

20 D. A. Keen, *Crystallogr. Rev.*, 2020, **26**, 143–201.

21 J.-L. Calais, *Int. J. Quantum Chem.*, 1990, **38**, 497–497.

22 I. M. Svishchev and P. G. Kusalik, *J. Chem. Phys.*, 1993, **99**, 3049–3058.

23 D. F. Shriver, M. T. Weller, T. Overton, J. Rourke and F. A. Armstrong, *Inorganic chemistry.*, 2014.

24 M. Senbayram, A. Gransee, V. Wahle and H. Thiel, *Crop Pasture Sci.*, 2015, **66**, 1219–1229.

25 V. M. van Essen, H. A. Zondag, J. C. Gores, L. P. J. Bleijendaal, M. Bakker, R. Schuitema, W. G. J. van Helden, Z. He and C. C. M. Rindt, *J. Sol. Energy Eng.*, , DOI:10.1115/1.4000275.

26 M. Blitz, S. Blitz, R. Hughes, B. Diner, R. Beasley, J. Knopp and B. H. Rowe, *Chest*, 2005, **128**, 337–344.

27 L. Duley, A. M. Gülmezoglu, D. J. Henderson-Smart and D. Chou, *Cochrane Database Syst. Rev*, 2010, **2010**, CD000025–CD000025.

28 T. O. Idama and S. W. Lindow, *J. Obstet. Gynaecol.*, 1998, **105**, 260–268.

29 H. Huai. Ting and W. L. McCabe, *Ind. Eng. Chem.*, 1934, **26**, 1207–1208.

30 R. C. Phutela and K. S. Pitzer, *J. Phys. Chem.*, 1986, **90**, 895–901.

31 G. Ferraris, D. Jones and J. Yerkess, *J. Chem. Soc., Dalton Trans.*, , DOI:10.1039/dt9730000816.

32 P. J. Rentzeperis and C. T. Soldatos, *Acta Crystallogr.*, 1958, **11**, 686–688.

33 A. D. Fortes, I. G. Wood, L. Vočadlo, H. E. A. Brand and K. S. Knight, *J. Appl. Crystallogr.*, 2007, **40**, 761–770.

34 F. E. Genceli, M. Lutz, A. L. Spek and G.-J. Witkamp, *Cryst. Growth Des.*, 2007, **7**, 2460–2466.

35 W. H. Baur, *Acta Crystallogr.*, 1964, **17**, 1361–1369.

36 G. Balasubramanian, S. Murad, R. Kappiyoor and I. K. Puri, *Chem. Phys. Lett.*, 2011, **508**, 38–42.

37 I. M. Abdulagatov, N. D. Azizov and A. B. Zeinalova, *Phys. Chem. Liq.*, 2007, **45**, 127–148.

38 R. A. Horne and D. S. Johnson, *J. Chem. Phys.*, 1966, **44**, 2946–2950.

39 E. Iype, S. V. Nedea, C. C. M. Rindt, A. A. van Steenhoven, H. A. Zondag and A. P. J. Jansen, *J. Phys. Chem. C*, 2012, **116**, 18584–18590.

40 W. H. Baur, *Acta Crystallogr.*, 1964, **17**, 1361–1369.

41 F. Corà and C. R. A. Catlow, *J. Phys. Chem. B*, 2001, **105**, 10278–10281.

42 R. Buchner, T. Chen and G. Hefter, *J. Phys. Chem. B*, 2004, **108**, 2365–2375.

43 W. W. Rudolph, G. Irmer and G. T. Hefter, *Phys. Chem. Chem. Phys.*, 2003, **5**, 5253–5261.

44 X. Zhang, Y. Zhang and Q. Li, *J. Mol. Struct.: Theochem*, 2002, **594**, 19–30.

45 S. I. Mamatkulov, K. F. Rinne, R. Buchner, R. R. Netz and D. J. Bonthuis, *J. Chem. Phys.*, 2018, **148**, 222812.

46 M. Kulichenko, N. Fedik, K. V. Bozhenko and A. I. Boldyrev, *J. Phys. Chem. B*, 2019, **123**, 4065–4069.

47 L. C. Smeeton, J. D. Farrell, M. T. Oakley, D. J. Wales and R. L. Johnston, *J. Chem. Theory Comput.*, 2015, **11**, 2377–2384.

48 X.-B. Wang, A. P. Sergeeva, J. Yang, X.-P. Xing, A. I. Boldyrev and L.-S. Wang, *J. Phys. Chem. A*, 2009, **113**, 5567–5576.

49 R. P. Matthews and K. J. Naidoo, *J. Phys. Chem. B*, 2010, **114**, 7286–7293.

50 C.-C. Wang, M. Wang, H.-Q. Cai, Q.-W. Zhang, Y.-Y. Li and H.-B. Yi, *J. Mol. Liq.*, 2019, **278**, 33–42.

51 A. K. Soper, *GudrunN and GudrunX*, ISIS, Oxford, ISIS, Oxford, 2012.

52 M. Ríos-López, J. G. Mendez-Bermúdez and H. Domínguez, *J. Phys. Chem. B*, 2018, **122**, 4558–4565.

53 E. Wernersson and P. Jungwirth, *J. Chem. Theory Comput.*, 2010, **6**, 3233–3240.

54 F. Sebastiani, A. V. Verde, M. Heyden, G. Schwaab and M. Havenith, *Phys. Chem. Chem. Phys.*, 2020, **22**, 12140–12153.

55 A. Zalkin, H. Ruben and D. H. Templeton, *Acta Crystallogr.*, 1964, **17**, 235–240.

56 A. R. Davis and B. G. Oliver, *J. Phys. Chem.*, 1973, **77**, 1315–1316.

57 H.-J. Li, D. Yan, H.-Q. Cai, H.-B. Yi, X.-B. Min and F.-F. Xia, *Phys. Chem. Chem. Phys.*, 2017, **19**, 11390–11403.

58 M. Fernández, J. Klapp, L. D. G. Sigalotti and F. Ruette, *Chem. Phys. Lett.*, 2018, **713**, 39–45.

59 K. J. Gaffney, M. Ji, M. Odelius, S. Park and Z. Sun, *Chem. Phys. Lett.*, 2011, **504**, 1–6.

60 C. Schmidt and C.E. Manning, *Geochem. Perspect. Lett.*, 2016, **3**, 66–74.

61 B. Gao and Z. Liu, *J. Chem. Phys.*, 2004, **121**, 8299–8306.

62 H. Knorke, H. Li, J. Warneke, Z.-F. Liu and K. R. Asmis, *Phys. Chem. Chem. Phys.*, 2020, **22**, 27732–27745.

63 V. Vchirawongkwin, B. M. Rode and I. Persson, *J. Phys. Chem. B*, 2007, **111**, 4150–4155.

64 Hitoshi. Ohtaki and Tamas. Radnai, *Chem. Rev.*, 1993, **93**, 1157–1204.

65 K. Amann-Winkel, M.-C. Bellissent-Funel, L. E. Bove, T. Loerting, A. Nilsson, A. Paciaroni, D. Schlesinger and L. Skinner, *Chem. Rev.*, 2016, **116**, 7570–7589.

66 L. B. Skinner, C. J. Benmore, J. C. Neuefeind and J. B. Parise, *J. Chem. Phys.*, 2014, **141**, 214507.

67 Pradyot. Patnaik, *Handbook of inorganic chemicals*, McGraw-Hill, New York, 2003.

Appendix A Parameters for Auxiliary Routines

A.1.1 Coordination Number

Atom 1	Atom 2	Min Distance	Max Distance
System Interactions			
Ow	Ow	1	10
Ow	Mg1	1	2.5
Mg1	Ow	1	2.5
Ow	S1	1	5
S1	Ow	1	5
Mg1	Mg1	1	10
Mg1	S1	1	6
S1	Mg1	1	6
Mg1	O1	1	2.5
O1	Mg1	1	2.5
S1	S1	1	10
O1	Hw	1	4
S1	Hw	1	5
O1	Ow	1	4
S1	Ow	1	5
Hydrogen Bonding			
Ow	Ow	1	3.4
Ow	Hw	1	2.5

A.1.2 Triangles/Bond Angles

nsize	180
atom-c	*
atom-z	*
atom-r	*
ndist	3

	ndist1	**ndist2**	**ndist3**
atom 1	Ow	Ow	O1
atom 2	Mg1	Mg1	Mg1
atom 3	Ow	O1	O1
ltype	1	1	1
rmin12	1	1	1
rmax12	2.4	2.4	2.4
rmin23	1	1	1
rmax23	2.4	2.4	2.4
rminrmaxc	1 2	1 2	1 2

A.1.3 SDF/SHARM

File Name	SO4-H2O	H2O-H2O	SO4-Mg	H2O-Mg
Species 1	SO4	H2O	O1	Ow
Species 2	H2O	H2O	Mg1	Mg
l1	0 1 2 3 4	0 1 2 3 4	0 1 2 3 4 5 6	0 1 2 3 4 5 6
l2	0 1 2 3 4	0 1 2 3 4	0	0
l3	0 1 2 3 4	0 1 2 3 4	0 1 2 3 4 5 6	0 1 2 3 4 5 6
n1	3	2	2	2
n2	2	2	0	0
atom-c	S1 O1 O1 O1 O1	Ow Hw Hw	O1	Ow
axisc1	z 2	z 2 3	z 2 3	z 2 3
axisc2	y 3	x 2	y 2	y 2
atom-s	Ow Hw Hw	Ow Hw Hw	Mg1	Mg1
axiss1	z 2 3	z 2 3	z	z
axiss2	x 2	x 2	y	y

Chapter 4 The Structure of 2.00 M $MgSO_4$ as a Function of Temperature

This chapter discusses the use of X-ray exclusive EPSR refinements of magnesium sulfate over a range of temperatures 274K, 298K & 343K. The aim is to understand the thermal effects on a 'standard' 2.00M solution and whether any of the structural features alter significantly as a result. This is a crucial step before going on to potentially use temperature as a way of controlling concentration as discussed in chapter 5.

Initially, a comparison of the dual X-ray/neutron with the X-ray only EPSR refinements allow for the feasibility of both X-ray only refinements but also confirming that the cryostream setup has minimal effects on the data and elucidated structure. By evaluating this approach not only does it validate the cryostream setup but also the use of X-ray only data for illuminating aqueous structure of both this system and future systems.

Upon validating this approach, investigating the structure over the temperature range stated will allow for a full understanding of the variations in local structure at both lower (near freezing point for pure water) and higher temperatures compared to the previous ambient structures. This allows for a deeper understanding of the cluster formation and will illuminate how the increased thermal energy affects the prenucleation structure. Using a similar methodology of analysis of the scattering data, auxiliary routines and probing the refined model, it is possible to compare both the temperature series solely but draw comparisons between the dual setup of chapter 3 and the X-ray only data.

4.1 Introduction to Variable Temperature Studies

Temperature is one of the key variable parameters to consider when investigating the structure of aqueous solutions as it is intimately linked with concentration and the total energy available to the system. In chapter 5, temperature will be required to increase the solubility and allow access to higher concentration solutions – it is therefore critical to investigate the effects of temperature alone on a fixed concentration. This will be done by comparing the solution structures at various temperatures.

4.1.1 Variable Temperature Studies

As discussed in previous chapters, EPSR is a relatively under-utilised technique for structural refinements, and this is even more apparent with respect to temperature studies. The most prominent of such studies are the structure of water in solid and liquid states, described by Soper[1], which examines the structure through phases. Other smaller scale studies involving species such as benzene[2], and 1-proanol[3] have been conducted utilising both X-ray and neutron scattering. These systems are relatively simple, being a single molecule type and further highlights the limited temperature studies available using an EPSR approach. Therefore, using an in-house setup it was possible to conduct variable temperature experiments on an ionic solution and extract meaningful models, showing the further scope available to solution structure.

4.1.2 Experimental Conditions

To enable collection of non-ambient temperature data an Oxford Cryosystems Cryostream 700 was installed to enable both heating and cooling of the capillary. Although heating with an open gas flow is not optimal for a uniform temperature across the length of the capillary (it disrupts the gas flow), it was assumed that the volume at which the X-ray beam focuses was at the set temperature - however, this does not preclude the possibility of convection currents forming. Ideally a cell setup with uniform heating and a thermocouple, such as the hydrothermal cell setup at I15-1, would have been better – but was unavailable. In contrast to our previous $MgSO_4$ studies, that used both X-ray and neutron data, only X-ray scattering data were collected.

4.1.2.1 X-ray Scattering Experiments

A sample of anhydrous magnesium sulfate was acquired from Sigma-Aldrich and 2.40 g was dissolved in 10 mL of deionised water to form a 2.00 M solution. The sample was introduced into a 2.0 mm borosilicate capillary purchased from Capillary Tubes Supplies Ltd. The capillary was mounted on the diffractometer and the Cryostream set at 274 K and ran for approximately 10 minutes to ensure the capillary had reached a stable temperature. The sample was run for a

total exposure time of 180 minutes with an exposure of 127 s/° oscillation. Data for the empty capillary and empty diffractometer were also collected utilising the same parameters to obtain container and empty scattering data sets. This setup was repeated at both 298 K and 343 K to create a temperature series over which any effects on the structure could be investigated. The same sample capillary was used for all measurements to ensure consistency throughout. The data sets were processed in GudrunX[4], using a sample composition of $MgSO_4 \cdot 27.75H_2O$ and number density 0.1074 atoms/Å^3 and other parameters adjusted to obtain the reduced total scattering function F(Q). Whilst the density, and therefore number density, of water does vary with temperature, the difference was deemed to be negligible and was not changed with temperature. However, temperature is included in the EPSR refinement to account for subtle changes. The total scattering structure function F(Q) and derived f(r) for the temperature series can be found in section 4.3. However, prior to examining the function over temperature, a comparison will be made between the X-ray only scattering and dual X-ray/neutron data found in chapter 3.

4.2 Comparison of X-ray Only to Combined X-ray/Neutron Data

To assess the validity of an X-ray only data approach it will be compared directly to the dual X-ray/neutron refinement, comparing the raw scattering data to examine changes that may be induced by the cryo-setup but more significantly any differences resulting from a model based on single and dual data sets respectively. Whilst we expect the raw data to exhibit minimal differences as they are effectively measured at the same temperature, the refined model may show small differences due to the complementary neutron data acting as an additional restraint.

In this section an examination of the experimental F(Q) data will be made to rule out any unexpected issues arising from use of a Cryostream, followed by comparison of the calculated F(Q) and derived f(r) from the EPSR refinement - this will allow an informed assessment of the effect on the final model of X-ray only data.

4.2.1 Comparing the Experimental X-ray 298K and RTP Scattering

To start, we will compare the experimental F(Q), figure 4-1, this will give the first indications of any effects of the temperature control. The inset highlights the low-Q doublet feature which have, in chapter 3, been attributed to the Ow-Ow intermolecular structure and Mg-O cluster structure respectively. The alterations in the general shape of this doublet feature does suggest a minor alteration but could be affected by a variety of factors ranging from the environmental changes between experiments, data processing slight changes to account for temperature and slight changes in the sample itself.

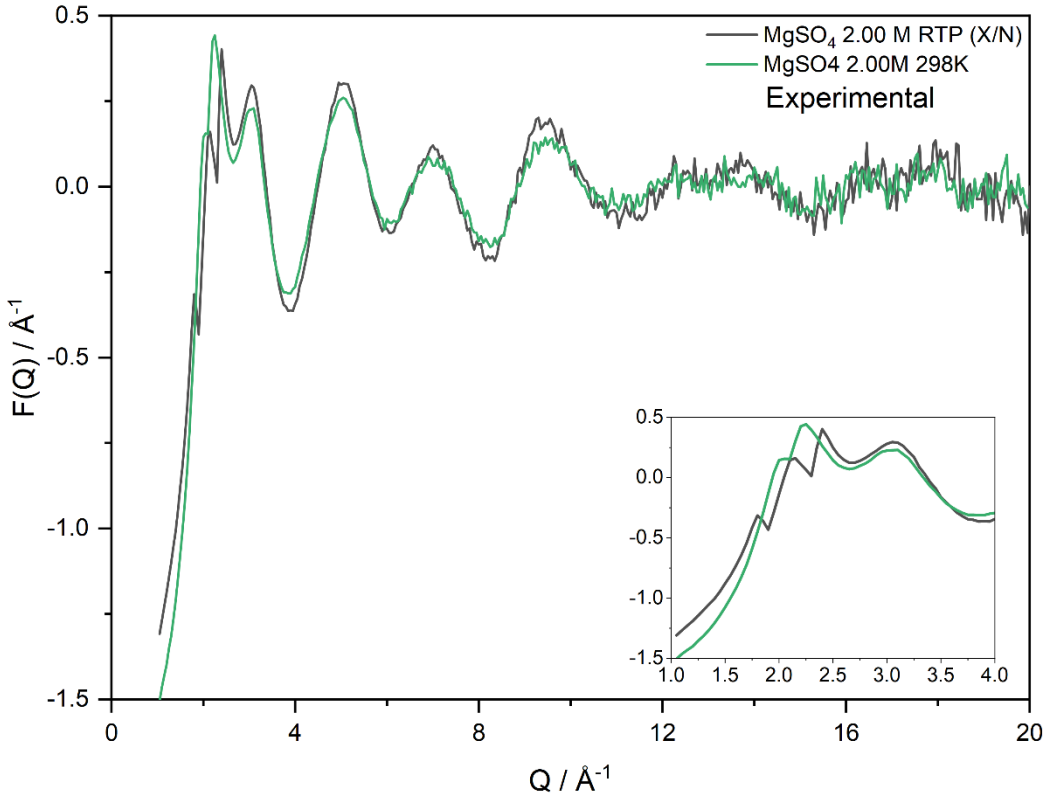

Figure 4-1. *Comparison of the experimental F(Q) scattering for 2.00M $MgSO_4$, where the black line demonstrates the RTP scattering used for the refinement in chapter 3 and the green line shows the scattering of 298K cryo-controlled setup. An inset is included to highlight the low Q region.*

As discussed in previous chapters, visually examining the F(Q) is difficult and it is far more intuitive to examine the real-space function. Figure 4-2 highlights the slight differences observed in the real space function f(r) derived mostly from the feature observed between Q = 1.0 – 4.0 $Å^{-1}$ in reciprocal space.

The experimental f(r) shown below, derived from the F(Q) found in figure 4-2, demonstrates that peak positions are the same for both experiments, as would be expected, as the atom separations are the same in both cases. Peak magnitudes do, however, vary in a more significant manner, which can be attributed to thermal motion (peak widths) and coordination number (peak area). Feature (a) of figure 4-2 describes the S-O sulfate feature, and as can be seen the magnitude is reduced by approximately 0.25 $Å^{-1}$, suggesting a lower coordination number (which is unlikely for identically concentrated samples) that must be attributed to propagating from another source, such as the background or data collection. A likely scenario is that the temperature control and subsequent data processing causes an alteration to the peak area, leading to an artificially decreased magnitude. This is unlikely to cause an issue in the refinement itself, where this peak area is representative of the total S-O coordination and therefore relative concentration of sulfate in the refinable box model, and therefore circumvents this issue.

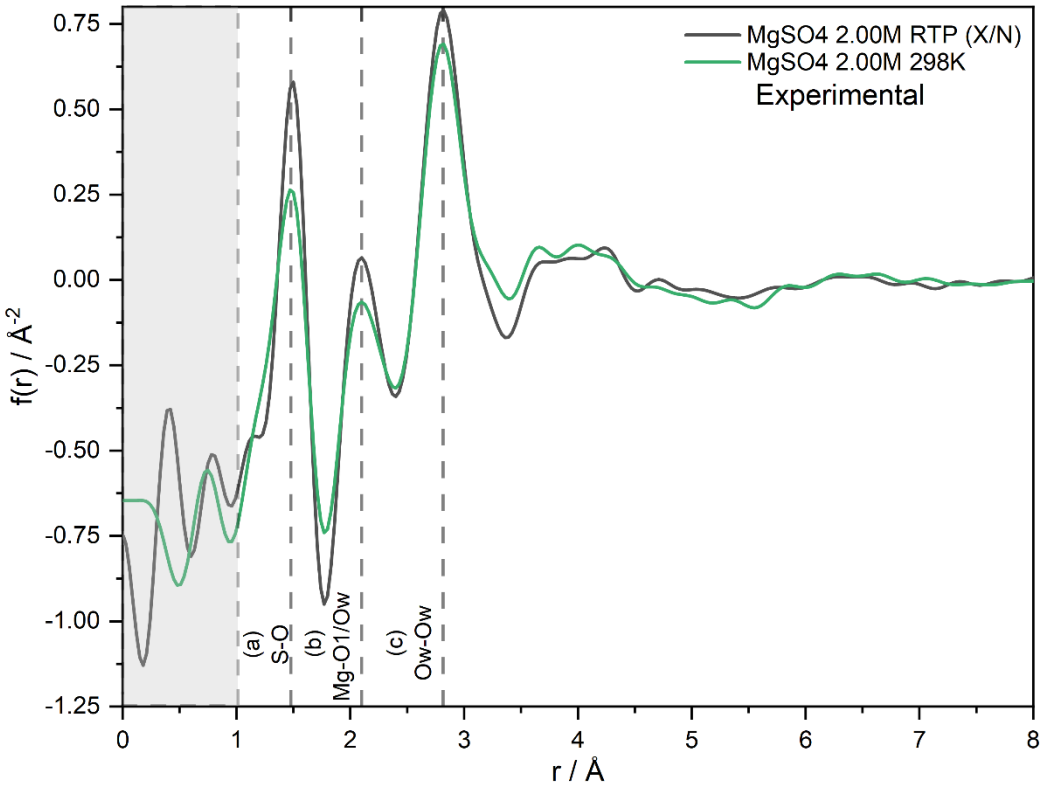

Figure 4-2. *Comparison of the f(r) for 2.00M MgSO4, where the black line represents the RTP data used for the refinement in chapter 3 and the green line shows the data of 298K cryo-controlled experiment. Key structural features have been labelled: (a) intramolecular S-O (sulfate),(b) intramolecular Mg-O (cluster) and (c) intermolecular Ow···Ow. Greyed out area represents data to be disregarded due to the fundamental limitations of PDFs.*

A similar narrative can be constructed for features (b) and (c), suggesting that the temperature control and subsequent processing may influence the overall magnitude of the resulting PDF. The differences found in feature (a) represents an inconsistency within the data reduction of temperature-controlled studies. Due to the weaker scattering of an in-house instrument compared to that of a traditionally used synchrotron source, this is likely to propagate in issues with the data reduction. Further studies should be conducted into the effects of temperature on the data and ways to circumvent these issues in other systems, however this is beyond the scope and time frame of this project.

Overall, it can be confirmed with confidence from both the experimental F(Q) and f(r) that the changes observed between ambient and cryocooled experiments are negligible. Therefore, one can confidently state that the cryostream has no effect on the sample and that any change in data is purely due to the change in energetics by altering the temperature and not due to the experimental setup.

4.2.2 Comparing the RTP X-ray/Neutron Refined and 298K X-ray Only Refined Models

In this section the quality of the X-ray only derived model will be determined by comparison to the dual X-ray/neutron derived model. This will not only allow for the comparison of the effects of the

cryostream setup on the model derived, but also an initial examination on whether X-ray only data can extract a meaningful and consistent model.

4.2.2.1 Comparing the Calculated Models

Starting with the calculated model itself, being able to compare both the calculated F(Q) and derived f(r), as seen in figure 4-1 and figure 4-2, it will be possible to understand the effects a reduced set of observations will have on the final model.

The calculated F(Q) found in figure 4-3 shows a remarkable similarity between the dual and X-ray only refinements suggesting that the combination of just the reference potentials and X-ray data is suitable to obtain a consistent model. For the most part, the refined models agree for the full Q-range expect for the feature at Q = 2.20 $Å^{-1}$, where the dual refinement shows to two separate features. This region is often home to the intermolecular water interactions, and therefore it is not surprising that the X-ray data has a poorer resolution with respect to this species. Often neutron scattering is utilised for the examination of aqueous systems due to its sensitivity to both water, hydrogen, and its isotopes whereas X-rays are more sensitive to the heavier scattering species. Neutrons can therefore model the position of the hydrogen, and its isotopes, to allow for confidence in the central oxygen position. Whilst X-rays are capable of determining the oxygen position solely, it cannot reliably determine the hydrogen position, leading to more ambiguity when compared to neutron data.

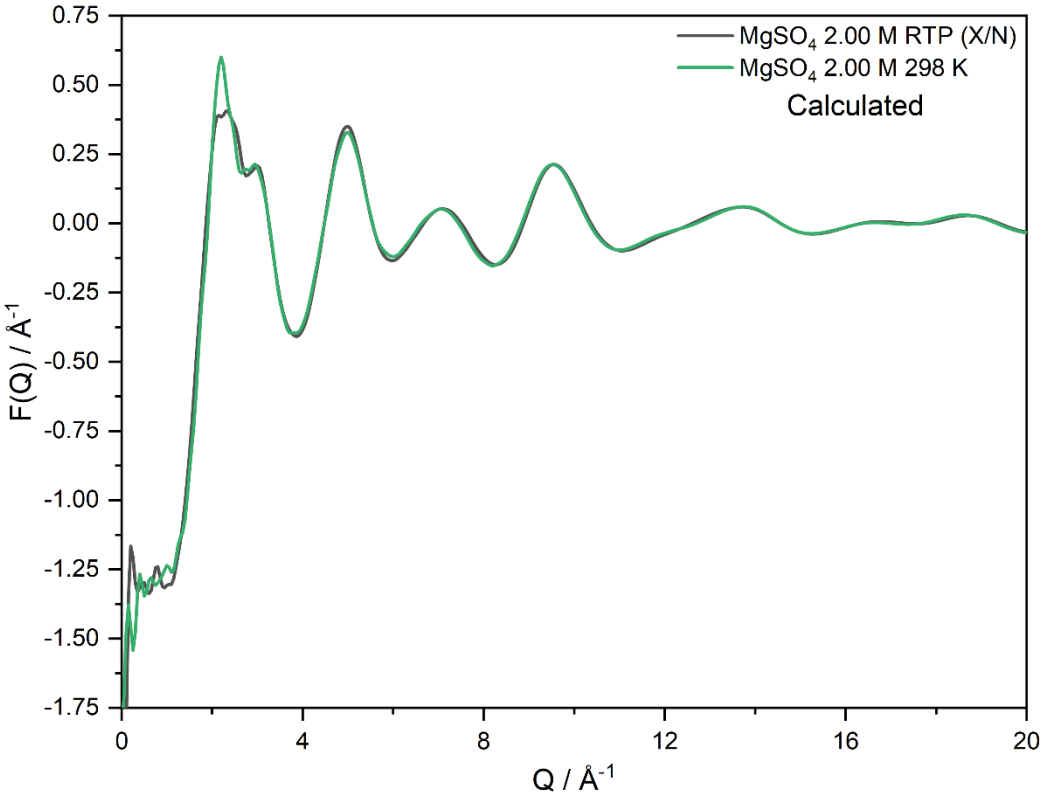

Figure 4-3. *Comparison of the F(Q) for 2.00M $MgSO_4$, where the black line represents the RTP data used for the refinement in chapter 3 and the green line shows the data of 298K cryo-controlled setup. An inset is included to highlight the low Q region.*

The derived f(r) shown in figure 4-4 highlights an even greater similarity between the two models than seen in the F(Q) shown above. The features at r < 1.75 Å are identical and this is purely due to them being from the input fragments, specifically the sulfate ion. Beyond this region is where intermolecular structural features originating from the refined model begin to emerge, such as the Mg-O and water structure, and these features also remain very similar, showing consistency between the two refinements.

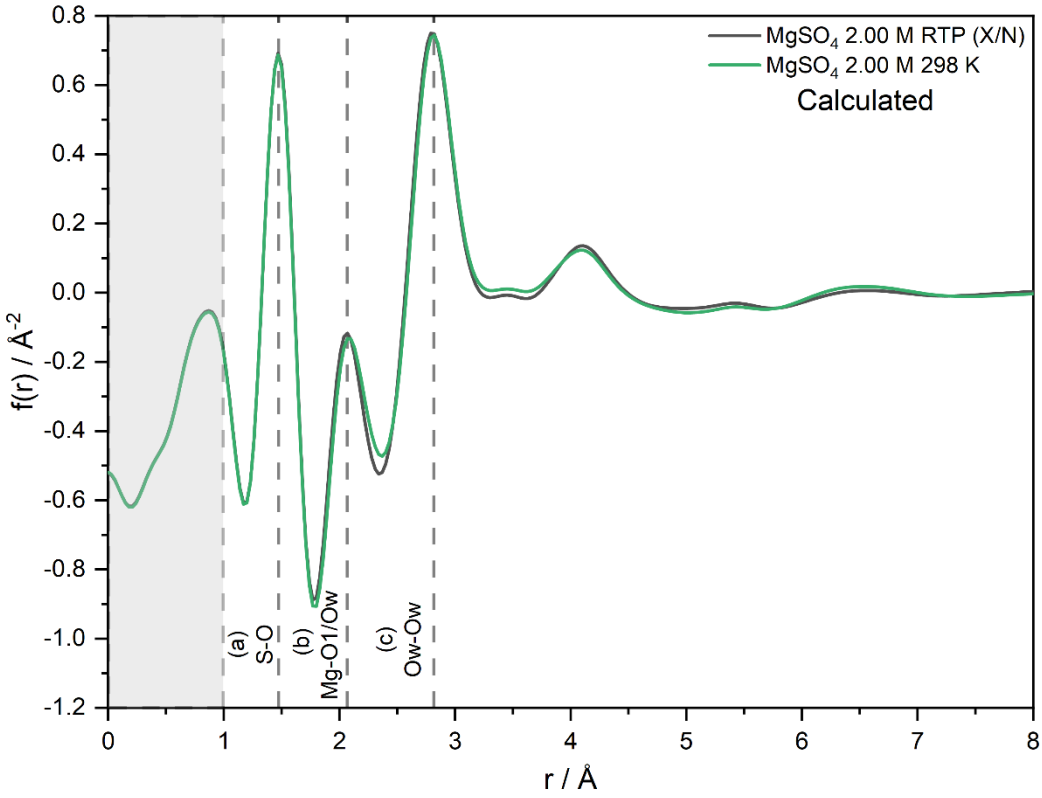

Figure 4-4. *Comparison of the f(r) data for 2.00M MgSO4, where the black line represents the RTP data used for the refinement in chapter 3 and the green line shows the data of 298K cryo-controlled setup. Key structural features have been labelled: (a) intramolecular S-O (sulfate),(b) intramolecular Mg-O (cluster) and (c) intermolecular Ow-Ow. Greyed out area represents data to be disregarded due to the fundamental limitations of PDFs.*

4.2.2.2 Comparing the Water Structure

Whilst there is a large amount of confidence in the refinements discussed in section 4.2.2.1, one point of concern is the water structure, with the F(Q) showing an observable deviation in the features directly linked to the water structure. Therefore, we must examine the water structure in more detail to understand any limitations of the X-ray only data. The main tools that will be used for this comparison are the site-site g(r) (figure 4-5) and coordination number (figure 4-6).

Starting with the Ow···Ow g(r) shown in figure 4-5, it is observable that the general shape or envelope of the site-site g(r) remains similar across the full range of r, however the peaks r > 3.0 Å begin to broaden and show less definable peaks. This is compelling between r = 3.5 – 5.0 Å, where there is an increase in magnitude relative to the dual refinement. This suggests less certainty in the water structure and an increased number of structural possibilities propagating from both a reduced number of observations (X-ray only) and radiation less sensitive to water scattering.

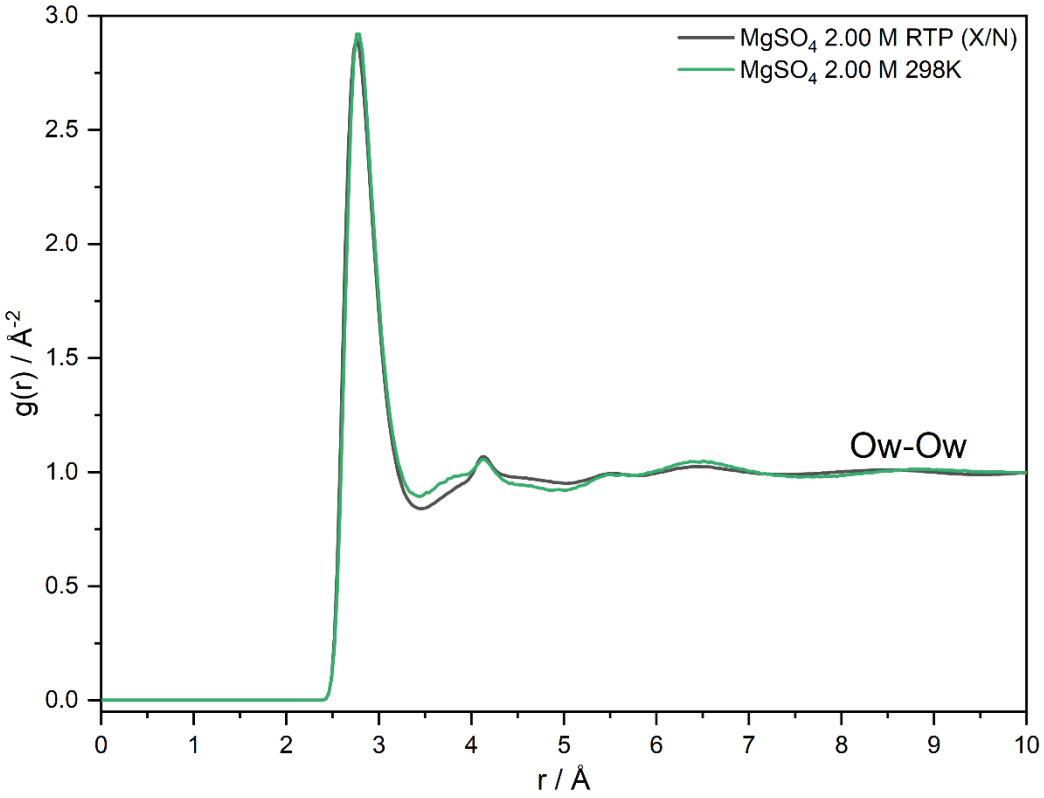

Figure 4-5. *Comparison of the dual RTP (black) and 298K X-ray only (green) Ow-Ow site-site g(r).*

Figure 4-6 shows the comparison of coordination number, and this is perhaps where the largest deviation in the water structure can be observed in both shape and relative magnitudes. Determining the median coordination for each system, the broader range of coordination exhibited in the X-ray only 298K model shows an increase in the median to 3.81 vs. 3.39 seen in the dual refinement. Despite the most probable coordination for the X-ray only system being lower, the overall coordination and therefore relative water molecule density increases slightly by 0.42. This is likely again due to the increased uncertainty in the water structure due to the limitations propagated by the use of X-ray only data.

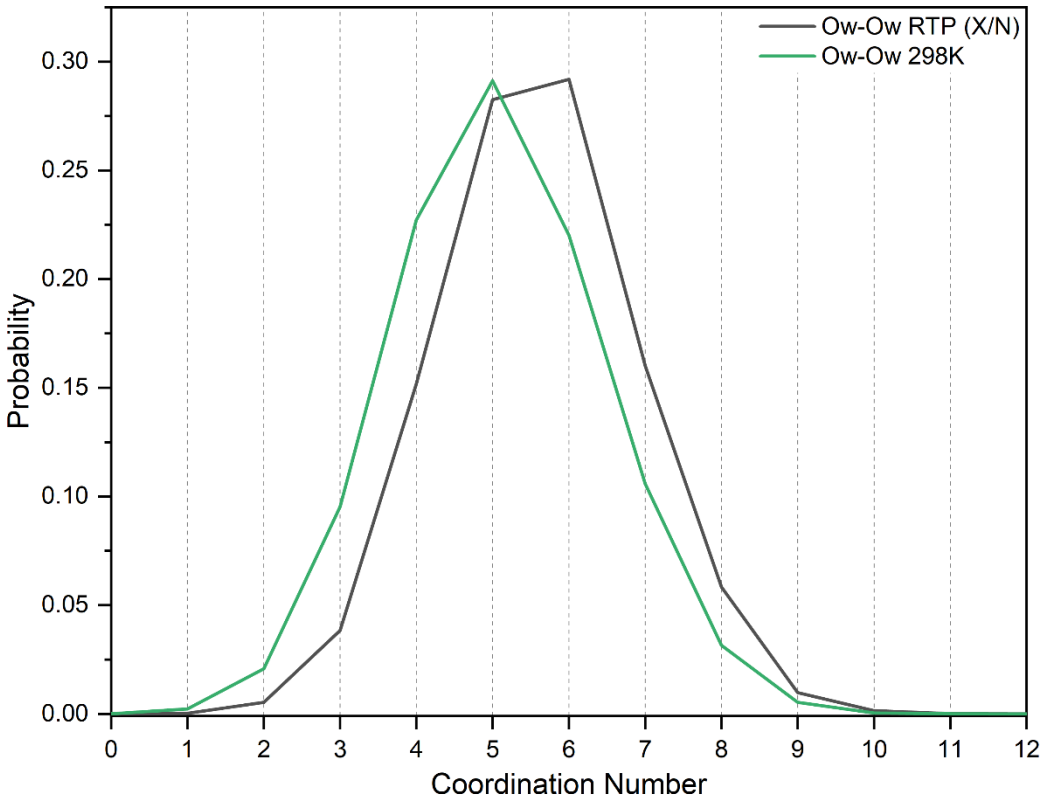

Figure 4-6. *Comparison of the dual RTP (black) and 298K X-ray only (green) Ow-Ow coordination number.*

Overall, whilst the water structure from X-ray only data does deviate slightly from that observed with the addition of complementary neutron data, these changes are minimal and show that X-ray only data can be suitable for extracting quantifiable structure. However, care must be taken with regards to the water structure, which appears to be home to the main differences between the models. The deviations are considered minor, but it does suggest that any final conclusions on the water structure observed may warrant deeper consideration, particularly with regards to future experiments where changes in conditions may drive a more significant change in the structure.

Establishing that the models derived from X-ray only data are broadly consistent with the dual refinements enables further experiments to be conducted where temperature will be varied to examine the effects on the prenucleation structure (section 4.3) and also for temperature to be used as a method of achieving higher concentrations (chapter 5).

4.3 Comparison and Understanding of Structural Changes with Change in Temperature

Having determined that the Cryostream has a negligible influence on the refined model and that the X-ray only refinements are broadly similar to their X-ray/neutron counterparts it is possible to conduct a variable temperature study with some confidence. This will follow the same format as previous sections, with an initial examination of the experimental scattering data, followed by the calculated model fit and finally a more in-depth evaluation provided by the auxiliary routines. This will enable a fuller understanding of any effects of temperature change on 2.00 M aqueous $MgSO_4$.

4.3.1 Interpreting the Temperature Total Scattering Data

Examining the unrefined data found in figure 4-7, we can see that the scattering remains remarkably similar across all temperatures, with the oscillations matching well across the entire Q range – although subtle variations at low Q are apparent. This gives the first hint that temperature probably has a minimal effect on the atomic structure of the system.

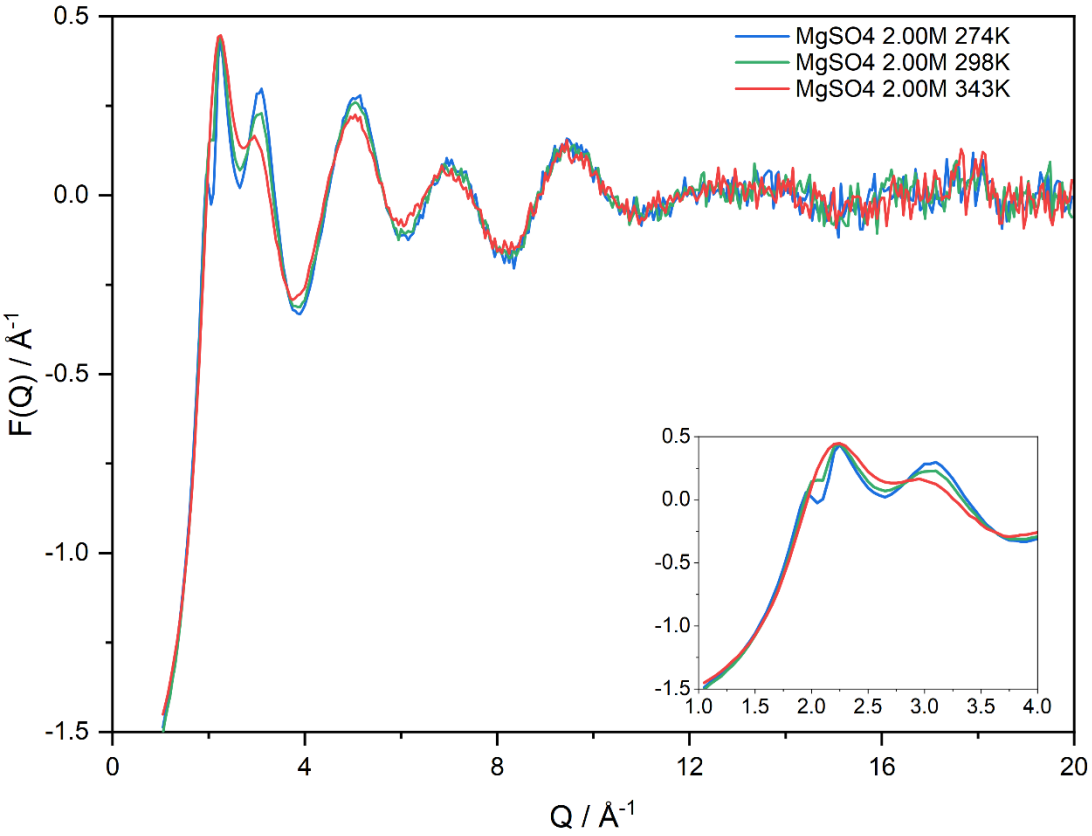

Figure 4-7. *Overlay of experimental F(Q) for 274K (blue), 298K (green) and 343K (red) with inset showing zoomed low Q regionhighlighting the subtle differences introduced by temperature variation.*

The above hypothesis may be difficult to extend across the entire Q-range, with the low Q region displaying observable differences in the scattering, suggesting a slight deviation to the structure

defined in chapter 3. As previously discussed, the doublet feature found at Q = 1.0 – 4.0 $Å^{-1}$ can be attributed to intramolecular Ow···Ow features, which roughly remains consistent albeit with a slight increase in the width, and the feature assigned to Mg-O showing a more substantial alteration. Whilst examination of the F(Q) enables a broad-brush comparison, examination of the derived (f(r)) and the refined structural models is required to truly understand the differences.

4.3.2 Variable Temperature EPSR Setup

Following a similar methodology to that of previous EPSR refinements, it was necessary to set appropriate starting parameters for the refinement. The same reference potentials were used as the chapter 3 refinement, but not as many restraints were required – these were limited to Mg-O1s (1.8 Å) and Hw-O1s (1.5 Å). These values were introduced to counteract the formation of overly large, calculated g(r) peaks observed for both interactions. It was also necessary to specifically set the temperature, rather than use the default ambient value. The empirical potential was incrementally increased to a value of 10, the same value as used in previous refinements. The same auxiliary routines were run to enable direct comparison across the temperature range.

4.3.3 Variable Temperature EPSR Refinements

Using the data processed in figure 4-7, it is possible to refine a model and derive other functions such as the f(r), these refinements can be found in figure 4-8 and figure 4-9. As it can be seen, a good agreement can be found between the experimental data and refined model, enabling confidence in the X-ray only data and refinements. Furthermore, access to the derived f(r) will allow for a further understanding to the deviations seen at low Q in the F(Q) by examining the real-space data.

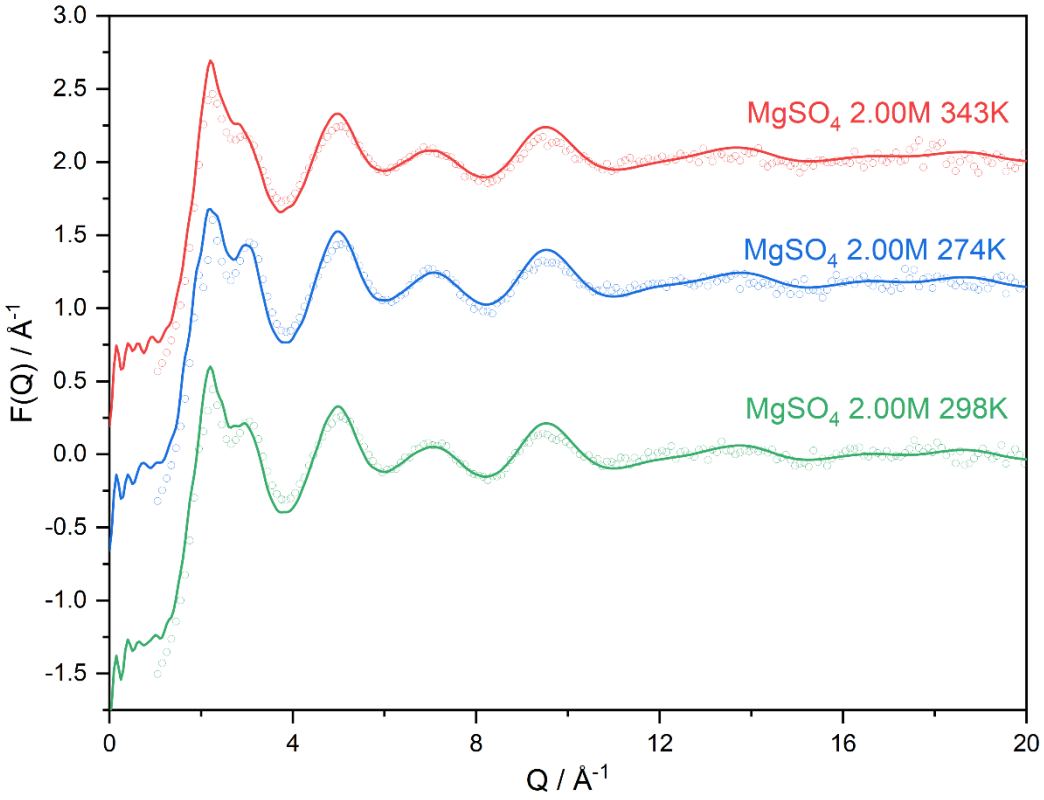

Figure 4-8. *F(Q) EPSR refined fits for 298K (black), 274K (blue) and 343K (red). Circles represent experimental data, and the calculated function is show as a solid line.*

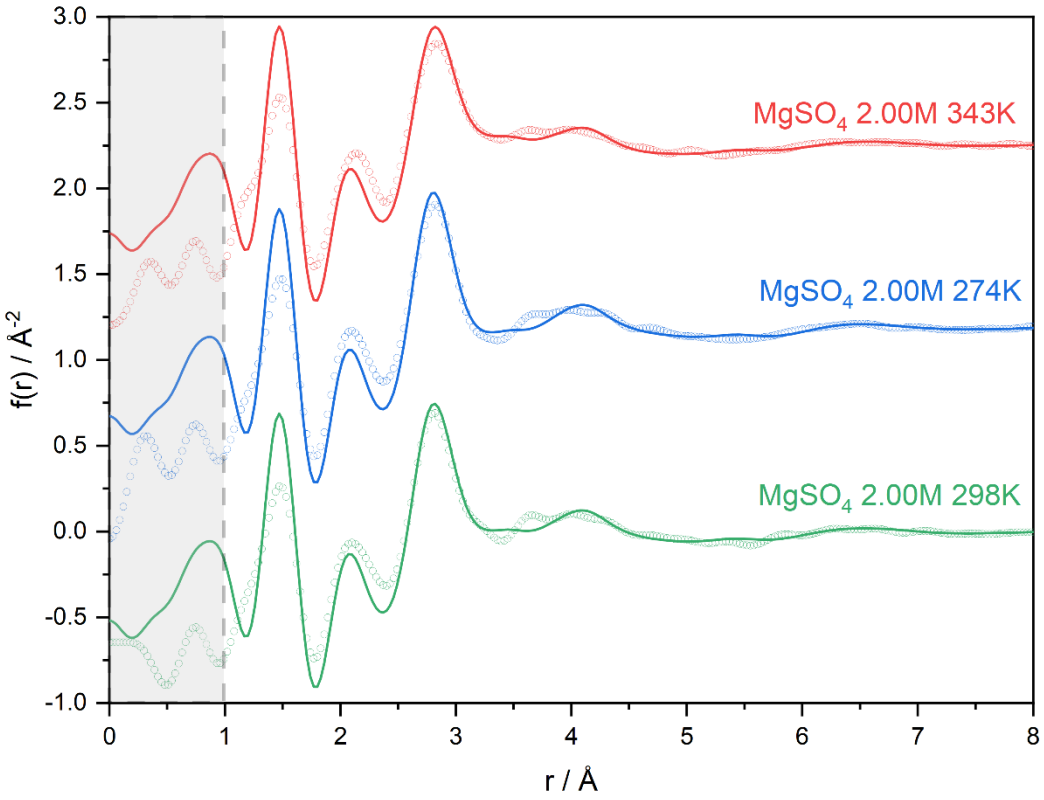

Figure 4-9. *Derived f(r) EPSR fits for 298K (black), 274K (blue) and 343K (red). Circles represent experimental data, and the calculated function is show as a solid line.*

The f(r) portrays a similar agreement between the experimental and calculated data. Overall, this suggests that the short-range ordering present in all aqueous systems has been modelled well by the EPSR approach. Some caveats need to be made, especially for the low-r features. Firstly, as with all such refinements, the features at about 1 Å represent intramolecular O···H distances and those smaller values are not physically meaningful and are usually ignored. The calculated features at or below 1.0 Å remain constant across the 3 measurements as they represent the intramolecular O···H bonds in water, and as both the bond length and abundance of water does not vary between models, this feature remains constant throughout. The other feature that does not fit as well as previous models in the 1.49 Å feature, which is attributed to the intramolecular S-O bond in sulfate. This feature should remain constant as the bond length and abundance of sulfate is constant throughout, however, this experimental peak remains smaller in magnitude than one might expect. We are still unsure of the cause of this anomaly, and this is a case where complimentary neutron data would be desirable to improve the fit.

Overall, the data show a good match between the experimental and the calculated, providing confidence in the data collected and the model obtained. This will enable further analysis of the system via auxiliary routines such as coordination number, bond angle, site-site g(r) and SDF. These results will in turn be compared with previous studies, both from this project and from the literature, and also provide a foundation for the later concentration studies, where temperature is used as a variable to aid super saturation.

4.3.4 Comparing the Experimental X-ray Temperature Scattering

Initially we examine the experimental F(Q) in section 4.3.1, where the raw scattering data was first introduced. Examining the data in more detail, the overall shape of the data remains consistent throughout the temperature range with similar oscillations being visible up to high Q, however as previously stated, there are some deviations at low Q suggesting a slight change in the structure of the samples. As extensively discussed, these lower Q features have been assigned to the Ow···Ow intermolecular and intramolecular Mg-O features respectively, and these increase in sharpness with decreasing temperature. This gives the first and perhaps most expected change in structure with temperature and that is the increasing similarity to an ice-like structure when approaching the freezing point of water. This type of behaviour has been documented by many authors, with water studies by Soper[1] being the most prominent.

Whilst this is expected, it is important to examine the derived experimental f(r), this is where further understanding of the deviations to short range order are more visible. As shown in the experimental f(r) in figure 4-10, the broad shape remains constant across the temperature range, and this suggests that the short-range ordering largely remains the same throughout and the structure

elucidated in chapter 3 does not change significantly, but this will be more rigorously investigated in the proceeding sections.

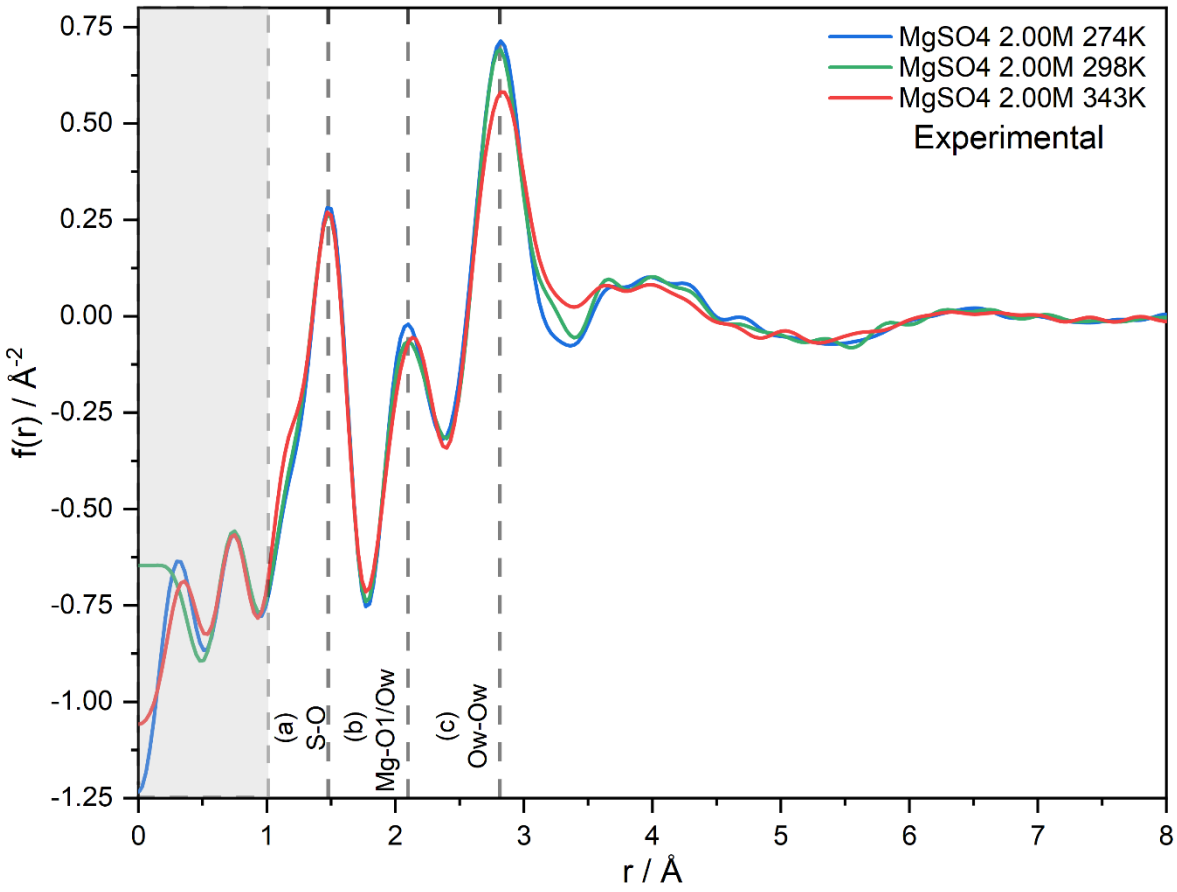

Figure 4-10. *Overlay of experimental f(r) for 274K (blue), 298K (black) and 343K (red). Key structural features have been labelled: (a) intramolecular S-O (sulfate),(b) intramolecular Mg-O (cluster) and (c) intermolecular Ow-Ow. Greyed out area represents data to be disregarded due to the fundamental limitations of PDFs.*

Whilst the shape broadly remains the same, there are a few minor deviations that warrant further comment; however, most can be attributed to the thermal energy and increase/decreased dynamics in the system that often accompanies it. Examining the key features (labelled (a) – (c)), small deviations occur, the first being the shoulder seen on feature (a) 343K, occurring at r ≈ 1.2 Å. This shoulder can be hypothesised to either represent a shorter S-O bonding mode existing at higher temperature, or a feature emerging that can only occur with increased temperature. Without additional routines it is difficult to extract what exactly is occurring in this region, and therefore will be discussed in future structure discussion sections.

Feature (b) results from the Mg-O cluster, this feature also remains constant with a singular outlier at lower temperature. The 274K structure shows an increase in sharpness and a slight decrease in the distance, this is suggestive of a more compact and rigid structure occurring within the metal clusters, again to be expected as a result of the reduced temperature and therefore thermal motion. It is worth noting that this peak contains a contribution from Ow…Hw intermolecular

interactions, which are likely to be more ordered as it approaches a more ice-like structure as described by Soper.[1] Again, this cannot be confirmed by the f(r) alone and warrants further probing with auxiliary routines.

The final noted feature at (c) represents the Ow···Ow intermolecular water interactions, and perhaps this shows the biggest variability of the three distinct features. However, this is the easiest to understand due to the extensive literature on the structure of pure water[1,5,6]. Soper particularly summarises this structural evolution, whereby the water loses its distinct tetragonal arrangement as we reach its boiling point, causing a change from a sharper feature to a broader one as the water molecules increase their range of probable locations.

Overall, the experimental g(r) suggests subtle and understandable changes as a function of temperature, but the main conclusion that can be made is that the structure remains mostly unchanged and consistent with the structure found via the dual refinement.

4.3.5 Comparing the Calculated X-ray Temperature Scattering

The experimental scattering and f(r) do allow for a basic understanding of the fundamental scattering occurring directly from the sample, but it is the model from which we can extract the more tangible real-space structure. Therefore, comparing the derived functions will enable a deeper understanding of the structure of these systems across the temperature range.

The F(Q) model obtained in figure 4-11 tells a similar story to that of section 4.2, whereby it is in good agreement across much of the Q-range with the exception of the doublet at low Q. Again, this is likely due to the increased atomic/molecular motion but will be examined in more detail via auxiliary routines. The calculated f(r) in figure 4-12 perhaps shows a more pronounced agreement, with features (a) and (b) being almost identical showing that the cluster structure is constant across the range. Feature (c) shows an observable trend, becoming broader with increasing temperature, a trend observed in the literature by Soper.[1] This trend is likely directly attributed to the increased molecular motion and less discrete structure, as it transitions from a fairly rigid tetrahedral structure at cooler temperatures to a more energetic and less well-defined structure at higher temperature.

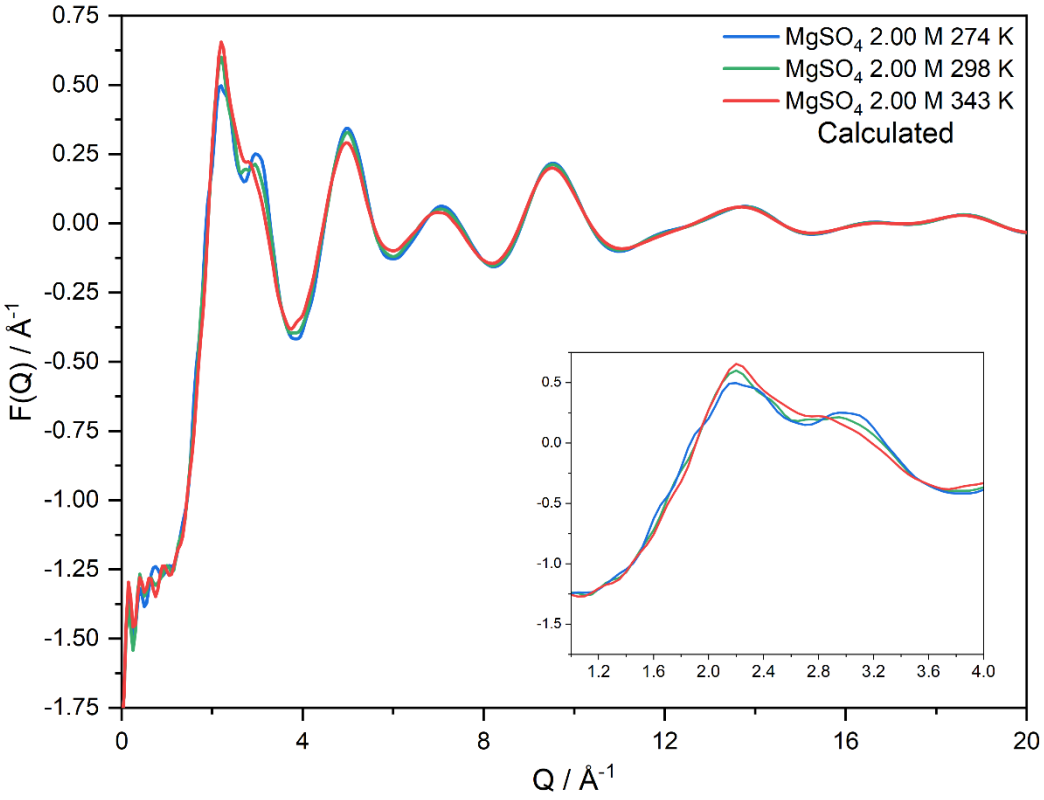

Figure 4-11. *Comparison of the F(Q) data for 2.00M $MgSO_4$ for the temperature series of 274K (blue), 298K (green) and 343K (red). An inset is included to highlight the low Q region.*

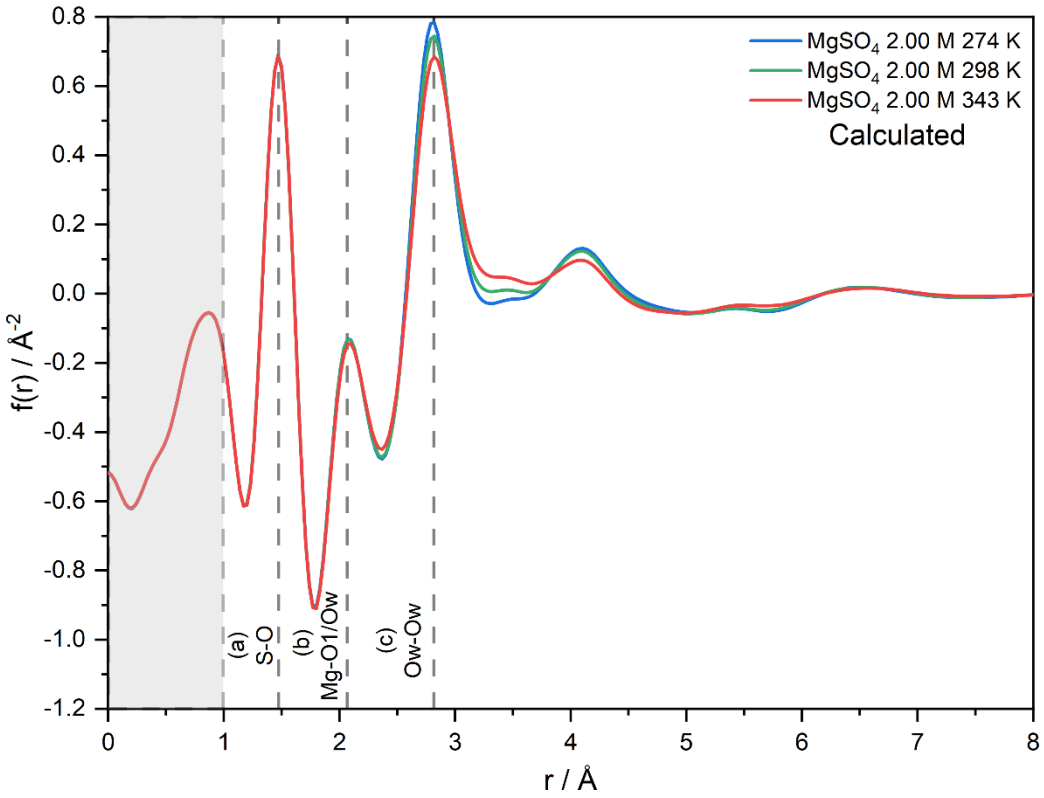

Figure 4-12. *Overlay of the f(r) for 274K (blue), 298K (black) and 343K (red). Key structural features have been labelled: (a) intramolecular S-O (sulfate),(b) intramolecular Mg-O (cluster) and (c) intermolecular Ow-Ow. Greyed out area represents data to be disregarded due to the fundamental limitations of PDFs.*

Overall, the calculated models still agree with the hypothesis that temperature has a minimal effect on the structure observed at a standard 2.00 M concentration. Minor deviations can be seen and warrant further probing to fully understand their significance, however it does set a good precedent for future experiments.

4.3.6 Probing the Structure Via Axillary Routines as a Function of Temperature

Whilst it has been established that the structure experiences minimal changes as a function of temperature, it is essential that the structural model itself is examined to elucidate any minor changes that may not be observable in the experimental or calculated data and derived functions. Therefore, in this section, we will follow a similar methodology to that of chapter 3 where each component (i.e., magnesium, sulfate and water local structure) will be examined in turn using various auxiliary routines to draw final conclusions concerning temperature effects.

4.3.6.1 Magnesium Local Environment as a Function of Temperature

Coordination-like magnesium clusters analogous to those found in the solid state are a common motif within aqueous $MgSO_4$ studies, both described in the literature[7–13] and observed previously in chapter 3. As discussed, these motifs are typically octahedral in nature with a varying ratio of sulfate to water oxygens.

Following a similar methodology as seen in chapter 3, evaluating the average Mg···O approach will help the understanding of the metal cluster consistency at both higher and lower temperatures. Starting with the site-site g(r) will enable a clearer image of the atom correlations between the magnesium and each oxygen type and is shown in figure 4-13. As found from the total RDF, seen in section 4.3.5, only small deviations occur suggesting that the structure of the metal-oxygen clusters remain consistent despite the change in temperature. Small deviations occur predominately in the direct Mg-O interactions where increasing temperature decreases the magnitude of the feature, this in itself is unsurprising when acknowledging the increased thermal motion. As atoms and molecules will have increased energy and movement, these interactions will occur less often with exchange likely to occur more often, resulting in a less defined structure. However, the signal difference here is <2.0 $Å^{-1}$ representing a very small decrease in the ordering around the magnesium ion and therefore it can be concluded that the Mg-O interactions here are not greatly influenced by the change in temperature.

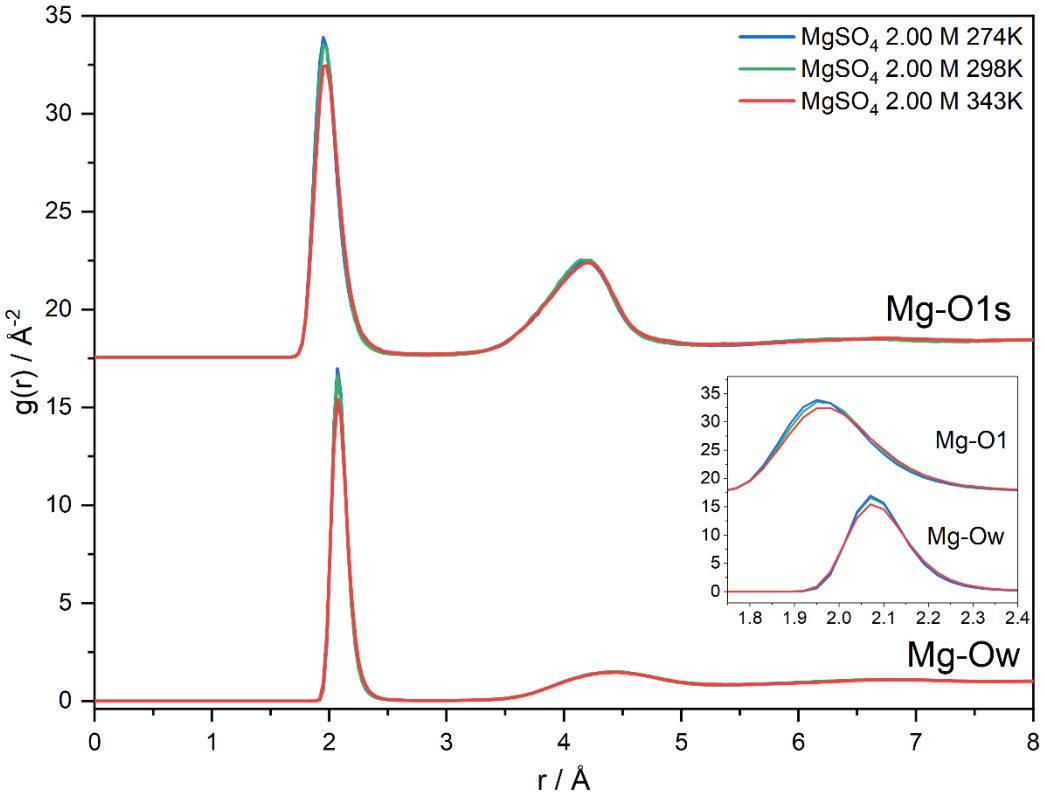

Figure 4-13. *Site-site g(r) for Mg-O1s (top) and Mg-Ow (bottom) over temperatures 274K (blue), 298K (green) and 343K (red). An inset is included for r = 1.75 – 2.4 Å to highlight the direct interactions between the magnesium and oxygens of sulfate and water respectively.*

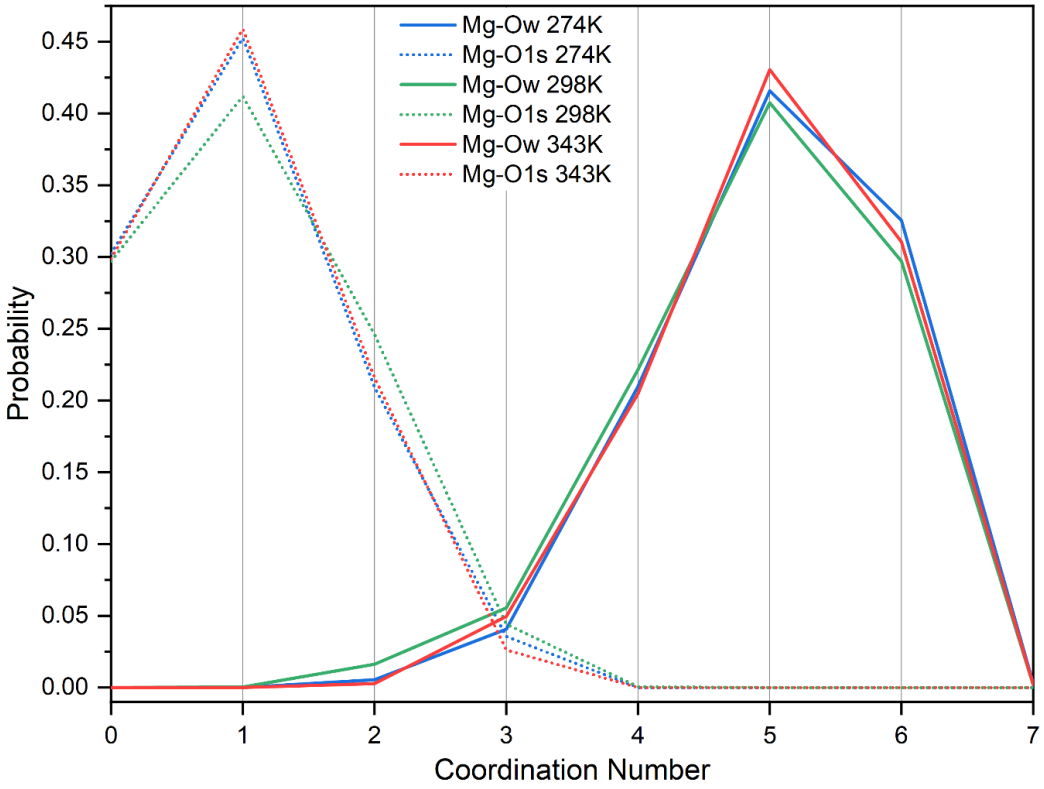

Figure 4-14. *Coordination number for Mg O1s (dotted line) and Mg Ow (solid line) for temperatures 274K (blue), 298K (green) and 343K (red).*

These observations can be quantified by looking at the coordination numbers as seen in figure 4-14 which are broadly consistent across all 3 temperatures. This suggests that the overall 6-coordinate octahedral cluster remains the basic building block throughout the series. Some subtle differences can be seen, particularly for the 298K experiment, where there is a slightly larger deviation in the Mg-O1s coordination with an approximate 5% decrease in the singularly coordinated sulfate, alongside a 3-4% increase in the doubly coordinated sulfate. This is suspected to be within error, especially when comparing to the coordination observed for the dual RTP coordination found in chapter 3 alongside the almost identical site-site g(r) seen above. Despite this, the general shape of the coordination remains consistent throughout the temperature range and further supports the minimal effects of temperature.

The final aspect of the magnesium cluster structure that can be analysed using a geometric approach is the O-Mg-O bond angles, enabling confirmation of the octahedral geometry first elucidated in chapter 3. Starting with the Ow-Mg-Ow bond angle, shown below in figure 4-15 (a), minimal changes are observed for most of the range. Small deviations can be observed, such as the increase in broadness with the larger angle value as we increase in temperature, which supports the hypothesis that increased temperature causes a slight increase in the structure's flexibility. A similar narrative can be seen in figure 4-15 (b), however here this increased flexibility is now prominent for both features. Figure 4-15 (c) highlights this the most, where the lowest temperature now shows a much larger feature at higher angle, whilst remaining centred in the same position, showing that these defined positions around the octahedra become more rigid as we cool the system. The bond angles, therefore, confirm that the octahedral metal cluster remains a consistent feature across all 3 temperatures studied, but the rigidity of these units decreases as we increase temperature.

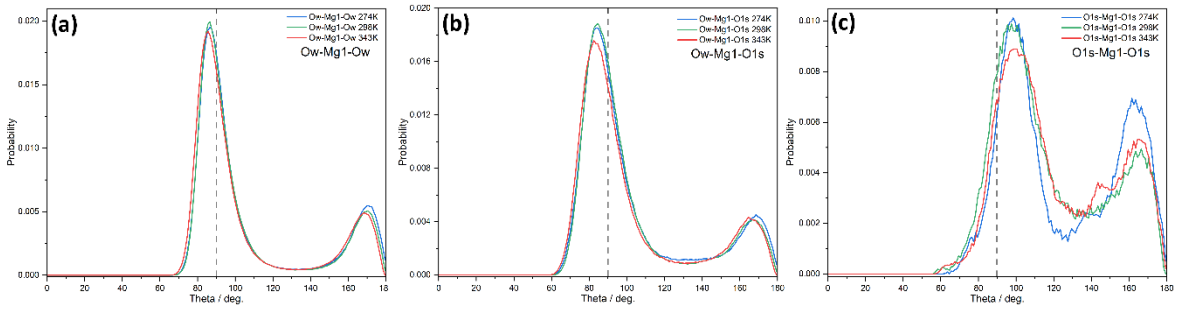

Figure 4-15. *Bond angles for (a) Ow-Mg1-Ow, (b) Ow-Mg1-O1s and (c) O1s-Mg1-O1s over temperatures 274K (blue), 298K (green) and 343K (red). Dashed line represents the ideal 90°, octahedral geometry.*

4.3.6.2 Sulfate Local Environment as a Function of Temperature

Following the same approach as applied to the magnesium local environment, it is important to clarify whether the sulfate local environment, particularly the sulfate-water environment is

impacted by the temperate. We expect the water structure to deviate with the alteration in temperature, as described in literature[1,5,6], but its impact on the sulfate stabilisation must be studied. The impact of the bulk water structure will subsequently be discussed in section 4.3.6.3.

Initially examining the site-site g(r) in figure 4-16, we can see almost no changes in the S1/O1s···Ow structure. That being said, very slight differences can be observed for the 343K g(r), however these changes are so miniscule that they are unlikely to be statistically relevant, simply suggesting the smallest decrease in the ordering and arrangement of the water around the sulfate ion. Overall, the distances and relative magnitudes are constant throughout the temperature range.

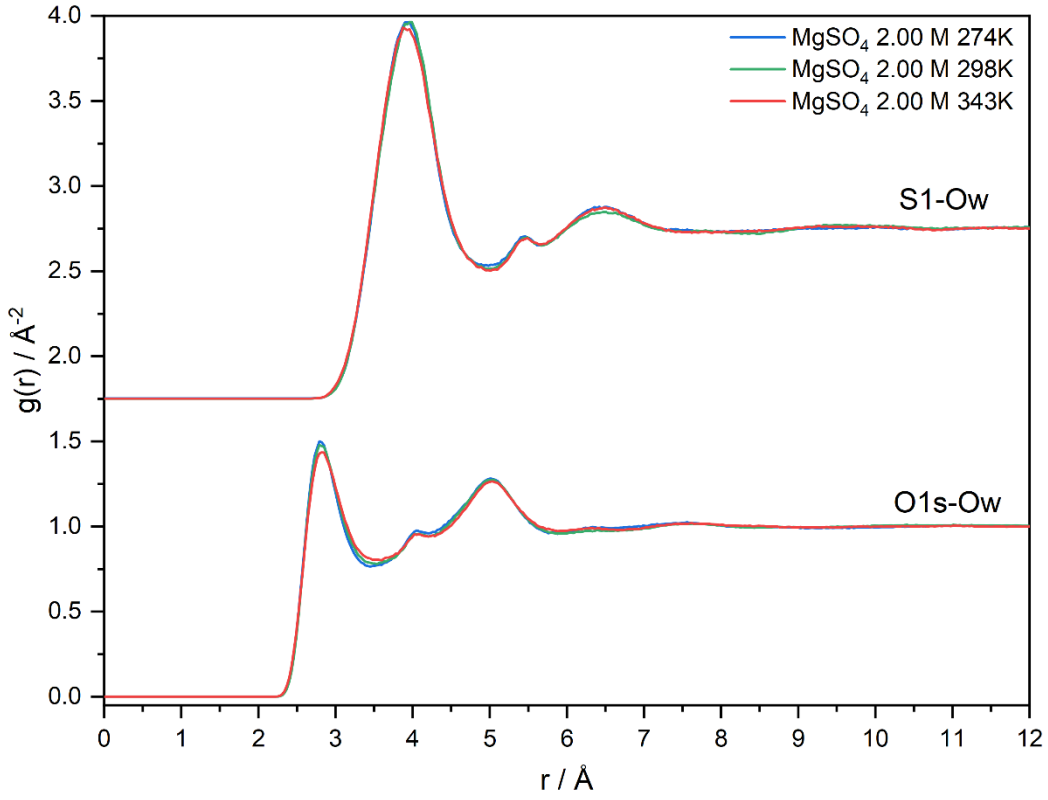

Figure 4-16. *Site site g(r) for S1-Ow (top) and O1s-Ow (bottom) over temperatures 274K (blue), 298K (green) and 343K (red)*

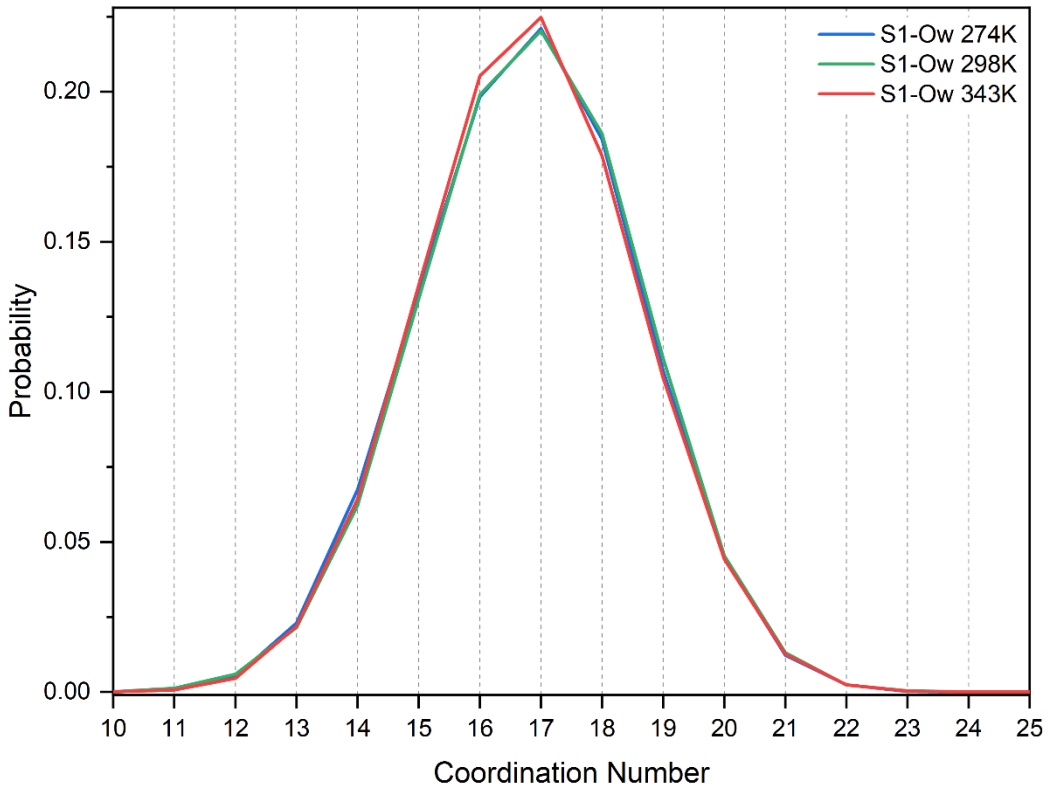

Figure 4-17. *Coordination number for S1-Ow over temperatures 274K (blue), 298K (green) and 343K (red).*

Corroborating this with the coordination number, seen below in figure 4-17, shows a similar narrative whereby the coordination between the sulfate and water remains consistent. This further

suggests that the solvent interaction with the sulfate ion is not affected in any significant manner with varying temperature. Figure 4-17 does display a slight shift to an overall lower coordination for higher temperature, likely induced by an increased movement of solvent molecules and less-defined structure. However, despite this slight deviation, the coordination remains remarkably similar.

The final routine that can be used to probe the structure is the SDF, shown in figure 4-18. Whilst the site-site g(r) and coordination number can provide a mass of information on the local environment; it does not directly provide 3D information. Consequently, whilst the above routines may suggest no change in the structure, the SDF must be investigated to ensure that no structural arrangement has taken place. However, upon the examination of figure 4-18, the tetrahedral/octahedral arrangement of water around sulfate can be seen to remain true to the discussion found in chapter 3, suggesting that temperature has very minimal effect on the interactions between the two species. From the SDF the only observable difference is the increased lobe size as the temperature increases, and this supports the hypothesis of increased temperature increasing the atomic motion.

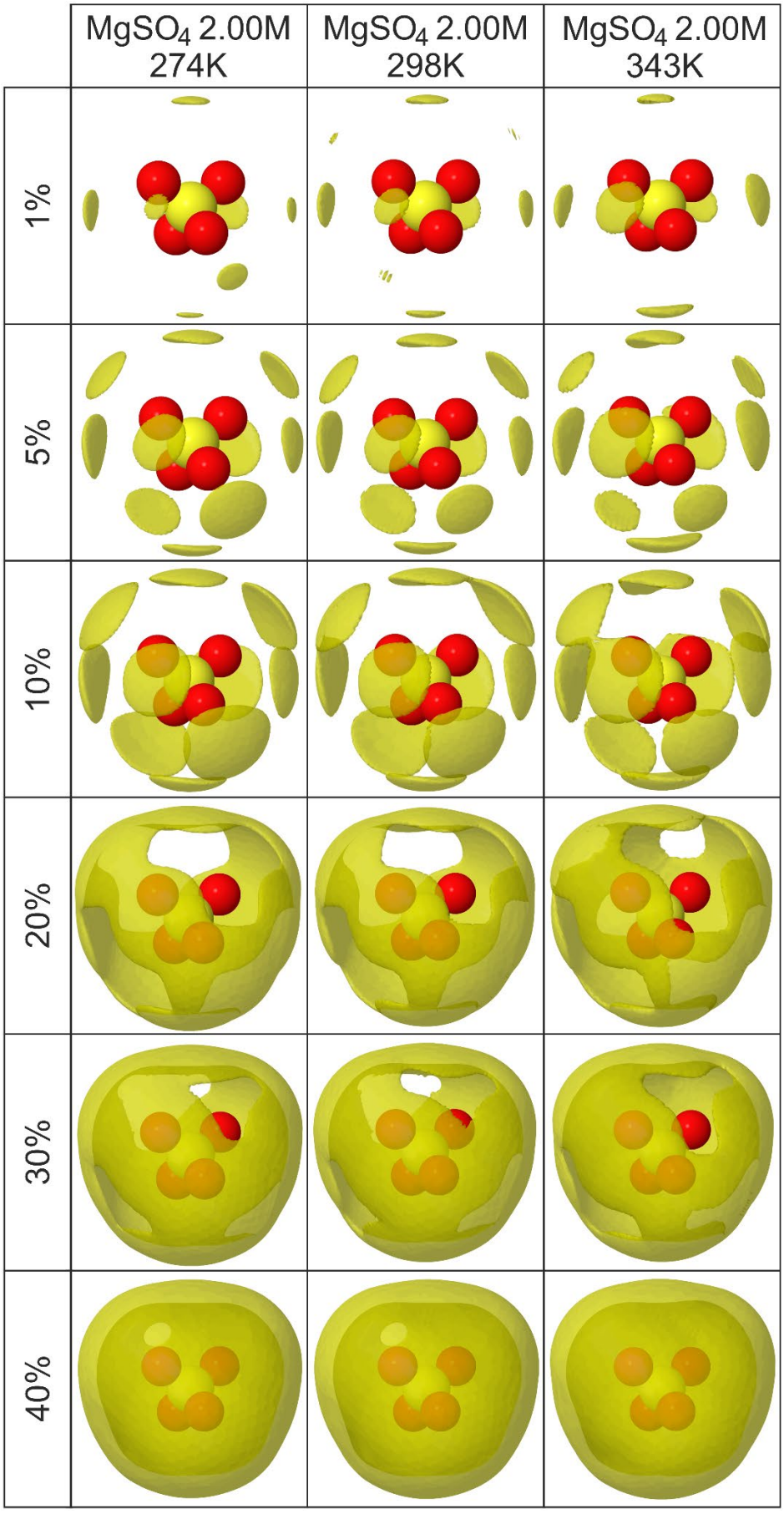

Figure 4-18. *SDF for $H_2O@SO_4$ over r = 1.0 – 5.0 Å, with isosurface % shown from 1 – 40%. Atoms displayed are sulfur (yellow) and oxygen (red) representing the central sulfate. Yellow density represents areas most likely to contain a water molecule.*

Overall, it has been observed that temperature has a minimal effect on the sulfate-water interactions, with the atomic correlations, coordination number and structure remaining the same.

4.3.6.3 Water Local Environment as a Function of Temperature

The final component of the system that requires investigation is the water-water interactions. Whilst the ion-ion and magnesium/sulfate-water interactions remain almost identical, previous studies on pure water systems suggest larger deviations in the bulk structure do occur as a function of temperature.[1,5,6,14]

Again, following a similar procedure, the site-site g(r), coordination number and SDF will be described in turn to fully understand the structure and comprehend any potential changes to the bulk water structure. Figure 4-19 below shows the Ow···Ow g(r), this depicts slightly more differences than found in previous site-site g(r) discussed in this chapter, however, based on previous literature this is not surprising.[1] The bulk water structure has often been found to be the most dynamic and dominant interaction within the system and therefore most influenced by external factors. The Ow···Ow g(r) shown below highlights a trend in the structure, whereby the overall shape and position of the features remain consistent, but the broadness and peak magnitudes change. The lowest temperature represents the most rigid configuration, and this is due to the lowest temperature sample within the range and therefore being the closest to the freezing point of water, where it will adopt a more tetrahedral ice-like configuration.[1,14] As we approach freezing point of the water, noting that the freezing point of the aqueous solution being altered by the addition of $MgSO_4$, the water molecules are more likely to adopt a more ordered configuration and therefore reduce the peak broadness and increase magnitude.

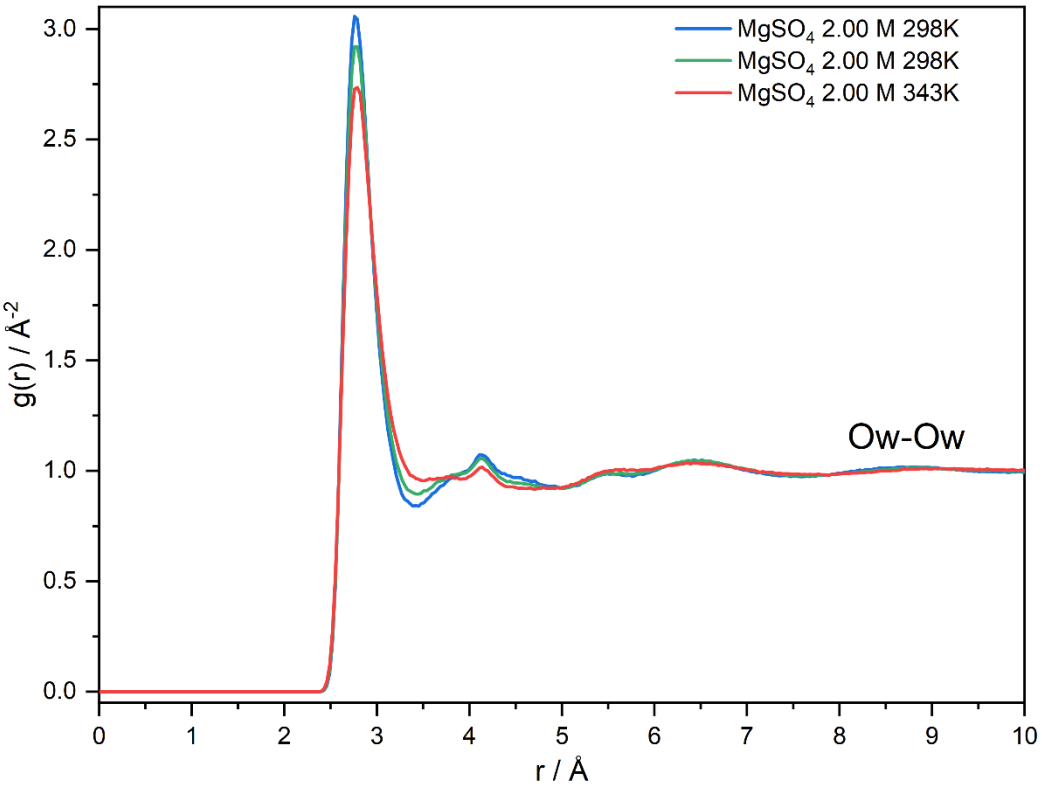

Figure 4-19. *Site site g(r) for Ow-Ow over temperatures 274K (blue), 298K (green) and 343K (red).*

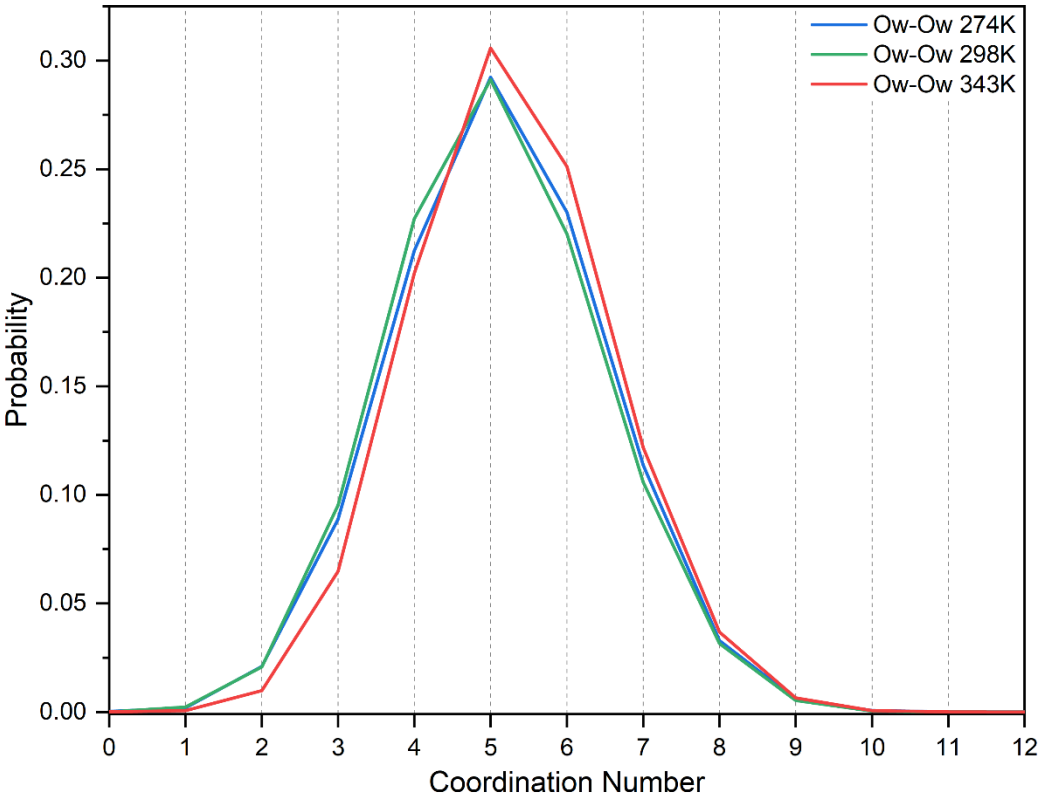

Figure 4-20. *Coordination numbers for Ow-Ow for 274K (blue), 298K (green) and 343K (red).*

To further quantify the Ow-Ow g(r) shown above, the coordination number will be investigated to understand whether the water molecule density per volume decreases or increases with temperature. Figure 4-20 shows the coordination numbers for the bulk water structure, and it can be observed that the general coordination does not vary significantly suggesting little change to the structure. The shape and probability of the coordination plots for all temperatures remains similar with the slight exception of the 343K model, where we see a slight increase in the coordination modal value as well as a larger affinity for larger coordination numbers. This can be attributed to the increased atomic movement within the system, allowing for a larger coordination number than permitted with lower overall energy systems i.e., 274K, 298K and RTP. This increase in coordination, whilst observable, is only a difference of 2-3%, again consistent with literature values.[1]

The final routine available for analysis of the bulk water structure is that of the SDF, which as previously discussed, allows for a deeper and more visual understanding of the in 3D – it is shown in figure 4-21. The general trend matches with the narrative established from the previous auxiliary routines above, in which the increase in temperature causes a decrease in the well-defined structure. Despite this decrease in structural definition, the tetrahedral lobe/anti-lobe structure can be observed throughout. The obvious disruption to the bulk structure due to the introduction of the ions that was established in chapter 3 can also be seen, where the structure is more homogenous than that of pure water, however the homogeneity does vary with temperature. At the cooler temperature of 274K, we see more pure water character with the arches found on the mirror plane and opposite the O-H bond being observed more clearly. The warmer 343K system shows a slight increase in the homogenous nature of the water structure, but despite this still shows large similarities to the 298K model and ultimately the SDF observed for the dual X-ray/neutron refinement. This finalises and confirms the hypothesis that the main effect on the water structure that can be observed when temperature is varied is the decrease in the defined structure due to the increased energetics of the water molecules, however the general tetrahedral arrangement remains.

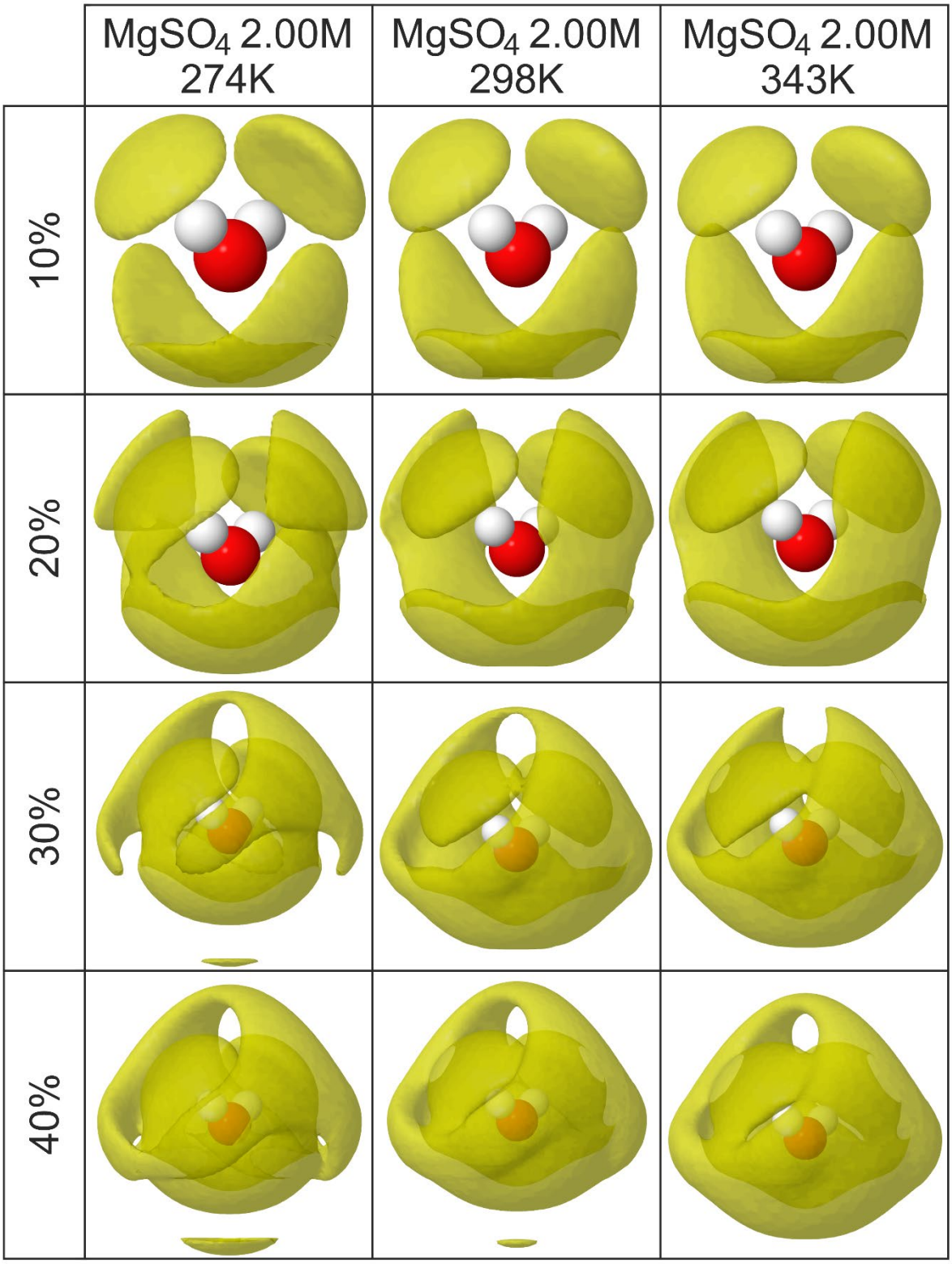

Figure 4-21. *SDF for H_2O@H_2O over r = 1.0 – 5.0 Å, with isosurface% shown from 1 – 40 %. Atoms displayed are oxygen (red) and hydrogen (white) representing the central water. Yellow density represents areas most likely to contain a water molecule.*

4.4 Conclusion

In this chapter, two main conclusions can be drawn: X-ray only refinements provide models very similar to dual X-ray/neutron refinements and that varying the temperature, within the range studied, has minimal effect on the structure. This shows a very positive foundation to further studies upon the system, particularly that of varying concentration.

As section 4.2 shows, the data obtained from X-ray only and a dual X-ray/neutron refinement yield very similar results, which provides the confidence needed to conduct X-ray only EPSR refinements for future experiments. Working with this confidence, a temperature series was produced to examine the effects of temperature on a standard 2.00 M $MgSO_4$ aqueous system. This also yielded minimal differences, we only slight variations to the local environment around both the ions and the water. The main structural characteristics found in chapter 3 remain consistent throughout, showing the stability of the structure elucidated via this total scattering approach.

With confidence in the variable temperature series, changes to the concentration can be induced with the assumption that any changes observed in the structure will purely be from the increased concentration and not the elevated temperature. Therefore, for the final chapter to this narrative, concentration will be increased to investigate how the structure varies as concentration progressively increases with the anticipation that prenucleation structures will be observed.

References

1 A. Soper, *Water and ice structure in the range 220 - 365K from radiation total scattering experiments*, 2014, vol. 187.

2 T. F. Headen, *Mol. Phys.*, 2019, **117**, 3329–3336.

3 P. Sillrén, J. Swenson, J. Mattsson, D. Bowron and A. Matic, *J. Chem. Phys.*, 2013, **138**, 214501.

4 A. K. Soper, *GudrunN and GudrunX*, ISIS, Oxford, ISIS, Oxford, 2012.

5 A. H. Narten, M. D. Danford and H. A. Levy, *Discuss. Faraday Soc.*, 1967, **43**, 97–107.

6 A. K. Soper, in *Experimental Methods in the Physical Sciences*, eds. F. Fernandez-Alonso and D. L. Price, Academic Press, 2017, vol. 49, pp. 135–211.

7 G. Balasubramanian, S. Murad, R. Kappiyoor and I. K. Puri, *Chemical Physics Letters*, 2011, **508**, 38–42.

8 C. Schmidt and C.E. Manning, *Geochem. Perspect. Lett.*, 2016, **3**, 66–74.

9 W. W. Rudolph, G. Irmer and G. T. Hefter, *Phys. Chem. Chem. Phys.*, 2003, **5**, 5253–5261.

10 C.-C. Wang, M. Wang, H.-Q. Cai, Q.-W. Zhang, Y.-Y. Li and H.-B. Yi, *J. Mol. Liq.*, 2019, **278**, 33–42.

11 A. R. Davis and B. G. Oliver, *J. Phys. Chem.*, 1973, **77**, 1315–1316.

12 F. Sebastiani, A. V. Verde, M. Heyden, G. Schwaab and M. Havenith, *Phys. Chem. Chem. Phys.*, 2020, **22**, 12140–12153.

13 X. Zhang, Y. Zhang and Q. Li, *J. Mol. Struct.: Theochem*, 2002, **594**, 19–30.

14 K. Amann-Winkel, M.-C. Bellissent-Funel, L. E. Bove, T. Loerting, A. Nilsson, A. Paciaroni, D. Schlesinger and L. Skinner, *Chem. Rev.*, 2016, **116**, 7570–7589.

Chapter 5 Investigation of the Prenucleation Narrative of Magnesium Sulfate Using an Increasing Concentration EPSR Structure Solution Approach

Thus far, the basic structural features of a saturated solution of aqueous $MgSO_4$ have been determined and described, including the primary magnesium/water cluster and the sulfate hydration shells as well as the disruption these cause to the bulk water structure. In this chapter the effect of increased concentration will be examined with the aim of replicating conditions just prior to crystallisation. A similar methodology will be employed to previous discussions where the refinement and model fit will first be established to understand both the quality of data and any significant differences to previous samples. These differences will then be explored through each local environment (magnesium/sulfate/water) and using the auxiliary routines available, further understanding of the structural changes will be sought. This section will also address the longer range or extended structures as these play a more significant role in the overall structure, and discussions will explore how the structure extends and adapts with the increasing ionic populations.

5.1 Previous Work

EPSR is an underutilised tool for aqueous structure refinement, as was discussed in previous chapters, and its application to investigating aqueous ionic solutions as a function of concentration is even more limited. [1–5] Studies of the effects of concentration on the structure of aqueous systems using other methodologies are more widespread, with 31,947 results in Web of Science (as of 01/04/2021) for the search terms “concentration” plus “aqueous structure” vs. the 20 results for “EPSR” plus “concentration”. This highlights both the desire to gain knowledge on the effects of concentration on solutions and the dearth of high-level atomistic studies in the area.

A limited number of studies of aqueous $MgSO_4$ as a function of concentration can be found in the literature using both an experimental and computational approach. The most substantial of these is a terahertz spectroscopy study of lower concentrations (0.1 – 2.4 M) by Sebastiani et al.[6] and the computational study of a wider range of concentrations (~0.1 – 4.0 M) by Balasubramanian et al.[7]. These provide useful conclusions against which this work can be compared but tend to focus on specific aspects of the structure rather than providing a wholistic description.

5.1.1 Solubility & Concentration vs. Temperature

Solubility and concentration, whilst describing amounts of solute within a solvent, both describe slightly different parameters and therefore must be defined accordingly, commonly used units will be given in brackets. Solubility typically describes the limits of solute (solid/liquid/gas in g) that can be dissolved in a solvent (liquid or gas, L) to create a solution (g/L). Solubility of a solute in a solvent can vary from miscible (infinitely soluble) to insoluble, and the descriptors of these values relate to the concentration. Concentration is the amount of solute within a solvent and can be measured by a variety of methodologies and units, however all describe the amount dissolved. The units can vary from mol dm^{-3}, molar (M), parts per million (ppm) etc. all of which share a common theme of describing the true amount of solute contained within a solvent. Therefore, the main difference between these values is that solubility describes the limits of concentration, whereas concentration quantitatively describes the actual amount of solute in any amount of solvent. Concentration can therefore be used to quantitatively describe the content of a solute in a solvent, an arbitrary scale, typically used is <1 ppm describes a very insoluble material and on the opposite end of the scale, >10,000 ppm describes an soluble system.[8] Concentrations that go beyond the solubility limits can be described as saturated or super saturated. In these states the solute may still be fully dissolved, but in a 'metastable' state, whereby a nucleation point, disruption of the sample or any crystallisation event will cause a crash out of the solute. Within this study, the extent of solute dissolved will be measured as concentration, with a goal of understanding the concentration at a solubility limit.

In order to study the effect of concentration on structure a number of accessible concentrations needed to be targeted. These are shown in figure 5-1 below and are put in the context of the those found in the literature. For this study, it was desirable to link both chapters 3 (2.00 M X-ray/neutron study) and chapter 4 (variable temperature) to create a series that encompasses all models whilst approaching a solubility limit within the temperature range studied. From this series we can observe if and how the structure changes to form an initial narrative of the prenucleation cluster (PNC) structure.

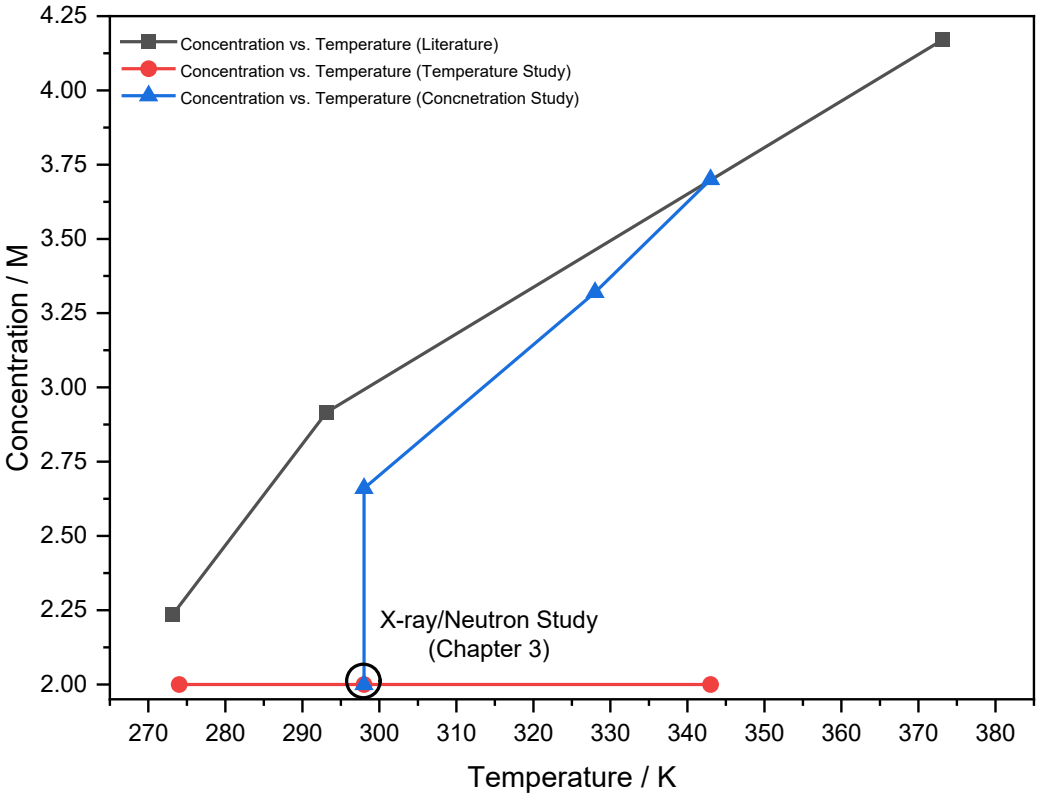

Figure 5-1. *Concentration vs. temperature plot showing the theoretical solubility curve (black), temperature study concentration (red) and variable concentration/temperature study (blue)*

Figure 5-1 demonstrates the almost linear relationship between the maximum concentration available and temperature, showing it is possible to almost double the concentration by raising the temperature by 100K. For clarity, the previous temperature study has been included, demonstrating how the series shown within this section lies within the temperature range that has been found to not alter the structure in a meaningful way. This allows for the concentration study to focus on the structural changes that are incurred due to increased solute.

The concentrations used within this experimental series were chosen to represent a wide range of conditions in which $MgSO_4$ may exist, and this is particularly important with the highest concentration experiment existing at the cusp of crystallisation to visualise a structure as close to the limits of the aqueous state. This model is most likely to represent the ions in a state prior to crystal formation and allows a glimpse as to what this structure may look like. Therefore, using the concentrations shown in figure 5-1, allows for the understanding of a variety of solution states and a deeper understanding of structure at both standard conditions, highly concentrated and on the cusp of crystallisation using an equal increase in concentration with each new system.

5.2 Experimental

5.2.1 Total Scattering Experiments

A sample of anhydrous magnesium sulfate was acquired from Sigma-Aldrich. To create the variable concentration series (B) 3.20g (2.66 M), (C) 4.00g (3.32 M) and (D) 4.45g (3.70 M) was dissolved in 10 mL of deionised water to create the desired concentrations. The 3.32 M and 3.70 M were heated on a hot plate until all solid had dissolved. All samples were loaded into 2.00 mm borosilicate capillaries purchased from Capillary Tubes Supplies Ltd. The 2.66 M sample was loaded at room temperature whilst the 3.32 M and 3.70 M was loaded hot (arbitrary temperature where no solute was visible) to ensure the correct concentration was maintained and no solute crashed out of the solution. Data collection broadly follows previous procedures; however, the 2.66 M was run without a cryostream, the 3.32 M and 3.70 M samples were heated to 328 K and 343 K respectively. The samples were heated in-situ until all solid had again fully dissolved. The samples were run for a total exposure time of 180 minutes with an exposure rate of 127 s/° oscillation. The empty capillary and empty diffractometer were then measured utilising the same parameters to obtain container and empty scattering data sets. The data sets were processed in GudrunX[9], using a sample composition and number density found in table 5-1. Other parameters, such as Compton scattering, (described in chapter 3) were adjusted to obtain the reduced total scattering function F(Q). Number density was calculated based on ambient water density due to minimal changes in the actual density of water with small changes in temperature. Density however was adjusted to account for the increased solute.

Table 5-1. *Experimental conditions for concentration series. * denotes that this measurement is the data acquired in chapter 4 (2.00 M, 298K, RTP). RTP denotes the sample was run with no external heating/cooling*

Concentration / M	Solution	Anhydrous $MgSO_4$ dissolved / g	Temperature / K	$MgSO_4 \cdot xH_2O$	Number density / atoms $Å^{-3}$
2.00*	A	2.40	RTP	27.75	0.1074
2.66	B	3.20	RTP	20.83	0.1099
3.32	C	4.00	328	16.75	0.1120
3.70	D	4.45	343	14.98	0.1137

5.2.1.1 EPSR Setup

The EPSR setups used for the concentration series largely follow the procedures, reference potentials and restraints discussed in previous sections (sections 4.1). The main aspects that required alteration were the $MgSO_4$:water ratio, but the total number of molecules was kept approximately the same for a good comparison, this allows for more direct comparisons for similar systems with regards to statistics and auxiliary routines. The box size will adjust, number density dependent, however having a similar number of atoms was decided to be the more statistically relevant variable. Temperature must also be varied to match the experimental conditions. It was also found that the same restraints used in chapter 4 could remain limited in comparison to chapter 3, and a good fit between the experimental data and model was still obtained. These values can be found in table 5-1. The only restraints utilised within the higher concentration refinements are Hw-O1s (1.50 Å) and Mg1-O1s (1.80 Å). The parameters for atomic composition are outlined in the table below.

Table 5-2. *EPSR experimental conditions. .* denotes that this measurement is the data acquired in chapter 4 (2.00 M, 298K, RTP).*

Concentration / M	**Sample**	**Number Mg^{2+}/SO_4^{2-}**	**Number of H_2O**	**Total Molecules**
2.00*	A	250	6938	7188
2.66	B	325	6770	7095
3.32	C	400	6700	7100
3.70	D	450	6741	7191

5.2.2 Refinements

Following the same checking procedures adopted in previous chapters, the refinement of the F(Q) provides affirmation of a well-fitting model. Examining figure 5-2, a good agreement between the experimental data and calculated model can be found, with the model fit accurately defining the changing total scattering as a function of concentration. These changes will be fully quantified in future sections but figure 5-2 does give the first indications that there are observable differences between the experimental data sets as concentration is increased.

The derived f(r) profiles, shown in figure 5-3, allowing for the observation of short-range interactions, also shows reasonably good agreement, suggesting that the interactions between the ions, particularly those of the metal/water clusters, are correctly modelled. Whilst there are larger

differences between the data and model than one might desire, this was attributed to the data quality, and would benefit from higher quality data, the model agrees sufficiently with the data to warrant further probing. Differences in the experimental features can be observed as we increase in concentration, and the model fit alters to incorporate these differences. Overall, both refined and derived functions suggest an alteration to the structure and therefore warrants further investigation.

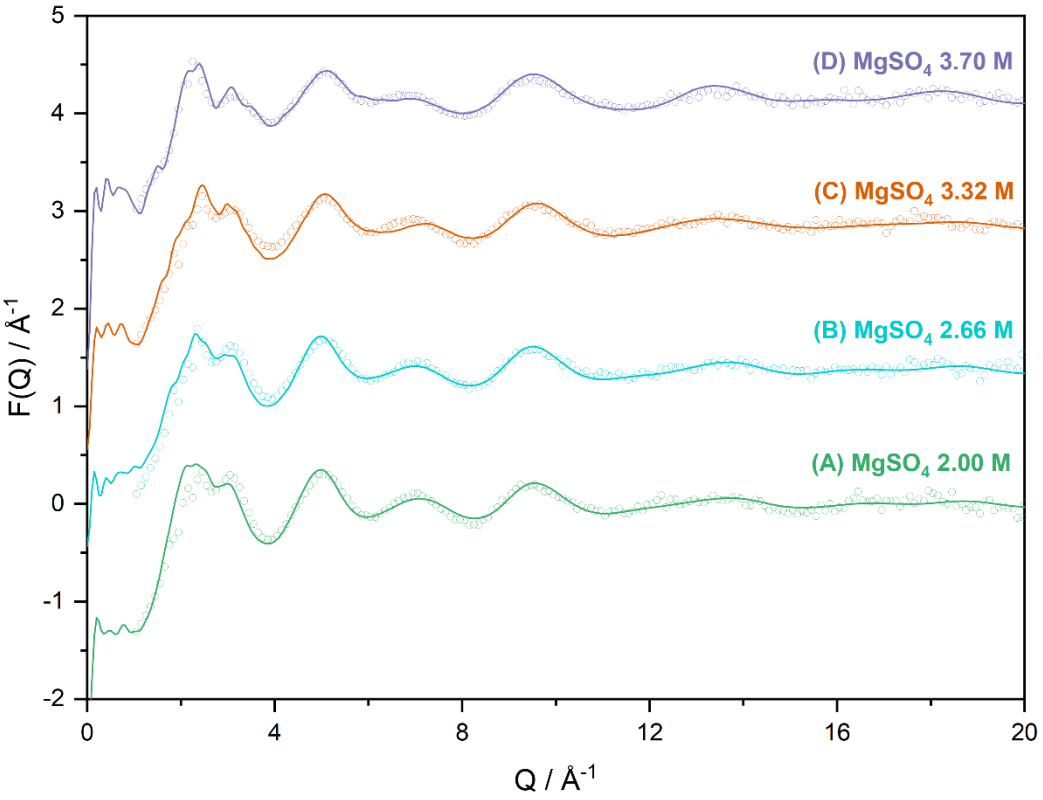

Figure 5-2. *F(Q) EPSR refined fits for (A) 2.00 M (chapter 4, green), (B) 2.66 M (cyan), (C) 3.32 M (orange) and (D) 3.70 M (purple). Circles represent experimental data, and the calculated function is show as a solid line. Refinements are offset for clarity.*

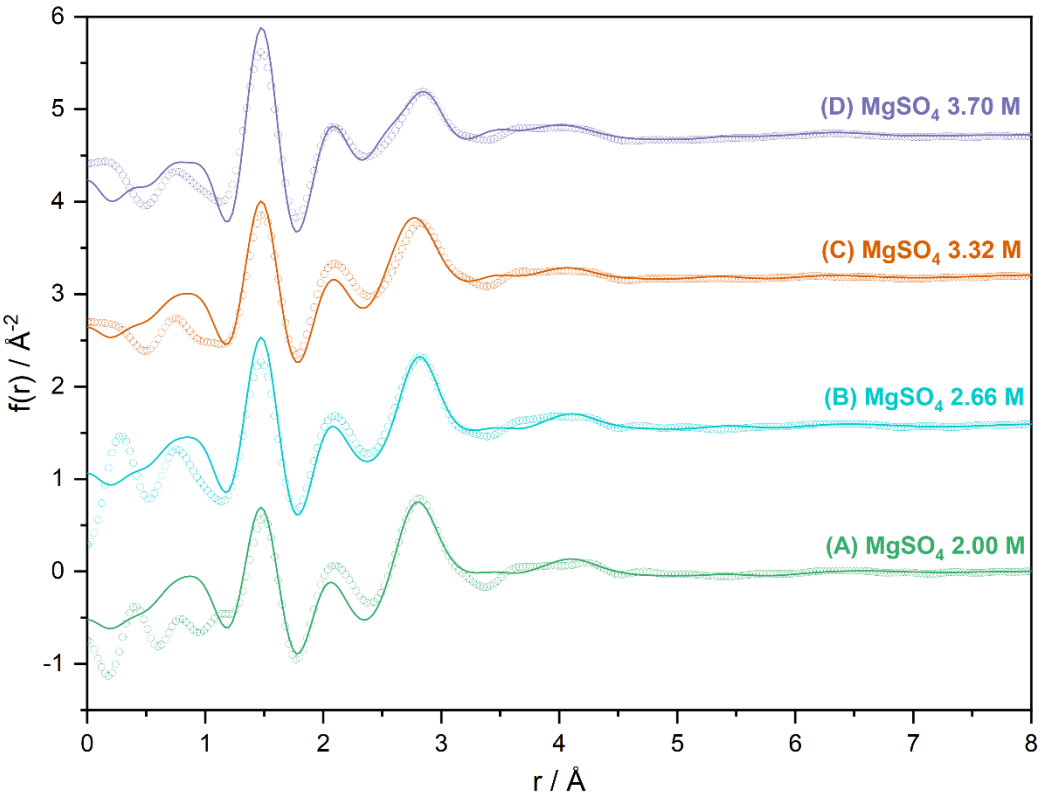

Figure 5-3. *f(r) derived EPSR refined fits for (A) 2.00 M (chapter 4, green), (B) 2.66 M (cyan), (C) 3.32 M (orange) and (D) 3.70 M (purple). Circles represent experimental data, and the calculated function is show as a solid line. Refinements are offset for clarity.*

5.2.3 Visual Interpretation of the Model Fit

As previously stated, there are observable differences between the concentrations for both the total scattering F(Q) and RDF f(r), suggesting changes in the structure due to the increased relative number of solute ions. Substantial trends can be seen in both the model F(Q) and f(r), indicating that concentration does play a role in directing structural changes within these samples. Focussing on the F(Q) initially, figure 5-4 shows many differences in the calculated fit, all indicating an increase in order as we increase the concentration. Starting in the low-Q region of the fit, we can observe the typical two peak feature between Q = 1.0 – 4.0 $Å^{-1}$, a standard feature characterised in chapter 3. These peaks become more resolved and alter in relative magnitude. The 2.00 M and 2.66 M samples remain relatively broad and unresolved, whereas at 3.32 M two sharper peaks are visible which only become properly distinct at 3.70 M, all suggesting a more 'crystalline' behaviour. By this, we are relating the structure evolving to show increasing similarities to that expected within a solid-state F(Q), sharper and more resolved features. As discussed in chapter 3 and 4, these peaks represent both the metal/water cluster and water structure, however as F(Q) is less intuitive, it is difficult to determine which part of the structure is changing to account for this difference, and therefore this will be investigated via the RDF and auxiliary routines.

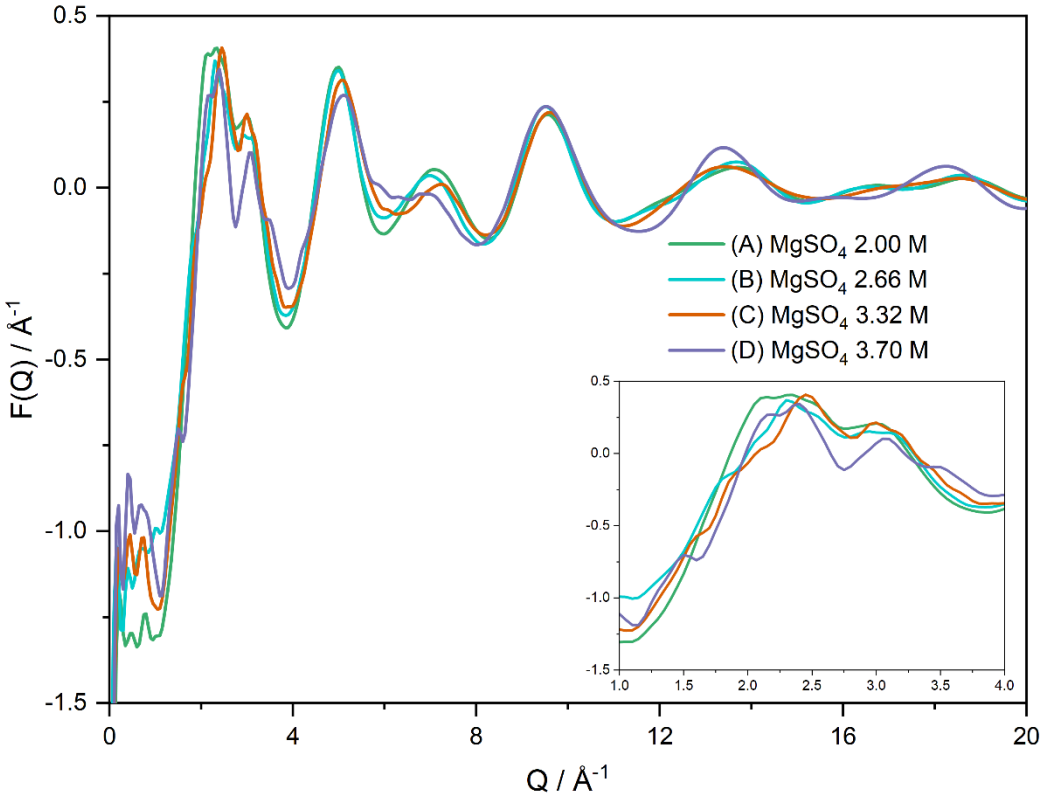

Figure 5-4. *Overlaid F(Q) calculated for (A) 2.00 M (chapter 4, green), (B) 2.66 M (cyan), (C) 3.32 M (orange) and (D) 3.70 M (purple). Inset highlights the low-Q region = 1.0 – 4.0 $Å^{-1}$.*

Looking at Q = 4.0 – 8.0 $Å^{-1}$, we can see the opposite trend occurring, where the two peaks begin to merge and become less resolved as we increase concentration. Previous discussions indicated that these two peaks are assigned to the water structure, and this decrease in the resolution indicates both further disruption to the bulk water structure but increased dominance by the $MgSO_4$ within

the total scattering. But again, the total scattering is more difficult to interpret, and further analysis will be used to quantify this statement.

The final significant difference found with the increase in concentration is oscillations in the 3.70 M sample extending to higher-Q, again more indicative of increasing order. Higher Q features in the F(Q) are indicative of longer-range structure in real space. This provides an additional piece of evidence from the total scattering that an increase in concentration allows for larger and potentially more complex structures combining the ionic components.

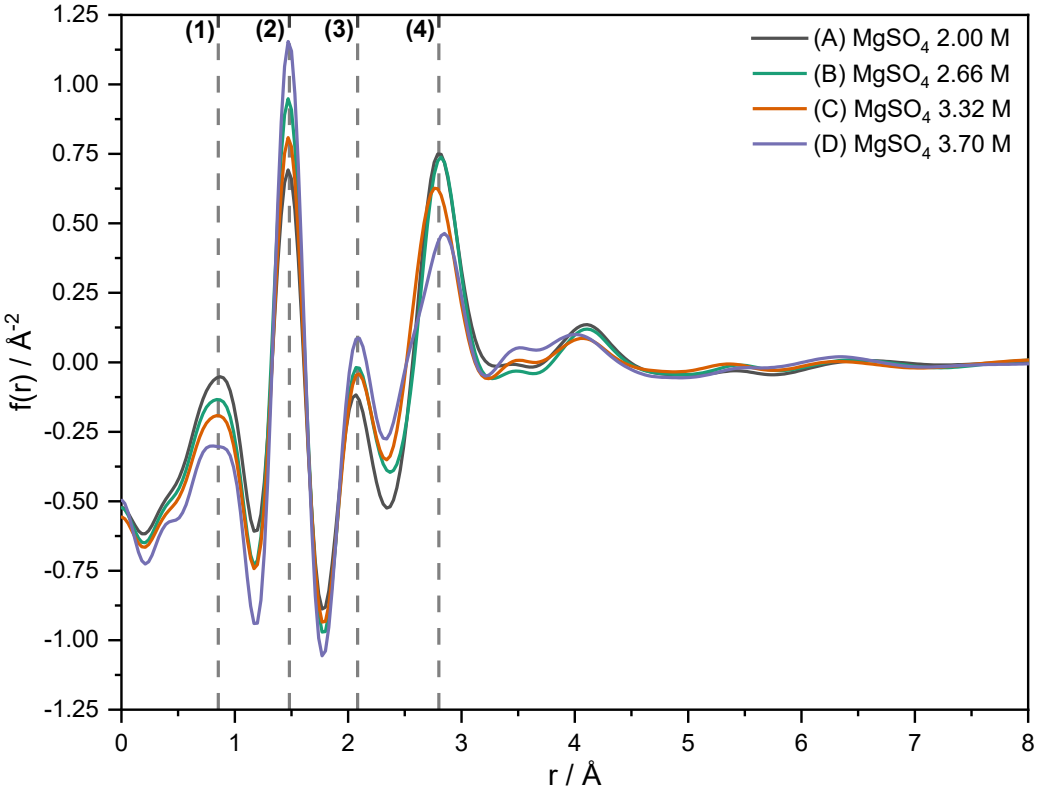

Figure 5-5. *Overlaid derived f(r) calculated for (A) 2.00 M (chapter 4, green), (B) 2.66 M (cyan), (C) 3.32 M (orange) and (D) 3.70 M (purple). Dashed lines represent key structural features (1) Ow-Hw intramolecular, (2) S1-O1Ss intramolecular, (3) Mg-Ow/O1Ss cluster and (4) Ow-Ow intermolecular.*

The derived f(r), shown in figure 5-5, gives a more intuitive description of the short-range structure. Key features observed within the RDF have been allocated as: (1) O-H water intramolecular (r = 0.85 Å), (2) S-O sulfate intramolecular (r = 1.47 Å), (3) Mg-O1S/Ow intermolecular (r = 2.07 Å) and (4) $H_2O\cdots H_2O$ intermolecular (r = 2.77 – 2.85 Å). Additional more complex features are present, and indicate further structure, particularly with regard to Mg···S intermolecular separations. These features are, however, more difficult to comprehend through simple visual inspection and these will be discussed through use of the auxiliary routines and examinations of the model.

Focussing on the intramolecular features at (1) and (2), these are determined via the fragment input rather than the refined model itself. The relative decrease in (1) and increase in (2) simply shows

the correct input of the fragment ratio, as concentration increases, the S-O will increase and O-H will decrease.

Beyond peaks (1) and (2), the features shown are representative of the structure evolving from EPSR. Peak (3) represents the metal – oxygen bond, and from previous studies in chapter 3, suggests the Mg-O1S/Ow *bond* as part of the metal/water cluster. As can be shown from this feature, the magnitude increases with concentration whilst the position remains static, this suggests that the Mg-O1S/Ow feature remains consistent in length throughout the concentrations but the coordination number increases. However, it is worth noting that the minimum occurring after this peak also increases in intensity with concentration, potentially suggesting a larger number of distances, but this needs clarification via the site-site RDF. Further queries arise from the similar magnitudes of the peaks in samples (B) and (C), where an increase in concentration does not change these peaks significantly, suggesting either structure remains constant through these samples or there is a change in the structure that does not alter the bond length or coordination. It is not possible to extract the exact change or lack thereof through visual inspection solely.

Peak (4) represents the intermolecular $H_2O\cdots H_2O$ interactions and both the peak maxima position and magnitude alter with each concentration. Overall, this indicates a progressive disruption to the bulk water structure with increasing concentration, which is to be expected with the increase in the ratio of ions:water. However, how this structure is altered cannot be determined from the RDF alone, and the atom-atom g(r), coordination number and SDF will be used.

Finally, there are features that lie beyond these four distinct peaks, and some do suggest the evolution of further and longer-range structures. The peak at r = 3.51 Å may represent an increase in the Mg-S separation, and hint at more complex structures evolving within these features. Visual inspection of both the F(Q) and f(r) indicate that the structure is changing to accommodate the increased ion ratio within the system.

5.3 Probing the Local Structure of Variable Concentration $MgSO_4$

Following the same analysis methodologies as the temperature series, each local environment will be examined in turn to probe for similarities and differences as we increase the solute concentration. This will be done by using the atom-atom g(r), coordination numbers, bond angles and SDF. Additionally, the chains routine will be utilised to compare the cluster size as we predict that the primary building blocks of the magnesium/water clusters will begin to conglomerate to form larger and more complex structures.

5.3.1 Magnesium Local Structure Changes as a Function of Concentration

The magnesium 6-coordinate structures have been a primary building unit throughout all previous refinements as well as in the literature. This is not expected to change with concentration; however, one must evaluate the g(r), coordination number and bond angle to test this hypothesis.

Figure 5-6 exhibits the atom-atom correlations for magnesium to the water and sulfate oxygens as a function of concentration. Over all concentrations, the peak positions for all magnesium-oxygen interactions remain constant, with small variations especially with regards to the Mg-O1s positions, which slowly increase from r = 1.95 Å to r = 2.01 Å. This slight increase in the Mg-O1s correlation length, does however still follow the trend of the Mg-O1s being shorter than the Mg-Ow. Bond lengths are inversely proportional to the strength of the bond, such that a bond length increase suggests a weakening bond strength.[8] This suggests a lower affinity between the magnesium and sulfate ions, and that there is potential the sulfate is being pulled away from the metal core or sharing between two magnesium ions, indicative of a more extended structure.

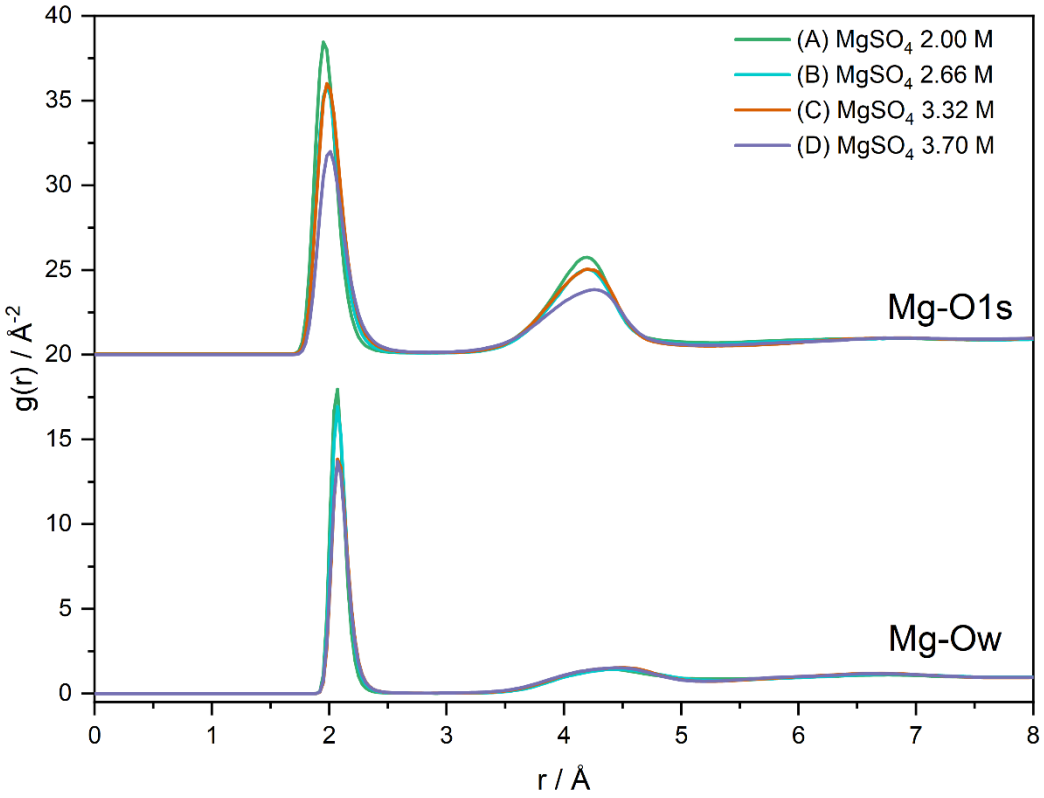

Figure 5-6. *Site-site g(r) for Mg-O1Ss (top) and Mg-Ow (bottom). Concentrations examined are (A) 2.00 M (chapter 4, green), (B) 2.66 M (cyan), (C) 3.32 M (orange) and (D) 3.70 M (purple).*

Examining the peak areas and inferring the coordination from the data allows for a deeper understanding of the structures evolving from the simulation. This is difficult to quantify by the g(r) solely, and therefore will be examined in further detail via the coordination number routine. However, one can use the integrated peak values to allow for an initial indication of the changes to coordination direct from the data itself, this is displayed in table 5-3.

Table 5-3. *Integrated areas of the features of Mg O1S/Ow (see* figure 5-6*) found using Origin integration tool.*

(Sample) Concentration/M	Mg-Ow 1st Peak Area (r = 1.80 – 2.50 Å)	Mg-Ow 2nd Peak Area (r = 3.30 – 5.40 Å)	Mg1-O1S 1st Peak Area (r = 1.60 – 2.60 Å)	Mg1-O1S 2nd Peak Area (r = 3.00 – 5.00 Å)
(A) 2.00 M	2.756	1.863	4.329	4.043
(B) 2.66M	2.741	1.811	4.069	3.714
(C) 3.32M	2.444	1.886	4.291	3.811
(D) 3.70M	2.400	1.899	3.430	3.338

By integrating the peaks, seen tabulated above, across each feature there does not appear to be a observable trend within the peak areas across all features. This suggests that changes are either

minimal or non-observable within the site-site g(r) or that these changes can only be correlated to localised differences in the structure. Examining each feature in more detail, Mg-Ow 1st peak shows a similarity in peak area for (A) & (B) and then (C) & (D), suggesting a similar higher coordination in the lower concentrations that change to a slightly lower coordination for the higher concentrations. This suggests a structural alteration to the Mg-Ow structure and less affinity for the water to the magnesium. This trend does not appear to continue with the 2nd Mg-Ow feature where the areas remain relatively consistent, suggesting no change to the longer-range structure.

The 1st Mg-O1s feature suggests that the first three concentrations (A to C) show small changes, however they do not follow a particular trend. This lack of trend is even more apparent with the significant drop in area by concentration (D), with a drop of 0.861 from (C). This warrants a more detailed inspection via more intuitive routes such as the coordination number which examines the model rather than the data. The 2nd feature shows more of a trend of an overall reduction in the peak area, but again this is not a consistent trend, with a plateauing/slight increase in the peak area between (B) and (C). Overall, the Mg-O1s peak areas do not show an obvious correlation, and therefore using the site-site g(r) to examine any changes in structure is rudimentary and requires more complex investigation to fully interpret these changes.

5.3.1.1 Coordination Number Mg-O1s/Ow as a Function of Concentration

The coordination numbers in figure 5-7 show a definite trend for the coordination environment around magnesium, where increasing concentration skews the 6-coordinate cluster towards higher sulfate coordination. A constant that has remained from previous refinements is the confirmation of a 6-coordiante species, as demonstrated once again by the almost symmetrical nature of the plot. This overall suggests that the 6-coordination metal cluster remains a constant primary building block throughout.

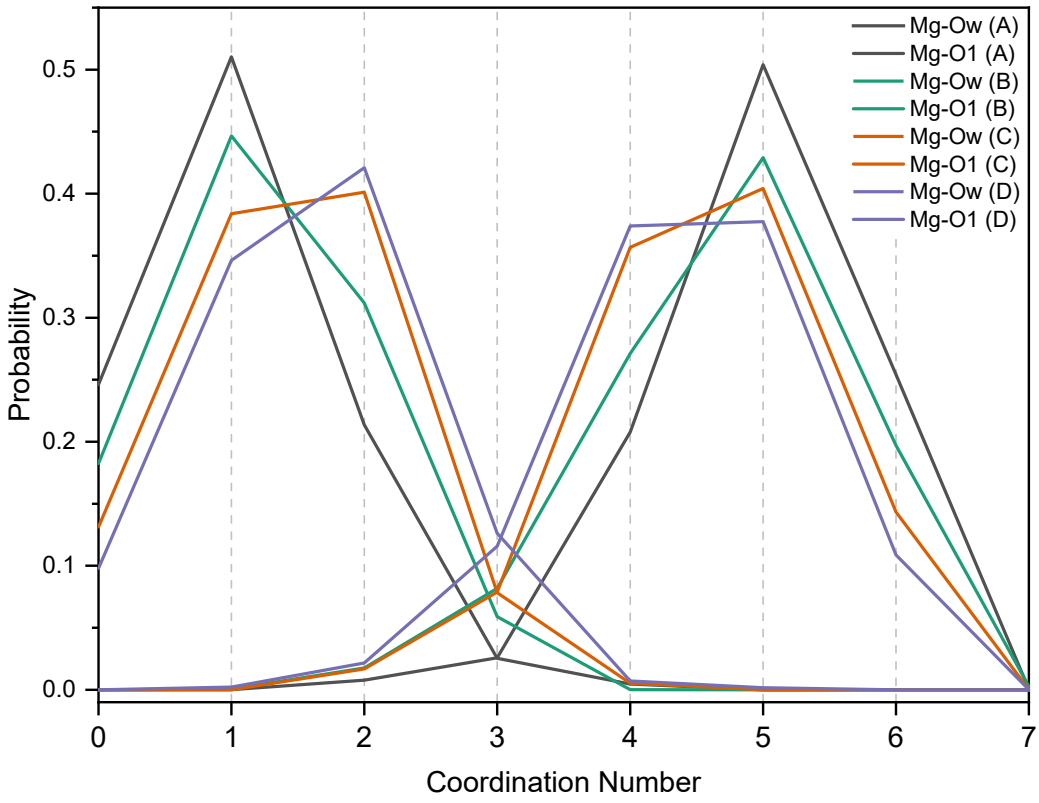

Figure 5-7. *Coordination numbers for Mg O1s (double line) and Mg Ow (solid line) over concentrations (A) 2.00 M (chapter 4, green), (B) 2.66 M (cyan), (C) 3.32 M (orange) and (D) 3.70 M (purple). Coordination exists over a range of r = 1.0 – 3.0 Å.*

Focussing on the coordination numbers here, the peak maxima increases towards higher sulfate coordination as we increase concentration. Previous refinements have shown that most of the magnesium clusters existed as $MgSO_4(H_2O)_5$ (~50%), $Mg(H_2O)_5$ (~25%) and $Mg(SO_4)_2(H_2O)_4$ (~20%), with coordination being mostly to water. However, as we increase the concentration, the $Mg(SO_4)_2(H_2O)_4$ becomes increasingly prominent to the point where it is the dominating species within the model at 3.70 M. This increase in sulfate coordination is paralleled by the decrease and change in maxima for Mg-Ow, showing how the increase in solute displaces the water within the coordination environment.

Overall, the skew towards higher sulfate coordination is likely fuelled by the increase in solute and decrease in water. This increases the probability of the two ions being within a coordinating range and this skew to higher sulfate coordination can be visualised in figure 5-8.

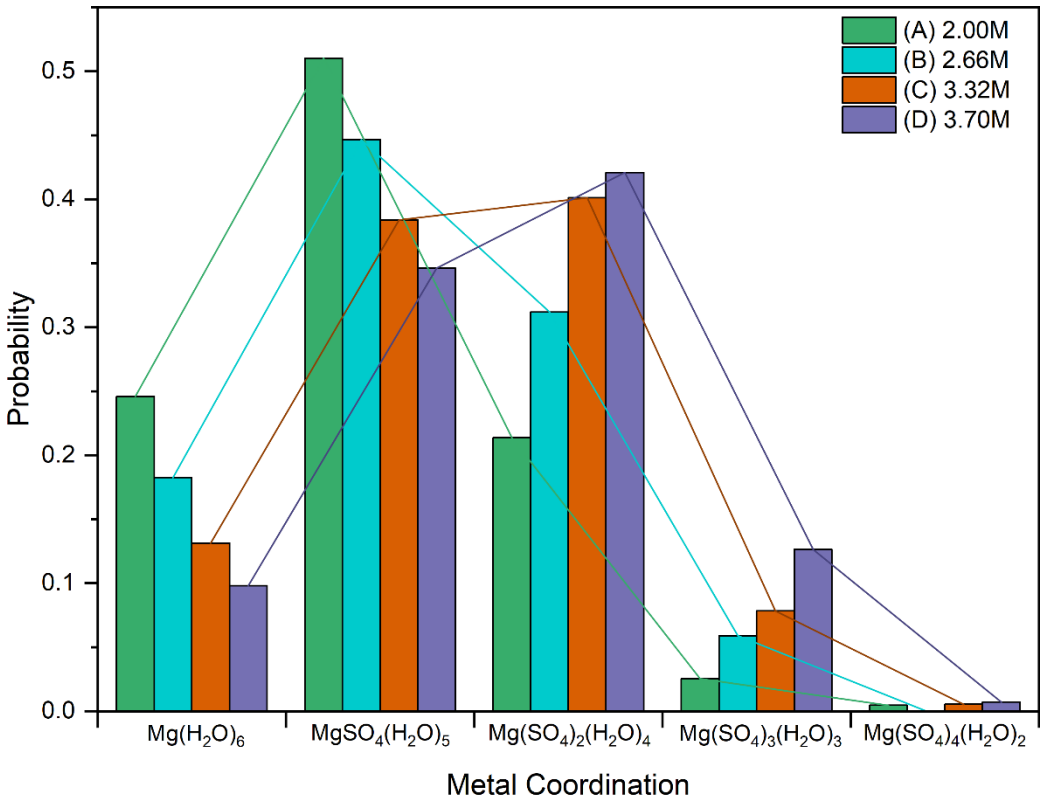

Figure 5-8. *Magnesium cluster probability defined by the probability of Mg-O1s interactions, found by the coordination numbers in figure 5-7. Concentrations examined are (A) 2.00 M (chapter 4, green), (B) 2.66 M (cyan), (C) 3.32 M (orange) and (D) 3.70 M (purple). Lines are used to define the overall trends found within the histogram.*

In summary, it can be found that the magnesium coordination becomes more sulfate rich as we increase the concentration. This is partly due to the increased density of solute within the model, increasing the probability of the ions being within a coordination range, as well as the reduced ratio of ion:water. The skew towards higher sulfate coordination does suggest the potential of larger structures forming, as two sulfate ions coordinated to one magnesium creates a negatively charged moiety. Therefore, it must be stabilised by either additional magnesium ions, creating a longer chain, or by water stabilisation, discussed previously in section 3.3.5.

5.3.1.2 Bond Angles Mg-O1s/Ow as a Function of Concentration

Inspecting the Ow-Mg-Ow bond angle, found below in figure 5-9, we can see that the ~90° and ~180° maxima still remain across the concentration range, but there is perhaps, more subtle structural variation observable. Examining the pseudo 90° angle, there is an overall trend of an initial decrease in angle (B), which eventually splits into two partly-resolved features in (C) and (D), the latter of these features existing at higher angle.

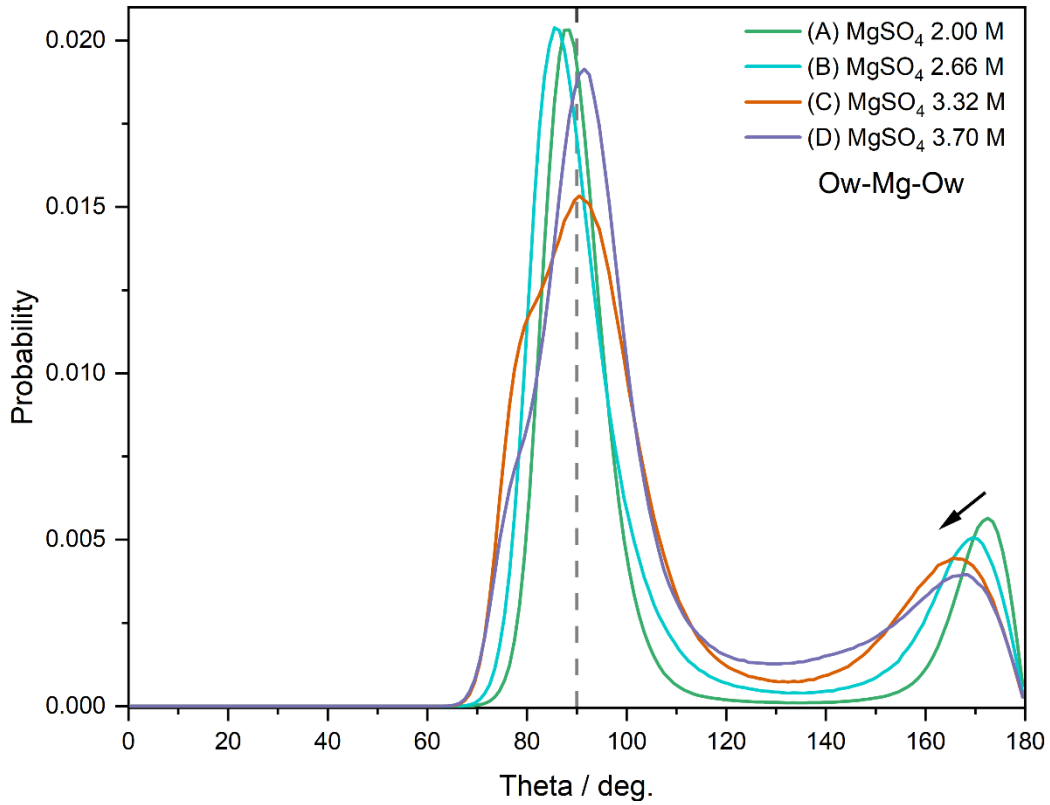

Figure 5-9. *Ow-Mg-Ow bond angle over concentrations (A) 2.00 M (chapter 4, green), (B) 2.66 M (cyan), (C) 3.32 M (orange) and (D) 3.70 M (purple). Arrows denote the overall trends observed within the routine.*

The 2nd derivative method, as implemented in Origin, was used to fit these features using a number of Gaussian peaks.[10] The results for (C) and (D) are show in figure 5-10 and figure 5-11. These peak fits truly highlight the range of coordination angles present for this relatively simple angle. For both (C) and (D) concentrations, the most dominant feature is that of the angle closest to 90°, unsurprising for the octahedral geometry. However, (C) does exhibit two fairly dominant features at 77.5° and 99.5°, showing a deviation of around 10° from the ideal, suggesting a significant structural change. The driving force for this observed deviation in bond angle is the increasing sulfate coordination to the magnesium. As discussed in section 3.3.4, the steric impact of these bulky constituents forces a larger range of bond angles to accommodate their presence, and therefore cause a greater range of angles.

The bond angle at approximately 180° becomes progressively broader as we increase from 2.00 M to 3.70 M. This implies a larger range of trans coordinated water angles, suggesting a larger range of conformations. Again, this increasing distribution is likely catalysed by the increasing sulfate coordination.

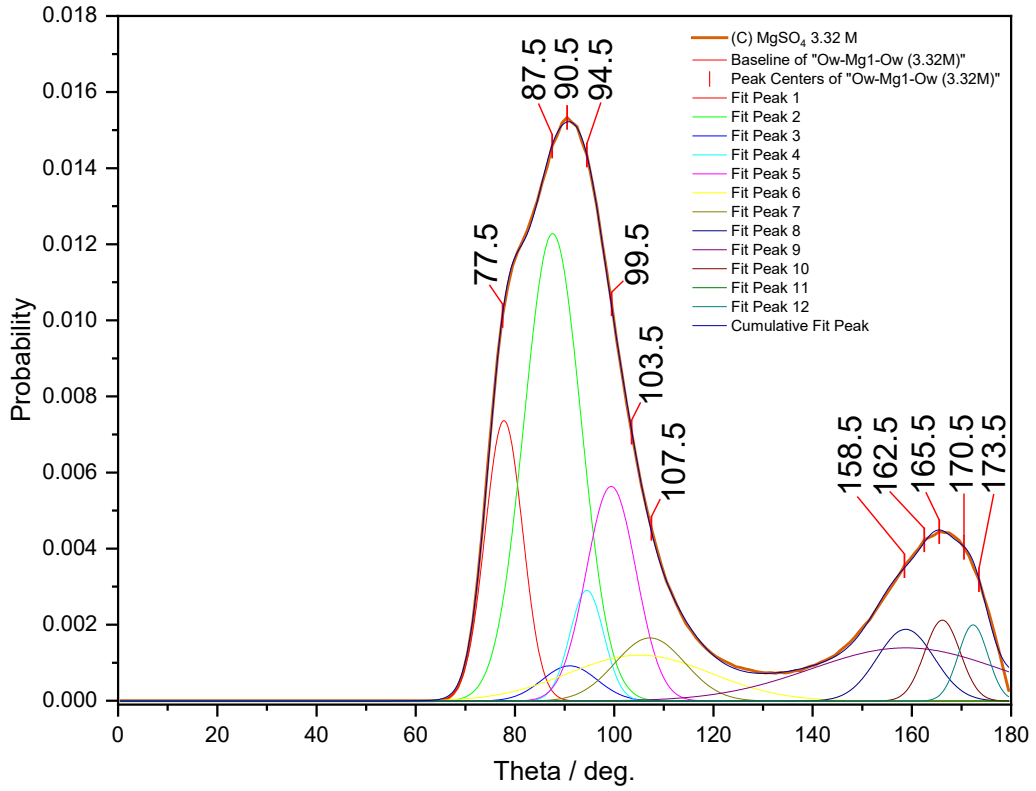

Figure 5-10. *Peak finder and peak fit in Origin for (C) 3.32M. Numbers represent the peaks found from the plot using 2nd derivatives, which were then used to fit Gaussian features to.*

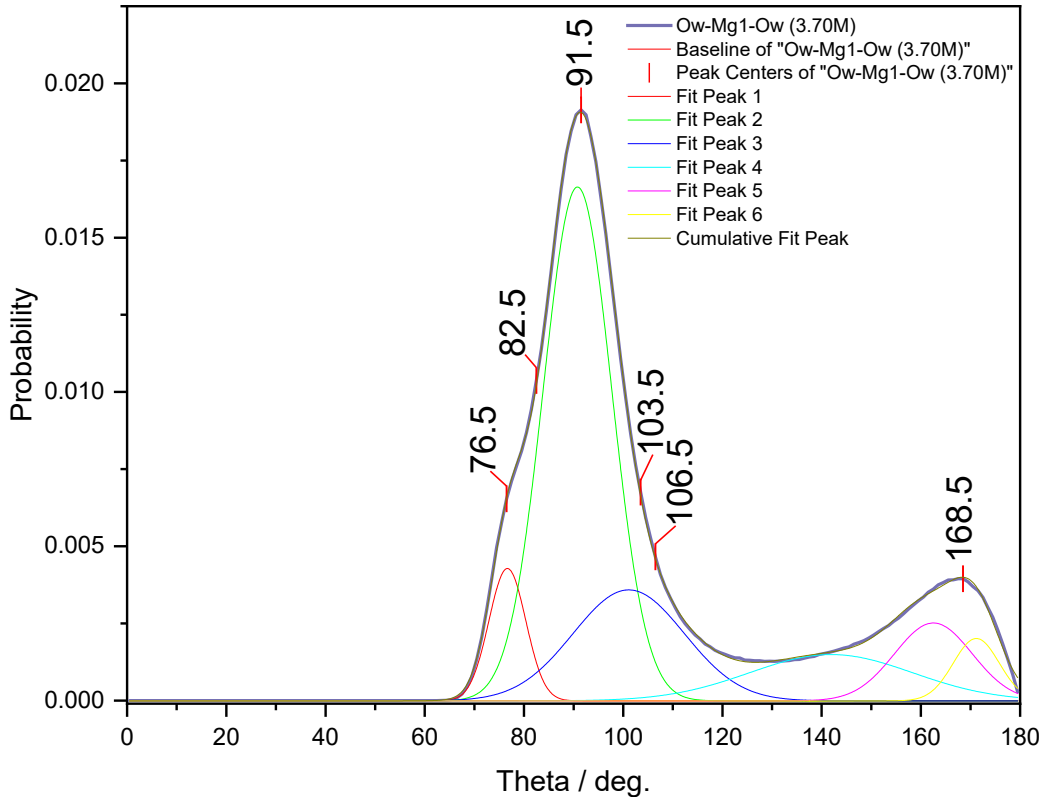

Figure 5-11. *Peak finder and peak fit in Origin for (D) 3.70 M. Numbers represent the peaks found from the plot using 2nd derivatives, which were then used to fit Gaussian features to.*

The Ow-Mg-O1S bond angle, shown below, follows a similar trend, where the bond angle peak centre for the <90° decreases with increasing concentration. The distribution of angles increases in

asymmetry, showing a preference to a lower bond angle. Although the pseudo-octahedral geometry is likely to remain throughout all concentrations, the decrease of approximately 10° demonstrates a fairly significant distortion to this structure.

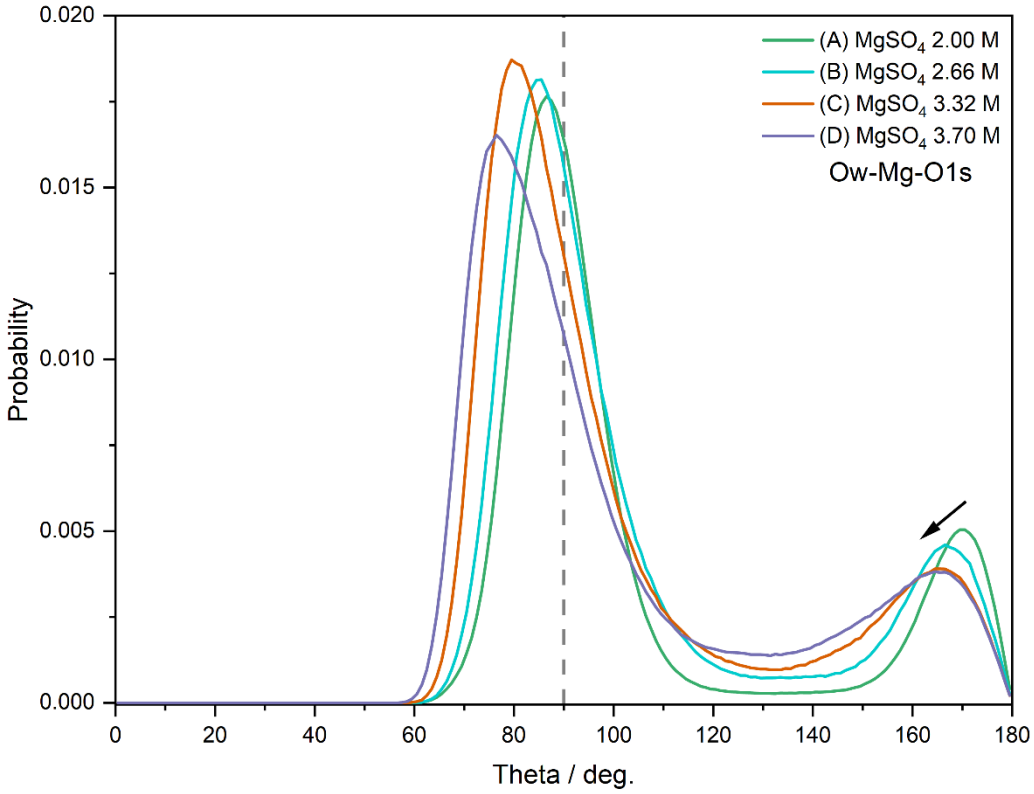

Figure 5-12. *Ow-Mg-O1s bond angle over concentrations (A) 2.00 M (chapter 4, green), (B) 2.66 M (cyan), (C) 3.32 M (orange) and (D) 3.70 M (purple). Arrows denote the overall trends observed within the routine.*

Larger angles at ~180° follow the same trend as seen in Ow-Mg-Ow, where the magnitude decreases but distribution increases with increasing concentration. This can again be explained by the increased sulfate coordination forcing a larger range of values to accommodate the bulkier sulfate.

O1S-Mg-O1S is the final bond angle distribution of interest, found in figure 5-13, demonstrating how the sulfates orientate around the magnesium ion, however, they do not exhibit an obvious trend. Angles around 90° do show two regions of angles, with the lower concentrations being approximately 105° and the higher concentrations at 96.5°, showing an increase in the concentration forces two sulfates closer to a perfect 90° angle. The increase in sulfate coordination with increased concentration is likely to force cis coordination sulfate closer to one another, overcoming the steric repulsion.

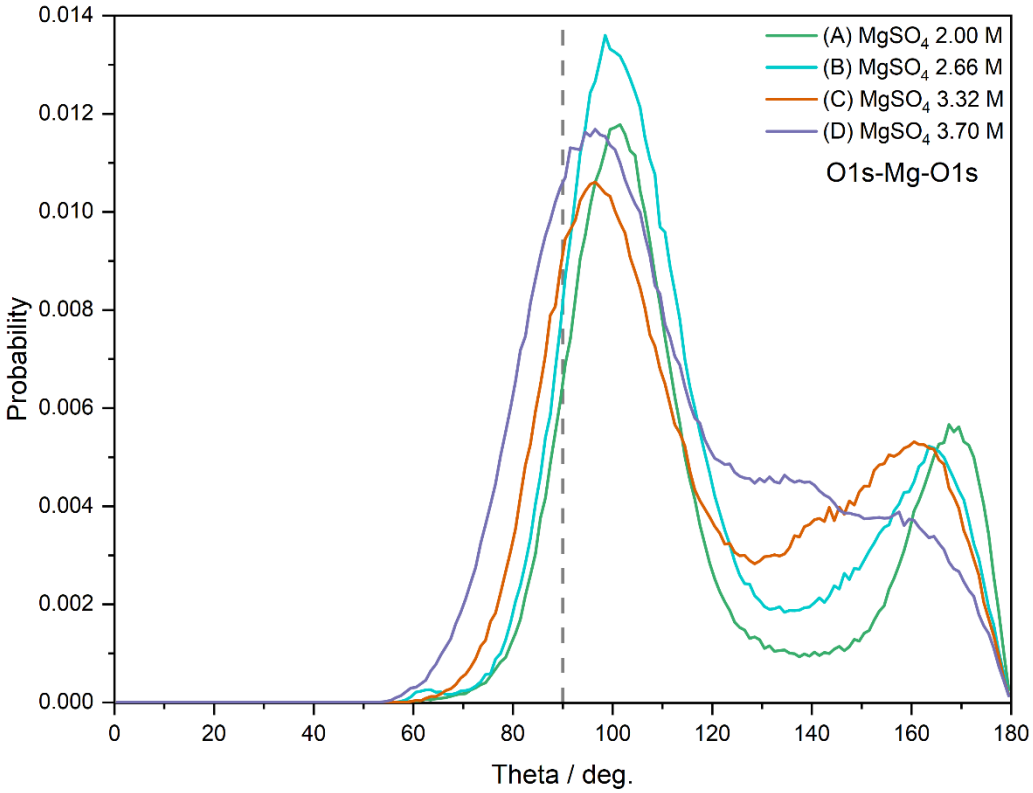

Figure 5-13. *O1s-Mg-O1s bond angle over concentrations (A) 2.00 M (chapter 4, green), (B) 2.66 M (cyan), (C) 3.32 M (orange) and (D) 3.70 M (purple). Arrows denote the overall trends observed within the routine.*

The larger angle here becomes much less defined, and eventually becomes a tail off from the peak at around 90° as we increase concentration. Increasing distributions suggest a less defined trans-sulfate structure, becoming almost non-existent at 3.70 M, and being replaced with a broad range of possible angles. Overall, this suggests a decrease in this configuration despite the increasing sulfate coordination and defining the cis-conformation as the more stable structure.

5.3.2 Extended Cluster Structure

As discussed in previous sections , the increased sulfate coordination to the magnesium/water clusters causes changes in the bond angles and ultimately suggests an increase in size of these connected structural elements. This is further corroborated in the f(r), which displays significant features to higher-r, indicating longer-range structure is forming as a result of the increasing concentration. Based on the primary magnesium MgO_6 octahedra, a chain lengths calculation was conducted to evaluate the extended structures. Using the S1-O1S-Mg as the target fragment, a search was made to identify chains of ···S1-O1S-Mg-O1S-S1···, with the calculation parameters defined in table 5-4.

Table 5-4. *Chains calculation parameters used in EPSR, the corresponding output can be found in figure 5-14. Atom 1 states the atom type, rmin/max12 states the minimum/maximum atom-atom*

correlations between atoms type 1 & 2 (interchangable between atom types). Anglemin/max213 states the minimum and maximum angles between atom types 2-1-3.

Parameter	Atom 1	Atom 2	Atom 3	rmin 12	rmax 12	rmin 13	rmax 13	rmin 23	rmax 23	anglemin 213	anglemax 213
Value	S1	O1s	Mg1	1.0 Å	3.0 Å	1.0 Å	6.0 Å	1.0 Å	3.0 Å	0.0°	180.0°

Figure 5-14 shows the chain length distribution effectively describing how many S1-O1S-Mg units are observed within this path and shows a definite increase in the cluster size with almost 3x the number of these units in the 3.70 M concentration compared to the original 2.00 M sample.

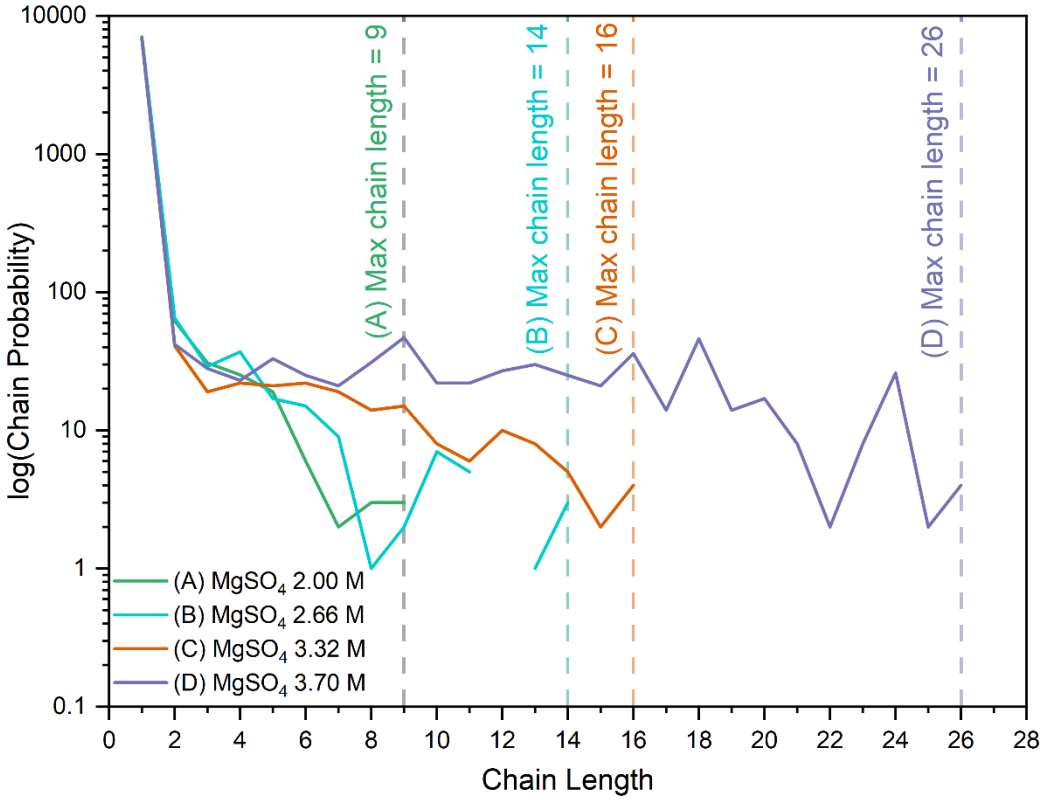

Figure 5-14. *Chain length distribution over concentrations (A) 2.00 M (chapter 4, green), (B) 2.66 M (cyan), (C) 3.32 M (orange) and (D) 3.70 M (purple). Dashed lines denote the maximum chain length.*

To put these chains length values into a more readily visualised context, the refined model was examined, and examples of common structural features identified by visual examination. '*Common fragments'* within each refined model are shown in figure 5-15, demonstrating the evolution of the structures found as concentration increases. Here 'common fragments' are defined as the most often observed through visual inspection of the model and reference to the chain lengths detailed in figure 5-14. Taking each concentration stepwise, we can see how these structures form from the primary magnesium octahedra building unit at 2.00 M, extending by joining these building blocks into chain like structures. These chains eventually begin forming ring structures and all eventually form a more extended branched structure.

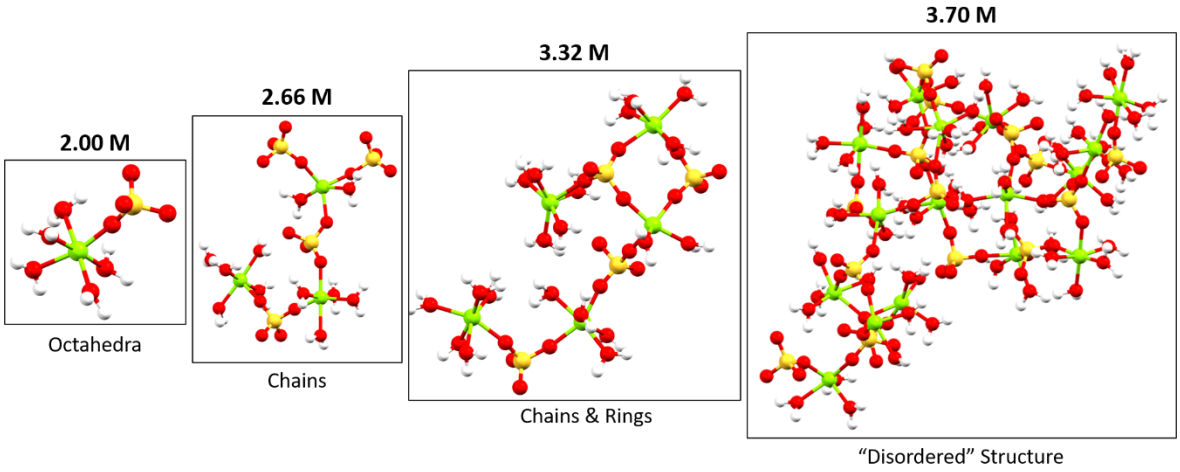

Figure 5-15. *Extracted 'common' fragments from each refined model concentration. These can be defined as the octahedra, elucidated from chapter 3, chains where octahedra are joined in straight and branched chains, rings where the linear structures join to form a ring, and "disordered" structure where all features are present and form structure that has similarities to the solid state.*

The structure fragment depicted for 2.00 M is representative of the bulk structure found at this concentration, as extensively discussed in chapter 3. The chains calculation in figure 5-14 shows that there are some occurrences of more extended structures in the form of longer linked chains, however these tend to be short and made up of no more than 3 of each ion. Another interesting observation is that when extended chains do occur, it is typical to find equal numbers of the oppositely charged ions. Treating each ion as a point charge rather than individually charged atoms, as defined by the reference potentials in EPSR, it is understandable that equal numbers of each ion are present in each chain to balance the overall charge and create a neutral molecule. Whilst EPSR and its code does not drive towards neutral molecules, it does however attempt to create a system in which energy is minimised, and a large stabilising factor here would be minimising charges. It is worth reiterating that the energy minimum in EPSR is not the most energetically minimal system, but the system in which the empirical potential is added to allow for interactions between molecule to occur rather than an unrealistic equilibrated state, as discussed in chapters 2 and 3. This agrees with the previous hypothesis that these ions interact as contact ion pairs (CIPs) in order to stabilise the charges and create an overall uncharged system. Whilst CIPs do not fully summarise all of the interactions around these octahedra, with solvent stabilisation being another contributing factor, it is shown how they are perhaps the biggest contribution to the ion stabilisation.

Increasing the concentration to 2.66 M, we observe both an increase in the chain length and the emergence of larger clusters in the refined model. The chain calculation suggests a 55% increase in chain length, with an apparent absence of any chains of length 12.

At 3.32 M, we observe a new structural motif forming, and that is the ring structure, with an 8-membered ring appearing to be the common size. This concentration is where we observe the

largest change in most calculations, such as g(r), coordination number and bond angles, and the formation of this ring structure. Observing the chain length, we only see an increase of 2 whilst seeing a significant change in the other auxiliary routines, suggesting that the chain lengths are not increasing significantly with the increased ion concentration, but we are actually observing a structural transformation from chains to rings.

Re-examining the coordination numbers, it is at 3.32 M that we first see the change from $MgSO_4(H_2O)_5$ to $Mg(SO_4)_2(H_2O)_5$ as the modal conformation, which agrees with the visual analysis and ring formation. As the rings form, each magnesium and sulfate will see at least two of its oppositely charged ion regardless of the position within the ring, causing this shift to this higher sulfate coordinating conformation. We can also observe an increase in the $Mg(SO_4)_3(H_2O)_3$ coordination, which can also be observed in the refined model and in figure 5-15, demonstrated by the branched chain off of the ring. As shown in figure 5-11, there are bond angle maxima occurring at 77.5°, 90.5° and 99.5° for the Ow-Mg-Ow bond angle, and these configurations are likely to be introduced from increased strain around the octahedra, such as the $Mg(SO_4)_3(H_2O)_3$ branched ring structure, where the water is likely pushed much closer together to allow for both the ring structure and 3-coordinating sulfate ions. As the sulfate is in a more locked position closer to 90°, as shown by the O1S-Mg-O1S bond angle in figure 5-13 as it forms this favourable ring, it allows for more freedom in the water ligands and larger angles between.

Finally, at the highest concentration within the series, at 3.70 M, we see another dramatic increase in the chain length - 62.5% longer than in the 3.32 M structure. This an increase in chain length rather than a structural change (such as the appearance of other structure modes) as was seen between 2.66 M and 3.32 M. This can be confirmed by looking at the coordination numbers and comparing them with the 3.32 M values, where we only see a slight increase in the $Mg(SO_4)_2(H_2O)_4$ conformer, suggesting no major increase in structure types. We do observe a slightly bigger increase in the $Mg(SO_4)_3(H_2O)_3$ conformer, suggesting formation of more branches within the chains as well as off of the rings. The emerging structure is beginning to appear more ordered and rigid and this is also evidenced in the tighter distribution of water-water bond angles at ~90°, suggesting that the increased ion concentration forces the structures to become less flexible. What we are observing therefore, is the emergence of what might be labelled “disordered structure”, where we begin to observe repeated patterns of fragment clusters and rings begin to join at both the edge and corner, resembling what would be expected in the crystalline hydrate structures.

Overall, we do see an evolution in the structure, with it slowly resembling a more solid-state structure with an increase in concentration. Whilst previous studies have elucidated some features, such as increasing coordination number and alterations to the atom-atom distances and

coordination, none have been able to extract structural information in such detail as this. Observing how the structure changes with concentration, we can begin to lay the foundations for how $MgSO_4$ begins to crystallise from the earliest points. Using the octahedral structure as a primary building block, these begin to join and create more complex structures to a point where solid-state structural features are observable within the model. Not only this, but we can also begin to narrow down at what concentration these motifs begin to occur, with a point between 2.66 M and 3.32 M ring formation becomes more prominent suggesting the very early stages of crystallisation. This study is very much a beginning in the elucidation of crystallisation, but it does go beyond the level of previously reported detail obtained via experimental and theoretical studies and lends itself to much further work.

5.3.3 Local Structure Around Sulfate as a Function of Concentration

The local structure around the sulfate has been of particular interest in this study, with limited previous information available, especially within a large-box model with access to the multitude of possible structural modes. Through the evaluation of the structure around the magnesium ion, it is shown how the sulfate becomes more involved within the coordination structure, however it is also important to probe the stabilisation provided by the intermolecular interactions with the water.

Using the g(r) will elucidate whether in general we observe the same structure as described in section 3.3.5. Whilst one may expect the structural relationships between the sulfate ion and water to remain relatively constant, the introduction of more extended structures in the form of chains and rings may well disrupt this and introduce a different local environment.

The atom-atom correlations observed in figure 5-16 show the interactions between the sulfate and surrounding water, and whilst the general shape of the features remains similar across the series, there are some obvious trends. Firstly, the fact that the general shape of the g(r) remains constant throughout the series suggests that the structural features elucidated in section 3.3.4 remain true even with the increased ion presence. In fact, the structure for S1-Ow suggests that the first solvation shell around the sulfate ion decreases in distance, suggesting that the solvation shell is compressed around the sulfate ion. This is corroborated with the increase in the magnitude of the peak area suggesting an increase in coordination number within this region. Beyond this region, the S1-Ow becomes less defined with increasing concentration, suggestive of a disruption caused by the additional ionic concentration, slightly diminishing the longer range sulfate-water structure.

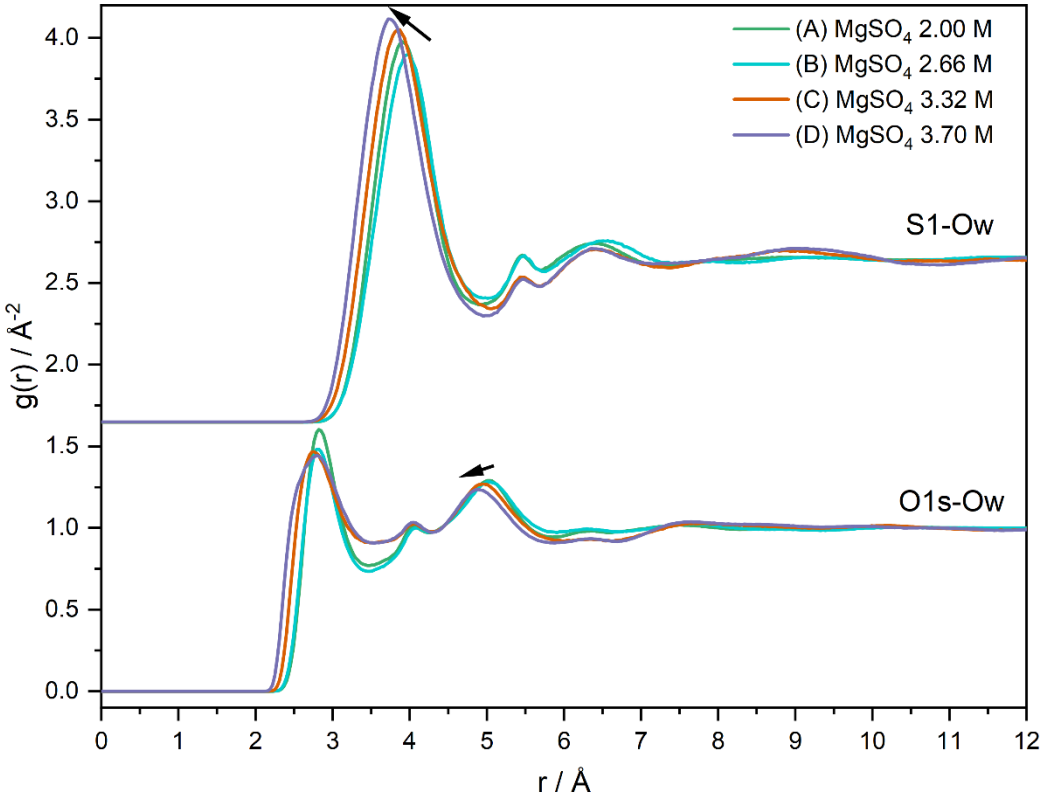

Figure 5-16. *Site-site g(r) for S1-Ow (top) and O1s-Ow (bottom). Concentrations examined are (A) 2.00 M (chapter 4, green), (B) 2.66 M (cyan), (C) 3.32 M (orange) and (D) 3.70 M (purple). Arrows denote the general trend in the features.*

The O1s-Ow structure is perhaps less defined than the S1···Ow structure, which is unsurprising considering the larger degree of freedom available to the sulfate oxygen compared to the sulfur itself. The general trend of the first feature for O1s···Ow is an increasing distribution of distances as concentration increases, all of which trend towards lower-r, agreeing with the hypothesis of the first shell structure being compressed and water-sulfate interactions being at a closer range. At r = 4.05 Å, containing some of the 2nd solvation shell character, the features mostly overlap at the peak maximum and suggests that this interaction remains unchanged. The other 2nd shell interactions situated at r = 4.90 – 5.02 Å, further confirm the compression of the water upon the sulfate structure.

Whilst the g(r) is useful for quantifying atom-atom distances, it is difficult to define the structure itself. The atom-atom RDF does suggest that the water interacts with the sulfate ion within closer proximity with the increase in ionic concentration, forcing the water within a closer range. This increase in water density around the sulfate will be further investigated.

5.3.3.1 Coordination Number for S1-Ow as a Function of Concentration

Coordination number was used within section 3.3.4 to compare with the literature to observe whether our EPSR model was similar to that found within the computational studies.[7,11–14] Furthering these comparisons, we will use the coordination number to define whether the

introduction of increasing numbers of Mg^{2+} and SO_4^{2-} ions to the water causes an increase in water density around the sulfate.

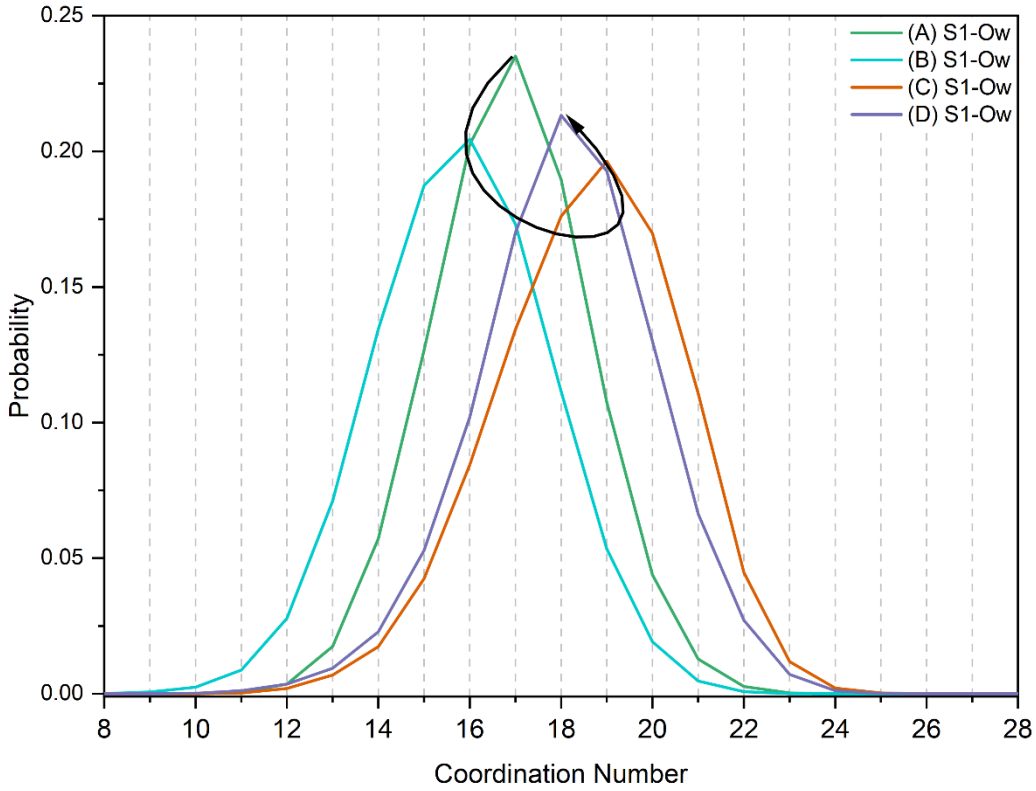

Figure 5-17. . *Coordination number for S1-Ow over concentrations (A) 2.00 M (chapter 4, green), (B) 2.66 M (cyan), (C) 3.32 M (orange) and (D) 3.70 M (purple). Coordination exists over a range of r = 1.0 – 5.0 Å.*

Figure 5-17, shown above, displays the S1-Ow coordination for all concentrations examined within this series, each displaying an almost Gaussian distribution. An interesting trend can be extracted from the coordination, showing that the lowest and highest concentrations (A & D) have similar maxima at 17 and 18 respectively, whilst the middle concentrations (B & C) have maxima at the upper and lower limits of 16 and 19. This is perhaps not what is expected from such a model, where one would expect the coordination to linearly increase with increasing concentration, however examining the model some reasonable outcomes can be formed.

As we increase concentration, a variety of structural changes take place to incorporate the increasing structures and building units, discussed in more detail in section 5.3.2. Essentially what we observe is a varying degree of sulfate···water interactions that are driven to accommodate the buildings units observed, such as the longer chains at concentration (B) and the ring formation at concentration (C). It can be found that the water can be used to stabilise these structures, particularly upon the sulfate ion, when more sterically hindered structures are forming.

Furthermore, it is likely that water forms part of the larger intermolecular structure, using hydrogen bonding to form stabilised structures. As they incorporate more into this larger structure, an

increasing number of water molecules can interact within the distance ranges specified and therefore increase coordination. Overall, this trend can be explained by the use of water molecules to stabilise the ever-growing structure being formed, and that more energetically favoured structures, such as chains and more complex, crystalline-like structures, require less water to stabilise compared to sterically hindered and isolated rings.

5.3.3.2 SDF for SO_4@H_2O as a Function of Concentration

As we try and understand how the water will typically arrange itself around sulfate, defined by the octahedral and tetrahedral probability densities discussed in previous chapters, we can investigate whether this structure alters to accommodate the increased number of ions.

At a high-level view the SDFs, shown in figure 5-18, follow a similar trend in shape and across the full range of concentrations and isosurfaces plotted suggesting, that in general, the $SO_4 \cdots H_2O$ structure does not undergo any abrupt change but only slight modification. Starting at 1%, sample (B) shows a preference to the tetrahedral mode rather than the octahedral seen in the other samples, and whilst the octahedral mode does emerge with an increase isosurfaces percentage, it still appears weaker than its counterparts. This deviation from the general trend does suggest that the bridging mode, discussed in section 3.3.4, is disrupted by the chain formation, but then reforms even stronger at higher concentrations. Throughout (B) the tetrahedral mode remains dominant, suggesting that more of the structure is along the S-O bond or capping this bond rather than the bridging mode suggested by the octahedral nodes.

Sample (B) shows a much closer resemblance to the original study (A) structure, dominated by both the octahedral and tetrahedral mode, showing that the ring and chain structure is stabilised in a similar way to the primary octahedral unit.

The highest concentration sample at (D) 3.70 M shows similar areas of probability density to previous samples, however they appear more defined and begin to show more distinct structural nodes. Prominently we observe the octahedral nodes joining to create an overarching structure, encompassing the sulfate ion and overpowering the tetrahedral bonding modes. These nodes appear more linear, suggesting a decreased distribution of molecular positions around the sulfate and a more discrete arrangement as seen in the solid-sate, not too dissimilar to the case of the environment around the magnesium. This is particularly interesting for this structure, and like the more crystalline behaviour being observed around the magnesium, similar intermolecular structure appears to be evolving around the sulfate. The octahedral mode is similar to the double H-bonded, bridging water structure at lower hydrations as discussed by Kulichenko et al.[15], and this would

agree with the disruption to the longer-range water structure, where a limited number of water molecules could actually interact with the sulfate.

The tetrahedral structure around the sulfate at this concentration is decreased with smaller nodes only beginning to be observed at 10% rather than 1-5% found in lower concentrations. This suggests that the increase in structure and ionic concentration inhibits this bonding mode in favour of the octahedral mode, which is not unexpected as the lower concentrations show a preference for this mode. Even at higher isosurfaces percentages, we see more discrete structure rather than the homogenous structures seen at lower concentration. By 30%, the SDFs for all concentrations are largely comparable, and any structure differentiating power is lost.

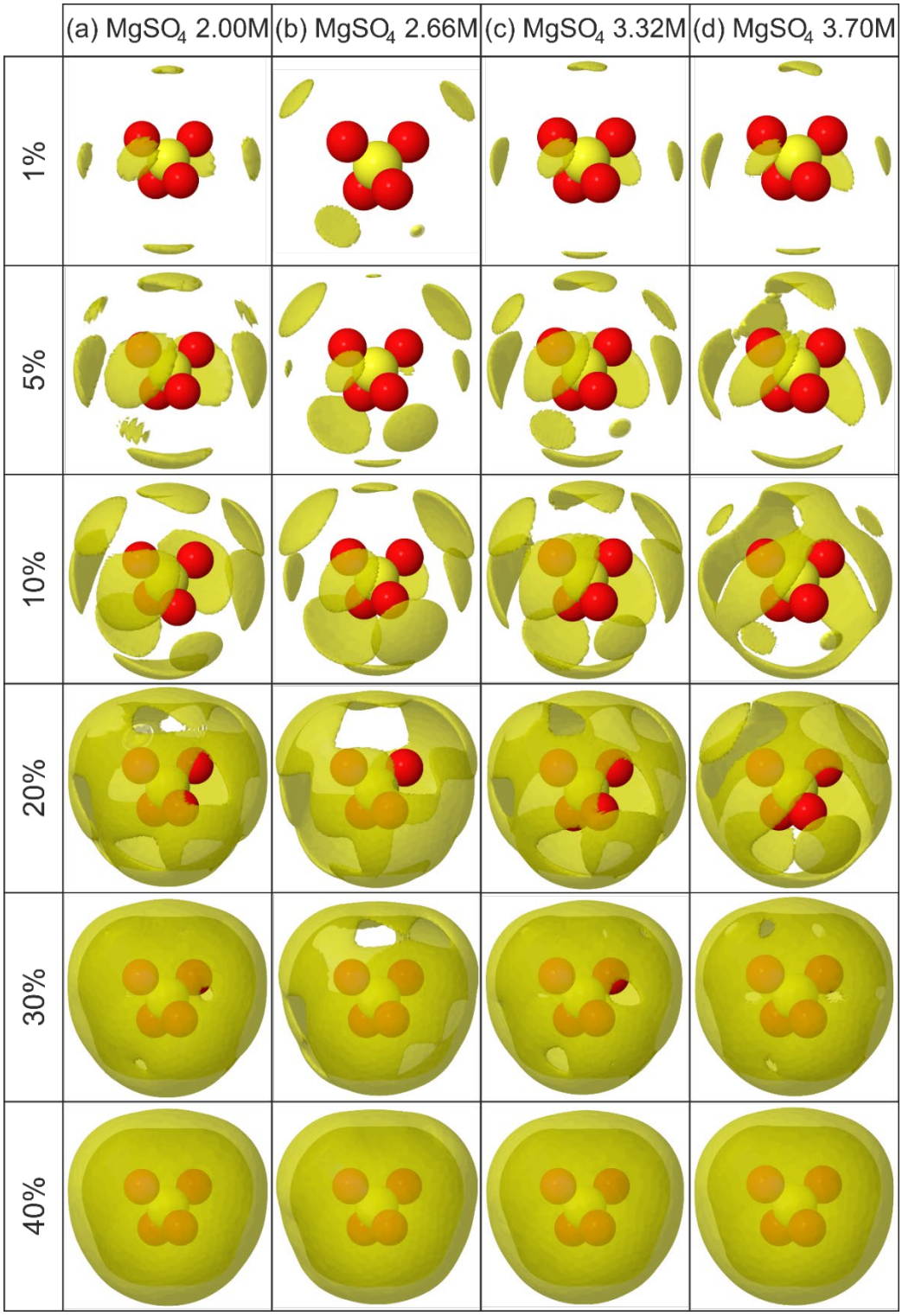

Figure 5-18. *SDF for $H_2O@SO_4$ over r = 1.0 – 5.0 Å, with isosurface% shown from1 – 40%. Atoms displayed are sulfur (yellow) and oxygen (red) representing the central sulfate. Yellow density represents areas most likely to observe a water molecule.*

The SDF displayed above demonstrates that despite the larger structures forming, represented by the chain, ring and disordered structure discussed in section 5.3.2, the secondary building units (SBUs) around the magnesium clusters and sulfate ions remain unchanged by the growing structure. Whilst the overall structure remains consistent, defined by the octahedral and tetrahedral nodes which exist in the same positions, however the area in which the node occupies decreases with

increasing concentration. The decreasing node area, particularly observable at low isosurface%, demonstrates that whilst the SBU structure can be defined in the same way, the structure becomes more rigid and suggests a more solid and less dynamic structure. This conclusion demonstrates that as we increase the concentration, the clusters increase but the overall structure remains consistent as we approach the crystallisation event.

5.3.4 Local Structure Around Water as a Function of Concentration

The final component of the aqueous $MgSO_4$ of interest is the bulk water structure. As examined in sections 3.3.5 and sections 4.3.6.3, the water structure deviates from that seen in pure water, with a major disruption to the second hydration shell, increased probability of closer interactions and general disruption to the long-range structure. With the increasing ion concentration, we expect this disruption to become more dramatic with less 'pure water' character observable, especially at the higher isosurface.

5.3.4.1 Atom-atom g(r) for Ow···Ow

Examining the g(r) it is fairly straightforward to spot the similarities and differences as we increase the concentration. As each feature has been well-defined within the literature, it is possible to allocate each peak to a structural feature and describe what may be changing.

Figure 5-19 shows the atom-atom distances for the Ow-Ow interactions, and whilst the overall envelope of the g(r) is broadly consistent, significant differences can be seen. The first peak, situated at $r \approx 2.80$ Å shows a slight deviation in the peak asymmetry (maxima occur at slightly different r values), however this probably only represents subtle variations in this first hydration shell. As discussed in section 3.3.5, this r-range also contains contributions from the Mg coordinating waters, at approximately $r = 2.85$ Å, and as the ionic concentration increases, the number of bound waters is going to increase, skewing this feature more towards this higher range.

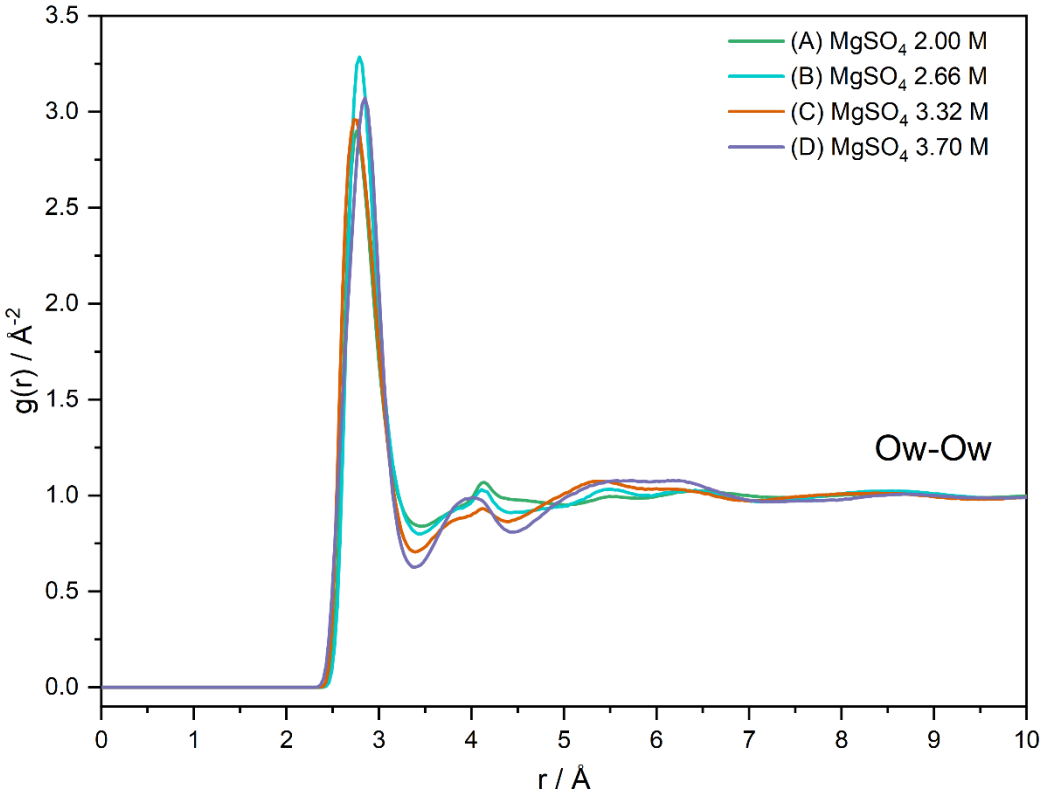

Figure 5-19. *Site-site g(r) for Ow-Ow. Concentrations examined are (A) 2.00 M (chapter 4, green), (B) 2.66 M (cyan), (C) 3.32 M (orange) and (D) 3.70 M (purple). Arrows denote the general trend in the features.*

At greater distances is where we begin to observe more significant variations in the structure between the different concentrations. From previous studies, it can be seen that the 2nd shell structure is largely disrupted, with a peak cut-off occurring after r = 4.14 Å, and this is true for all concentration where the broad feature is cut short of the pure structure.

A trend however can be observed for the lower and upper concentrations where A & B appear similar, and C & D also appear similar. This implies that there is an alteration to the water structure that can be attributed to the increased concentration. Alterations to the g(r) are particularly observable in the r = 3.5 – 5.0 Å region, where the higher concentration samples show a lessened signal at higher r, whereas a stronger albeit broader signal in a closer proximity to the first shell feature. This suggests that as the ionic concentration increases the water moleculars are within a closer proximity to one another to allow for the ionic structure to increase in complexity. In addition to this, the water molecules are likely to interact more with the ionic structure, forming a stabilising intermolecular network. This is a unique observation not previously reported in the literature and suggests a novel $H_2O\cdots H_2O$ solvation shell for the high concentration aqueous $MgSO_4$ samples.

Above r = 5.0 Å, the observable features rapidly broaden, and any structure becomes difficult to interpret. However, at approximately r = 5.5 Å, we begin to observe a peak emerging, which increases in magnitude and broadness as we increase the concentration, suggesting that we may

be observing some 2nd/3rd shell structure for the higher concentrations. For pure water we expect this region to be host to the 2nd shell, ranging from approximately r = 3.5 – 5.5 Å according to Soper[16], however it is difficult to assign the features seen within the variable concentration series as either a continuation of the 2nd shell character, simply with an interruption at r = 4.5 Å, a 3rd solvation shell observed at a closer range or interactions of water between ionic structures.

5.3.4.2 Coordination Number for Ow-Ow as a Function of Concentration

The coordination number has provided useful information on the density of water molecules around a central water and gives quantitative information on whether a contraction of the solvation shells can be observed. From the coordination numbers shown in figure 5-20 we can see a maximum at 5-6 coordination, with higher concentration trending towards a slightly higher coordination. This agrees with the increased water molecule density argument, whereby the increased ionic population causes a densification of the bulk water structure.

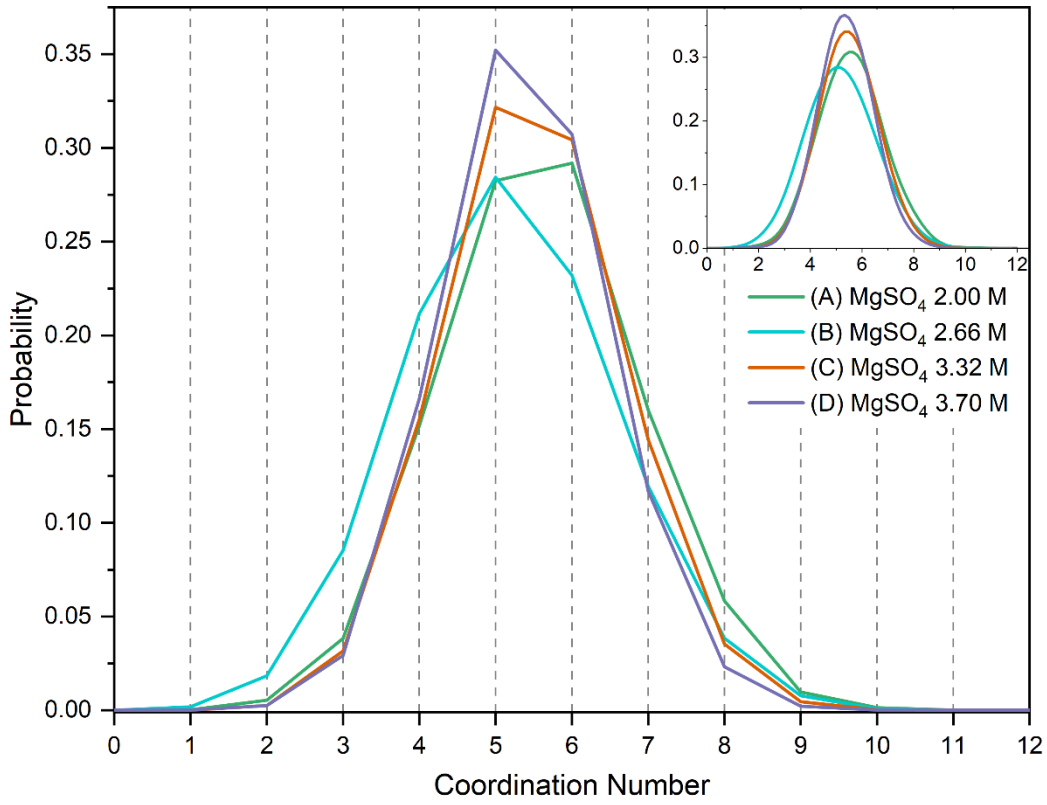

Figure 5-20. *Coordination number for Ow-Ow over concentrations (A) 2.00 M (chapter 4, green), (B) 2.66 M (cyan), (C) 3.32 M (orange) and (D) 3.70 M (purple). Coordination exists over a range of r = 1.0 – 3.4 Å. An inset is provided as a connect spline line graph to highlight the trend in coordination.*

The overall trend does tend towards lower coordination and closer to the values expected for a pure water model, i.e., closer to 4.86 for pure water vs. 6.21 for 2.00 M $MgSO_4$ seen in section 2.4.5.

After confirmation of the relatively unchanged 1st solvation shell structure, questions still remain as to what is happening to the longer-range structure as the concentration increases. The g(r) does

suggest some alteration in the structure; however, it remains difficult to interpret this though 2D information. Coordination numbers provide some useful information for short-range interactions but it becomes hard to differentiate interactions from closely spaced shells as this requires some slightly arbitrary decisions on the r-ranges for each shell. SDF will hopefully be more useful in highlighting the subtle longer-range differences.

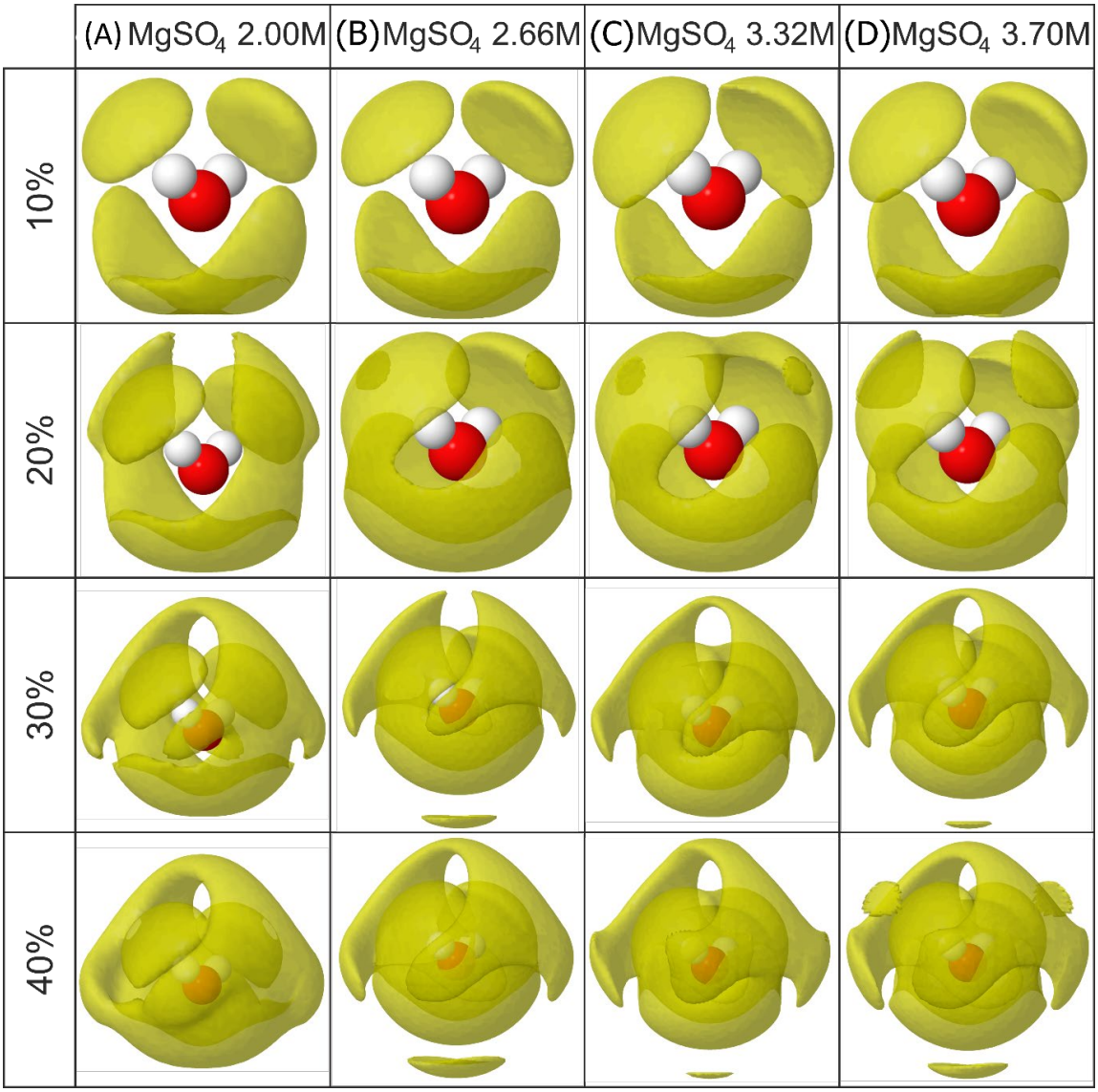

Figure 5-21. *SDF for H_2O@H_2O over r = 1.0 – 5.0 Å, with isosurface% shown from1 – 40%. Atoms displayed are sulfur (yellow) and oxygen (red) representing the central sulfate. Yellow density represents areas most likely to observe a water molecule. Figures 5-21 a-d represent a fragment of this figure for ease of viewing.*

The SDF for the H_2O@H_2O interactions can be found in figure 5-21, and the general trend throughout shows an increasing degree of density as concentration is increased which is to be expected from the increasing ionic population within the simulation box. To understand these interactions in more detail, each % range will be examined in turn to understand how concertation truly affects the SDF.

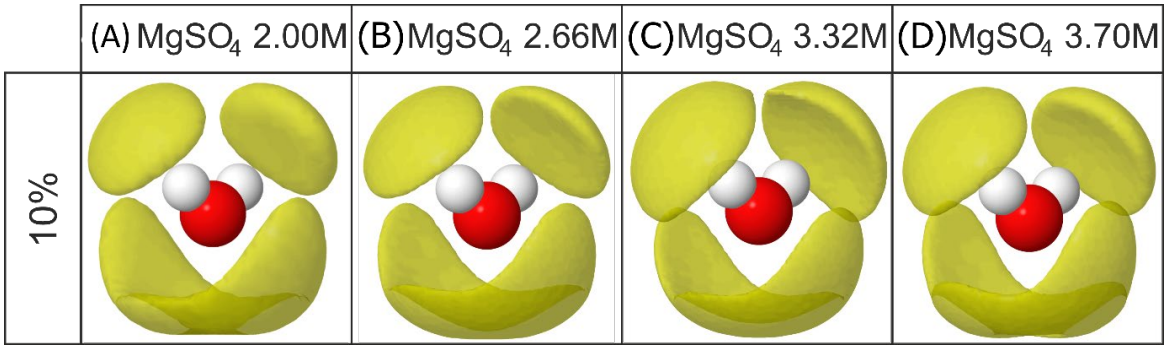

Figure 5-21a. *SDF for H_2O@H_2O over r = 1.0 – 5.0 Å, with isosurface% = 10%. Atoms displayed are sulfur (yellow) and oxygen (red) representing the central sulfate. Yellow density represents areas most likely to observe a water molecule.*

Starting at 10%, we can see that the overall form of the probability density does not change, reaffirming the stability of the 1st shell structure. However, whilst the general shape and position of these features are similar, there is a definite increase in the density above the O-H bond, suggestive of a preference for bonding towards the hydrogen rather than the lone pairs of the oxygen. Regardless of this, the most likely intermolecular interaction between water molecules remains consistent with previous literature and previous data within this project.

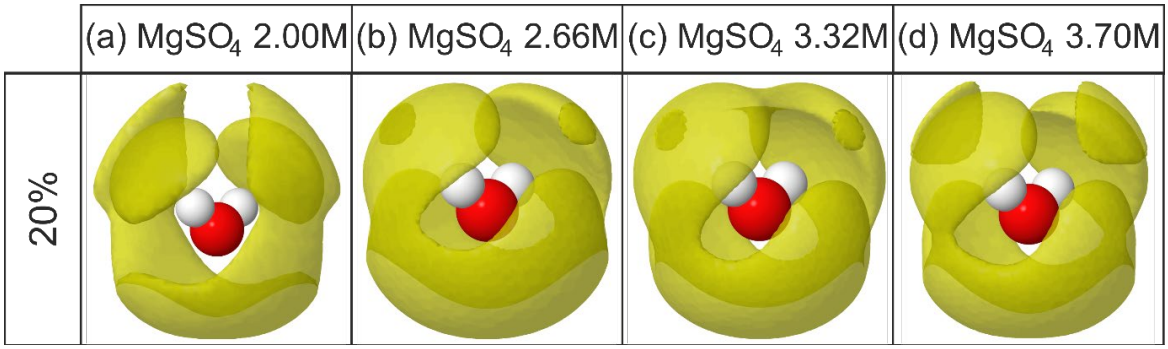

Figure 5-21b. *SDF for H2O@H2O over r = 1.0 – 5.0 Å, with isosurface% = 20%. Atoms displayed are sulfur (yellow) and oxygen (red) representing the central sulfate. Yellow density represents areas most likely to observe a water molecule.*

Expanding the isosurface to 20% we begin to see more significant changes to the probability density. As discussed in section 3.3.5, the 2.00 M sample (A) shows an amalgamation of what in pure water is two separate areas of density, specifically the 1st and 2nd solvation shells. At higher concentrations, this area of probability density is still focussed on the 1st shell interactions, however the densities above the hydrogen (originating from the lone pair acceptor) and below oxygen (originating from the lone pair donation) join to create an encompassing structure. One substantial difference seen between the 2.00 M sample and the higher concentrations is a more defined distinction between the 1st and 2nd hydration shells, and this becomes more obvious at higher isosurface percentage. However, here we can observe the first indications of the more defined structure, where the origins of the arch-like structure sitting at 90° rotation from the O-H density is no longer merged with the 1st shell structure. Furthermore, this structure is far slower to emerge,

where at 2.00 M the arch is half formed, but at higher concentrations it is a simple node. In summary, at 20% we can see the 1st hydration shell becoming more encompassing around the origin, with less free space available at higher concentrations. The distinction between the 1st and 2nd shell becomes more obvious, where at 2.00 M we can see a merging of the two, as concentration increases, we can make out two separate areas of probability.

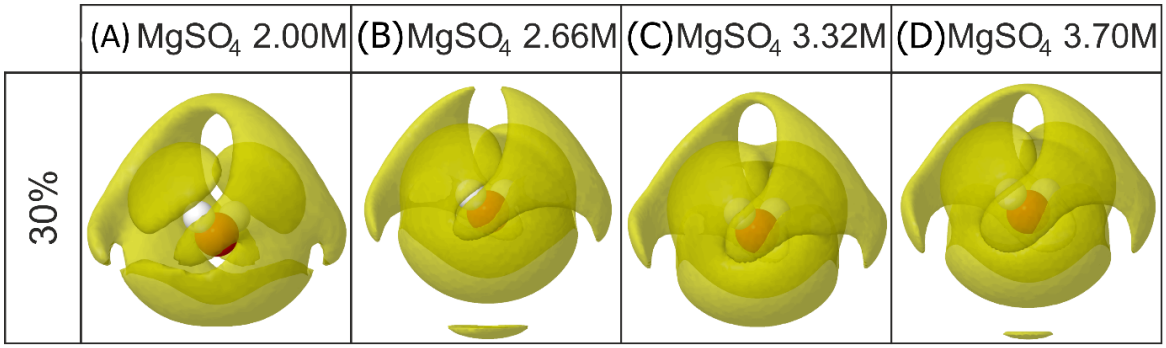

Figure 5-21c. *SDF for H2O@H2O over r = 1.0 – 5.0 Å, with isosurface% = 30%. Atoms displayed are sulfur (yellow) and oxygen (red) representing the central sulfate. Yellow density represents areas most likely to observe a water molecule.*

At 30%, the distinction between the 1st and 2nd shell is far more obvious, with a 3-pronged trigonal distribution being defined as we increase the concentration. At 2.00 M this feature effectively merges with the 1st shell character making it hard to characterise as a separate solvation shell, suggesting that the water structure is a little less defined at this concentration. The increase in definable features suggests that the increased ionic concentration and overall structure forces an increased ordering in the water structure, showing an almost phase like change in the bulk water structure. Whilst we can see a pseudo-phase/anti-phase structure, the 1st shell is almost fully encompassing whereas the 2nd shell shows behaviour more similar to pure water structure. At this percentage we can also observe the beginnings of what can only be assumed to be the 3rd solvation shell, occurring underneath the origin water molecule, suggesting a higher probability of longer-range structure for the higher concentrations. Finally, an outlier must be addressed for the 30% structures, and that is the lack of link in the overriding arch structure for (B), and whilst this may be just an outlier from the model it may be significant and forced by the chain formation occurring at this concentration.

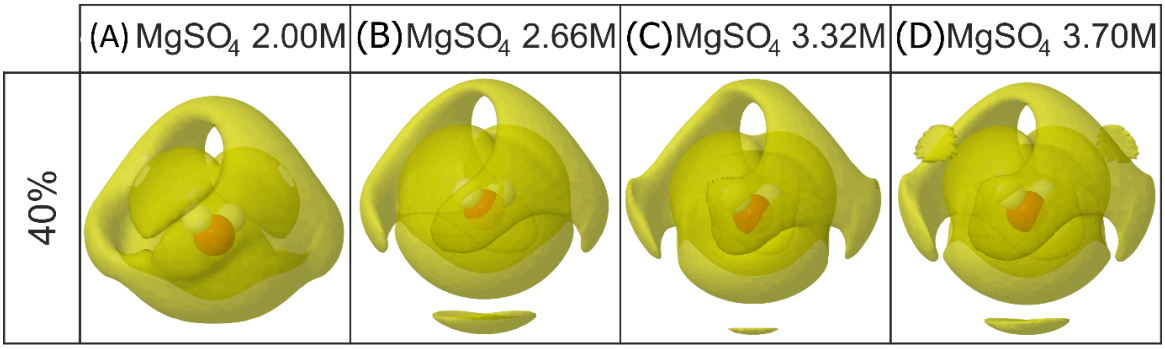

Figure 5-21d. *SDF for H2O@H2O over r = 1.0 – 5.0 Å, with isosurface% = 40%. Atoms displayed are sulfur (yellow) and oxygen (red) representing the central sulfate. Yellow density represents areas most likely to observe a water molecule.*

The 40% isosurface further supports the trends previously discussed, with distinct 1st and 2nd shell character being obvious, however expanded particularly for (C) and (D). The shell character remains mostly distinct and separate for the higher concentrations, confirming that the water structure does become more defined as we increase the $MgSO_4$ concentration. We can also observe areas where the O-H node does merge slightly with the 2nd shell probability density, however the arch-like structure remains separate and un-merged unlike the 2.00 M SDF. The incomplete arch along the O-H vector remains present in all concentrations, suggesting that this area is occupied by a different structural motif, likely from the ionic structure interrupting this area. What is interesting about this arch is the increased broadness, suggesting more distributions and bonding modes being adopted within the bulk water structure. It is harder to define exactly what causes this probability density, especially as it belongs to the more difficult 2nd shell structure. This density is likely due to the aforementioned g(r) feature seen at around 4.0 Å, as this is the only differentiating feature occurring in both the g(r) and SDF. The final probability density of interest occurs in sample (D), showing that the highest concentration of 3.70 M has some distinct 3rd shell character, in-phase with the O-H nodes seen within the 1st shell. This suggests that the increased concentration does contract the bulk water structure, to a point where extended structure is visible within the standard r = 1.0 – 5.0 Å SDF range used throughout this project. Overall, the 40% isosurface shows a continuation of the trends found throughout, plus some unique structural modes not seen within other aqueous phases studied.

Throughout the SDF discussion significant trends have been observed as both the concentration and isosurface fraction increase, creating an interesting narrative describing how the water structure adapts to accommodate the increasing number and size of ionic cluster structures. Whilst overall it follows a similar phase/anti-phase type structure to that of pure water, many unique features do emerge with the introduction of $MgSO_4$ at various concentrations. In general, throughout all concentrations an encompassing 1st shell structure is followed by the 3-pronged

2nd shell arch structure. This sheds light on a unique and previously unreported change in the bulk water structure as a direct result of introducing ions over a concentration range.

5.4 Conclusion

Using EPSR to model the structure as the concentration of $MgSO_4$ is increased shows a dramatic increase in complexity, showing how, as the solubility limits are approached, the clusters slowly begin to resemble those found in the solid-state structure.

Initially in chapter 3, it was determined that the ions arrange themselves in solution to exist as primary magnesium-based octahedra building units with varying ratios of sulfate/water ligands. Upon the increase of the ionic component, these primary building units begin to assemble to create more complex chain and ring structures. These structures were discussed in detail in section 5.3.2, where these structures were elucidated, but by the highest concentrated solution clusters were forming that resembled an almost solid-like structure. Despite the increase in structure with regards to the ionic interactions, the primary building units of the magnesium octahedra remain consistent with the only changes being the sulfate:water ligand ratio.

Considering the $SO_4\cdots H_2O$ structures it was found that overarching description of the structural interactions does not change greatly but as the concentration series progresses the finer detail does change. The interactions become both sharper and occur at a lower r, representing how these species approach each other at shorter range consistent with a higher concentration. This can be reaffirmed by the SDF which shows smaller areas of probability density, demonstrating how the movement and occupation of space of the interacting molecule decreases and defines a more rigid structure.

A similar narrative can be established for the $H_2O\cdots H_2O$ structure where the structure remains similar through the concentration series, but akin to the $SO_4\cdots H_2O$ structure, it becomes more refined and compressed. This is particularly highlighted by the emergence of third shell structure in the highly concentrated samples, demonstrating a preference of interactions closer to the origin molecule. This can be attributed to a more rigid and defined structure, like that of ice[17] and a compression of the solvent system due to ions occupying a larger percentage of the system overall.

The $SO_4/H_2O\cdots H_2O$ interactions can also be related back to the stabilising effects of intermolecular interactions on the ionic structure. This is particularly prominent in the $SO_4\cdots H_2O$ interactions, where the octahedral and tetrahedral nodes are likely both stabilising the bulk water but also the *coordinated* water. This can be observed for the $H_2O\cdots H_2O$ intermolecular structure to a lesser degree, where it mostly resembles a pure water system[16], however alterations to the SDF densities do suggest an alteration to both accommodate but likely also stabilise the ionic structure.

Overall, it can be found that increasing the concentration of the $MgSO_4$ system causes an increase in the number of ionic interactions where the octahedra and tetrahedra eventually join to create

chain and ring structures. At the highest concentration, these begin to cluster and mimic the solid-state structure, particularly of $MgSO_4 \cdot 7H_2O$. It can also be found that intermolecular interactions originating from the $SO_4 \cdots H_2O$ and $H_2O \cdots H_2O$ both resemble what can be found in the literature but also novel interactions that can be found to stabilise the ionic structure.[6,11,15]

The work described both this chapter and throughout this study provides a deeper understanding of the aqueous phase structure of $MgSO_4$ utilising an X-ray and neutron scattering, EPSR methodology. The structure of the primary building blocks was shown to largely agree with previous work found in the literature, but previously unreported intermolecular interactions between $SO_4 \cdots H_2O$ and $H_2O \cdots H_2O$ were observed. To the authors knowledge this is the first reported modelling of aqueous magnesium sulfate determined through total scattering and the extension of this to higher concentrations has enabled an insight into possible crystallisation pathways.

5.5 Future Work

This project has enabled studies into the structure of aqueous magnesium sulfate not previously possible due to limitations in instrumentation and experimental approaches. It has been shown that total scattering experiments and large-box refinement approaches are an ideal combination for unlocking a truly monumental amount of information pertaining to the emergent features of highly concentrated solutions. However, whilst the work presented within this project is novel, many improvements and further experiments are certainly possible.

Focussing initially on $MgSO_4$, increasing the number of concentration points within the series would provide a more detailed view of the evolving structures. As time was limited, data for only four concentrations could be collected and analysed, and whilst this provides an interesting narrative, further questions remain regarding the structure evolution. One such example is how the ring formation occurs, as between 2.66 M and 3.32 M there is a smaller change in structure observed despite the similar change in concentrations between the other samples. This suggests additional measurements close to this concentration might yield more detail. Two possible experimental routes could be taken to probe this concentration range, either additional fixed concentration experiments with smaller gaps between the values or an in-situ increase in concentration with rapid experiments to probe the system change over a full range of concentrations. The former of these experiments would be possible in the laboratory but the latter would need a more complex in-situ setup and short exposure times only possible at a synchrotron.

Further experiments could also be envisaged such as varying the solvent to examine how the magnesium clusters would interact and potentially inhibited by this simple change to the system. $MgSO_4$ is very soluble in water but less so in other solvents, so it would be interesting to examine what structure evolves from both mixed solvent systems but also non-aqueous systems. Varying this system even further, introducing other ions to the system may increase interest in both ion-ion interaction but also begin the foundations of material formation and pre-cluster structure.

This work would also benefit massively from additional neutron scattering data, with varying deuterations, enabling a more detailed examination of the structure, specifically the water structure. Whilst X-ray data do provide accurate structural information for the water, specifically the oxygen, it does not provide information on the hydrogen locations and therefore this is an area that is less well defined in the EPSR models. Finally, whilst the in-house instrument is particularly good for aqueous-phase experiment, exceeding data quality of other such instruments, the X-ray data could be improved upon further by use of X-ray synchrotron data. However, this is perhaps less crucial than collection of neutron data.

References

1 Y. Zhou, T. Yamaguchi, K. Yoshida, C. Fang, Y. Fang and F. Zhu, *J. Mol. Liq.*, 2019, **274**, 173–182.

2 D. T. Bowron and S. D. Moreno, *J. Phys.: Condens. Matter*, 2013, **25**, 454213.

3 D. Bowron, J. Finney and A. Soper, *J. Phys. Chem. B*, 1998, 102, 3551–3563.

4 F. Lo Celso, R. Triolo, F. Ferrante, A. Botti, F. Bruni, R. Mancinelli, M. Ricci and A. Soper, *J. Mol. Liq.*, 2007, **136**, 294–299.

5 T. Yamaguchi, S. Imura, T. Kai and K. Yoshida, *Z. Naturforsch. A.*, 2013, **68**, 145–151.

6 F. Sebastiani, A. V. Verde, M. Heyden, G. Schwaab and M. Havenith, *Phys. Chem. Chem. Phys.*, 2020, **22**, 12140–12153.

7 G. Balasubramanian, S. Murad, R. Kappiyoor and I. K. Puri, *Chemical Physics Letters*, 2011, **508**, 38–42.

8 P. W. Atkins and Julio. De Paula, *Atkins' Physical chemistry*, 2014.

9 A. K. Soper, *GudrunN and GudrunX*, ISIS, Oxford, ISIS, Oxford, 2012.

10 *Origin(Pro) Version 9.8.0.200 (Academic)*, OriginLab Corporation, Northampton, MA, USA.

11 R. Buchner, T. Chen and G. Hefter, *J. Phys. Chem. B*, 2004, **108**, 2365–2375.

12 E. Iype, S. V. Nedea, C. C. M. Rindt, A. A. van Steenhoven, H. A. Zondag and A. P. J. Jansen, *J. Phys. Chem. C*, 2012, **116**, 18584–18590.

13 C.-C. Wang, M. Wang, H.-Q. Cai, Q.-W. Zhang, Y.-Y. Li and H.-B. Yi, *J. Mol. Liq.*, 2019, **278**, 33–42.

14 S. Lenton, N. H. Rhys, J. J. Towey, A. K. Soper and L. Dougan, *Nat Commun*, 2017, **8**, 919–919.

15 M. Kulichenko, N. Fedik, K. V. Bozhenko and A. I. Boldyrev, *J. Phys. Chem. B*, 2019, **123**, 4065–4069.

16 A. K. Soper, *ISRN Phys. Chem.*, 2013, **2013**, 279463.

17 A. Soper, *Water and ice structure in the range 220 - 365K from radiation total scattering experiments*, 2014, vol. 187.